



UNIVERSIDAD DE CHILE.
FACULTAD DE CIENCIAS FÍSICAS Y MATEMÁTICAS.
DEPARTAMENTO DE FÍSICA.

PHASE SHIELDING SOLITONS

**TESIS PARA OPTAR AL GRADO DE
MAGISTER EN CIENCIAS MENCIÓN FÍSICA**

YAIR DANIEL ZÁRATE DEVIA

PROFESOR GUÍA:
MARCEL CLERC GAVILÁN

MIEMBROS DE LA COMISIÓN:
**IGOR BARASHENKOV VLADILENOVICH
MÓNICA GARCÍA ÑUSTES
MARIO MOLINA GÁLVEZ**

SANTIAGO DE CHILE
AGOSTO 2013

*...Dedicado a mis seres más queridos,
aquellos que nunca leerán esta tesis.*

Resumen

Los solitones son el fenómeno universal más profundamente estudiado, debido a los innumerables sistemas físicos en los cuales se observa. Estas soluciones corresponden a estados localizados y coherentes que surgen naturalmente en sistemas extendidos, siendo una de sus propiedades más fascinantes el hecho de que pueden ser tratados como partículas macroscópicas a pesar de estar formados por numerosos componentes microscópicos.

Desde su primera descripción, realizada por J. S. Russell en 1884, el estudio de solitones se centró en sistemas conservativos por más de cien años. Sin embargo, los pioneros trabajos de Alan Turing e Ilya Prigogine demostraron que los sistemas fuera del equilibrio se auto-organizan por medio de la generación de estructuras disipativas. Hoy en día, sabemos que es justamente este mecanismo el que permite la formación de solitones disipativos en sistemas con inyección y disipación de energía.

Nuestro principal interés ha sido caracterizar de forma analítica y numérica a los solitones que emergen en sistemas forzados paraméricamente—sistemas forzados por medio de un parámetro efectivo que varía en el espacio y/o tiempo. Los sistemas forzados paraméricamente pueden experimentar una resonancia paramétrica, la cual se caracteriza por una respuesta subarmónica (submúltiplos de la frecuencia natural del sistema). Dada la complejidad que presentan los sistemas paraméricos, focalizamos nuestro estudio en la ecuación de Schrödinger no lineal disipativa forzada paraméricamente (PDNLS). Este modelo caracteriza bien la dinámica de sistemas forzados paraméricamente, en torno al punto de aparición de la resonancia paramétrica, en el límite de baja disipación e inyección de energía. Los solitones disipativos, presentes en PDNLS, típicamente muestran una estructura de fase uniforme. Dichas estructuras han sido ampliamente utilizadas para describir a los solitones hidrodinámicos que aparecen en el experimento de Faraday, estados localizados de la magnetización en un hilo magnético, o los clásicos solitones presentes en una cadena de péndulos con soporte verticalmente vibrado, entre otros.

Por medio de simulaciones numéricas interactivas de solitones disipativos en la ecuación PDNLS, hemos logrado observar una interesante dinámica de frentes de fase hasta ahora desconocida. Estos frentes de fase se propagan hasta alcanzar un punto de equilibrio estacionario arbitrario. A este tipo de solitones los hemos llamado solitones escudados por la fase (phase shielding solitons), dado que la estructura final de fase pareciera proteger al módulo del solitón. Hemos logrado caracterizar analíticamente estas soluciones localizadas, determinando ocho posibles configuraciones. Los solitones estudiados poseen una talla característica dada por el tamaño de la estructura de fase estacionaria.

Además, extendimos nuestro estudio al caso bidimensional, mostrando los resultados, dos tipos de phase shilding solitons bidimensionales; axialmente simétricos y asimétricos. Los primeros pueden ser entendidos como una rotación en 2π de las soluciones simétricas encontradas en el caso unidimensional. Por su parte, las soluciones asimétricas bidimensionales

presentan propiedades mucho más interesantes, ya que su estructura final de fase contiene todas las configuraciones halladas en el caso unidimensional.

Con el fin de corroborar la existencia de solitones disipativos con estructura de fase no uniforme en sistemas físicos, realizamos simulaciones numéricas de diversos sistemas paramétricos reales. Satisfactoriamente, concluimos que el fenómeno phase shielding soliton es universal, y esperamos que pueda ser prontamente observado experimentalmente.

Abstract

Solitons are the universal phenomenon more deeply studied, due to the many physical systems in where they emerge. These solutions correspond to localized and coherent states naturally arising in extended systems, one of its most fascinating properties is that they can be treated as macroscopic particles despite being composed by many microscopic components.

Since its first description, done by J. S. Russell in 1884, the study of solitons was held to conservative systems for over hundred years. However, the pioneering work of Alan Turing and Prigogine showed that nonequilibrium systems are self-organizing through generating dissipative structures. Nowadays, we know that it is precisely this mechanism that allows the formation of soliton in systems with gain and loss of energy.

Our main interest has been to characterize analytically and numerically the solitons that emerge in parametrically forced systems—systems forced through an effective parameter that varies in space and/or time. Parametrically forced systems may experience parametric resonance, which is characterized by a sub-harmonic response (sub-multiples of the natural onscillation frequency of the system). Given the complexity that parametric systems have, we focused our study on the parametrically driven and damped nonlinear Schrödinger equation (PDNLS). This model characterizes well the dynamics of parametric systems around the onset of the parametric resonance, in the limit of small dissipation and injection of energy. Dissipative solitons present in the PDNLS equation, typically show a uniform phase structure. Such localized structures have been widely used to describe the non-propagating hydrodynamic solitons arising in the Faraday’s experiment, and localized states of magnetization in magnetic wire among others.

By means of interactive numerical simulations of dissipative solitons in PDNLS equation, we have observed an interesting phase fronts dynamics hitherto unknown. These phase fronts propagate until reaching an arbitrary steady point. Such kind of solitons have been called phase shielding solitons (PSS), since the phase structure seems to protect the modulus of the soliton. We achieved an analytically characterization to these localized solutions, determining eight possible configurations. Studied solitons have a characteristic length given by the size of the stationary phase structure.

In addition, we extended our study to the two-dimensional case, results show two types of $2D$ PSS; axially symmetric and non-symmetric. The former can be understood as a 2π rotation of the symmetric solutions found in the one-dimensional case. For its part, $2D$ asymmetric solution have properties much more interesting, since its final phase structure contains all configurations found $1D$.

With the aim of corroborating the existence of dissipative solitons with non-uniform phase structure in physical systems, we conducted numerical simulations of various real parametric systems. Successfully, we conclude that phase shielding solitons are a universal phenomenon, and we hope that they can be observed experimentally.

Agradecimientos

Primero que nada y antes que todo agradezco profundamente a mi madre por su constante apoyo y entrega. Ella me enseñó que los sueños siguen siendo ilusiones mientras uno no haga nada por alcanzarlos, y que lo más importante en la vida es la felicidad. Hoy estoy logrando un sueño y te lo debo a tí. De igual forma, no tengo palabras para agradecer a mi esposa quien con su amor infinito me ha convertido en una mejor persona y ha aceptado los sacrificios que implica mi carrera. A mi preciosa hija que día a día me contagia con su curiosidad por entender al mundo. Ambas iluminan mi vida llenandola de felicidad.

Esta tesis no hubiese sido posible sin Marcel Clerc, quien me acepto como discipulo y terminó convirtiendose en mi *best man*, extendiendo su enseñanza más allá de lo meramente académico. Él me introdujo al verdadero quehacer científico, logrando que cada día ame más esta labor.

Agradezco a toda mi familia de Iquique, que me vieron partir hace mucho y siempre hicieron grato mi regreso. En especial a mi padre y hermano por los días y noches de relaxo junto al mar. De igual forma, a mi abuelita quien me crió y consintió desde pequeño. A todos mis compañeros de Licenciatura que siguen en la lucha por convertirse en científicos, especialmente a Guillermo Retamales, Alejandro Martínez, Santiago Rojas y Pablo Ortíz, a quienes considero grandes amigos, espero pronto concreten también ellos sus sueños. A toda la familia de mi esposa, quienes me brindaron mucho más de lo que hubiese imaginado. Estoy realmente agradecido por su acogida y hoy me hace muy feliz el poder decir que soy uno más del clan.

Quisiera además extender mi gratitud a Mónica García Ñustes quien me enseñó que en cada ámbito importante de nuestra vida poseemos un jefe, a los cuales nunca le debemos fallar; irónicamente ella se convirtió en uno de los míos. De la misma forma quisiera dedicar unas palabras a Nicolas Verschuere por su tiempo, disposición y amistad, fue grato haber trabajado junto a él. Espero que el vínculo creado con ambos no se pierda con los años.

Extiendo mi gratitud a todos mis profesores que forman parte de mi educación y fomentaron mi motivación por la ciencia. Quisiera dentro de ellos destacar a David Gotlieb, Alejandro Valdivia, Mario Molina, Enrique Tirapegui, Claudio Falcón, Saliya Coulibaly y Leopoldo Soto, ellos en conjunto forman el científico que aspiro ser. De igual forma agradezco a los miembros de la comisión por su tiempo y disposición. Sus correcciones y comentarios me ayudaron a mejorar la version final de esta tesis.

Finalmente, agradezco a mis compañeros de postgrado, quienes me mantuvieron al tanto de los progresos actuales en Física, tanto a nivel nacional como internacional. Una de las instancias que siempre recordaré con nostalgia es el *lunch meeting*, ya que me permitio conocer a mis compañeros de trabajo más allá de la investigación que desarrollaban. Agradezco al DFI por su acogida y a todo el personal que mantiene todo funcionando.

Contents

Abstract	iv
Agradecimientos	v
I Introduction & Conceptual Overview	1
1 Solitons in Nature	2
2 Theoretical Background	7
2.1 Parametric resonance.	7
2.2 Amplitude equation.	10
2.2.1 Fredholm method.	12
2.3 Hilbert transform.	15
2.3.1 Hilbert transform relations for complex sequences.	16
II Solitons in Parametrically Forced System	19
3 Dissipative Solitons	20
4 Parametrically Driven and Damped Nonlinear Schrödinger Equation	22
4.1 The universality of the PDNLS model.	22
4.2 The bifurcation scenario of PDNLS	23
4.3 Uniform phase solitons in PDNLS	25
4.4 UPS in two-dimensional systems	28
III Control of Dissipative Localized Structures	30
5 Non-propagative Hydrodynamics Solitons in Inhomogeneous Media	31
5.1 Hydrodynamic soliton motion in a tilted basin	31
5.1.1 Experimental setup and procedure	32
5.1.2 Experimental results	33
5.2 Theoretical description	35
5.2.1 Dissipative solitons in homogeneous media	36
5.2.2 Effect of channel inclination	37

IV	Phase Shielding Solitons	41
6	Phase Shielding Solitons in PDNLS	42
6.1	Preliminary numerical results	43
6.2	Analytical approach to dominant order	46
6.2.1	Higher order corrections	49
6.3	Phase front dynamics	51
6.4	Stability analysis for uniform phase soliton	52
7	Phase Shielding Solitons in Two-Dimensional System	57
7.1	Numerical observation of phase shielding solitons in $2D$ -PDNLS	57
7.2	Phase front profile in $2D$	60
7.3	Phase front dynamics	62
8	PSS in Physical Systems	63
8.1	Magnetic wire	63
8.1.1	PSS in the magnetic wire	65
8.2	Forced magnetic layer	66
8.2.1	PSS in the magnetic layer	67
	Conclusions & Future Work	68
	Bibliography	77
	Appendices	78
A	Contributions	79
A.1	Can non-propagating hydrodynamic solitons be forced to move?	79
A.2	Dissipative localized states with shieldlike phase structure	91
A.3	Phase shielding soliton in parametrically driven systems	96

Part I

Introduction & Conceptual Overview

Chapter 1

Solitons in Nature

Certainly, solitons are the most paradigmatic structures that we can find in nature since they can be understood as macroscopic particles despite being composed of countless microscopic constituents. Furthermore, they are characterized by a family of continuous parameters, typically used to describe particles, such as: position, charge, width, to name a few. The soliton phenomenon was first discovered and described by John Scott Russell (1808–1882), who observed a solitary wave (a wave packet or pulse) that maintains its shape while propagating at constant speed on the Union Canal in Scotland. Notwithstanding this, nonlinear waves appear naturally in any system which has the capability to produce waves. For example, they can be observed in several fields such as fluids, plasma, and solids (at both macroscopic and microscopic level) [1]. Undoubtedly, its intriguing properties have captivated scientists for decades. Even more so nowadays where potential technological applications are more evident, the thorough understanding of these structures becomes a crucial task.

In the beginning, these localized wave phenomena were only explored in conservative systems. Since its first description (J. S. Russell), the mechanisms necessary to generate a soliton were unknown. In the 1870's it was Rayleigh [2] who envisioned that the combination of dispersion and nonlinearity can lead to the formation of solitary waves, feature which had been ignored by the previous models for shallow water. In 1895 Korteweg and De Vries [3] derived a model of shallow water waves that combined dispersion and nonlinearity. That model, known as the Korteweg-deVries (KdV) equation, admits solitary wave solutions that fit the description of Russell's solitary waves. Subsequently, the study of solitary waves remained on hold for sixty years because it was considered a phenomenon restricted to the context of shallow water waves. It was not until the results of the Fermi, Pasta and Ulam problem in 1955 [4] that the interest in this topic was renewed. They conducted numerical simulations of strong interacting phonons in a lattice, in order to characterize the heat transfer. Surprisingly, the energy did not exhibit thermalization, that is, the system did not exhibit an equipartition process. On the contrary, it developed a localized (quasi-periodic) oscillatory state. Zabusky and Kruskal (1965) [5] demonstrated that by using a continuous approximation, the FPU problem can be described by the KdV equation. They argued that it was the fact that soliton¹ solutions of the KdV equation can pass through one another without affecting the asymptotic shapes that explained the quasi-periodicity of the waves in the FPU experiment. In short, thermalization process could not occur because of a certain “soliton symmetry” in the system which broke ergodicity. In 1967 Gardner, Greene, Kruskal

¹They called these waves solitons to emphasize the fact that these special solitary waves have photon-like collision properties.

and Miura [6] developed a method, called the inverse scattering transform (IST), to solve analytically the KdV equation. All the aforementioned discoveries marked the birth of the theory of solitons [7]. Even more, they triggered the development of future theories to solve nonlinear problems in integrable physical systems such as nonlinear Schrödinger (NLS) and sine-Gordon (SG) equations [8, 9, 10]. Moreover, the development of the nonlinear science allows the study of new phenomena such as: patterns, kinks, vortices, breathers, to name a few.

The development of the soliton theory as well as the nonlinear techniques was based on idealized integrable models that serve only as approximations to many natural phenomena. Such integrability property is very fragile, and the smallest perturbations can destroy it. Many of these perturbations inherently arise in physical problems, and include dissipative effects, external driving, non-local effects and inhomogeneities. A detailed description of these so-called near-integrable equations is described in a comprehensive review by Kivshar and Malomed (1989) [11]. They showed that solitons are observed in many near-integrable equations, and those solutions do not share the same properties as their integrable counterparts. For example, in most cases collisions between near-integrable solitons are inelastic, resulting in the formation of radiation, the formation of breathers or even the disintegration of solitons. Indeed unstable soliton solutions are frequently encountered in near-integrable equations. Although these solutions clearly do not satisfy the “indestructible” criteria of Zabusky and Kruskal’s [5] (original definition), the term “soliton” is widely used to define these spatially localized waves. Soon after the development of soliton theory, it was realized that the inverse scattering transform method can be used to study the effect of perturbations on solitons. Further efforts were done to achieve an analytical method to study solitons in near-integrable equations [12].



Figure 1.1: Several dissipative localized structures found in nature.

The pioneer works of A. Turing and I. Prigogine [13, 14] unveiled that macroscopical systems maintained out of equilibrium, by the injection and dissipation of energy, are self-organizing, showing a wide range of universal phenomena which are independent from the microscopic details of the system under consideration. Most systems found in nature in our

daily scale, are not in thermodynamic equilibrium; they are changing or can be triggered to change over time; furthermore, they are continuously and discontinuously subject to flux of matter, momentum and energy to and from other systems. Due to the complexity of non-equilibrium systems, are required more adequate concepts to achieve an accurate description of the universal phenomena exhibited by them. The capability of self-organization of non-equilibrium systems allows the emergence of dissipative structures such as patterns and localized states [15, 16, 17] [see Fig. 1.1]. Among the latter are found dissipative solitons. These localized dissipative solutions correspond to a coherent collective state despite the fact that they are formed by countless constituents. As its conservative counterpart, they exhibit properties typically associated with particles. Consequently, one can characterize them with a family of continuous parameters. Hence, they can be also considered a particle-type solutions. In the last decades, this kind of localized solutions or dissipative solitons have been observed and studied in several non-equilibrium systems including: chains of coupled oscillators, fluids, optic, magnetic and granular media, to mention a few [17, 18, 19]. The variety of systems exhibiting these solutions confers them a universal nature (robust phenomenon).

The purpose of this thesis is to investigate dissipative localized structure arising in a subclass of non-equilibrium system: parametrically forced systems—systems driven through the temporal (spatial) modulation of its parameters. Although these systems are a very small part of all possible non-equilibrium systems found in nature, they have been the focus of several studies because of the many universal phenomena exhibited for them. Among these we find, vibrated container with Newtonian fluid [20], fluidized and vibrated granular beds [21, 22], magnetic media driven by oscillating external magnetic fields [23], and optical parametric oscillator [24]. The new nonlinear techniques, available to characterize these kind of systems theoretically, have shown that universal phenomena can be contained in more reduced equations that govern the physical system in particular. These equations are derived from the physics of the problem and finally used to describe robust phenomena. The interesting thing is that these models do not depend on the particular underlying physics of the particular system under study. In particular we will focus our study on dissipative solitons exhibited in the well-known parametrically driven and damped nonlinear Schrödinger equation (PDNLS), which is a minimal and universal model that describes the dynamics of numerous physical, parametrically forced systems in the limit of small injection and dissipation of energy. These localized structures have been studied by decades [25, 26, 27, 28]. Historically these localized structures have been characterized under the assumption of having a constant phase. However, they lose its uniform steady-state in the presence of inhomogeneities, as well as also in the interaction with other dissipative solitons [29, 30]. Moreover the phase profile apparently leads the dynamics of interaction between this kind of structures [31].

This thesis contains a detailed study of the phase structures of dissipative solitons which appears surrounding the bell-shaped modulus of a single dissipative soliton, even in homogeneous media. We characterize the front phase propagation exhibited by the dissipative solitons in PDLS after slight perturbations. These phase fronts undergo a non-trivial propagation until reaching the steady final structure, far from the soliton core. Solitons with a phase structure represent a novel type of solution unknown in PDNLS, and for our knowledge it has not been reported in experiments or theoretical studies conducted in parametrically forced system. In this work we show the relation between the dissipative solitons with uniform phase and this novel solution that exhibits a steady phase structure. Moreover, we have extended this study to two-spatial dimensional system. The extra dimension produce interesting effects on phase structure showing two type of solutions in $2D$ -PDNLS, one with

an axial symmetry, and other asymmetric that can be understood as a composition of two phase structures with semi-axial symmetry.

The readers of this manuscript will find here all the tools needed for understanding of phase shielding solitons up to the level achieved after almost three years of research. This thesis is organized into four parts composed by various chapters, comprising the main research developed during the course of this work.

In the first part of the thesis, we deliver an historical contextualization for the solitons, which are the main topic of this research work. Then, in Chapter 2, we introduce the basic theoretical concepts used in the developed of this thesis. This background will allow us to comprise the different aspects of the main topic (dissipative solitons with phase structure). In this Chapter is clarified the concept of parametric forcing and resonance, the nonlinear technique of amplitude equations, and finally we show an useful application of the Hilbert transform when dealing with analytic signals.

Part II comprises the state-of-the-art of solitons. Chapter 3 clarifies the main differences found between conservative solitons—solitons found in system in (thermodynamic) equilibrium—and its extension, dissipative solitons, arising in non-equilibrium system, which are of particular interest in this thesis. Chapter 4 brings a review of dissipative solitons typically exhibited in parametrically forced systems. The parametrically driven and damped nonlinear Schrödinger equation is presented and its universality discussed. This model is highly used to describe parametrically forced system near to the quasi-reversal limit. Uniform phase solitons (UPS), naturally arising in PDNLS, are characterized in both one-dimensional case as well as in two-dimensional systems. They constitute the basis of the novel soliton solution, arising in parametrically forced system, which is the main result of the present research work.

Part III exposes a theoretical and numerical study conducted to describe the dynamics of non-propagating hydrodynamic solitons naturally arising in surface of Newtonian fluids vertically vibrated. PDNLS equation models this system in the limit of small gain and loss of energy. Chapter 5 shows that the dissipative solitons with uniform phase naturally arising in PDNLS are a good description for the hydrodynamic solitons exhibited in the Faraday's experiment. A mechanism of manipulation for this localized structures is proposed since the inclination of the channel produce drifts of the solitons. The study shows good agreement between theoretical predictions and numerical analysis with experimentally observed dynamics for these localized structures. These results represent one of the first achievements of the present research work.

Part IV discloses the most relevant discovery obtained during the research work; phase shielding solitons (PSS). In Chapter 6 we study the emergence of phase fronts on dissipative solitons, which represent a new perspective of solitons study in parametrically driven systems. Until now, the phase of single solitons was always considered uniform in most of the aforementioned physical systems. However, a more complete analysis could demonstrate the existence of PSS solutions in such physical scenarios. In the present chapter we conduct analytical and numerical studies of phase shielding solitons in one-dimensional system. Moreover, an analytical description of PSS solutions and their dynamics is presented. A numerical stability analysis is also performed to establish the connection between UPS and PSS solutions.

In Chapter 7 the study of localized structures, presented in the previous sections, is extended for two-dimensional systems. This extension is not evident. The principal motivation to conduct this extension is that most of the experimental observations of localized dissipative structures in parametrically driven systems have been reported in two spatial dimensions.

For instance, in fluid surface waves [32], oscillons in granular media [33], and isolated states in thermal convection [34]. Furthermore, the greatest difficulty to characterize theoretically localized states in two spatial dimensions is the lack of analytical expressions of these states. In this Chapter we conduct an analytical and numerical study of the dissipative solitons arising in two spatial dimensional PDNLS in order to understand the existence, stability properties, and dynamical evolution of its front phase, which appear for proper both system size and parameter region in PDNLS.

To corroborate the results obtained in both $1D$ and $2D$ -PDNLS a study of magnetic physical system is performed. In Chapter 8 we analyze two classical examples: an easy-plane ferromagnetic spin chain and an easy-plane ferromagnetic layer when both are submitted to an external parametrical forcing by means of a constant and a time-periodic external magnetic field perpendicular to the hard axis. In the quasi-reversible limit these system are ruled by the $1D$ and $2D$ -PDNLS equation, respectively. Numerical simulations of magnetic solitons are conducted. The phase of this localized states is reconstructed by means of the Hilbert transform, exhibiting a non-trivial phase structure. That agrees with the result obtained for dissipative solitons in the PDNLS equation.

Finally, in the Conclusions we summarize the most significant results and suggest new ideas for continuing with the research in this subject. The appendices contain three publications on the topic that contain the principal discoveries made during the different stages of this research.

Chapter 2

Theoretical Background

2.1 Parametric resonance.

A non-Equilibrium system is any system that is not in thermodynamic equilibrium. Hence, the gain and loss of energy are nonzero, and therefore its effects should be taken into account. A non-equilibrium system is not isolated from the rest of the universe but is kept in contact with an external source that provides energy for the smaller sub-system. Therefore, the dissipation is essential for the transfer of pumped energy to a cooler part. Hence, the notion “dissipative system” is more complicated. It assumes that there is also an energy supply part, rather than just losses. The most efficient mechanism to provide energy to a system, through a oscillating external force, is making this undergo a resonance phenomenon [35], where even small periodic driving forces can produce oscillations with a large amplitude. Among these, when an effective system parameter is temporally (or spatially) modulated we say that the system is being parametrically excited. Systems parametrically driven can experience a parametric resonance, which is characterized by exhibiting a subharmonic response, i. e. the system develops oscillations at submultiples of the force frequency [35].

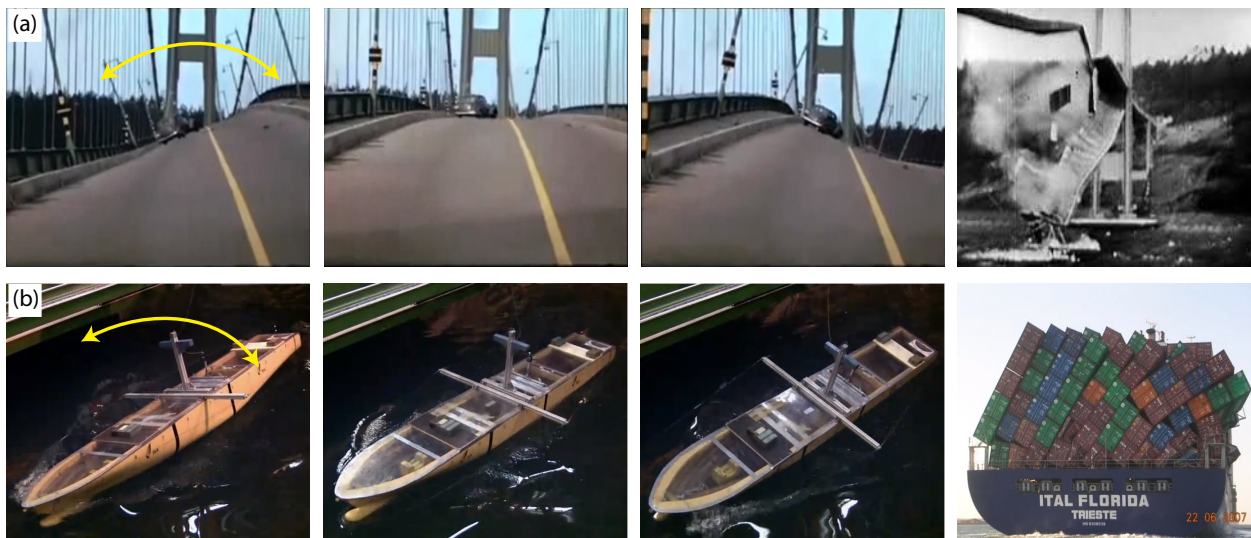


Figure 2.1: Resonance phenomena. (a) Normal resonance (the Tacoma bridge collapse). (b) Parametric (roll) resonance (containership catastrophe).

Figure 2.1 shows two systems undergoing a resonance phenomenon. Normal resonance example is shown as a sequence in Fig. 2.1a. It corresponds to the total collapse of the Tacoma Narrow Bridge (1940). Sequence Fig. 2.1b displays snapshots of a parametrical roll resonance experiment, final image corresponds to a container vessels catastrophe as consequence of this kind of resonance. It is important to mention that not only mechanical systems such as vehicles, motorcycles, aircraft, sparse offshore platforms and marine craft but also microelectro-mechanical systems are prone to parametric roll resonance [36].

In order to illustrate the phenomenon of parametric resonance let us consider the classical example of a vertically forced pendulum with dissipation. In this case the effective parameter is the gravity which varies periodically as result of the oscillating support [cf. Fig. 2.2]. This system is described by the differential equation

$$\ddot{\theta}(t) = - [\omega_0^2 + \Gamma \cos(\omega t)] \sin(\theta) - \mu \dot{\theta}, \quad (2.1)$$

where $\theta(t)$ accounts for the angle of the pendulum respect to the vertical, ω_0 is the natural oscillating frequency of the system. μ is the dissipation coefficient. Parameters Γ and ω account for the amplitude and frequency of forcing, respectively. Dissipation has been introduced phenomenologically and is proportional to the angular speed $\dot{\theta}$. As we know, if the system had no energy loss and gain, the pendulum would swing at its natural frequency and therefore the solution of the system [Eq. (2.1)] would be given by

$$\theta_l(t) = Ae^{i\omega_0 t} + \bar{A}e^{-i\omega_0 t}. \quad (2.2)$$

Nevertheless, since the pendulum is parametrically driven it exhibits a subharmonic response. To determine the frequency of resonance of the forced pendulum, we perform a linear analysis. In this limit the dynamic equation (2.1) takes the form

$$\ddot{\theta}(t) = - [\omega_0^2 + \Gamma \cos(\omega t)] \theta - \mu \dot{\theta}. \quad (2.3)$$

This expression allows us to determine the condition which must be satisfied by the force frequency, such that the system undergoes a parametrical resonance.

$$\begin{aligned} \ddot{\theta} = -\omega_0^2 \theta & - \underbrace{\Gamma \cos(\omega t) \theta}_{(e^{i\omega t} + e^{-i\omega t}) (Ae^{i\omega_0 t} + \bar{A}e^{-i\omega_0 t}) \Gamma/2} - \mu \dot{\theta} \\ & \sim \underbrace{e^{i(\omega_0 \pm \omega)t} + c.c.} \end{aligned} \quad (2.4)$$

where *c.c.* means complex conjugate. As a result of this analysis, the subharmonic response of the system (parametric resonance) occurs when the forcing frequency is $\omega_f = 2\omega_0$. Furthermore, this analysis shows that the nonlinear terms are important while having the same frequency of oscillation. Numerical simulations of the parametrically driven pendulum near the parametric resonance have been performed. Figure 2.2b shows the Fourier spectrum of the signal $\theta(t)$. There appear two peaks, which correspond to the frequency of forcing $\omega_f = 2\omega_0$, and the system respond at $\omega_f/2$.

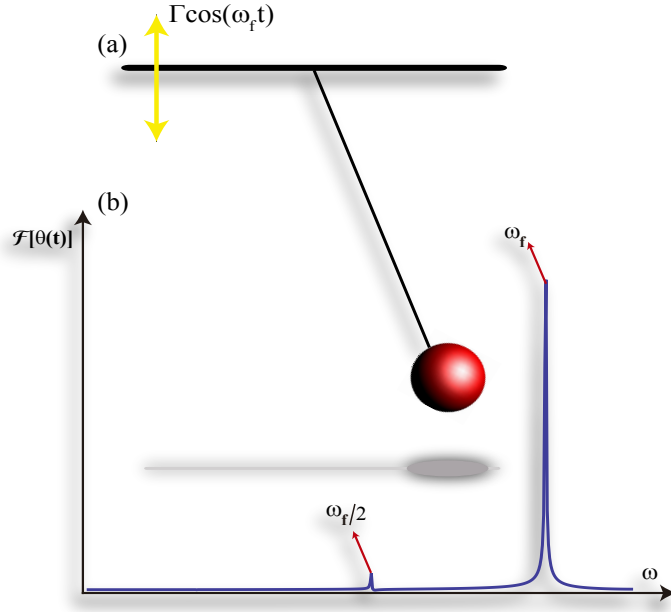


Figure 2.2: (a) Schematic representation of a vertically forced pendulum. (b) Power spectrum of the pendulum angle ($\theta(t)$) obtained by numerical simulations of the Eq. (2.1) near to the parametric resonance frequency ($\omega_f \simeq 2\omega_0$).

Historically, Faraday was probably the first to observe and report the appearance of subharmonic oscillations on the surface of a fluid in a rectangular container vibrated [20]. His experiment and preliminary results have been studied for a hundred years until this day. Meanwhile Mathieu, through his study conducted in elliptical vibrating membranes, was the first to derive a single equation to explain the phenomenon of parametric forcing [37]. However, was Rayleigh who gave a universal character to the phenomenon of parametric oscillations [38, 39]. Another remarkable feature of the parametric resonance phenomenon is that it can be developed even in system which do not posses a natural frequency of oscillation [40]. In brief, subharmonic response occurs in any system which is parametrically forced. For

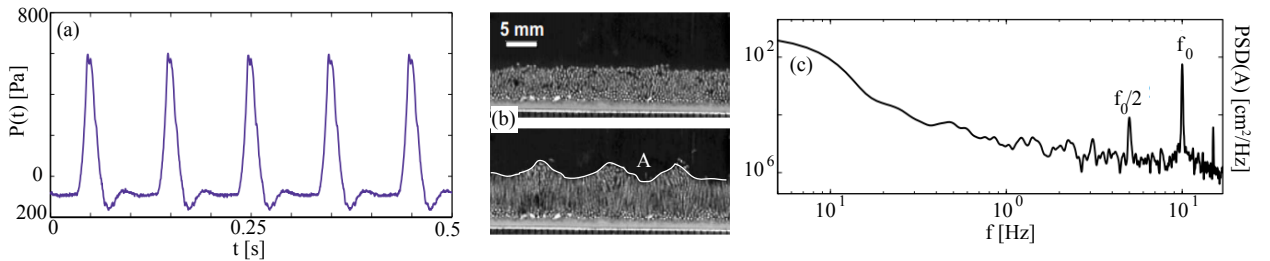


Figure 2.3: Experimental result of the experiment conducted in Ref. [21]. (a) Signal of the periodic pressure of the air flow which fluidizes the quasi-one-dimensional granular bed. (b) The system exhibits a spatial instability, emerging a pattern. An imaging process is done to obtain the envelope (A). (c) The power spectrum density (PSD) of A reveals the subharmonic response of the system ($f_0/2$)

instance, Figure 2.3 shows the experimental results obtained in quasi-one-dimensional noisy fluidized shallow granular bed forced by a periodic air flow [21]. The system exhibits a modulation instability [see Fig. 2.3b] which oscillates at subharmonic frequency [cf. Fig. 2.3c].

2.2 Amplitude equation.

Undoubtedly, since the birth of nonlinear physics and particularly due to the interest in non-equilibrium systems, it was evident the necessity of new techniques, in order to achieve a description of novel phenomena present in such systems. Hence, diverse techniques arose offering new methods to characterize the dynamics of a system around to accidents (bifurcations) [15, 16]. However, the aim of these techniques is clearly the same; get a more simplified equation than the original one that allows us to characterize completely the observed dynamical behavior suffered by the solution of interest. In other words, by applying these techniques we get a minimal and universal model which brings to us the necessary tools to achieve a thorough understanding of the universal phenomena exhibited by the system under study. Within these universal phenomena are found the emergence of patterns, localized structures, period doubling and chaos, to name a few [14, 15, 16, 17, 19].

Due to the injection and dissipation of energy present in non-equilibrium system, the behavior will be determined by its central manifold, which is composed by the relevant variables that lead the observed dynamics. Since we are interested in parametrically forced systems we know that the ulterior dynamics will be described by the slower scales [14]. That is how the amplitude equation stands as the best technique addressing these kind of systems, since it describes slow envelope modulations in space and/or time. The amplitude equations concept was introduced by L. Landau [41]. In the context of parametrically forced systems, this technique can be performed to describe the envelope of the upper layer of a Newtonian-fluid in a vertically vibrated container, the magnetization of a easy plane ferromagnetic driven by a oscillating magnetic field, the amplitude of oscillation of a pendulum (chain) with a periodically oscillating support, the electromagnetic field in a optical parametric oscillator, among others [24, 31, 42, 43].

For the sake of simplicity and a better understanding of the amplitude equation technique we consider a coupled chain of parametrically forced pendulum [see Fig. 2.4]. The goal is derive the minimal equation which accounts for the dynamics near the parametric resonance described above [Sec. 2.1]. The force equation of the pendula chain is obtained, in the continuous limit, by adding to the equation for one parametrically forced pendulum (2.1) the spatial coupling among pendulums,

$$\ddot{\theta}(t) = - [\omega_0^2 + \Gamma \cos(\omega t)] \sin(\theta) - \mu\dot{\theta} + \kappa\partial_{xx}\theta. \quad (2.5)$$

Where κ accounts for the elastic coupling. From the linear analysis developed for a simple pendulum [see Sec. 2.1] we already know that the parametric resonance occurs when the forcing frequency is $\omega_f = 2\omega_0$. Therefore, we are able to introduce an unfolding parameter which accounts for the detuning between the half of the forcing frequency and the natural oscillation frequency, $\nu \equiv (\omega - 2\omega_0)/2$. This parameter enables us to explore in a region near the emergence of the instability. Hence, we start the derivation of the amplitude equation proposing an ansatz based on the solution found in the linear analysis of a single pendulum

[Eq. (2.2)].

$$\theta(x, t) = A(x, t)e^{i\omega_0 t} + \bar{A}(x, t)e^{-i\omega_0 t} + \mathcal{W}(A(x, t); t), \quad (2.6)$$

where $A(x, t)$ is a slow variable, $\partial_{tt}A \ll \omega_0 \partial_t A \ll \omega_0^2 A$, which stands for the spatial amplitude of the coupled chain of pendulum. $\bar{A}(x, t)$ is the complex conjugate of the complex field $A(x, t)$. $\mathcal{W}(A(x, t); t)$ accounts for the nonlinear correction produced by the dissipation and nonlinear terms. We assume that at first order, its spatial variations depends on $A(x, t)$, which is spatially smooth.

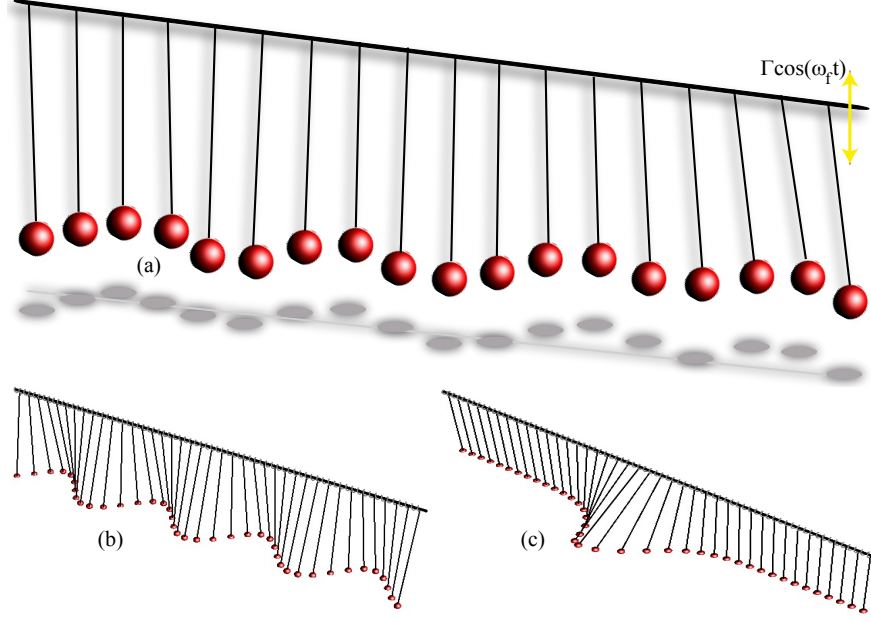


Figure 2.4: (a) Schematic representation of coupled chain of parametrically forced pendulum. (b) Shows Faraday instability which naturally arise in this system. A dissipative soliton is displayed in (c)

It is important to mention that the resulting amplitude equation describes the slower variable which, in this case, is the envelope of the system. Moreover, this equation is valid in the region of parameters close to the point of instability (small injection and dissipation of energy). The amplitude equation is obtained by a recursive method of change of variable. It is assumed that the slow variable is small as well as its spatial (temporal) changes. Thus, we consider the weakly nonlinear approximation—i. e. , in the perturbative limit where the parameters satisfy $\mu \sim \Gamma \sim \nu \ll \epsilon$, with ϵ an arbitrary small scale, $\epsilon \ll 1$ —for the system [Eq. (2.5)] to perform the recursive method,

$$\ddot{\theta}(x, t) = - [\omega_0^2 + \Gamma \cos(\omega t)] \theta + \omega_0^2 \frac{\theta^3}{6} - \mu \dot{\theta} + \kappa \partial_{xx} \theta. \quad (2.7)$$

By replacing (2.6) in the above relation and considering only the relevant terms one obtains,

after straightforward calculations, a differential equation for the nonlinear correction,

$$\begin{aligned} \partial_{tt}\mathcal{W} + \omega_0^2\mathcal{W} = & \left(2i\omega_0\partial_t A + \frac{\omega_0^2}{2}|A|^2 A - i\mu\omega_0 A - \frac{\Gamma}{2}\bar{A}e^{2i\nu t} + \kappa\partial_{xx}A \right) e^{i\omega_0 t} \\ & + \left(\frac{\omega_0^2}{6}A^3 - \frac{\Gamma}{2}Ae^{2i\nu t} \right) e^{3i\omega_0 t} + c.c. \end{aligned} \quad (2.8)$$

Notice that we know neither \mathcal{W} nor A . Defining the linear operator $\mathcal{L} \equiv \partial_{tt} + \omega_0^2$ the above equation can be rewritten as

$$\mathcal{L}\mathcal{W} = b, \quad (2.9)$$

where

$$\begin{aligned} b \equiv & \left(2i\omega_0\partial_t A + \frac{\omega_0^2}{2}|A|^2 A - i\mu\omega_0 A - \frac{\Gamma}{2}\bar{A}e^{2i\nu t} + \kappa\partial_{xx}A \right) e^{i\omega_0 t} \\ & + \left(\frac{\omega_0^2}{6}A^3 - \frac{\Gamma}{2}Ae^{2i\nu t} \right) e^{3i\omega_0 t} + c.c. \end{aligned} \quad (2.10)$$

Thus, Eq. (2.9) corresponds to a inhomogeneous linear equation. In order to solve this problem we introduce here the Fredholm alternative.

2.2.1 Fredholm method.

The Fredholm method is a useful alternative when we are dealing with inhomogeneous linear equations as

$$\mathcal{L}\vec{W} = \vec{B}. \quad (2.11)$$

This option ensures that either

a) For each $\vec{B} \in Im(\mathcal{L})$ the above equation has a unique solution

or

b) The homogeneous equation $\mathcal{L}\vec{W} = 0$ has a non-trivial solution ($\vec{W} \neq 0$). In this case the respective inhomogeneous equation (2.11) is solvable (invertible) if and only if the inhomogeneity \vec{B} belongs to the orthogonal space of the Kernel of the adjoint of \mathcal{L} , that is $\vec{B} \in Ker(\mathcal{L}^\dagger)^\perp$.

Noticed that this alternative can be extended for any eigenfunction \vec{V} associated to a eigenvalue λ of the linear operator ($\mathcal{L}\vec{V} = \lambda\vec{V}$). It is only necessary redefine the linear operator as $\mathcal{L}_\lambda \equiv \mathcal{L} - \lambda\mathcal{I}$, with \mathcal{I} the identity matrix.

The Fredholm alternative imposes a solvability conditions that must to be fulfilled in order to solve the inhomogeneous linear problem (2.11). They are, (a) the inhomogeneity must belong to the images of \mathcal{L} , $\vec{B} \in Im(\mathcal{L})$ or (b) in the case the homogeneous problem has a non-trivial solution, then $\vec{B} \in Ker(\mathcal{L}^\dagger)^\perp$. Both requirements can be contained in a

single condition: The inhomogeneity \vec{B} has to be orthogonal to the eigenfunction with zero eigenvalue,

$$\langle \vec{W} | \vec{B} \rangle = 0. \quad (2.12)$$

This can be easily demonstrated in one direction of the implication ($a \Rightarrow b$). We assume that $\vec{B} \in Im(\mathcal{L})$, i.e. there is \vec{u} which satisfies $\mathcal{L}\vec{u} = \vec{B}$. For any $\vec{K} \in Ker(\mathcal{L}^\dagger)$ the value of the inner product between \vec{B} and \vec{K} will always be

$$\langle \vec{B} | \vec{K} \rangle = \langle \mathcal{L}\vec{u} | \vec{K} \rangle = \langle \vec{u} | \mathcal{L}^\dagger \vec{K} \rangle = 0. \quad (2.13)$$

This means that \vec{B} is orthogonal to any \vec{K} in the Kernel of the adjoint of the linear operator, $\vec{B} \in Ker(\mathcal{L}^\dagger)^\perp$. Formal demonstration of the Fredholm alternative is beyond of the scope of this thesis. For additional information review any regular Differential Equations book.

Continuing with our calculation of the amplitude equation for the parametrically driven and damped pendulum chain, we adopt the Fredholm alternative. Consistently, we introduce the inner product

$$\langle f | g \rangle \equiv \frac{\omega_0}{2\pi} \int_T^{T+\frac{\omega_0}{2\pi}} f(t)g^*(t)dt, \quad (2.14)$$

where T denotes a period (of the oscillating function), and $g(t)^*$ means the complex conjugate of the function $g(t)$. Under this definition we can determine the Kernel of the adjoint of the linear operator ($\vec{K} \in Ker(\mathcal{L}^\dagger)$). Fortunately, the linear operator is self-adjoint, $\mathcal{L} = \mathcal{L}^\dagger$, and therefore the Kernel of the adjoint of \mathcal{L} are exactly the eigenfunction with zero eigenvalue of \mathcal{L} . That is, functions of the form $K = \{e^{i\omega_0 t}, e^{-i\omega_0 t}\}$ [see Eq. (2.2)]. Hence, accordingly to the solvability condition (point (b) of the Fredholm alternative, Sec. 2.2.1), the inhomogeneity b [Eq. (2.10)] has to be orthogonal to any function in the Kernel K .

$$\langle b | K \rangle = 0. \quad (2.15)$$

Thus, after evaluating the inner product one obtains two conditions that must be fulfilled with four different terms in each one. Nevertheless, we notice that there appear only two different types of integrals

$$I_1 = \frac{\omega_0}{2\pi} \int_T^{T+\frac{\omega_0}{2\pi}} f(A(x, t))dt, \quad (2.16)$$

$$I_2 = \frac{\omega_0}{2\pi} \int_T^{T+\frac{\omega_0}{2\pi}} g(A(x, t)) e^{in\omega_0 t} dt. \quad (2.17)$$

Both, $f(A(x, t))$ and $g(A(x, t))$, are a compressed representation of all terms resulting for the inner product between the inhomogeneity b and the Kernel of the adjoint of the linear operator \mathcal{L} . However, it is important to mention that $f(A(x, t))$ can only be the expression which accompanies $e^{i\omega_0 t}$ in b [Eq. 2.10] and its complex conjugate. Meanwhile, $g(A(x, t))$ has more possibilities depending on the value of n , which is a nonzero even number.

Since $A(x, t)$ is a slow variable, in this consideration, the temporal variation is negligible, $t = 2\pi/\omega_0 \rightarrow 0$. Thus, the first kind of integral can be rewritten as

$$I_1 \simeq \lim_{\omega_0 \rightarrow \infty} \frac{\omega_0}{2\pi} \int_T^{T+\frac{\omega_0}{2\pi}} f(A(x, t)) dt.$$

Hence, by using the integral form of the mean value theorem, we obtain

$$\begin{aligned} I_1 &\simeq \lim_{\omega_0 \rightarrow \infty} \frac{\omega_0}{2\pi} \left[f(A(x, \tau)) \frac{2\pi}{\omega_0} \right] \\ I_1 &\simeq f(A(x, \tau)). \end{aligned} \quad (2.18)$$

Here, τ accounts for the slow temporal variable, $\tau \equiv \epsilon t$, where $\epsilon \ll 1$ is the arbitrarily chosen small scale.

To solve the second type of integral we perform a recursive integration by parts. When we iterate this integration method N times, the integral I_2 takes the form,

$$\begin{aligned} I_2 &= \lim_{\omega_0 \rightarrow \infty} \frac{\omega_0}{2\pi} \left[\sum_{n=1}^{n=N} \frac{(-1)^{n+1} e^{in\omega_0 t}}{(2in\omega_0)^n} \partial_t^{[n-1]} g(A(x, t)) \right]_{T}^{T+\frac{2\pi}{\omega_0}} \\ &\quad + \frac{(-1)^N}{(2in\omega_0)^N} \int_T^{T+\frac{\omega_0}{2\pi}} \partial_t^{[N]} g(A(x, t)) e^{in\omega_0 t} dt, \end{aligned}$$

where $\partial_t^{[j]} f(t)$ corresponds to the j th temporal derivation of $f(t)$. Notice that the integral becomes a power series of $1/\omega_0$, which is small. Therefore, at dominant order the relevant term is the first one in the sum, that is

$$\begin{aligned} I_2 &\simeq \lim_{\omega_0 \rightarrow \infty} \frac{\omega_0}{2\pi} \left[\frac{e^{in\omega_0 t}}{2in\omega_0} \{g(A(x, t + 2\pi/\omega_0)) - g(A(x, t))\} \right] \\ &\simeq \lim_{\omega_0 \rightarrow \infty} \frac{e^{in\omega_0 t}}{2in\omega_0} \frac{\partial g(A)}{\partial A} \partial_t A \\ I_2 &\simeq 0. \end{aligned} \quad (2.19)$$

Thus, the second type of integral, Eq. (2.17), does not contribute in the evaluation of the inner product (2.15). Hence, we are able to evaluate the inner product between the inhomogeneity b and the kernel K ,

$$\langle b | e^{i\omega_0 t} \rangle = 2i\omega_0 \partial_\tau A + \frac{\omega_0^2}{2} |A|^2 A - i\mu\omega_0 A - \frac{\Gamma}{2} \bar{A} e^{2i\nu\tau} + \kappa \partial_{xx} A, \quad (2.20)$$

$$\langle b | e^{-i\omega_0 t} \rangle = -2i\omega_0 \partial_\tau \bar{A} + \frac{\omega_0^2}{2} |A|^2 \bar{A} + i\mu\omega_0 \bar{A} - \frac{\Gamma}{2} A e^{-2i\nu\tau} + \kappa \partial_{xx} \bar{A}. \quad (2.21)$$

Notice that the first relation corresponds exactly to the evaluation of $I_1 = f(A(x, \tau))$ and the second relation is the complex conjugate of the first one, which is in agreement with the above discussion of $f(A(x, t))$. Therefore, by imposing the condition of solvability (2.15), we obtain a partial differential equation that has to be fulfilled by the amplitude of the system,

$$\partial_\tau A = -i \frac{\omega_0}{4} |A|^2 A - \frac{\mu}{2} A - i \frac{\Gamma}{4\omega_0} \bar{A} e^{2i\nu\tau} - i \frac{\kappa}{2\omega_0} \partial_{xx} A. \quad (2.22)$$

Thus, by introducing the change of variables $A = \sqrt{4/\omega_0} B e^{i\nu\tau}$, $X = \sqrt{2\omega_0/\kappa} x$ one obtains

$$\partial_\tau B = -i\nu B - i|B|^2 B - \frac{\mu}{2} B - i\frac{\Gamma}{4\omega_0} \bar{B} - i\partial_{XX} B. \quad (2.23)$$

Finally, introducing $B = \psi e^{-i\pi/4}$, $\mu/2 \rightarrow \mu$, and $\gamma \equiv \Gamma/4\omega_0$ the above expression becomes

$$\partial_\tau \psi = -i\nu\psi - i|\psi|^2 \psi - i\partial_{XX} \psi - \mu\psi + \gamma\bar{\psi}. \quad (2.24)$$

As we can see, this equation is balanced at order $\epsilon^{3/2}$. Equation (2.24) corresponds to the well known parametrically driven and damped nonlinear Schrödinger equation, which is a prototype model highly used to describe parametrically forced systems in the limit of small losses and gain [see Chap. 4 and references therein]. Moreover, this equation is the cornerstone of this work. Notice that, since the second type of integrals vanished [Eq. (2.19)], that part of the inhomogeneity b [Eq. (2.10)] belongs to the images of the linear operator \mathcal{L} (terms proportional to $e^{3i\omega_0 t}$ in b). Therefore, exists a unique solution for the nonlinear correction

$$\partial_{tt} \mathcal{W} + \omega_0^2 \mathcal{W} = \frac{\omega_0^2}{6} A^3 e^{3i\omega_0 t} - \frac{\Gamma}{2} A e^{i(3\omega_0 + 2\nu)t}. \quad (2.25)$$

Due to the slow varying of $A(x, t)$ in the time, we introduce the ansatz

$$\mathcal{W} = \alpha A^3 e^{3i\omega_0 t} + \beta A e^{i(3\omega_0 + 2\nu)t}, \quad (2.26)$$

where the constants A and B are to be determined. Replacing in Eq. (2.25), we obtain

$$\alpha = -\frac{1}{48} \quad \text{and} \quad \beta = \frac{\Gamma}{16\omega_0^2}. \quad (2.27)$$

Finally, the dynamics of the system at this order, $\theta(x, t)$ in Eq. (2.6), is given by

$$\begin{aligned} \theta(x, t) &= \sqrt{\frac{4}{\omega_0}} \psi(X, \tau) e^{i\{(\omega_0 + \nu)t - \pi/4\}} \\ &+ \left(\frac{1}{\omega_0}\right)^{3/2} \left[\frac{\gamma}{2} \psi(X, \tau) e^{-i\pi/4} + \frac{1}{6} \psi(X, \tau)^3 e^{i\pi/4} \right] e^{i\{3(\omega_0 + \nu)t\}} + c.c. \\ &+ \text{h.o.t.}, \end{aligned} \quad (2.28)$$

where *c.c.* and *h.o.t.* means complex conjugate and higher order terms, respectively. The field $\psi(X, t)$ is given by Eq. (2.24). It is important to mention that $\theta(x, t)$ is a real signal [Eq. (2.5)] and the above (approximate) nonlinear change of variable is an analytic function of the angle $\theta(x, t)$.

2.3 Hilbert transform.

The Hilbert transform is a powerful tool to process data signal. It provides a concrete means for realizing the harmonic conjugate of a given function or Fourier series. Furthermore, in harmonic analysis, it is an example of a singular integral operator, and of a Fourier multiplier. The Hilbert transform is also important in the field of signal processing where it is used to derive the analytic representation of a signal $u(t)$. The analytic representation of a

real-valued function or signal facilitates many mathematical manipulations of the signal. The basic idea is that the negative frequency components of the Fourier transform (or spectrum) of a real-valued function are superfluous, due to the Hermitian symmetry of such a spectrum. These negative frequency components can be discarded with no loss of information, thereby generating a complex-valued function instead. That makes certain attributes of the signal more accessible and facilitates the derivation of modulation and demodulation techniques. As long as the manipulated function has no negative frequency components (that is, it is still analytic), the conversion from complex back to real is just a matter of discarding the imaginary part.

The Hilbert transform of a signal $u(t)$ is defined as the convolution of $u(t)$ with the function $h(t) = 1/(t)$. Because $h(t)$ is not integrable the integrals defining the convolution do not converge. Instead, the Hilbert transform is defined using the Cauchy principal value explicitly, the Hilbert transform of a function (or signal) $u(t)$ is given by

$$H[u](t) \equiv P.V. \left\{ \int_{-\infty}^{\infty} u(\tau)h(t - \tau)d\tau \right\} = P.V. \left\{ \int_{-\infty}^{\infty} \frac{u(\tau)}{t - \tau}d\tau \right\}, \quad (2.29)$$

where $P.V.\{\cdot\}$ means the Cauchy principal value of the integral. Alternatively, by changing variables, the Hilbert transform can be written explicitly as

$$H[u](t) = -\frac{1}{\pi} \lim_{\epsilon \rightarrow 0^+} \int_{\epsilon}^{\infty} \frac{u(t + \tau) - u(t - \tau)}{\tau} d\tau. \quad (2.30)$$

When this transformation is applied twice in succession to a function u we obtain $H[H[u]](t) = -u(t)$. For instant, the Hilbert transform of $u(t) = \cos(\omega t)$ is given by

$$H[u](t) = \cos\left(\omega t - \frac{\pi}{2}\right) = \sin(\omega t), \quad (2.31)$$

and in the same way

$$H[\sin](t) = \sin\left(\omega t - \frac{\pi}{2}\right) = -\cos(\omega t), \quad (2.32)$$

which is consistent with $H(H(u)) = -u$. Note that the above transformation can be obtained by shifting the phase in 90-degrees.

2.3.1 Hilbert transform relations for complex sequences.

In the context of signal processing, the Hilbert transform plays a fundamental role to reconstruct analytic signals. That is, the analytic representation of a complex signal $u(t)$,

$$u_a(t) = u_r(t) + iu_i(t), \quad (2.33)$$

with $u_r(t)$ and $u_i(t)$ real fields, can be obtained by means of the Hilbert transform [44]. This is really useful since many of the solutions of differential equations, which describes physical systems, as well as experimental measurements are real signals. Therefore, the Hilbert transform technique allows us to reconstruct a complex variable (analytic signal). In

order to achieve this, let us express the analytic signal in terms of complex polar coordinates, $u_a(t) = A(t)e^{i\phi(t)}$ where

$$A(t) = |u_a(t)| = \sqrt{u_r(t)^2 + u_i(t)^2}, \quad (2.34)$$

$$\phi(t) = \text{Arg}(u_a(t)). \quad (2.35)$$

Here, $\text{Arg}(\cdot)$ corresponds to the argument function. Thus, the original real field $u(t)$ can be express as,

$$u(t) \equiv u_r(t) = \text{Re} \left(A(t)e^{i\phi(t)} \right), \quad (2.36)$$

where $\text{Re}(\cdot)$ represent the real part, $A(t)$ the amplitude of the envelope and $\phi(t)$ the phase. The Hilbert Transform technique allows us to obtain the imaginary part, $u_i(t)$, of the analytic field $u_a(t)$ [Eq. (2.33)] from the original real data $u_r(t)$ and its one-sided Fourier Transform $S_r(\omega)$,

$$S_r(\omega) = \int_{-\infty}^{\infty} u_r(t)\Theta(\omega)e^{-i\omega t} dt \quad (2.37)$$

where $\Theta(\omega)$ is the Heaviside step function. To obtain the one-sided Fourier Transform of the imaginary part $S_i(\omega)$, we used the following relation,

$$S_i(\omega) = H(\omega)S_r(\omega) \quad (2.38)$$

where

$$H(\omega) = \begin{cases} -i, & 0 \leq \omega < \pi \\ i, & -\pi \leq \omega < 0 \end{cases} \quad (2.39)$$

is a 90-degree phase shifter or Hilbert Transformer [45]. Therefore, the reconstructed imaginary part $u_i(t)$ of the analytic signal is obtained by calculating the inverse Fourier Transform of $S_i(\omega)$. This method gives a good description of the amplitude and phase for band-limited signals. It is noteworthy that the above application of the Hilbert transform is not altered if we now consider an analytic field that also depends on the space, $u(x, t)$. Thus, the Hilbert transform becomes a spatiotemporal function, $H(u)(x, t)$ but its calculation only applies for the time parameter of the field under study. That is, the one-sided Fourier Transform only be carried out on the time parameter, leaving unchanged the spatial coordinate.

To illustrate the above described application of the Hilbert transform, let us consider a vertically vibrated pendulum chain [see Sec. 2.2]. This system is described, in its continuous limit, by the Eq. (2.5). Here, the spatiotemporal real field $\theta(x, t)$ accounts for the angle respect to the vertical of the pendulum in the position x at the time t . Numerical simulations of a dissipative soliton, commonly exhibited in this system, were conducted [see Fig. 2.5]. Then, from the numerical real part of the analytic signal $\text{Re}(\theta_a(x, t)) \equiv \theta(x, t)$ is reconstructed the imaginary part. More precisely, we reconstruct the phase $\phi(x, t)$, Eq. (2.35), of the dissipative soliton. Surprisingly, two-counter propagating phase front which moves away from the soliton position appear. A detailed and appropriate description of these phase fronts will be delivered in the following chapters. Figure 2.5c shows the phase $\phi(x)$ at a given value t .

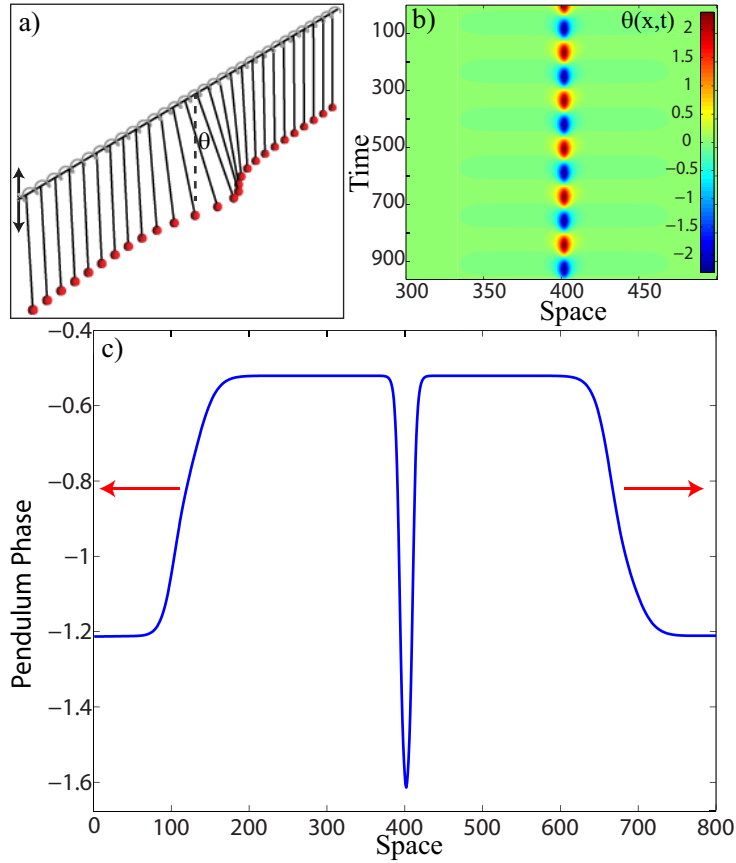


Figure 2.5: (a) Schematic representation of coupled chain of parametrically forced pendulum. (b) Shows Faraday instability which naturally arise in this system. The phase of a dissipative soliton, reconstructed by means of the Hilbert transform, is displayed in (c)

It is noteworthy that the slot observed at the center of the phase angle is a consequence that the Hilbert transform is calculated via the original field $\theta(x, t)$, including all the nonlinear corrections of the envelope. Such corrections are described by higher order terms in the amplitude equation [30]. Far from the core position, higher order terms are negligible due to the exponentially small tail of the envelope. However, close to the center corrections become relevant producing the characteristic hole.

Part II

Solitons in Parametrically Forced System

Chapter 3

Dissipative Solitons

The aim of this chapter is to establish the main differences existing between conservative solitons—solitons which appears naturally in conservative system—and the extension of this soliton concept to localized dissipative structures that arises in non-equilibrium systems such as parametrically forced systems, which are of our particular interest.

Conservative solitons are born as a balance between the nonlinearity and the dispersion of the medium [46]. They are the first nonlinear wave reported. Surprisingly, this localized structure can be treated as a particle-type solution. One of its most intriguing properties is that their shape remains invariant during its propagation in a homogeneous media. Furthermore, several studies related with the interaction of these conservative localized structures have demonstrated that they also maintain its bell–shape invariant during this collective dynamics [47]. They have constituted the mechanism of transport in numerous system such as action potential in a neuron, deformations along a solid, waves on the free surface of fluids, to name a few [1]. They represent the most classical and observed example of an extended particle.

As mentioned in the Introduction section, systems maintained out of equilibrium by injection and dissipation of energy are self-organizing. That is, they distribute the energy by forming different kinds of structures [see Fig. 1.1] with properties impossible to achieve in equilibrium systems. Thus, a dissipative soliton is a localized coherent structure which exists for an extended period of time, even though parts of the structure experience gain and loss of energy and/or other quantities, such as momentum, mass, among others. These solitons exist in “open” systems which are far from equilibrium. Thus, energy and matter can flow into the system through its boundaries. Therefore, a soliton in a non-equilibrium system exists indefinitely in time, as long as the parameters in the system remain constant. It may evolve (i.e. change its shape periodically or otherwise) but it only disappears when the source of energy or matter is switched off, or if the system parameters take values outside the region of existence of the soliton. Hence, as its conservative counterpart, they can be considered as a particle–type solution since these dissipative localized states are characterized by continuous parameters such as position, width, charge, length, etc. In contrast to solitons in conservative systems, dissipative solitons are dynamical objects that have non–trivial internal energy flows. Therefore, they do not need to have a stationary profile [48]. Since they are produced by dissipative systems, they depend strongly on an energy supply from an external source. As we can see, pump of energy is essential, and this means that the structures are defined

by the rules of the system (gain, loss, dispersion, nonlinearity, etc.), rather than by the initial conditions [28]. However it is important to mention that these solutions usually do not emerge spontaneously. Therefore, to generate these localized solutions, it is often necessary to perturb the system in order to exceed a certain nucleation barrier.

Solitons or localized states in macroscopical extended dissipative systems have been observed in different fields, such as: domains in magnetic materials, chiral bubbles in liquid crystals, current filaments in gas discharge, spots in chemical reactions, localized states in fluid surface waves, oscillons in granular media, isolated states in thermal convection, solitary waves in nonlinear optics. The variety of this type of phenomena evidences the universality of these particle-type solutions [see Fig. 3.1].

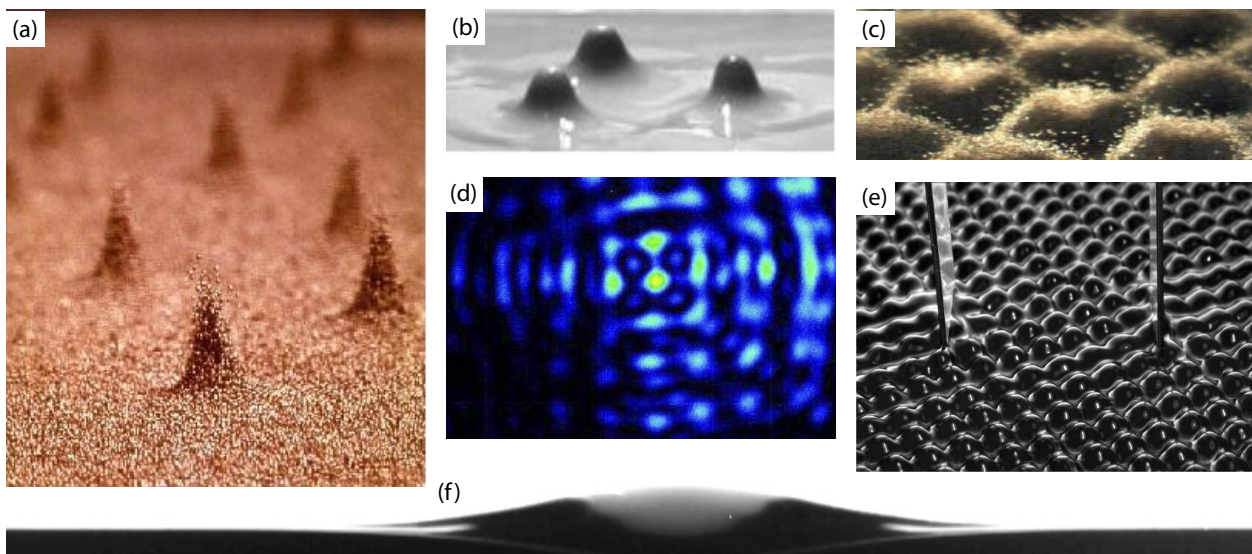


Figure 3.1: Diverse dissipative structures and pattern found in parametrically forced system such as: Oscillons found in vertically vibrated granular bed (a) and colloidal vibrated fluid (b). Patterns formation in granular (c) and optical (d) media. (e) and (f) show a hydrodynamic solitons found in Farady's experiment.

In brief, non-equilibrium systems have opened a new field to study universal phenomena. Especially by the variety of both irreversible processes and non-variational effects that occur in these systems. Among them we can find the retro-injection, the dissipation, nonlocal interaction, inhomogeneities, among others. As a consequence of the above, dissipative solitons arising in such systems possess innumerable properties [19] that often cannot be observed even in near integrable systems (near hamiltonian limit). Some of the most fascinating characteristics of dissipative solitons are the presence of oscillating tails, wave emission, period doubling, and development of chaos, to name a few. This can be understood directly from the non-equilibrium system properties, since in such systems there are no (necessarily) conserved quantities and, hence, localized structures are not related to the conservation of energy, momentum, or some other amount as in its conservative counterpart. Dissipative solitons have opened a new spectrum for localized structure phenomena, showing potential applications in technology which depends heavily on the level of understanding that we possess of such solitons. Dissipative solitons are solutions extremely rich and largely unexplored.

Chapter 4

Parametrically Driven and Damped Nonlinear Schrödinger Equation

The parametrically driven and damped nonlinear Schrödinger equation (PDNLS) constitutes the *alma mater* of several studies related to dissipative localized structures arising in extended systems forced parametrically. PDNLS is the most minimal model describing the emergence of a parametrical resonance. Some universal phenomena that can be found in PDNLS are the emergence of pattern, localized structures, bounded states, and more complex dynamics as spatiotemporal chaos, among others.

4.1 The universality of the PDNLS model.

The parametrically driven and damped nonlinear Schrödinger equation is a model that describes parametrically forced systems in the quasi-reversal limit. That means, the system has a time-reversal part which is perturbed with small injection and dissipation of energy [49, 50]. This model can be understood as the prototype equation of a chain of nonlinear dissipative oscillators parametrically forced.

$$\partial_t \psi = -i\nu\psi - i|\psi|^2\psi - i\vec{\nabla}^2\psi - \mu\psi + \gamma\bar{\psi}, \quad (4.1)$$

where $\psi(\vec{x}, t)$ is a complex field that accounts for the envelope of the oscillation of the system under study. $\bar{\psi}$ stands for the complex conjugate of ψ , and $\{\vec{x}, t\}$ describes the spatial and temporal coordinates, respectively. Parameter ν represents the detuning between the forcing and the system response. More precisely, it is proportional to the difference between the half of the forcing frequency and the natural frequency of the forced oscillator. μ is the damping parameter which accounts for the energy dissipation process, and the parameter γ stands for the amplitude of the parametric forcing. It is important to note that the spatial operators ($\vec{\nabla}, \vec{\nabla}^2$) depend on the dimension of the system under study as well as the coordinate system chosen¹ to describe the system under study.

The PDNLS model describes an oscillatory focusing media with dispersive coupling [51], since the nonlinear term and spatial coupling have the same sign. This equation provides

¹That is, for instance, in the case of one-dimensional system the spatial operators are described for $\vec{\nabla} = \partial_x \hat{x}$ and $\vec{\nabla}^2 = \partial_{xx}$. Meanwhile in two-dimensional system, for example, the Laplacian in cartesian coordinates is given by $\vec{\nabla}^2 = \partial_{xx} + \partial_{yy}$ whereas its polar representation takes the form $\vec{\nabla}^2 = \rho^{-1}\partial_\rho + \partial_{\rho\rho} + \rho^{-2}\partial_{\theta\theta}$.

a good description of parametric systems and phenomena arising in them, in the quasi-reversal limit $\nu \sim \mu \sim \gamma \ll 1$. Following the amplitude equation technique [see Sec. 2.2], parametrically driven and damped nonlinear Schrödinger equation has been derived in different physical contexts, such as vertically oscillating layer of water [42, 52], parametrically driven easy-plane ferromagnetic wire [26, 43], degenerate optical parametric oscillator [24], parametrically driven pendulum chain [31], and parametrically driven arrays of nonlinear resonators [30].

4.2 The bifurcation scenario of PDNLS

With the aim of characterizing the phase space of the PDNLS model, we introduce the Madelung transformation for the complex field in the PDNLS equation (4.1). Namely, replacing $\psi(\vec{x}, t) = R(\vec{x}, t)e^{i\phi(\vec{x}, t)}$ one obtains

$$\partial_t R = R\vec{\nabla}^2\phi + 2\vec{\nabla}R \cdot \vec{\nabla}\phi - \mu R + \gamma R \cos(2\phi), \quad (4.2)$$

$$R\partial_t\phi = -\nu R - R^3 - \vec{\nabla}^2 R + R(\vec{\nabla}\phi)^2 - \gamma R \sin(2\phi). \quad (4.3)$$

The uniform equilibrium solutions are determined by setting the modulus and the phase as constant values, $R \equiv R_0$ and $\phi \equiv \phi_0$.

$$\cos(2\phi_0) = \frac{\mu}{\gamma}, \quad (4.4)$$

$$R_0^2 = -\nu \pm \sqrt{\gamma^2 - \mu^2}. \quad (4.5)$$

Obviously, the trivial quiescent solution $R_0 = 0$ exist in all the parameters space. Equation (4.5) describes the different uniform solutions that we can find when moving across the different regions of parameters. Notice that for amplitude of forcing in the region $\mu < \gamma < \sqrt{\mu^2 + \nu^2}$ and negative detuning $\nu < 0$, the system has five possible equilibrium solution. Meanwhile, for amplitude of forcing lower than the damped parameter, that is $\gamma < \mu$, only the zero solution is possible, $R_0 = 0$. Figure 4.1 shows the different regions of existence for the uniforms solutions and their mechanism of emergence.

To characterize the emergence of the spatial extended solutions we perform the stability analysis of the quiescent solution ($R_0 = 0$). Introducing the cartesian representation of the complex field $\psi(\vec{x}, t) \equiv X(\vec{x}, t) + iY(\vec{x}, t)$ in PDNLS [Eq. (4.1)], we obtain

$$\partial_t \mathcal{X} = \nu \mathcal{Y} + (\mathcal{X}^2 + \mathcal{Y}^2) \mathcal{Y} + \vec{\nabla}^2 \mathcal{Y} - \mu \mathcal{X} + \gamma \mathcal{X}, \quad (4.6)$$

$$\partial_t \mathcal{Y} = -\nu \mathcal{X} + (\mathcal{X}^2 + \mathcal{Y}^2) \mathcal{X} - \vec{\nabla}^2 \mathcal{X} - \mu \mathcal{Y} - \gamma \mathcal{Y}. \quad (4.7)$$

By neglecting the nonlinear terms, a linear system for the perturbation of the zero solution is obtained. It can be rewritten in a matrix form as

$$\begin{pmatrix} \dot{\mathcal{X}} \\ \dot{\mathcal{Y}} \end{pmatrix} = \begin{bmatrix} \gamma - \mu & \nu + \vec{\nabla}^2 \\ -\nu - \vec{\nabla}^2 & -\mu - \gamma \end{bmatrix} \begin{pmatrix} \mathcal{X} \\ \mathcal{Y} \end{pmatrix}. \quad (4.8)$$

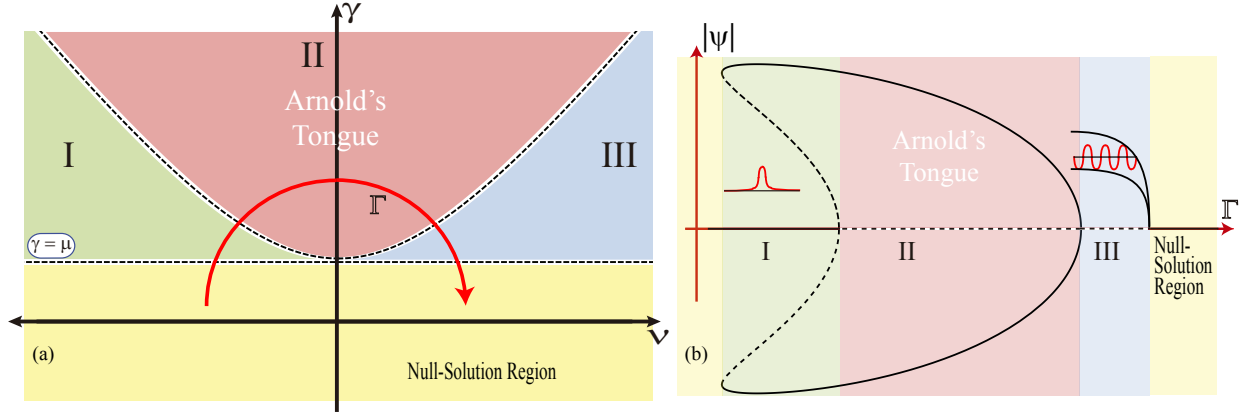


Figure 4.1: Regions of existence for PDNLS solutions. (a) Solitons are found in the region I, meanwhile pattern formation occurs for positive detuning (region III). Inside the Arnold's tongue the spatial temporal chaos leads the dynamics of the system. (b) As we move along the curve Γ , we can determine the bifurcations experienced by PDNLS equilibria: In region I we can find five possible equilibria, however, only three of them are stable solutions. In region II, there are two stable equilibria and the quiescent solution is unstable. In the region III only exists the quiescent solution and is unstable.

Considering a solution of the form

$$\begin{pmatrix} \mathcal{X} \\ \mathcal{Y} \end{pmatrix} = \begin{pmatrix} \mathcal{X}_0 \\ \mathcal{Y}_0 \end{pmatrix} e^{\lambda t + i\vec{k} \cdot \vec{x}},$$

and replacing it in the above eigenvalue problem, we obtain the stability condition for the quiescent solution

$$\lambda(\vec{k}) = \mu \pm \sqrt{\gamma^2 - (\nu - \vec{k}^2)}. \quad (4.9)$$

To establish the region of destabilization of the null solution we must determine the exact point at which the curve of $\lambda(\vec{k})$ crosses the zero. For this we looking for a real vector \vec{k}_c such that satisfies the condition

$$\left. \frac{\partial \lambda(\vec{k})}{\partial \vec{k}} \right|_{\vec{k}=\vec{k}_c} = 0. \quad (4.10)$$

That is,

$$2\vec{k}_c \left(\frac{(\nu - \vec{k}_c^2)}{\sqrt{\gamma^2 - (\nu - \vec{k}_c^2)}} \right) = 0. \quad (4.11)$$

This relation gives us two possible solutions $\vec{k}_c = \vec{0}$ and $\vec{k}_c^2 = \nu$. Therefore, the spatial modulation occurs for $\nu > 0$ (pattern formation) [53]. When $\lambda(\vec{k}_c = 0)$ cross the zero the

system undergoes a stationary bifurcation (without a wavelength), this region is known as the Arnold's tongue. In this case, it is placed in the region of parameters which satisfy

$$\begin{aligned}\lambda(\vec{k}_c = 0) &= \mu \pm \sqrt{\gamma^2 - \nu^2} \geq 0 \\ \gamma^2 &\geq \mu^2 + \nu^2.\end{aligned}\tag{4.12}$$

Inside this region the system exhibits stationary patterns, kinks, and spatiotemporal chaos dynamics. As we already know, the region of five uniform equilibrium solutions is delimited by values of the amplitude of forcing in $\mu < \gamma < \sqrt{\mu^2 + \nu^2}$ and a negative detuning $\nu < 0$ [c.f. Eq. (4.5), and Fig. 4.1]. Therefore, the localized dissipative structures can be found in this region since they represent a homoclinic solution connecting asymptotically the quiescent solution.

4.3 Uniform phase solitons in PDNLS

Certainly, the parametrically driven and damped nonlinear Schrödinger Eq. (4.1) has brought a vast territory for the studies of diverse physical phenomena. One of the most paradigmatic solution that appears in this model is the dissipative soliton with a uniform phase (UPS). This localized structure arises naturally as a nonlinear surface wave in experiments of vertically vibrated container with Newtonian fluid [54]. Hydrodynamic solitons have also been characterized analytically starting for ideal equations for the fluid in basin and introducing the dissipation effect phenomenologically [42, 55].

In order to achieve a thorough understanding of the stationary localized solution with a uniform phase in a one-dimensional system, we set our ansatz in modulus and phase accordingly, $R(x, t) \equiv R_s(x)$ and $\phi(x, t) \equiv \phi_0$. Replacing it in the polar representation for the complex field of PDNLS [Eqs. (4.2) and (4.3)] we obtain

$$\cos(2\phi_0) = \frac{\mu}{\gamma},\tag{4.13}$$

$$\partial_{xx}R_s = (-\nu - \gamma \sin(2\phi_0))R_s - R_s^3.\tag{4.14}$$

Notice that Eq. (4.13) determines four different phase uniform solutions in the range $[-\pi, \pi]$ which are important for future discussion. Equation (4.14) accounts for the modulus shape of the UPS. Taking into account the effective potential energy $U(R_s) = -\delta_{\pm}R_s^2/2 + R_s^4/4$, with $\delta_{\pm} = -\nu \pm \sqrt{\gamma^2 - \mu^2}$, Eq. (4.14) can be understood as a Newton-type equation in the extended system,

$$\frac{\partial^2 R_s}{\partial x^2} = -\frac{\partial U(R_s)}{\partial R_s}.$$

Multiplying this equation by the integrating factor $\partial_x R_s$, we obtain a *energy*-type equation

$$\frac{\partial}{\partial x} \underbrace{\left[\frac{1}{2} \left(\frac{\partial R_s}{\partial x} \right)^2 + U(R_s) \right]}_{E(R_s, \partial_x R_s)} = 0.\tag{4.15}$$

The above relation implies that the *energy* is conserved, $E(R_s, \partial_x R_s) = E_0$. Since we are interesting in the spatial solution which connects asymptotically the quiescence solution with itself, we set $E_0 = 0$. Thus, we are able to integrate the modulus shape equation

$$\int \frac{dR_s}{\sqrt{-2U(R_s)}} = \int \frac{dR_s}{\sqrt{\delta_{\pm} R_s^2 - R_s^4/2}} = \int dx.$$

Introducing the change of variable $R_s = \sqrt{2\delta_{\pm}} \operatorname{sech}(y)$, the above relation takes the form

$$\int dy = \int \sqrt{\delta_{\pm}} dx.$$

Integrating this we obtain the modulus shape of the UPS

$$R_s(x, x_0) = \sqrt{2\delta_{\pm}} \operatorname{sech}\left(\sqrt{\delta_{\pm}}(x - x_0)\right). \quad (4.16)$$

Which, as we can see, is invariant under translations (parameterized continuously by the position x_0). This was expected since this localized solution is associated with a Goldstone mode (zero eigenvalue). Moreover, the width and the height of the above solution are given respectively by δ_+^{-1} and $(2\delta_+)^{1/2}$ [see Fig. 4.2b].

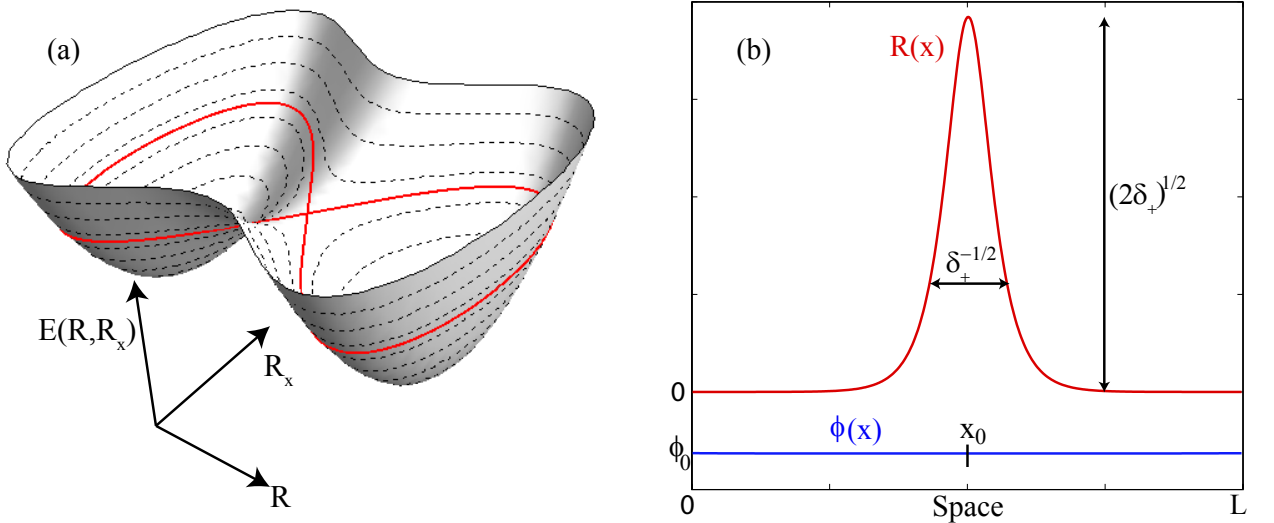


Figure 4.2: (a) Schematic representation of the *energy* $E(R, \partial_x R)$. The Homoclinic solution (red curve) is obtained fixing $E = 0$. Dashed curves correspond to different unstable extended solutions ($E \neq 0$) in the spatiotemporal system. (b) Uniform phase soliton solution for the parameters $\gamma = 0.105$, $\mu = 0.1$, $\nu = -0.1$, system size $L = 100$, characteristic parameter $\delta_+ = 0.132$. x_0 stands for the soliton position

As mentioned before, UPS exists in the region of parameters where we can find localized structures in PDNLS—region where the five uniform equilibria are found, and the zero solution is stable [see Sec. 4.2]. It is important to note that the UPS is a non-trivial stationary homoclinic solution in the extended (or stationary) phase space $\{R, \partial_x R\}$, as shown

in Fig. 4.2a. This solution connects the quiescent state with itself [see Fig. 4.2b] and, then, is the only solution which is unstable in the extended system. Therefore, is the only stable solution in the spatiotemporal system inside the region of parameters mentioned above. Formal demonstration of the latter statement is beyond of the scope of this thesis. It is noteworthy that although it is possible to find (integrate) other localized structures by fixing different values of *energy* $E(R_s, \partial_x R_s) = E_0$ [see Eq. (4.15) and dashed curves in Fig. 4.2a], they are unstable solutions in the spatiotemporal system.

It is vital to clarify here that it is possible to find more than one type of dissipative solitons within the mentioned region of parameters. In fact, as mentioned before, the relation $\cos(2\phi_0) = \mu/\gamma$ [Eq. (4.13)] admits four equilibria in the interval $[\pi, -\pi]$. Therefore, there are four different dissipative solitons with uniform phase. Nevertheless, they are not all stable. This depends on the value taken by the uniform phase of equilibrium, determined by relation (4.13). Figure 4.3 illustrates this relation and the respective stability regions of the different particle-type solutions. From this figure one can infer that the localized states appear or disappear by simultaneous saddle-node bifurcations when the injection and dissipation of energy are equal ($|\gamma| = \mu$). The stable soliton solutions are characterized by $\text{Re}(\psi)\text{Im}(\psi) < 0$ [$\text{Re}(\psi)\text{Im}(\psi) > 0$] for $\gamma > 0$ ($\gamma < 0$), thus both fields have different signs when $\gamma > 0$ [26]. This implies that stable UPS solution are characterized by the parameter δ_+ , which was defined above [see Eq. (4.14)], meanwhile for δ_- only unstable solutions are found.

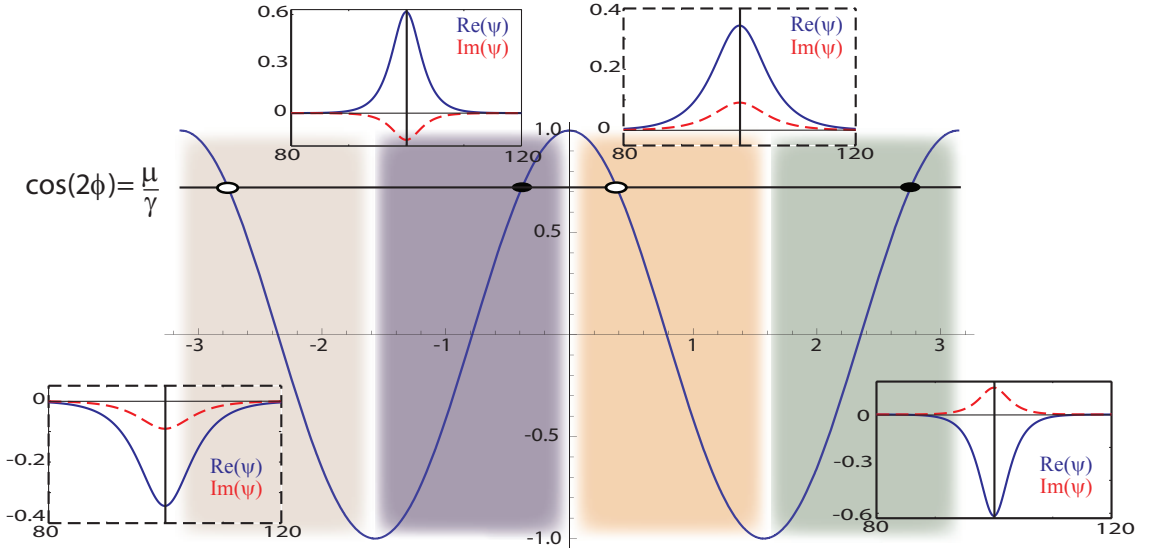


Figure 4.3: Schematic representation of the different stability regions of dissipative solitons. The circles represent the different solutions of $\cos(2\phi_0) = \mu/\gamma$: closed circles correspond to stable phase ϕ_0^s of localized states. Open ones correspond to unstable localized states with uniform phase ϕ_0^{us} . The insets depict the different types of dissipative solitons with $\mu = 0.10$, $\gamma = 0.13$, $\nu = 0.12$, and $L = 200$, where $\delta_+ = 0.203$ and $\delta_- = 0.037$.

A detailed analysis of the stability region and the bifurcation diagram of the uniform phase solitons were performed by Barashenkov and collaborators in Ref. [26]. They showed that only for δ_+ a stable UPS is obtained. This kind of dissipative soliton can develop more complex dynamics. Furthermore, two interacting solitons exhibit a rich dynamics, forming in

some cases bounded states, double period oscillations, and chaos. For a deeper understanding of such phenomena see the articles [56, 29, 57], and references therein.

4.4 UPS in two-dimensional systems

Several studies have been conducted in the two dimensional spatial extension of the dissipative solitons [58, 59] reviewed in the previous section. Notwithstanding such extensions are not evident, the localized structures found in this mentioned studies have the same characteristics properties of its analogous in one-dimensional system. That is, two-dimensional dissipative solitons exhibit a bell-shaped modulus and a uniform phase [see Ref. [59] and references therein].

Most of the experimental observations of localized structures in parametrically driven systems have been reported in two spatial dimensions. For instance, in fluid surface waves [32], solitary waves in Faraday’s water experiment [60], oscillons in granular media [33], and isolated states in thermal convection [34]. Note that all these observations have been realized in dissipative systems. Furthermore, the greatest difficulty to characterize theoretically localized states in two spatial dimensions is the lack of analytical expressions of these states.

In the context of conservative systems in two spatial dimensions perturbed with energy injection through parametrical temporal modulation and dissipation—namely, quasi-reversible systems [49, 50, 61, 62]—a prototype model where we can find this types of structures is the two-dimensional parametrically driven and damped nonlinear Schrödinger model (4.1). This equation has been derived in two spatial dimensional physical systems such as the parametrically driven magnetic layer [59] and Kerr type optical parametric oscillators [24]. In the conservative limit ($\mu = \gamma = 0$), the mentioned model becomes the well-known nonlinear Schrödinger equation. This model is widely applied to understand wave phenomena in hydrodynamics, nonlinear optics, nonlinear acoustics, quantum condensates, heat pulses in solids and various other nonlinear instability phenomena [63]. The nonlinear Schrodinger equation is an universal model for weakly dispersive and nonlinear media.

In order to obtain the polar coordinate representation of the PDNLS model [Eq. (4.1)], we introduce the Madelung transform of the complex field

$$\psi(\rho, \theta; t) \equiv R(\rho, \theta; t)e^{i\phi(\rho, \theta; t)}, \quad (4.17)$$

and the polar representation of the spatial operators $\vec{\nabla}^2 \equiv \rho^{-1}\partial_\rho + \partial_{\rho\rho} + \rho^{-2}\partial_{\theta\theta}$, obtaining

$$\partial_t R = \rho^{-1}\partial_\rho\phi R + \partial_{\rho\rho}\phi R + \rho^{-2}\partial_{\theta\theta}\phi R + 2\partial_\rho R\partial_\rho\phi + 2\rho^{-2}\partial_\theta R\partial_\theta\phi - \mu R + \gamma R \cos(2\phi), \quad (4.18)$$

$$R\partial_t\phi = -\nu R - R^3 - \rho^{-1}\partial_\rho R - \partial_{\rho\rho}R - \rho^{-2}\partial_{\theta\theta}R + (\partial_\rho\phi)^2 R + \rho^{-2}(\partial_\theta\phi)^2 R - \gamma R \sin(2\phi). \quad (4.19)$$

The above set of equations represents the two-dimensional parametrically driven and damped nonlinear Schrödinger model in polar coordinate. It is important to mention that the bifurcation scenario of the PDNLS model in two-dimensions [58] is exactly the same that found in the one-dimensional case [see Sec. 4.2]. And therefore, its possible solutions are

found for the same sets of parameters aforementioned. Moreover, dissipative solitons found in this 2D model are characterized for exhibit, just like its one-dimensional analogue, a bell-shape in its modulus and an uniform state in the phase. Therefore, these structures posses axial symmetry; that is, there is not an explicit angular dependence. Hence, analogously to the one-dimensional problem, we assume the strategy of fixing a constant phase $\phi \equiv \phi_0$ and a stationary modulus without angular dependency $R \equiv R_s(\rho)$. Introducing these in the above set of equations,

$$\cos(2\phi_0) = \frac{\mu}{\gamma}, \quad (4.20)$$

$$\partial_{\rho\rho}R_s = \delta R_s - R_s^3 - \rho^{-1}\partial_{\rho}R_s. \quad (4.21)$$

where $\delta \equiv \delta_+ = -\nu + \sqrt{\gamma^2 - \mu^2}$ corresponds to the characteristic value for the stable UPS [see Sec. 4.3]. Unfortunately, the equation that determines the shape of the module [Eq. (4.21)], has no analytical solution. Figure 4.4 shows a UPS solution obtained by numerical simulations conducted for 2D-PDNLS. The uniform phase solution (ϕ_0^s) of the localized state is one of the equilibrium solutions admitted by relation (4.20), which is the same that rules the uniform phase for the one-dimensional case [see Fig. 4.3].

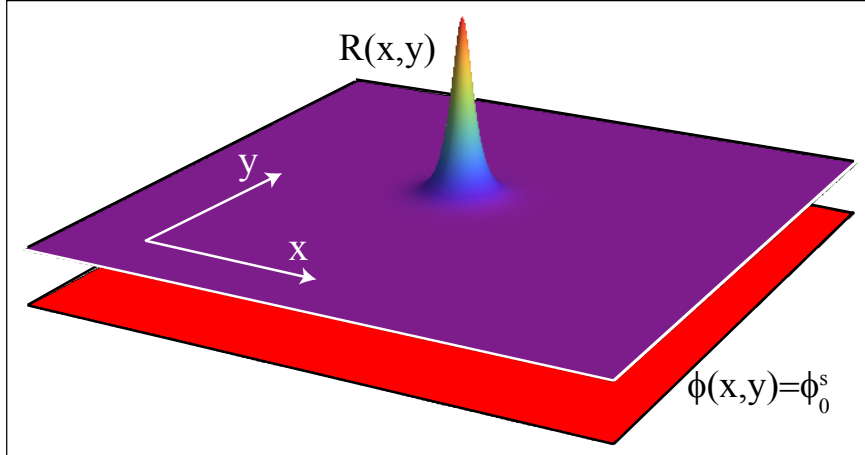


Figure 4.4: Stable uniform phase soliton in two-dimensional PDNLS with $\mu = 0.10$, $\gamma = 0.105$, $\nu = 0.05$, and $L = 100$

As we have mentioned before, there is no analytical expression to describe the shape of two-dimensional localized state. However, using a variational method, one can obtain a good approximation [59, 64],

$$R_s(\rho) \approx A_0 \sqrt{\delta} \operatorname{sech} \left(B_0 \sqrt{\frac{\delta}{2}} \rho \right), \quad (4.22)$$

where $A_0 = 2.166$ and $B_0 = 1.32$. However, this approximation does not describe the asymptotic behavior of the dissipative soliton (exponential tail) which is known, Ref. [59], to be ruled by the expression

$$R_s(\rho \rightarrow \infty) \rightarrow \frac{e^{-\sqrt{\delta}\rho}}{\sqrt{\rho}}, \quad (4.23)$$

which will be very useful in further discussion.

Part III

Control of Dissipative Localized Structures

Chapter 5

Non-propagative Hydrodynamics Solitons in Inhomogeneous Media

Macroscopic particle-type solutions or localized states in extended dissipative systems have been observed in different fields, such as: domains in magnetic materials, chiral bubbles in liquid crystals, current filaments in gas discharge, spots in chemical reactions, localized states in fluid surface waves, oscillons in granular media, isolated states in thermal convection, solitons in nonlinear optics, among others. The variety of this type of phenomena evidences the universality of these particle-type solutions [19].

In the last two decades, the properties and mechanisms of creation of localized structures have been established as well as their interactions. However, few studies have focused on manipulation and control of these coherent states. In the pioneering work of Wu et al. [54], the authors mentioned that hydrodynamic non-propagating solitons were sensitive to depth gradients. They found that solitons move toward less deep regions. Moreover, recent study in the context of optical cavities in semiconductors have demonstrated that a phase gradient induces propagation of cavity solitons [65]. Furthermore, it is possible to control the spatially localized modes arising in two-dimensional chirped photonic lattices [66, 67]. All this suggests that inhomogeneities can be used as a spatial control tool, as it induces drift of solitons.

5.1 Hydrodynamic soliton motion in a tilted basin

Non-propagating hydrodynamic solitons arise naturally in a quasi 1-D rectangular basin filled with water excited vertically at certain range of frequencies and amplitudes [54]. These localized states have a subharmonic nature depicted by oscillations at half the forcing frequency. They appear as localized transverse *sloshing* structures on the free surface. The dissipative solitons nucleate from disturbances of the stable flat state [54].

The aim of this Section is to characterize the effects produced by the inhomogeneities on non-propagating hydrodynamic solitons. More precisely, we have performed a theoretical and experimental study of the dynamics of non-propagating hydrodynamic soliton in a tilted basin. We observe that by changing the tilt angle we can control the behavior of the soliton and, therefore, this can be used as a manipulation mechanism.

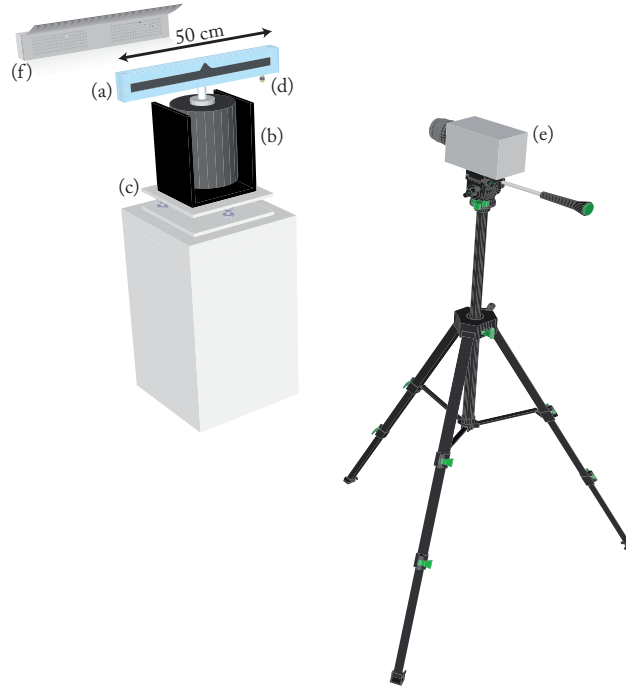


Figure 5.1: The basin filled with a dyed mixture of water and Kodak Photo Flo (a) is vibrated vertically by an electromechanical shaker (b). Different tilt angles can be obtained using a three-point level system (c). Acceleration is measured using an accelerometer (d). A high speed camera (e) acquires images of the fluid illuminated from behind by an array of LED lamps (f).

5.1.1 Experimental setup and procedure

The experiments were done in a rectangular plexiglas basin, $L_x = 50$ cm long, $L_y = 2.54$ cm wide and $L_z = 10$ cm high. The basin is filled up to $d = 2$ cm in depth with a mixture of 252 cm^3 of water, 2 cm^3 of Kodak Photo Flo[®] 200¹ and some drops of black ink for contrast. Free surface saturation with contaminants plays an important role for reproducibility [25].

The cell is driven vertically by an electromechanical vibrator lying on a three-point leveling system which allows longitudinal tilting [see figure 5.1]. The shaker is fed with an amplified sine wave signal generated by a function/arbitrary waveform generator and a power amplifier. Solitons can exist at frequencies slightly below 11 Hz and accelerations around $0.1 g$ (g acceleration of gravity) [68]. The basin acceleration is measured using a piezoelectric accelerometer attached to the basin bottom. The analog signal of the device is connected to a sensor signal conditioner and a lock-in amplifier synchronized with the forcing signal [see figure 5.2a]. Acceleration values are provided with precision of $0.01 g$. An analog tilt sensor is placed on the external bottom of the basin. This microelectromechanical (MEM) device is connected to an analog/digital converter which sends angle values to a computer within an error of 0.01° .

¹This chemical product creates a film which improves significantly wetting at the walls.

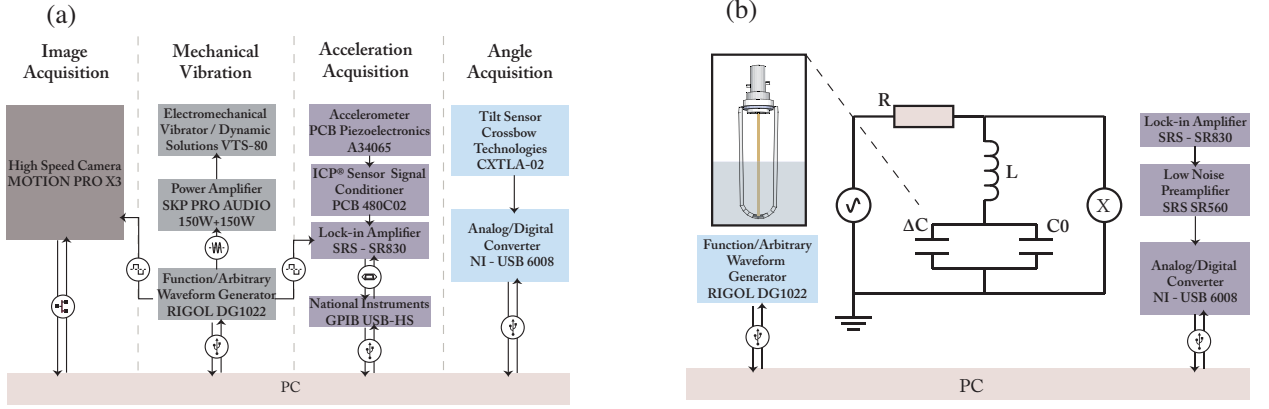


Figure 5.2: (a) The scheme shows the measurement procedures used for spatial acquisitions. (b) Local acquisitions scheme. The capacitor ΔC represents capacity fluctuations and can be negative. C_0 represents parasitic and zero-level capacity.

Two different types of measurements are made on the free surface. Sequences of images taken with a high speed camera provide spatial measurements. On the other hand, local measurements are done using phase fluctuations of the output signal of a resonant capacitive device [cf. Fig. 5.2].

5.1.2 Experimental results

We report measurements performed at a fixed vibration frequency of 10.4 Hz and amplitudes around 0.1 g, region in which the existence and features of non-propagating hydrodynamic solitons have been studied in detail [69]. Typical tilt angles were between $\pm 1^\circ$.

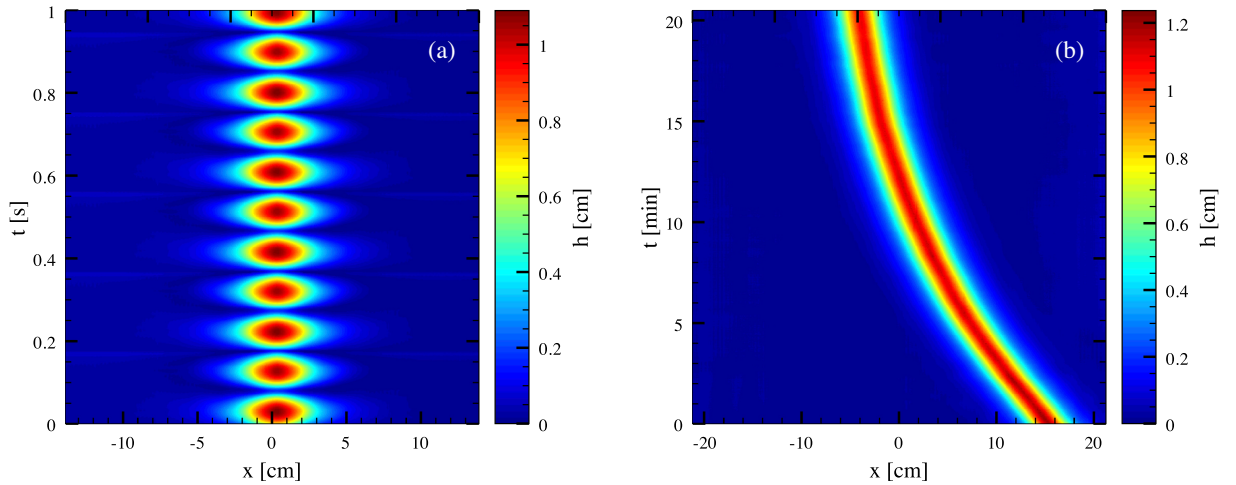


Figure 5.3: Spatio-temporal diagrams for solitons at different timescales. (a) A soliton *slashes* back and forth with half the driven frequency (10.4 Hz) at $a_{RMS} = 0.062 g$ and zero tilt angle. (b) A soliton travels to a shallower region when the basin is tilted in 0.66° clockwise. Driven frequency and amplitude are 10.4 Hz and $0.078 g$ respectively. Images were taken stroboscopically when soliton reaches its maximum after every eight cycles.

Figure 5.3 show spatial-temporal diagrams for two different solitons with different time scales and tilt angles. Contact line profiles are extracted from images taken with a high speed camera and plotted against time. In Figure 5.3a, the soliton stands at a fixed position on the center of the basin. The tilt angle is zero and the forcing amplitude is 0.062 g. The acquisition rate is 400 Hz, so the soliton fast *sloshing* motion can be observed. However, motion beneath the water baseline cannot be detected as no contrast is available. The contact lines at the front and rear walls switch on the image at each half cycle. Figure 5.3b shows a long-time acquisition for a basin tilted 0.66° clockwise. Normal acceleration of the basin is 0.078 g. The soliton was created at $t = 0$ and images were taken stroboscopically at a fixed rate of 650 mHz. The diagram shows the drifting of the non-propagating hydrodynamic soliton, in this case toward shallower regions. These dissipative solitons can be attracted to lateral boundaries and even pinned on them depending on the driving amplitude and frequency [60]. In general, our dissipative solitons remain far enough from lateral walls as they propagate across the principal axis so boundary effects seem to be negligible. Boundary effects studies are still in progress.

Trajectory of the dissipative soliton reveals a non-trivial time dependence. At a first stage, the modulus of the solution attains rapidly a constant speed. Wu et al. referred to this as short-time scale stage in their work [54]. At a long-time scale stage, the soliton motion seems to converge to a fixed position rather than to a constant velocity as is clearly illustrated in Figure 5.3b. Long-time acquisitions were strongly motivated by the fact that the initial velocity for short-time acquisition depends on the position where the soliton is created. The break of translational symmetry, characteristic of this type of solutions, suggests that the speed does not depend only on the depth gradient but also on the local depth.

For more details about experimental setup and procedure, as well as the acquisition method performed see the Appendix Sec. A.1 and the PhD dissertation work [70].

Velocity vs. position

Soliton dynamics on tilted basins can be well understood by means of the velocity versus position plane. Figure 5.4a shows *phase plane tracks* for different solitons at different angles. For each image sequence, the contact line profile is fitted using the 4-parameters function predicted by theory [see Sec. 5.2 and Fig. 5.5]. The positions plotted in Figure 5.4a are obtained from the parameter which represents the position at which maximum height takes place.

From the results obtained in the central area of the cell—where edge effects are negligible—the diagram shows that solitons are governed by the motion law [cf. Fig. 5.4]

$$\dot{x}_0 = -\frac{1}{\tau(\phi)} [x_0 - P(\phi)], \quad (5.1)$$

where x_0 stands for the position of the maximum of the dissipative soliton, ϕ is the tilt angle of the basin, τ accounts for a relaxation time which characterizes the soliton dynamics, P/τ is a characteristic speed of propagation and P is the equilibrium position towards which the dissipative soliton converges.

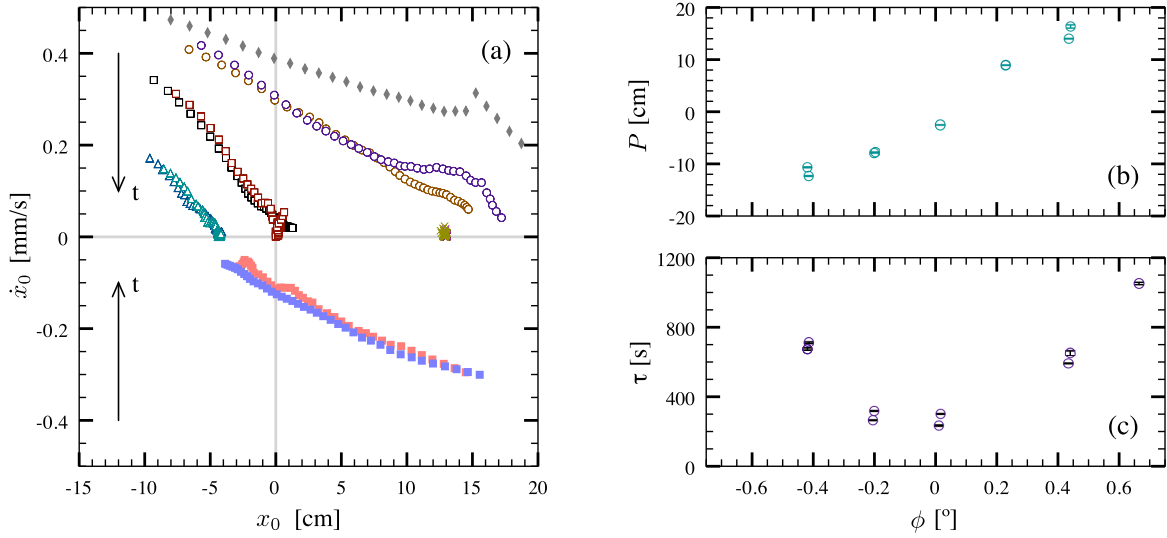


Figure 5.4: (a) Velocity vs. position plots for different skew angles: \blacksquare , -0.42° , \triangle , -0.20° , \square , -0.01° , \times , 0.23° , \circ , 0.43° , \blacklozenge , 0.66° . The arrows show time direction in the series of points. Solitons can propagate upward (\circ , \blacklozenge), downward (\triangle , \square , \blacksquare), or even stay at their position (\times), depending on their relative position to the equilibrium. Two experiments were run for each angle except for $\phi = -0.66^\circ$ (\blacklozenge). In this particular case, the equilibrium position is *virtually* located beyond the channel edge. (b) Equilibrium position vs. tilt angle plot. P moves toward shallower regions as ϕ increases. (c) Position decay time τ dependence on the skew angle ϕ . As angle increases, convergence to equilibrium position becomes slower.

The proposed model, Eq. (5.1), is invariant under spatial and time translations as expected. Lateral boundary effects appear as a change in the slope for positions above $|x_0| = 15$ cm [see Fig. 5.4a]. This Equation implies that solitons are attracted to its equilibrium position $P(\phi)$ by an exponential law. The dynamics of solitons do not have inertia, in the sense that their dynamics break galilean invariance. Notice that both the equilibrium position P and the exponential decay time τ depend on ϕ . As the tilt angle increases, the equilibrium position is pulled out from the center of the basin even surpassing the basin boundaries. Figure 5.4a shows phase-space tracks on which solitons get pinned at their equilibrium positions after moving *upward*² or downward, respectively. Angle dependence of these two parameters is shown in figure 5.4b. Note that the decay time τ increases for larger angles. Dependence on the angle is plotted in figure 5.4c.

5.2 Theoretical description

Close to the Faraday instability, the parametrically driven damped nonlinear Schrodinger equation models this system [cf. Sec. 4.1]. The non-propagating hydrodynamic solitons are well described by the non-trivial stationary homoclinic solution with constant phase, UPS solution, found in PDNLS [see Sec. 4.3].

²We define *upward* direction against depth gradient.

In order to characterize the role of the container inclination we incorporate a spatial variation of the system parameters. Considering that the tilt angle is small, we deduce a dynamic equation for the position of non-propagating hydrodynamic solitons. This equation is characterized by two terms: a constant speed and a linear relaxation process. Therefore, at a given inclination of the cell, the dissipative soliton travels to an equilibrium position through a relaxation process. Consequently, for the sake of simplicity, we analyze the case in which only the detuning parameter is a function of the space. Theoretical result shows a good agreement with the proposed dynamics of dissipative hydrodynamic solitons observed in the experiment performed in a vertically forced tilted water container, detailed in the previous sections.

5.2.1 Dissipative solitons in homogeneous media

As mentioned before, the dynamics of a layer of incompressible fluid that is driven by a sinusoidal force with frequency Ω_f normal to the free surface is modeled by the one-dimensional parametrically driven and damped nonlinear Schrödinger equation [42, 52],

$$\partial_t \psi = -i\nu\psi - i|\psi|^2\psi - i\partial_{xx}\psi - \mu\psi - \gamma\bar{\psi}, \quad (5.2)$$

where the order parameter $\psi(x, t)$ is a one dimensional complex field related with the surface displacement from flat interface $h(x, t)$ and the velocity potential at the free surface $\varphi(x, t)$ by the relations $h = \psi e^{-i\Omega_f t/2} + c.c.$ and $\varphi(x, t) = -i\psi e^{-i\Omega_f t/2} + c.c.$, respectively [see Ref. [52] and references therein]. ν is the detuning parameter, which is proportional to the difference between the observed standing wave frequency and $\Omega_f/2$. μ is the damping parameter which is proportional to the kinematic viscosity of the fluid, which accounts for the dissipation mechanisms of the system and γ is the forcing acceleration amplitude. The terms proportional to μ and γ break the time reversal symmetry. The higher-order terms in equation (5.2) are ruled out by a scaling analysis, since $\mu \ll 1$, $\nu \sim \mu \sim \gamma$, $|\psi| \sim \mu^{1/2}$, $\partial_x \sim \mu^{1/2}$, and $\partial_t \sim \mu^{1/2}$. By introducing the polar representation of the complex field, $\psi(x, t) \equiv R(x, t)e^{i\phi(x, t)}$, in the one-dimensional PDNLS equation (5.2), one obtains

$$\partial_t R = R\partial_{xx}\phi + 2\partial_x R\partial_x\phi - \mu R + \gamma R \cos(2\phi), \quad (5.3)$$

$$R\partial_t\phi = -\nu R - R^3 - \partial_{xx}R + R(\partial_x\phi)^2 - \gamma R \sin(2\phi). \quad (5.4)$$

Note that these equations are exactly the same as we would have obtained by replacing the spatial operators, $\vec{\nabla} \rightarrow \partial_x$ and $\vec{\nabla}^2 \rightarrow \partial_{xx}$, in relations (4.2) and (4.13). The trivial uniform solution of equation (5.2) is the homogeneous state $\psi_0 = 0$, which represents the flat or quiescent solution of the fluid layer.

The localized structure that arises naturally in PDNLS is the well known uniform phase soliton (UPS). This dissipative soliton corresponds to a non-trivial stationary homoclinic solution in the extended (or stationary) phase space $\{R, \partial_x R\}$ connecting the quiescent state with itself [42, 26]. In the context of fluids UPS describes the amplitude of the nonlinear solitary waves exhibited in the surface. This solution is characterized by a constant phase

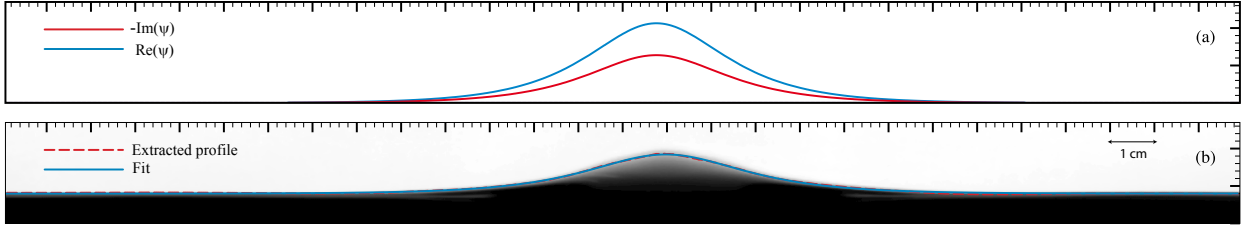


Figure 5.5: Dissipative soliton in parametrically resonant systems. (a) Stable dissipative soliton observed in the parametrically driven and damped nonlinear Schrödinger model (5.2). (b) Snapshot of a non-propagating hydrodynamic soliton observed in a vertically driven 50 cm long and 2.54cm wide rectangular container, filled with $H = 2$ cm of water. The solid blue and red curve are, respectively, instantaneous surface profile and fit $h(x) = A_s \operatorname{sech}[(x - x_0)/w + h_0]$. Adjusted relevant parameters are $A_s/H = 0.523 \pm 0.001$ and $w/H = 0.786 \pm 0.004$.

and bell-shape type in the modulus [cf. Eqs. (4.13) and (4.16)]

$$\cos(2\phi) = \frac{\mu}{\gamma},$$

$$R_s(x, x_0) = \sqrt{2\delta_{\pm}} \operatorname{sech}\left(\sqrt{\delta_{\pm}}(x - x_0)\right).$$

Figure 5.5 shows a typical dissipative soliton observed in the parametrically driven and damped nonlinear Schrödinger equation and the typical dissipative soliton observed experimentally, which shows a very good agreement with the UPS shape (4.16). Note that this localized states exists in the region of parameters bounded by negative detuning $\nu < 0$ and the amplitude of forcing $\mu < \gamma < \sqrt{\mu^2 + \nu^2}$. The stable dissipative solitons are characterized by $\operatorname{Re}(\psi)\operatorname{Im}(\psi) < 0$, so both fields have different sign [see Ref. [26] and Sec. 4.3]. Hence, there are two stable dissipative solitons, which are related by the reflection symmetry ($A \rightarrow -A$), these solutions correspond to dissipative solitons in phase or out of phase.

5.2.2 Effect of channel inclination

The inclination of the basin produces inhomogeneity on the physical parameters of the system (dissipation, injection and detuning). Furthermore, experimental results have shown that the non-propagating hydrodynamic soliton moves towards the shallow water regions by a relaxation process. Consequently, we infer that the energy injection and dissipation have a similar spatial behavior meanwhile detuning has a convex behavior along the channel. In fact, this is a simple consequence of small tilting angles (θ) since the local depth can be considered as a space function, $d(x) = H - x \tan(\theta)$.

To account for these effects in our theoretical description, we consider that detuning, dissipation and injection of energy parameters in parametrically driven and damped nonlinear Schrödinger equation become all inhomogeneous

$$\begin{aligned} \mu(x) &\equiv \mu_0 + \mu_1(x), \\ \nu(x) &\equiv \nu_0 + \nu_1(x), \\ \gamma(x) &\equiv \gamma_0 + \gamma_1(x). \end{aligned} \tag{5.5}$$

Here $\{\mu_0, \nu_0, \gamma_0\}$ and $\{\mu_1, \nu_1, \gamma_1\}$ account for homogeneous and inhomogeneous spatial variation, respectively. Given that the parametrically driven and damped nonlinear Schrödinger equation is valid in the quasi-reversible limit ($\nu \sim \mu \sim \gamma \sim \epsilon \ll 1$, where ϵ is an arbitrary parameter of scale) we consider the inhomogeneities as perturbative effects, i.e. $\mu_1(x) \ll \mu_0$, $\gamma_1(x) \ll \gamma_0$ and $\nu_1(x) \ll \nu_0$. Hence, Equations (5.3) and (5.4) read

$$\partial_t R = 2\partial_x R \partial_x \phi + \partial_{xx} \phi - \mu_0 R + \gamma_0 R \cos(2\phi) - \mu_1(x) R + \gamma_1(x) R \cos(2\phi), \quad (5.6)$$

$$R \partial_t \phi = -\nu_0 R - R^3 - \partial_{xx} R + R(\partial_x \phi)^2 - \gamma_0 R \sin(2\phi) - \nu_1(x) R - \gamma_1(x) R \sin(2\phi). \quad (5.7)$$

For small angles, the bell-shaped amplitude of the dissipative solitons does not change during the propagation. However, inhomogeneity generates two effects: (i) localized states are modified by the perturbation, and (ii) the spatial translational mode of the dissipative solitons–Goldstone mode–acquires a non trivial dynamic as a result of the translational symmetry breaking. In order to achieve a theoretical description for such dynamics, we consider the ansatz

$$R(x, t) = R_s(x - x_0(t)) + \rho(x, x_0), \quad (5.8)$$

$$\phi(x, t) = \phi_0 + \Omega(x, x_0), \quad (5.9)$$

where $\rho(x, x_0)$ and $\Omega(x, x_0)$ are the corrective functions, respectively. The modulus R_s and the constant phase ϕ_0 are given by relations (4.16) and (4.13), respectively. Note that we have conferred all the dynamics to the soliton position $x_0 \equiv x_0(t)$. Furthermore, we considered it as a slow variable ($\ddot{x}_0 \sim \mathcal{O}(\epsilon^2)$), and the soliton velocity $\dot{x}_0(t)$ has the same order of the perturbation ($\dot{x}_0 \sim \mathcal{O}(\epsilon)$). Introducing the above expressions in the set of equations (5.7) and (5.6), one finds after linearizing the perturbation functions

$$[2\partial_x R_s \partial_x + R_s \partial_{xx} - 2\gamma_0 \sin(2\phi_0) R_s] \Omega = \mu_1(x) R_s - \gamma_1(x) \cos(2\phi_0) R_s - \partial_z R_s \dot{x}_0, \quad (5.10)$$

$$[-\nu_0 - \gamma_0 \sin(2\phi_0) - 3R_s^2 - \partial_{xx}] \rho = 2\gamma_0 R_s \cos(2\phi_0) \Omega + \nu_1(x) R_s + \gamma_1(x) R_s \sin(2\phi_0), \quad (5.11)$$

where $z \equiv x - x_0(t)$ is the coordinate in the co-moving frame. As we can see, the resulting equation for the phase perturbation $\Omega(x, t)$, Eq. (5.10), does not depend on the correction of the modulus $\rho(x, t)$. Therefore, we can find directly the solution for the phase correction. Multiplying the partial differential equation (5.10) by the integrating factor R_s , we obtain after straightforward calculations

$$\begin{aligned} \Omega(x) &= \int^x \frac{2\gamma_0 \sin(2\phi_0) dx'}{R_s^2(x')} \int^{x'} dx'' \Omega(x'') R_s(x'') \\ &+ \int^x \frac{dx'}{R_s^2(x')} \int^{x'} dx'' [\mu_1(x'') - \gamma_1(x'') \cos(2\phi_0)] R_s^2(x'') - \int^x \frac{\dot{x}_0}{2} dx', \end{aligned} \quad (5.12)$$

which is a Fredholm integral equation [71]. Since the system is at the quasi-reversible limit it holds that $\gamma \sin(2\theta_0) = \sqrt{\gamma^2 - \mu^2} \ll 1$. Based on this, we consider that, at first order, the solution for the Fredholm integral (5.12) is given by the approximation

$$\Omega(x) \approx \int^x \frac{dx'}{R_+^2(x')} \int^{x'} dx'' [\mu_1(x'') - \gamma_1(x'') \cos(2\phi_0)] R_s^2(x'') - \int^x \frac{\dot{x}_0}{2} dx'. \quad (5.13)$$

It is important to note that one can iteratively calculate the corrections to the previous approximation in a power series in the small parameter $\sqrt{\gamma^2 - \mu^2}$ [71]. Introducing the linear operator

$$\mathcal{L} \equiv -\nu_0 - \gamma_0 \sin(2\theta_0) - 3R_+^2 - \partial_{xx},$$

equation (5.11) can be rewritten as

$$\mathcal{L}\rho = 2\gamma_0 R_s \cos(2\phi_0)\Omega + \nu_1(x)R_s + \gamma_1(x)R_s \sin(2\phi_0). \quad (5.14)$$

In order to achieve a solution for the correction of the modulus $\rho(x, t)$, we must be able to determine if the linear operator \mathcal{L} is invertible. To solve this we use the Fredholm alternative (see Sec. 2.2, Ref. [16] and references therein). Accordingly, we introduce the inner product $\langle f|g \rangle = \int_{-\infty}^{\infty} f(x)g(x)dx$. Hence, under this definition, the linear operator \mathcal{L} is self-adjoint ($\mathcal{L} = \mathcal{L}^\dagger$). Therefore its kernel—the set of functions $\{v\}$ that satisfy $\mathcal{L}v = 0$ —is of dimension 1. As a result of the spatial translation invariance of the soliton solution, the expression $\mathcal{L}\partial_x R_s = 0$ is satisfied. Thus, the linear equation (5.14) has a solution if the condition³

$$\langle \partial_x R_s | 2\gamma_0 \cos(2\phi_0)R_s\Omega + \nu_1(x)R_s + \gamma_1(x) \sin(2\phi_0)R_s \rangle = 0 \quad (5.15)$$

is fulfilled. Using the approximation for the phase perturbation, Eq. (5.13)), in the evaluation of this inner product one obtains, after straightforward calculations,

$$\begin{aligned} \dot{x}_0 = & \frac{1}{\int_{-\infty}^{\infty} dx x \partial_x R_s^2(x)} \left[\frac{1}{\mu_0} \int_{-\infty}^{\infty} dx [\gamma_1(x) \sin(2\phi_0) + \nu_1(x)] \partial_x R_s^2 \right. \\ & \left. + 2 \int_{-\infty}^{\infty} dx \partial_x R_s^2(x) \int^x \frac{dx'}{R_s^2(x')} \int^{x'} dx'' (\mu_1(x'') - \gamma_1(x'') \cos(2\phi_0)) R_s^2(x'') \right]. \end{aligned} \quad (5.16)$$

This expression gives us information of the dynamics of dissipative soliton as a function of general spatial disturbance. For the sake of simplicity and better understanding of the effects produced by small tilt angles, we consider that the dissipative and forcing parameters ($\mu(x), \gamma(x)$) are homogeneous, $\mu_1(x) = \gamma_1(x) = 0$. Meanwhile the detuning parameter has a quadratic spatial profile,

$$\nu(x) = \nu_0 + \bar{\nu}_1 x + \bar{\nu}_2 x^2, \quad (5.17)$$

which is consistent with experimental observations. Then, the soliton velocity (5.16) is ruled by the relation

$$\dot{x}_0(t) = \frac{2\bar{\nu}_2}{\mu_0} \left[x_0(t) + \frac{\bar{\nu}_1}{\bar{\nu}_2} \right]. \quad (5.18)$$

³This is known as the solvability condition or Fredholm alternative, see Ref. [16] and Sec. 2.2.1.

By defining $\tau^{-1} \equiv -(2\bar{\nu}_2)/\mu_0$, $P \equiv -\bar{\nu}_1/\bar{\nu}_2$, we obtain exactly the same experimental behavior observed for the non-propagating hydrodynamic soliton (5.1). Figure 5.6 presents numerical simulation results obtained considering a quadratic dependence on space for detuning. As would be expected, the relaxation dynamic evolution exhibited by the UPS soliton in these numerical simulations has a very good agreement with the experimental results since they have the same motion law [cf. Eqs. (5.18) and (5.1)].

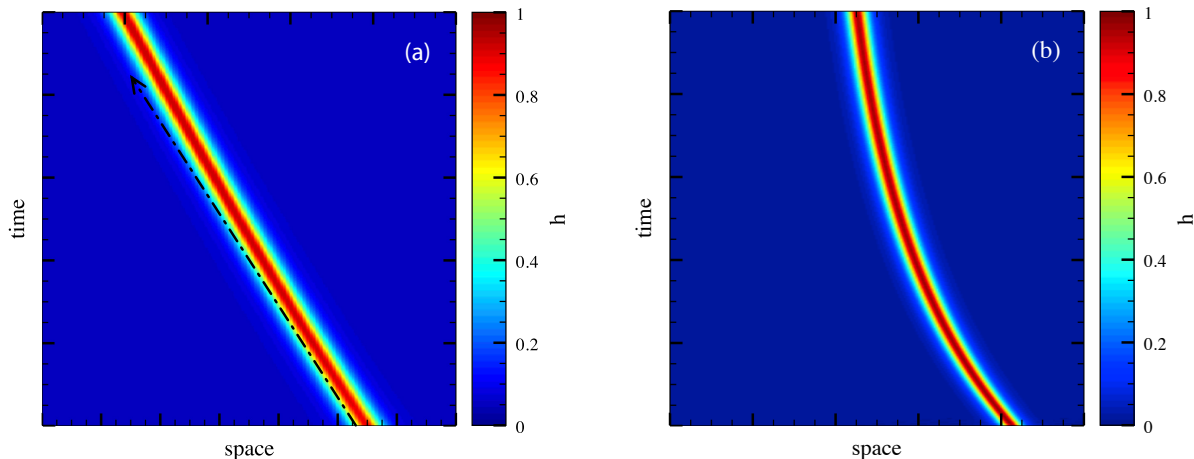


Figure 5.6: Spatiotemporal diagram of dissipative solitons obtained by numerical simulations of parametrically driven and damped nonlinear Schrödinger model (5.2) over 250 points with periodic boundary conditions. The diagrams show 8000 cycles calculated with a time resolution of $1/200$ period. (a) $\gamma(x) = 0.42$, $\nu(x) = -0.09$, and $\mu(x) = 0.15(10.04x)$, the arrow evidences a non-constant drift velocity. (b) $\gamma(x) = 0.40$, $\nu(x) = -0.12 + 0.03x - 0.04x^2$, and $\mu(x) = 0.10 - 0.03x + 0.04x^2$.

It is important to note that the equilibrium position depends on the tilt angle, which is modeled theoretically by the introduction of the inhomogeneous detuning parameter ν . In this system, dissipation, energy injection and detuning are inhomogeneous. Dissipation grows in the direction of depth gradient, but changes are small. Indirect evidence from soliton local phase indicates that energy injections varies less or similarly than dissipation. In contrast, the detuning exhibits a convex behavior along channel [cf. Secs. 5.1.2 and 5.2.2]. Moreover, due to the inclination of the basin we conclude that the profile of this physical parameters takes a quadratic form, Eq. (5.17). This is in agreement with the soliton dynamics observed in the tilted channel [cf. Figures 5.4 and 5.6].

Part IV

Phase Shielding Solitons

Chapter 6

Phase Shielding Solitons in PDNLS

The dissipative soliton has been observed in several parametrically forced systems such as vertically oscillating layer of water [42, 52, 72], parametrically driven easy-plane ferromagnetic wire [26, 43], degenerate optical parametric oscillator [24] and the parametrically driven pendulum chain [31]. All these systems can be described by the well known parametrically driven and damped nonlinear Schrödinger equation in the limit of small injection and dissipation of energy. Typically, the localized structure found in this model is characterized by a bell-shape in the modulus of the amplitude and a constant phase (UPS) [see Chap. 4]. This solution describes quite well the profile of the dissipative solitons arising in the aforementioned parametrical systems.

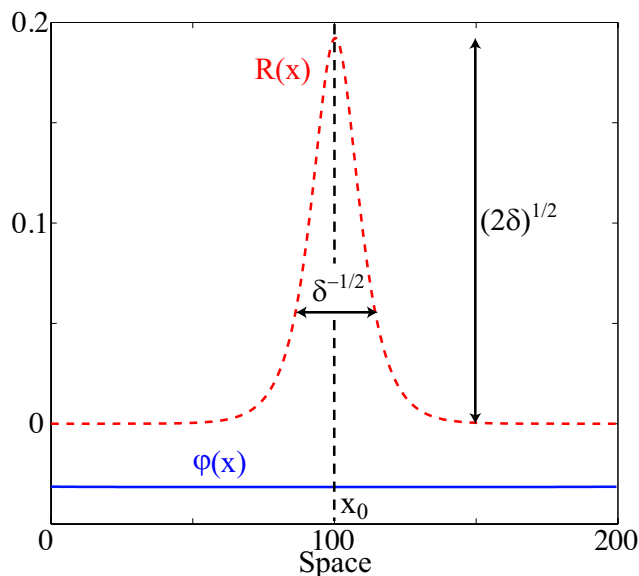


Figure 6.1: Uniform Phase Soliton found in PDNLS. Its modulus is $R(x)$ (red dashed line) and the phase $\phi(x)$ (blue solid line). Parameter values are $\mu = 0.1000$, $\nu = -0.0122$, $\gamma = 0.1002$, $\delta = 0.0185$ and $L = 200$. x_0 stands for the soliton position. The soliton width and height are indicated.

As we can see, until now the phase of these dissipative solitons have always been considered uniform. However, Barashenkov et al. [29] were the first to report the evidence of a complex, non-uniform phase structure in dissipative solitons when studying its dynamics of interaction

(bounded states). In such work, the authors consider the non-uniform phase as a consequence of the interaction among solitons. Nevertheless, numerical simulations of PDNLS have shown that even when a single dissipative soliton is perturbed, two unexpected counter-propagative phase fronts arise from the soliton position x_0 , surrounding the bell-shape modulus [73, 74]. The phase front dynamics is characterized by a rather slow motion which suddenly reaches a steady state distant from the soliton position. During this process the shape of both the phase front and the modulus remain unchanged. These novel type of solitons have been called phase shielding solitons (PSS) since the phase structure seems to shield the soliton modulus [73]. This section attains an adequate analytical description and numerical characterization of these localized states.

6.1 Preliminary numerical results

Experiments on dissipative localized structures are always performed in systems that possess a finite dimension (length). Likewise, numerical simulations also have a limitation on the size of the systems that are able to calculate. These constraints are crucial when we are interested in develop a theoretical description of such solutions. In other words, the system size is an important parameter to take into consideration and plays a vital role in the characterization of the solutions that emerge in a system.

Taking into account the above, we have conducted numerical simulations of dissipative solitons in parametrically driven and damped nonlinear Schrödinger equation for appropriately sized systems. Figure 6.2 shows the phase front that commonly appears after making a slight perturbation to the soliton. The soliton position is found at the center.

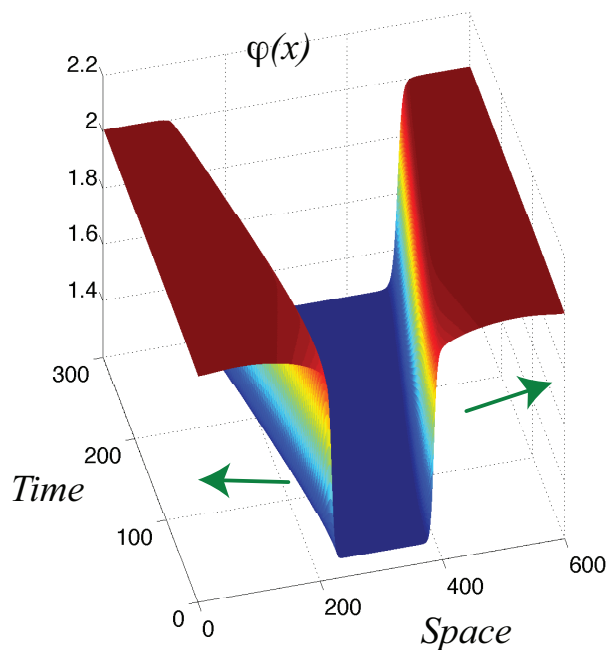


Figure 6.2: Typical phase propagation ($\varphi(x, t)$) of dissipative soliton found in the PDNLS.

The simulation was performed as follows: A soliton is created by slightly perturbing an initial

homogenous state. The soliton position was fixed at the left edge of the system. The parameters are chosen to fulfill the conditions for the appearance of UPS solutions, i.e. negative detuning $\nu < 0$, and an amplitude of forcing that satisfies $\mu < \gamma < \sqrt{\mu^2 + \nu^2}$. Initially, the perturbation quickly evolves to a well defined bell-shaped modulus. After some transient wave emission, which rapidly disappears by the edges of the system, the phase around the core of the localized state becomes uniform, taking the value corresponding to the stable uniform soliton (UPS) [cf. Sec. 4.3 and Ref. [26]]. From this initial behavior, a propagative phase front emerges far from the core of the modulus [see Fig. 6.3a], moving away from the position of the latter. The front propagation is characterized by a rather slow motion which suddenly reaches a steady state [see Fig. 6.2b].

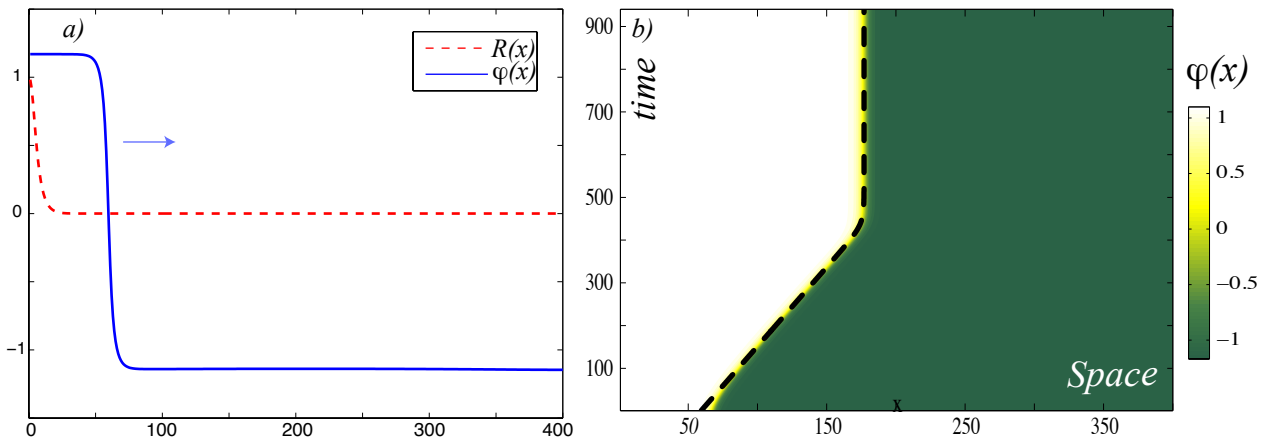


Figure 6.3: Half of phase shielding soliton. a) initial phase front profile reached after some transients. b) spatiotemporal diagram of phase front. The set of parameters are $\gamma = 0.083$, $\nu = -0.063$, and $\mu = 0.058$.

It is important to mention that the phase structure of PSS is composed by two different phase fronts at each side of the modulus [cf. Fig. 6.4]. Moreover, detailed analysis of the numerical results reveals that these phase fronts always connect (asymptotically) an stable phase equilibrium—the definition of stable and unstable phase is related with the stability of the UPS solutions detailed in Sec. 4.3 and Ref. [26]—with one (two) unstable uniform phase given by Eq. (4.13), in the interval $[-\pi, \pi]$. Figure 6.4 shows a phase shielding soliton, the phase structure connects three UPS phase equilibrium solution.

Therefore, since there are four possible uniform equilibrium solutions for the phase (two stable, and two unstable), we can find eight possible stationary configurations of phase shielding solitons. They are determined by different combinations of equilibrium connections. Thus, these steady phase structures strongly depend of initial conditions and are equally likely to appear in the same set of parameters. Figure 6.5 displays the all different Phase Shielding Solitons

The emergence of phase fronts on dissipative solitons represents a new perspective in the study of parametrically driven systems. Until now, the phase of single solitons was always considered uniform in most of the aforementioned physical systems. However, a

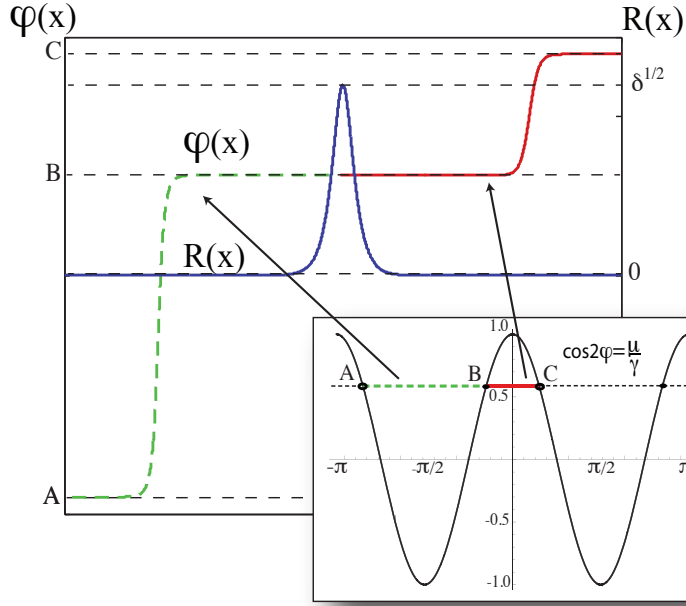


Figure 6.4: Stationary phase front structure which connects different equilibrium solutions (A, B, C) of UPS (4.13) illustrated in the inset

more complete analysis could demonstrate the existence of PSS solutions in such physical scenarios. In the present chapter we extend the analytical and numerical studies of phase shielding solitons in one-dimensional system. Moreover, an analytical description of PSS solutions and their dynamics is presented. A numerical stability analysis is also performed to establish the connection between UPS and PSS solutions.

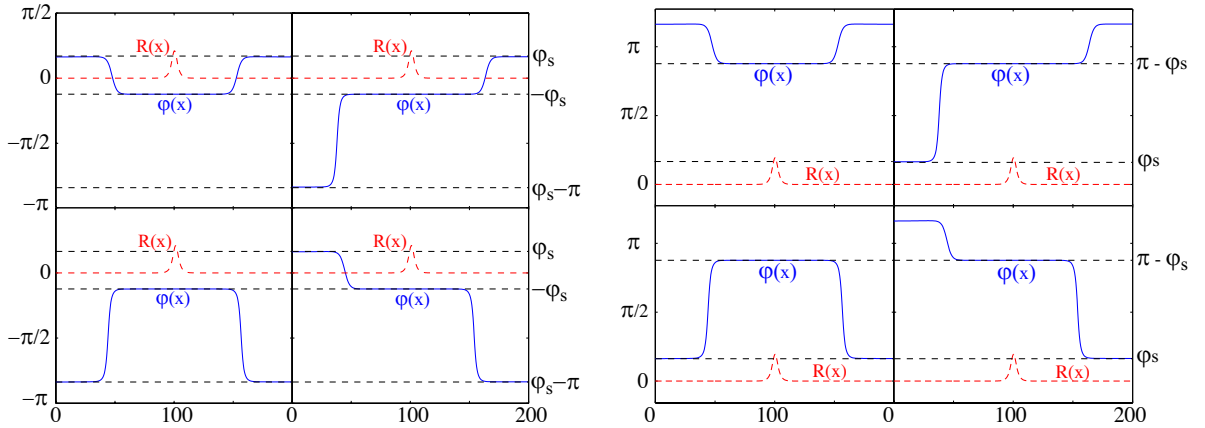


Figure 6.5: Different Phase Shielding Soliton states (PSS) in the parametrically driven damped nonlinear Schrodinger equation with $\mu = 0.10$, $\nu = -0.12$, $\gamma = 0.14$, and $L = 200$. Right and left panel: PSS states supported by the inner uniform phase $-\phi_s$ and $\pi - \phi_s$, respectively. Dashed (red) and solid (blue) lines account for the modulus and phase of the complex field ψ , respectively.

6.2 Analytical approach to dominant order

To provide an analytical background to these phase structures and its dynamics, we take advantage of the $x \rightarrow -x$ symmetry of the PDNLS model (4.1). That is, we only perform an analytical description of one of the two counter-phase fronts that emerge after disturbing the soliton. The final phase structure can be understood as the combination of those fronts. In order to achieve the above, we consider a semi-infinite domain. According to the numerical results, the appearance of the phase front occurs far from the soliton position x_0 [see Fig. 6.3a]. Thus, the phase front position x_f , which stands for the point with the highest spatial variation of the phase, initially satisfies $x_f \gg 1/\sqrt{\delta_+}$. And therefore, near to the front phase position the modulus contribution can be reduced to its exponential tail. Based on these observations, we propose the ansatz

$$R(x, x_0) \simeq 2\sqrt{2\delta_+}e^{-\sqrt{\delta_+}(x-x_0)} \quad (6.1)$$

and

$$\phi(x) = \phi_F(x - x_f), \quad (6.2)$$

for the modulus and the phase of the soliton, respectively. As we can see, in this limit we have only considered the asymptotic exponential decay of the stable UPS modulus ($\delta_+^{1/2}$). After substituting the former ansatz in Eq. (4.2), we obtain the following equation that describes the profile of the phase front,

$$\partial_{xx}\phi_F = 2\sqrt{\delta_+}\partial_x\phi_F + \mu - \gamma \cos(2\phi_F). \quad (6.3)$$

Introducing the following effective potential energy $U(\phi_F) \equiv -\mu\phi_F + (\gamma/2)\sin(2\phi_F)$, Eq. (6.3) can be written as a Newton-type equation which describes a particle moving in a tilted periodic potential with an injection of energy proportional to the speed $\partial_x\phi_F$,

$$\partial_{xx}\phi_F = -\frac{\partial U(\phi_F)}{\partial \phi_F} + 2\sqrt{\delta_+}\partial_x\phi_F. \quad (6.4)$$

The uniform equilibrium states of Eq. (6.3) correspond exactly with the uniform phase equilibria of the UPS, i.e. $\cos(2\phi_0) = \mu/\gamma$ in the range $[-\pi, \pi]$. Therefore, the phase front solutions represent heteroclinic orbits in the extended system, $\{\phi, \phi_x\}$ -space, which connect one equilibrium to another of the Newton-type equation (6.4) [see Fig. 6.4]. Furthermore, since there are no spatial oscillations between asymptotically-connected phase equilibria one can consider the Newton-type equation in its respective overdamped limit.

With the aim to obtain an analytic expression for the shape of the front phase we introduce the change of scale $x = 2\sqrt{\delta_+}x'$ in Eq. (6.3). This substitution allows us to perform an asymptotic series expansion in orders of the perturbation parameter $\Lambda \equiv 1/4\delta_+ \ll 1$

$$\phi_F(x) = \varphi_0(x) + \Lambda\varphi_1(x) + \Lambda^2\varphi_2(x) + \dots \quad (6.5)$$

It is important to note that the above expansion allows us to determine the phase front profile at any order. Introducing this expansion, and expanding up zero order in Λ , we obtain

$$\partial_{x'}\varphi_0 = -\mu + \gamma \cos(2\varphi_0). \quad (6.6)$$

Which can be written in the integral form

$$I = \int \frac{d\varphi_0}{-\mu + \gamma \cos(2\varphi_0)} = \int dx'. \quad (6.7)$$

Obviously the right side of the integral is equal to x' then, we only need to calculate the left side. By using the trigonometric equalities $\cos(2\alpha) = \cos^2(\alpha) - \sin^2(\alpha)$ and $\sec^2(\alpha) = \cos^{-2}(\alpha) = 1 + \tan^2(\alpha)$ in the integral,

$$I = \frac{\gamma}{\gamma + \mu} \int \frac{\sec(\varphi_0)d\varphi_0}{\left(\frac{\gamma-\mu}{\gamma+\mu}\right) \tan^2(\varphi_0) - 1}. \quad (6.8)$$

Introducing the change of variable $z = \sqrt{(\gamma - \mu)/(\gamma + \mu)} \tan(\varphi_0)$ we obtain

$$I = -\frac{\gamma}{\sqrt{\gamma^2 - \mu^2}} \int \frac{dz}{1 - z^2}. \quad (6.9)$$

Integrating and matching with the right side ($I = x'$) we finally obtain (at zero order) an analytical expression for the shape of the front phase given by

$$\phi_F(x, x_f) \approx \varphi_0(x) = \begin{cases} f_{sol} - \pi & \text{for } [-\pi, -\pi/2) \\ f_{sol} & \text{for } (-\pi/2, -\pi/2) \\ f_{sol} + \pi & \text{for } (\pi, \pi/2] \end{cases} \quad (6.10)$$

where

$$f_{sol} = \arctan \left[\sqrt{\frac{\gamma \pm \mu}{\gamma \mp \mu}} \tanh \frac{\sqrt{\gamma^2 - \mu^2}(x - x_f)}{2\sqrt{\delta_+}} \right]. \quad (6.11)$$

The different combination of signs are given by the mentioned symmetry of PDNLS ($x \rightarrow -x$) that can be used before start to integrate (6.7). Furthermore, due to the multi evaluation of the *tangent* function, we add a π displacement in the front phase solution. Figure 6.6 shows a phase shielding soliton and its theoretical approximation computed from (4.16) and (6.10).

In order to calculate the higher orders in the asymptotic expansion we replace the expansion of the phase front (6.5) into the phase front shape equation (6.3) and considering only the term proportional to Λ we obtain,

$$\partial_{x'}\varphi_1 + 2\gamma \sin(2\varphi_0)\varphi_1 = \partial_{x'x'}\varphi_0. \quad (6.12)$$

Multiplying the above differential equation by the integrating factor $\exp[2\gamma \int \sin(2\varphi_0)dx']$,

$$\partial_{x'} \left[\varphi_1 e^{2\gamma \int \sin(2\varphi_0)dx'} \right] = e^{2\gamma \int \sin(2\varphi_0)dx'} \partial_{x'x'}\varphi_0. \quad (6.13)$$

Due to the invariance of PDNLS under the transformation $x \rightarrow -x$ the phase front solution φ_0 also satisfies

$$-\partial_{x'}\varphi_0 = -\mu + \gamma \cos(2\varphi_0). \quad (6.14)$$

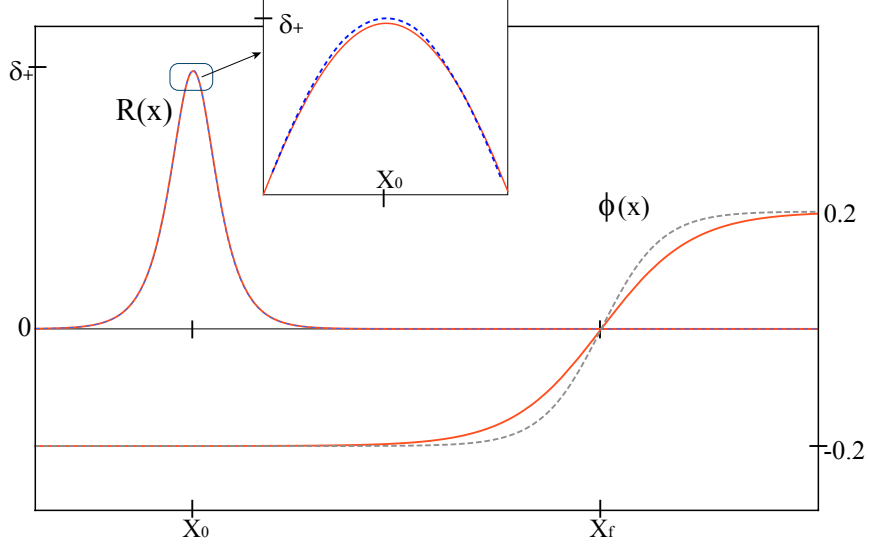


Figure 6.6: Phase shielding soliton in a semi-infinite domain. Dashed line are the analytical approximation for the PSS solution obtained by computing its theoretical shape equations (4.16) and (6.10). The set of parameters are $\gamma = 0.12$, $\nu = -0.1$, and $\mu = 0.1$.

Deriving this and after straightforward calculations, one obtains

$$2\gamma \sin(2\varphi_0) = \frac{\partial_{x'x'}\varphi_0}{\partial_{x'}\varphi_0} = \partial_{x'} \ln(\partial_{x'}\varphi_0), \quad (6.15)$$

and therefore

$$e^{2\gamma \int \sin(2\varphi_0) dx'} = e^{\ln(\partial_{x'}\varphi_0)} = \partial_{x'}\varphi_0. \quad (6.16)$$

Substituting this in (6.13), we obtain

$$\partial_{x'} [\varphi_1 \partial_{x'}\varphi_0] = \partial_{x'}\varphi_0 \partial_{x'x'}\varphi_0 = \frac{\partial_{x'} (\partial_{x'}\varphi_0)^2}{2}. \quad (6.17)$$

Thus,

$$\varphi_1(x') = \pm \frac{\partial_{x'}\varphi_0}{2}. \quad (6.18)$$

The phase front profile at first order in the corrections is then given by

$$\phi_F^{[1]}(x, x_f) = \varphi_0(x) \pm \frac{\sqrt{\Lambda}}{2} \partial_x \varphi_0(x). \quad (6.19)$$

Notice that this correction is significant only near the phase front position x_f (region where the derivative of $\varphi_0(x)$ [Eq. (6.10)] is not negligible). Further corrections have the same consequences. In fact, we conduct the calculus for the next order in the series expansions, Λ^2 . Following the same procedure adopted for the first correction, we obtain

$$\partial_{x'}\varphi_2 - 2\gamma \sin(2\varphi_0)\varphi_2 = 4\gamma\varphi_1^2 \cos(2\varphi_0). \quad (6.20)$$

After introduce the integrating factor $\exp[-2\gamma \int \sin(2\varphi_0)dx'] = \partial_{x'}\varphi_0$ (obtained from (6.6)) and the first correction φ_1 (6.18), the above expression yields

$$\partial_{x'} [\varphi_2 \partial_{x'} \varphi_0] = \gamma \partial_{x'} \varphi_0 (\partial_{x'} \varphi_0)^2 \cos(2\varphi_0). \quad (6.21)$$

To solve this we derive twice the Eq. (6.6),

$$4\gamma \partial_{x'} \varphi_0 (\partial_{x'} \varphi_0)^2 \cos(2\varphi_0) = 2\gamma \sin(2\varphi_0) \partial_{x'x'} \varphi_0 + \partial_{x'x'x'} \varphi_0, \quad (6.22)$$

introducing the already known integrating factor $\exp[2\gamma \int \sin(2\varphi_0)dx'] = \partial_{x'}\varphi_0$, we obtain

$$4\gamma \partial_{x'} \varphi_0 (\partial_{x'} \varphi_0)^2 \cos(2\varphi_0) = \partial_{x'} [\partial_{x'x'} \varphi_0 \partial_{x'} \varphi_0]. \quad (6.23)$$

Replacing it in (6.21) the second correction is obtained

$$\varphi_2(x') = \frac{\partial_{x'x'} \varphi_0}{4}. \quad (6.24)$$

Therefore, the phase front shape at second order in the corrections is given by

$$\phi_F^{[2]}(x, x_f) = \varphi_0(x) \pm \frac{\sqrt{\Lambda}}{2} \partial_x \varphi_0(x) + \frac{\Lambda}{4} \partial_{xx} \varphi_0(x). \quad (6.25)$$

Which is consistent with the above prediction. Any higher order correction is negligible since they are functions of the derivatives of φ_0 and have order bigger than Λ . Furthermore, we can conclude that the perturbation series corresponds to a gradient expansion of the solution to zero-order.

6.2.1 Higher order corrections

A deeper analysis of numerical simulations reveals that the modulus of the PSS solutions possess an intriguing spatial profile; its exponential tail bends notoriously right at the position of the phase front x_f . Moreover, there is a crossover region between both exponential decay rates of UPS solution characterized by a transition point which exactly coincides with the phase front position x_f . Such a point outlines the border transition between two qualitatively different regions: the Inner and Outer regions. The former is defined as the central region where the PSS behaves as a stable UPS, i.e. The modulus and the asymptotic phase of PSS coincide with the modulus and the uniform phase of the stable UPS [Sec. 4.3]. Obviously the soliton position x_0 is found in this region. The latter corresponds to the region where both the exponential decay rates and the asymptotic phase of PSS take the value of the unstable UPS respectively, δ_- and ϕ_0^{us} .

The unexpected spatial dependence of the modulus could only be noticed when we conducted a semi-log plot of this field since the transition mentioned is exponentially suppressed (it occurs in the exponential tail of the modulus). Figure 6.7 shows the logarithm of PSS modulus as a function of the space and the inner and outer region bounded by the phase front position x_f .

All this allows us to consider a PSS solution as a soliton built up by the stable (inner region) and the unstable (outer region) UPS solutions connected at the transition point x_f . Therefore, the assumption done in Sec. 6.2, specifically the ansatz taken for the modulus

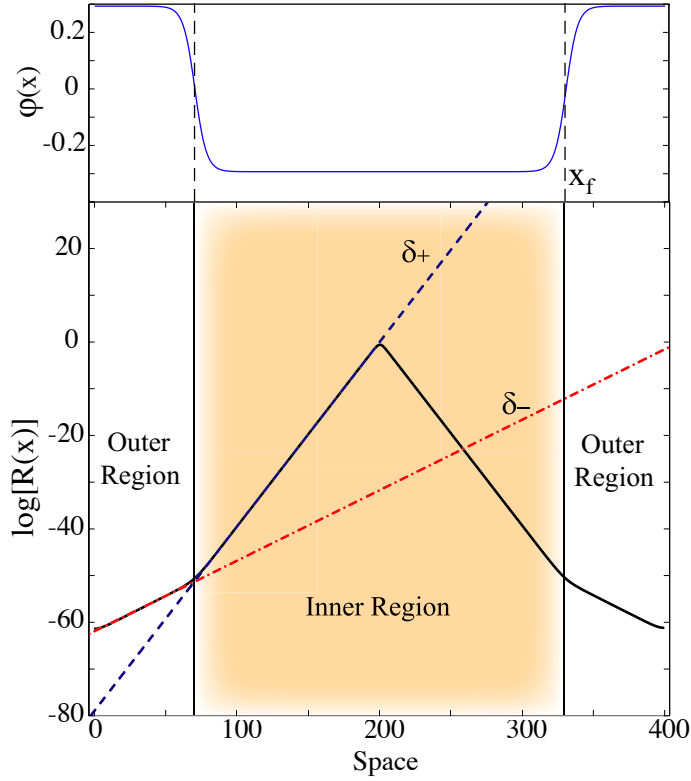


Figure 6.7: The phase $\phi(x)$ (Top) and logarithm of the modulus $R(x)$ (bottom) of a PSS solution, with $\mu = 0.1$, $\nu = -0.09$, $\gamma = 0.12$, and $L = 400$. An inner and outer region are defined. The exponential decay value changes from $\sqrt{\delta_+} = 0.3946$ (Theoretical $\sqrt{\delta_+} = 0.3954$) inside the inner region to $\sqrt{\delta_-} = 0.1508$ (Theoretical $\sqrt{\delta_+} = 0.1538$) in the outer one. The transition point between both regions coincides with the phase front position x_f .

approximation Eq. 6.1, can be improved in order to achieve a more accurate description of the phase front profile. Let us consider the exponential decay rate of the modulus of PSS as

$$f(x, x_0) \approx \sqrt{\delta_+}(x - x_0) + \left[\sqrt{\delta_-} - \sqrt{\delta_+} \right] \Theta(x - x_f)(x - x_f), \quad (6.26)$$

where $\Theta(x - x_f)$ denotes the Heaviside function. Note that the exponential tail of the modulus of PSS is a smooth function [cf. Fig.6.7], and therefore its exponential decay rate $f(x, x_0)$ is smooth also. However, its approximation (6.26) is continuous but not differentiable at $x = x_f$. The new ansatz for the modulus of PSS is then given by

$$R(x, x_0) = 2\sqrt{2\delta_+}e^{-f(x, x_0)}, \quad (6.27)$$

with $f(x, x_0)$ is the approximation (6.26). The previous ansatz done for the phase (6.2) is maintained. Following the same procedure showed in the Sec. 6.2 and after straightforward calculations an amended front phase profile is obtained,

$$\varphi_0(x) = \arctan \left[\frac{\sqrt{\gamma \pm \mu}}{\sqrt{\gamma \mp \mu}} \tanh \frac{\sqrt{\gamma^2 - \mu^2}(x - x_f)}{2\delta(x, x_f)} \right], \quad (6.28)$$

with

$$\delta(x, x_f) \equiv \left[\sqrt{\delta_+} + (\sqrt{\delta_-} - \sqrt{\delta_+})\Theta(x - x_f) \right]. \quad (6.29)$$

It is important to note that ansatz (6.1) considers an uniform exponential decay rate of the modulus. Such assumption leads, at dominant order, to obtain phase front solutions [Eq. (6.10)]. Higher order corrections allow us to get an improved description of the phase shield soliton where the modulus also exhibit an amplitude shielding structure (see Fig. 6.7). However, this structure is exponentially suppressed in comparison to the soliton height $\sqrt{2\delta_+}$. In contrast, the phase shielding structure is of order one. Therefore, a possible experimental characterization of PSS could be achieved by means of direct phase measurements.

6.3 Phase front dynamics

As discussed in the previous sections, the transient preceding the formation of the phase profile is governed by the front dynamics. Here we propose an analytical study of the dynamical evolution of these fronts. For this purpose let us consider the typical evolution of a soliton in a semi infinite system, as shown in Fig. 6.3b. As can be seen from this figure, the phase front displays a dynamical behavior characterized by a nontrivial motion. During this front propagation both soliton position (x_0) and the phase profile (ϕ_F) remains unchanged. Those remarks allow us to confer the dynamics of the phase front to its position, i.e. we promote the phase front position to a time depending function $x_f \equiv x_f(t)$. For the sake of simplicity we reconsider the ansatz proposed for the modulus (6.1) and the phase (6.2) at dominant order [see Sec. 6.2]. Substituting all in Eq. 4.3, we obtain the equation for the phase front position,

$$-\dot{x}_f \partial_x \phi_F = -(\nu + \delta_+) - 8\delta_+ e^{-2\sqrt{\delta_+}x} + (\partial_x \phi_F)^2 - \gamma \sin(2\phi_F). \quad (6.30)$$

Multiplying the above equation by $\partial_z \phi_F(z)$ with $z \equiv x - x_f$, and introducing the following inner product $\langle f|g \rangle \equiv \int f g dz$, we obtain after straightforward calculations, the ordinary differential equation that rules the core of the phase front

$$\dot{x}_f = A + B e^{-2\sqrt{\delta_+}x_f}, \quad (6.31)$$

where

$$A \equiv \frac{\langle [\nu + \delta_+ + \gamma \sin(2\phi_F) - (\partial_z \phi_F)^2] | \partial_z \phi_F \rangle}{C},$$

$$B \equiv 8\delta_+ \frac{\langle e^{-2\sqrt{\delta_+}z} | \partial_z \phi_F \rangle}{C} \quad \text{and} \quad C = \langle \partial_z \phi_F | \partial_z \phi_F \rangle$$

are real numbers, which can be either positive or negative depending on the shape of the phase front. For example, when one considers a front that increases monotonically with the spatial coordinate, A (B) is a positive (negative) constant. Notice that the term proportional to A accounts for the constant speed at which the stable phase value (asymptotically ϕ_0^s) invades the unstable one (asymptotically ϕ_0^{us}) forming a phase front which propagates away from the position of the soliton x_0 . This speed can be understood as a consequence the difference of the effective potential energy ($U(\phi_F)$) between both equilibria (ϕ_0^s, ϕ_0^{us}). In contrast, the term proportional to B accounts for the effect of spatial variation of the tail of the amplitude soliton, which induces a *force* that pushes the phase front position to move towards the soliton position x_0 . Consequently, the superposition of these two antagonistic *forces* generates a stable equilibrium position for the phase front, which is consistent with

the dynamical behavior illustrated by the spatiotemporal diagram of Fig. 6.3b. Solving Eq. (6.31), we get an analytical solution for the typical trajectory,

$$x_f(t) = \frac{\log\left(\frac{B}{A}\right)}{2\sqrt{\delta_+}} + \frac{\log\left(e^{-2\sqrt{\delta_+}A(t-t_0)} - 1\right)}{2\sqrt{\delta_+}} - A(t-t_0). \quad (6.32)$$

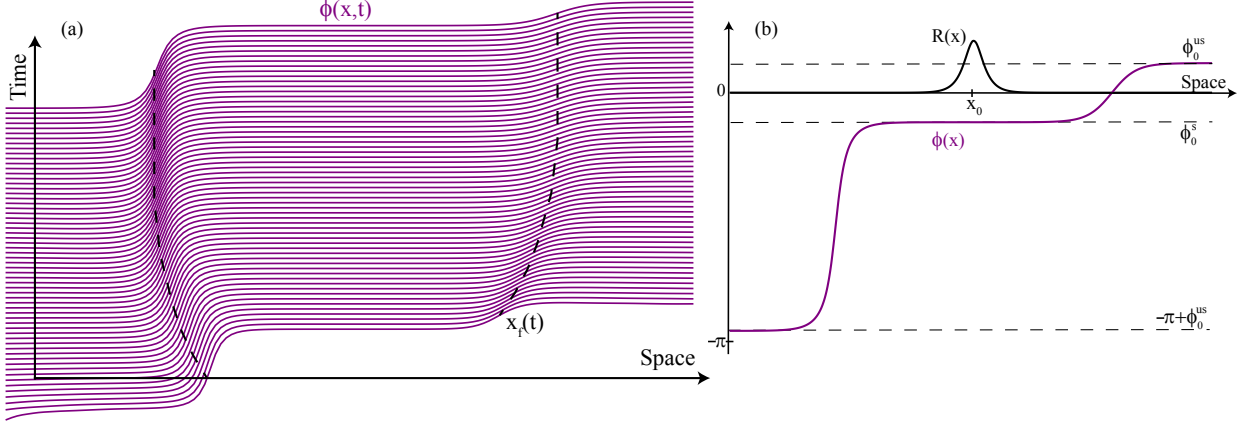


Figure 6.8: Spatiotemporal diagram of two different phase fronts that form a PSS solution. (b) The final steady phase structure is shown. Although the phase front are different (connect different phase equilibria) the behavior of its positions is qualitatively the same. The simulation parameters are $\mu = 0.1$, $\nu = -0.1$, $\gamma = 0.13$, and $L = 128$.

Dashed curves shown in Fig. 6.8 are obtained using the above formula wherein A and B are used as fitting parameters. Note that the constant $\log(B/A)/2\sqrt{\delta_+}$, which accounts for the steady equilibrium position of the front, allows us to introduce a characteristic size of the shell structure in phase. This is a novel feature for the dissipative solitons arising in PDNLS since, as we have mentioned before, the phase of these localized states has been always considered uniform.

6.4 Stability analysis for uniform phase soliton

As we have already shown, the uniform phase and phase shielding solitons are solutions of the one-dimensional PDNLS model (5.2). Therefore, a natural question arises: what is the relation between these localized states? Here, we examine this question, performing a numerical linear stability analysis of the UPS solution based on Ref. [26]. Given the complexity of the linear operator, an analytical stability analysis is not feasible. We consider small perturbations ρ and Ω around solutions $R_s(x)$ and ϕ_0 , respectively, i.e.

$$R = R_s(x) + \rho(x, t) \quad \text{and} \quad \phi = \phi_0 + \Omega(x, t), \quad (6.33)$$

where $\rho, \Omega \ll 1$. Replacing in (4.2) and (4.3), and after linearize we obtain

$$\partial_t \rho = 2\partial_x R_s \partial_x \Omega + R_s \partial_{xx} \Omega + 2\sqrt{\gamma^2 - \mu^2} \Omega R_s, \quad (6.34)$$

and

$$R_s \partial_t \Omega = \delta_+ \rho - 3R_s^2 \rho - \partial_{xx} \rho - 2\mu R_s \Omega, \quad (6.35)$$

respectively. Equation (6.34) and (6.35) represent an eigenvalue problem that can be written in the following matrix representation,

$$\frac{\partial}{\partial t} \begin{pmatrix} \rho \\ \Omega \end{pmatrix} = \mathbb{M} \begin{pmatrix} \rho \\ \Omega \end{pmatrix} \quad (6.36)$$

where

$$\mathbb{M} \equiv \begin{pmatrix} 0 & 2\partial_x R_s(x) \partial_x - R_s(x) \partial_{xx} - 2R_s(x) \sqrt{\gamma^2 - \mu^2} \\ \frac{1}{R_s(x)} [\delta - 3R_s(x)^2 - \partial_{xx}] & -2\mu \end{pmatrix}. \quad (6.37)$$

An analytical solution to Eq.(6.36) is a difficult task since the linear operator has a spatial dependency [26]. Therefore, in order to obtain the spectrum—set of eigenvalues associated with the linear stability analysis—we adopt a numerical strategy. We proceed to discretize the space with grid points, $x \rightarrow j\Delta x$, $F(x, t) \rightarrow F(j\Delta x, t) \equiv F_j(t)$ with $j = 1, \dots, N$ and N the number of points of the system of size $L = N\Delta x$. In such case, the differential operator \mathbb{M} with *spatial* coefficients, turns into a matrix of rank $2N$. We also consider $\mu = \mu_0$ and $x_0 = L/2$ for different values of $\{\gamma, \nu\}$ in the region of existence of solitons, i.e. $\mu < \gamma < \sqrt{\nu^2 + \mu^2}$ with $\nu < 0$. The L parameter controls the size effect, and we can vary it easily by changing N for a fixed Δx . In previous reports, this parameter was not considered as a relevant, being usually a small constant. We shall see that parameter L plays a main role in the stability properties of dissipative states.

Hence, let us consider L as a control parameter with the system parameters $\{\mu, \nu, \gamma\}$ fixed. When L is small enough the spectrum is characterized by being centered on an axis parallel to the imaginary one, where every single eigenvalue has negative real part. Such behavior of the eigenvalues is typical of quasi-reversible systems [49, 50]. Increasing L , the set of eigenvalues begin to collide creating a continuum set. Up to a critical value of L_c , where a conjugate pair cross the imaginary axis at a non zero frequency, exhibiting an Andronov-Hopf bifurcation [75, 76]. Figure 6.9(A)–6.9(C) outline the spectrum before, during and after the bifurcation, respectively. The main plot of Figure 6.9 illustrates the real part of the largest eigenvalue $\max[Re(\lambda)]$ (red circles) and the eigenvalue related to the Goldstone mode (blue triangles) as function of the system size L . As a result of the translational invariance, the eigenvalue related to the Goldstone mode is at the origin of the complex plane [16]. For $\gamma = 0.105$, $\mu = 0.1$, and $\nu = -0.05$, we observe that below the critical value $L_c = 304$, the largest eigenvalue corresponds to the Goldstone mode [see Fig. 6.9(A)]. Close to the bifurcation, the largest conjugate pair of eigenvalues crosses the real axis destabilizing the uniform phase solution [see insets Fig. 6.9(B) and 6.9(C)].

The numerical stability analysis of UPS solutions reveals a strong dependance on the system size. Such result is in accordance with the inner and outer region crossover. The inner region has a definite length for a given set of system parameters $\{\mu, \nu, \gamma\}$. If the system size is small enough (L is less than the length of the inner region), the crossover does not

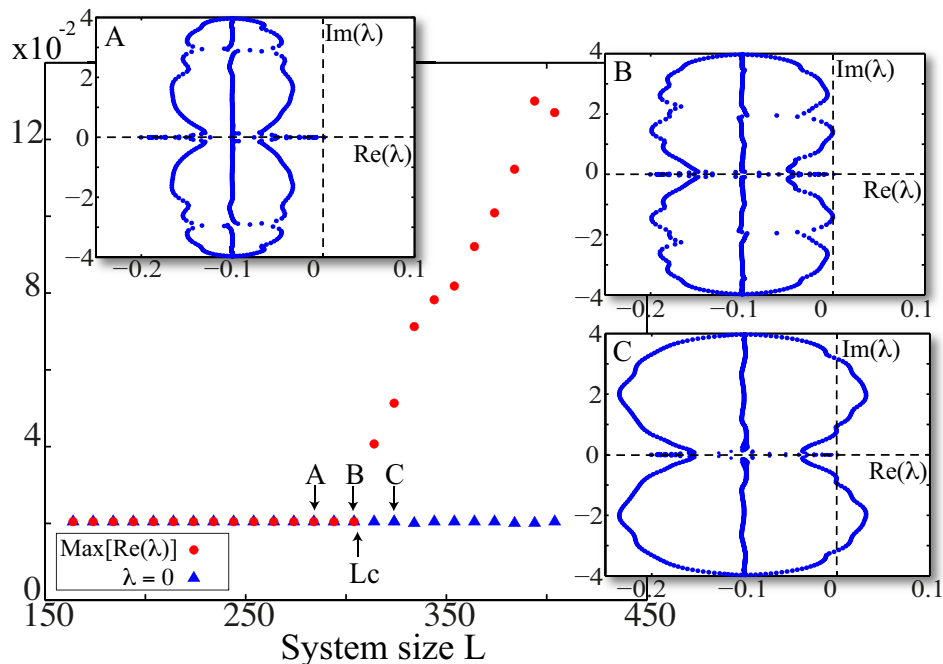


Figure 6.9: The real part of the largest eigenvalue $\text{Max}(\text{Re}(\lambda))$ (red circles) and the eigenvalue related to the Goldstone mode (blue triangles) as function of system size. The stability of solitons is shown in the spectra of the soliton with constant phase (A) before (system size $L = 284$), (B) during ($L = 304$), and (C) after ($L = 324$) the bifurcation for $\gamma = 0.105$, $\mu = 0.1$, and $\nu = -0.05$.

occur. Then, the PSS solution does not appear and UPS is a stable solution. For L greater than the length of inner region, the UPS destabilizes, generating the PSS solution.

Given that the exponential decay of the stable UPS, and therefore the length of the inner region, is a function of the system parameters $\{\mu, \nu, \gamma\}$ it is natural to infer that varying such parameters with L fixed, the UPS destabilization will take place as well. Indeed, following the above strategy, we perform a numerical stability analysis of the UPS varying γ for L fixed with $\mu = 0.1$ and $\nu = -0.05$. We choose the same parameter region $\{\nu, \gamma\}$ with a $L = 280$ (before bifurcation) [see Fig.6.9] to assure a initial stable UPS solution. Figure 6.10 displays the eigenvalue spectrum evolution as γ varies. As before, up to a critical γ_c , the system exhibits an Andronov-Hopf bifurcation which leads to the appearance of PSS solution similar to the one observed in Fig. 6.9(A)-6.9(C).

As we can notice, the above instability mechanism is a robust phenomenon. Nonetheless, the bifurcation scenario strongly depends on the proper choice of parameter as well as on the system size, see Figs. 6.9 and 6.10. Furthermore, both critical values are related to the length of the inner region, i.e., to the exponential decay of the stable solution [cf. Sec. 6.2.1]. In order to verify this and also show the effect of the two parameters combined, we have also performed a stability analysis of the solutions in cartesian representation of the field ψ . By replacing in the cartesian representation of PDNLS, Eqs. (4.6) and (4.7), the spatial

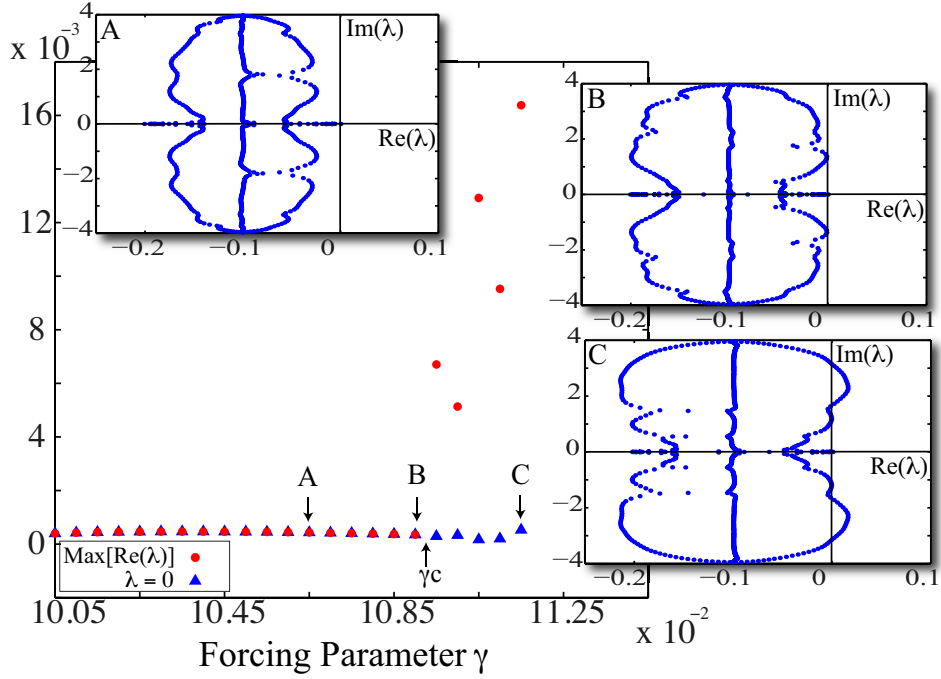


Figure 6.10: The real part of the largest eigenvalue $\text{Max}(\text{Re}(\lambda))$ (red circles) and the eigenvalue related to the Goldstone mode (blue triangles) as function of the forcing parameter γ . The stability of solitons is shown in the spectra of the soliton with constant phase (A) before ($\gamma = 0.1065$), (B) during ($\gamma = 0.1090$) and (C) after ($\gamma = 0.1115$) the bifurcation for $\mu = 0.1$, $\nu = -0.05$, and $L = 280$ fixed.

operators $\vec{\nabla}^2$ and $\vec{\nabla}$ for ∂_{xx} and $\partial_x \hat{x}$, respectively, we obtain

$$\partial_t \mathcal{X} = \nu \mathcal{Y} + (\mathcal{X}^2 + \mathcal{Y}^2) \mathcal{Y} + \partial_{xx} \mathcal{Y} - \mu \mathcal{X} + \gamma \mathcal{X}, \quad (6.38)$$

$$\partial_t \mathcal{Y} = -\nu \mathcal{X} - (\mathcal{X}^2 + \mathcal{Y}^2) \mathcal{X} - \partial_{xx} \mathcal{X} - \mu \mathcal{Y} - \gamma \mathcal{Y}. \quad (6.39)$$

The solution for this set of Eqs. (6.38)–(6.39) is

$$\mathcal{X}_s = R_s \cos(\phi_0), \quad (6.40)$$

$$\mathcal{Y}_s = R_s \sin(\phi_0), \quad (6.41)$$

where R_s and ϕ_0 are given by the formulas (4.16) and (4.13).

We follow the same procedure shown above and take into account small perturbations ($\delta \mathcal{X}, \delta \mathcal{Y} \ll 1$) around the solutions $(\mathcal{X}, \mathcal{Y})$. Linearizing and using relations (4.16) and (4.13), we get the dynamical system

$$\frac{\partial}{\partial t} \begin{pmatrix} \delta \mathcal{X} \\ \delta \mathcal{Y} \end{pmatrix} = \begin{pmatrix} -\mu + \gamma - R_s^2 \sqrt{\gamma^2 - \mu^2} / \gamma & \nu + R_s^2 (2\gamma - \mu) / \gamma + \partial_{xx} \\ -\nu - R_s^2 (2\gamma + \mu) / \gamma - \partial_{xx} & -\mu - \gamma + R_s^2 \sqrt{\gamma^2 - \mu^2} / \gamma \end{pmatrix} \begin{pmatrix} \delta \mathcal{X} \\ \delta \mathcal{Y} \end{pmatrix}. \quad (6.42)$$

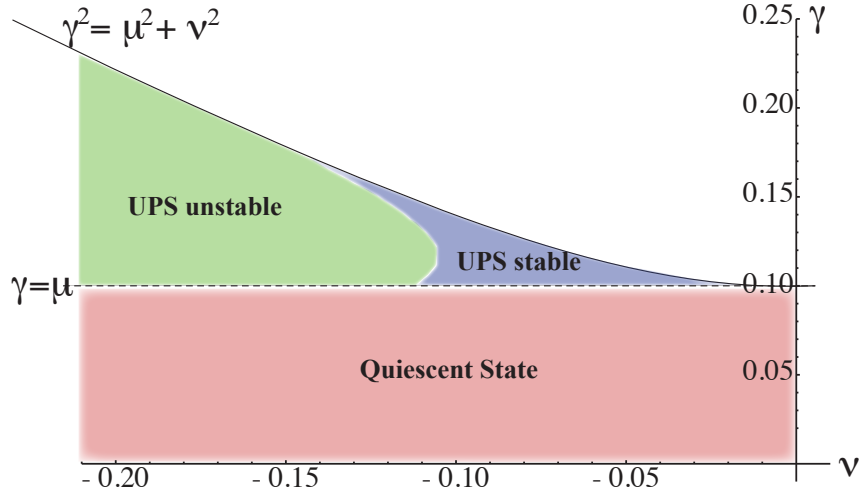


Figure 6.11: (color online) PSS bifurcation diagram in the $\gamma - \nu$ space obtained from solving (6.36) numerically for $\mu = 0.050$ and $L = 400$.

Figure 6.11 displays the UPS stability over a wide parameter region $\{\nu, \gamma\}$ for $\mu = 0.05$ and $L = 400$ fixed. For a system size smaller than the critical one, we observe that for parameters $0 < \gamma - \mu \ll 1$, the soliton with constant phase is stable. Notwithstanding, increasing the forcing amplitude γ or the detuning parameter ν , the soliton becomes unstable again by an Andronov-Hopf bifurcation followed by the appearance of the PSS as the stable solutions of the system. Hence, the system (6.42) yields similar results as those already observed using polar representation. It is important to mention that in the case that the system size is large enough, the UPS solution exhibits an Andronov-Hopf bifurcation that leads to a PSS solution. Further increasing the system parameters $\{\nu, \gamma\}$, there occurs a secondary bifurcation where the soliton undergoes a periodic oscillation, like those observed in [56]. Conversely, for small L the Andronov-Hopf bifurcation leads directly to localized periodic solitons without a secondary one.

Chapter 7

Phase Shielding Solitons in Two-Dimensional System

Localized structures presented in the previous sections were considered only in one spatial dimension. Now we are interested in the study of such dissipative solitons with nontrivial phase structures in two-dimensional systems. This extension is not evident. For instance, conservative solitons observed in the nonlinear Schrödinger equation in one spatial dimension collapse in two spatial dimensions by undergoing a blow-up in finite time [77], i.e. these solutions are unstable in two spatial dimensions. Most of the experimental observations of localized structures in parametrically driven systems have been reported in two spatial dimensions systems such as, in fluid surface waves [32], oscillons in granular media [33], and isolated states in thermal convection [34]. Note that all these observations have been realized in dissipative systems. Furthermore, the greatest difficulty to characterize theoretically localized states in two spatial dimensions is the lack of analytical expressions that describe these states. In this Chapter we perform an analytical and numerical study of the dissipative solitons arising in two spatial dimensional PDNLS in order to understand the existence, stability properties, and dynamical evolution of their phase structure. Moreover, we show that, for both proper system size and parameter configuration, solitons with surrounding phase structures are exhibited.

7.1 Numerical observation of phase shielding solitons in $2D$ -PDNLS

As seen in the Sec. 4.4, the PDNLS model (4.1) exhibits stable non-propagative dissipative solitons in two spatial dimensions [58]. These localized structures are characterized by presenting a constant phase and a bell-shaped modulus, Eqs. (4.20) and (4.22). Moreover, these solutions possess axial symmetry as well as invariance under translations (they are related to the Goldstone mode). Based on the previous simulations carried out in $1D$ (see Sec. 6.1), we perform numerical simulations of single dissipative solitons in two-dimensional PDNLS. We explore similar parameter region in the $2D$ case—close to the Arnold tongue—in order to observe the possible formation of phase shielding solitons.

Indeed, we have characterized two types of phase shielding configurations. The first type consists of a phase front with axial symmetry in the range $[0, 2\pi]$. The asymptoti-

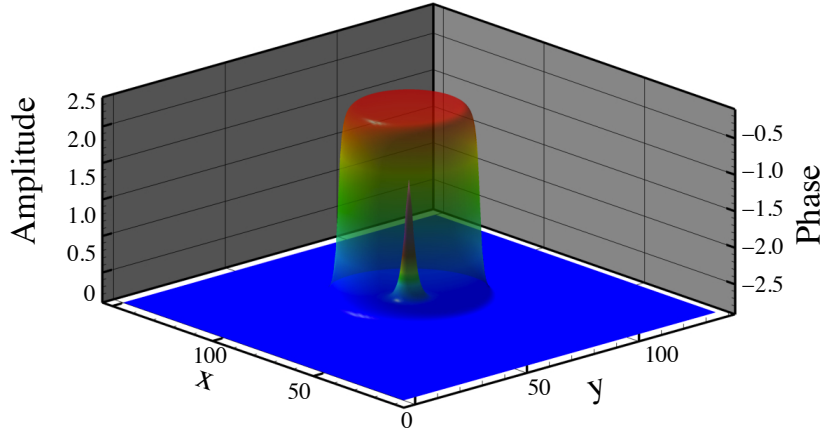


Figure 7.1: Stationary 2D symmetric phase shielding soliton observed in two-dimensional numerical simulations of the parametrically driven and damped nonlinear Schrödinger model with $\gamma = 0.560$, $\nu = -0.068$ and $\mu = 0.250$. Phase and amplitude field are represented simultaneously. Colored shadow renders the phase shell-like structure ($\phi(x, y)$) that surrounds the amplitude soliton localized at the center ($R(x, y)$).

cally connected uniform states are, analogously to the 1D case, given by the phase equilibria determined by relation (4.20). Figure 7.1 shows the typical phase structure of this symmetrical state around the soliton position. If we consider a 1D stationary front solution in a semi-infinite domain ($\rho > 0$), the 2D-symmetric phase solution corresponds to a 2π -rotation around an axis whose origin is placed at the position of the dissipative soliton. It is important to note that the process of formation of this symmetrical state is complex, since one needs special initial conditions close to the equilibrium state.

The second type of two-dimensional PSS found is much more intriguing since it possess an asymmetric phase front structure [see Fig. 7.2]. This asymmetric structure can be split into two symmetric configurations by considering a non-usual polar description of the system.

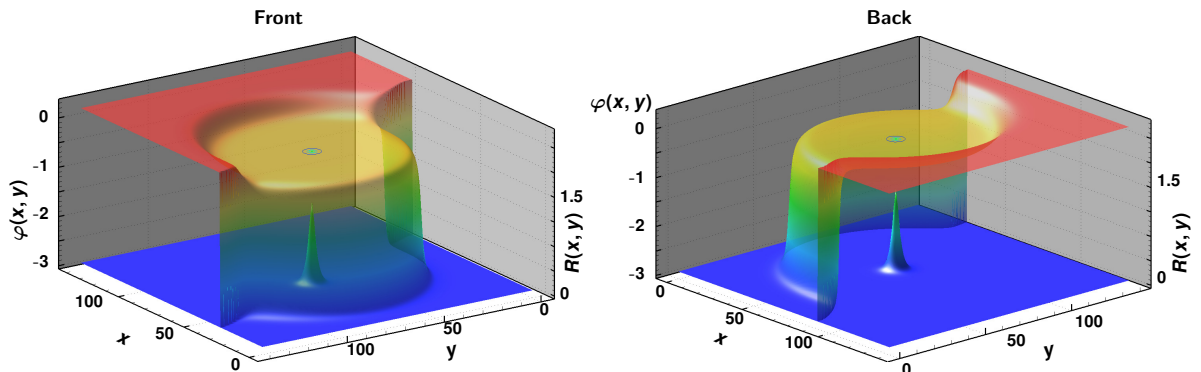


Figure 7.2: Front and back view of a stationary phase shielding soliton observed in two-dimensions for the parametrically driven and damped nonlinear Schrödinger model with $\gamma = 0.140$, $\nu = -0.068$ and $\mu = 0.125$. Phase and amplitude field are represented simultaneously. Colored shadow renders the phase shell-like structure ($\varphi(x, y)$) that surrounds the amplitude soliton localized at the center ($R(x, y)$).

Under this consideration, the nonsymmetric phase front is characterized by a phase front axially symmetric from $[0, \pi]$ and an analogous front with different asymptotic states from $[\pi, 2\pi]$, i.e. the two-dimensional PSS with asymmetric phase state can be seen as the composition of two phase front with semi-axial symmetry which connect different asymptotic states.

The process of formation of this configuration starts with a well-formed 2D soliton that is slightly perturbed. After some complex phase transient state, the system exhibits the appearance of a circular phase front that spreads rather slowly. Figure 7.3(a) displays this primary stage. However, asymptotically, the circular structure becomes asymmetrical, giving rise to a new semicircular front that still propagates in the range $[\pi, 2\pi]$ [cf. Fig. 7.3(b)]. Finally, the whole structure becomes stationary, creating a 2D asymmetric phase shielding soliton. Unlike the symmetric case, the steady phase solutions coincide only with a π rotation around the soliton position as the center of rotation [see Fig. 7.3(c)]. Additionally, numerical simulations performed in a close region of parameters show the same dynamical behavior. Figure 7.2 give us a comparison between the stationary configuration of this shield-like phase and the soliton size for a different set of parameters values $\{\mu, \nu, \gamma\}$.

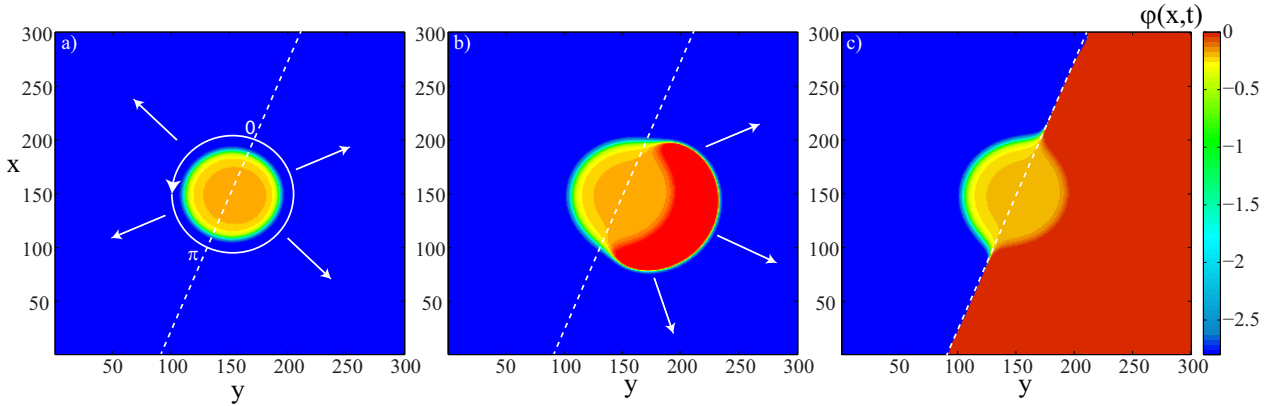


Figure 7.3: Snapshots of the phase evolution of a typical 2D-PSS after a perturbation with $\gamma = 0.083$, $\nu = -0.063$, and $\mu = 0.058$. (a) Initially the soliton is slightly disturbed. A circular front starts to propagate. (b) An additional propagative semicircular front appears. (c) The final steady configuration exhibiting a semi-axial symmetry. The dashed curve represents the θ -axis.

It is noteworthy that two-dimensional PSS solutions have similar characteristics to those observed for one-dimensional PSSs [see Fig. 7.1]. For instance, as in the one-dimensional case, the final state of both symmetric and nonsymmetric phase structure of the two-dimensional PSS is far from the soliton position found in the core of the modulus. Notwithstanding, the asymmetric two-dimensional PSS state has features much more intriguing since it is composed of all the solutions found in one dimension simultaneously. Indeed, Fig. 7.4 shows different cuts containing the center of an asymmetric PSS state, one can clearly recognize the observed solutions in one dimension [cf. Fig. 6.5]. Another interesting property appears when one calculates the phase change on a path that connects two opposite points with respect to the soliton position ($\int_{\Gamma} \vec{\nabla} \varphi d\vec{s}$). Within the region close to the position of the soliton one finds that this is zero. Nevertheless, if one takes this type of path far away of the soliton

position one finds a π shift in the phase, $\int_{\Gamma'} \vec{\nabla} \varphi d\vec{s} = \pm\pi$.

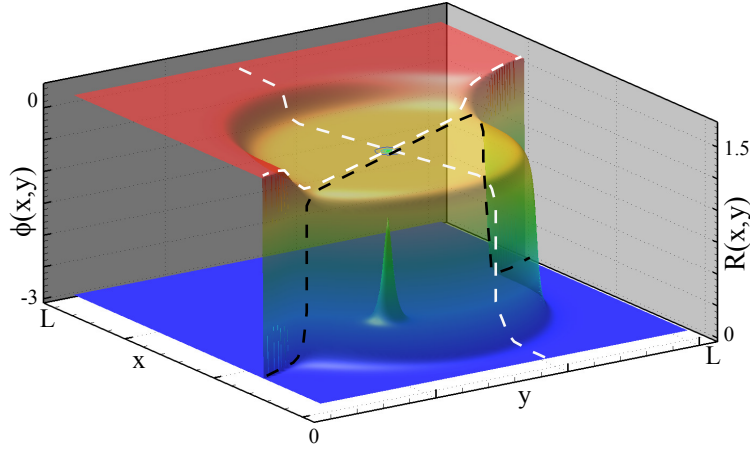


Figure 7.4: Final structure of the asymmetric two-dimensional PSS with $\gamma = 0.140$, $\nu = -0.068$ and $\mu = 0.125$. Asymmetric two-dimensional PSS is composed by all the PSS solutions found in the 1D case (Fig. 6.5) simultaneously.

As an additional remark, we would like to comment on the stability of the 2D-phase shielding solitons. Axial-symmetrical PSS are attained only by setting up special initial conditions, close to the steady state. A slightly perturbation in its modulus leads to a symmetry breaking where the axial symmetry is lost and a semi-axial symmetry appears. Hence, numerically the second type of PSS solitons (asymmetric one) has a large basin of attraction.

7.2 Phase front profile in 2D

In this section we discuss an analytical approach for the two types of shielding phase solitons observed in 2D. From numerical simulations [see Figs. 7.1 and 7.2] we can observe that the phase structure emerges far from the soliton position. In the same manner as Sec. 6.2 to obtain the phase front profile at dominant order, we consider the exponential asymptotic decay of the modulus. Under this consideration ($\rho \rightarrow \infty$), we propose the ansatz for the modulus and the phase

$$R_s(\rho \rightarrow \infty) \cong \frac{e^{-\sqrt{\delta}(\rho-\rho_0)}}{\sqrt{\rho}}, \quad (7.1)$$

$$\phi(\rho \rightarrow \infty) = \phi_F(\rho - \rho_F(t)). \quad (7.2)$$

Here ρ_0 describes the soliton position which corresponds to the position of the maximum amplitude of the soliton modulus. Moreover, we have promoted the position of the phase front core to a time-dependent function $\rho_F(t)$. For the sake of simplicity and without loss of generality, we can choose $\rho_0 = 0$ as the coordinate origin. At dominant order, we get a similar Newton-type equation as in the 1D case ($\rho \gg 1$),

$$\partial_{\rho\rho}\phi_F \approx 2\sqrt{\delta}\partial_{\rho}\phi_F + \mu - \gamma \cos(2\phi_F). \quad (7.3)$$

Thus, $2D$ phase solutions have a front solution at dominant order of the form,

$$\phi(\rho, \theta, \rho_F) \approx \arctan \left[\sqrt{\frac{\gamma \pm \mu}{\gamma \mp \mu}} \tanh \frac{\sqrt{\gamma^2 - \mu^2}(\rho - \rho_F)}{2\sqrt{\delta}} \right]. \quad (7.4)$$

Here we come to a crucial point that is important to clarify: The ansatz proposed, Eqs. (7.1) and (7.2), considers that the PSSs possess an axial symmetry for the modulus and the phase, but this is only partially true. Obviously, in the case of the symmetric $2D$ PSS this assumption agrees with the numerical observation [cf. Fig. 7.1]. Nevertheless, we have proved the existence of non axial-symmetric PSS solution [see Figs. 7.2]. In order to achieve a proper theoretical description of this solutions let us introduce an adequate coordinate system. Defining a non usual polar coordinate $\{\mathbf{r}, \theta\}$, $|\mathbf{r}| = \rho$ and $\theta \in [0, \pi)$, we get a total description of the two-dimensional space. This description of the space allows us to split the asymmetric phase structure into two symmetric phase state connected in $\mathbf{r} = 0$. Therefore, we can perform our calculation for two different regions, that is $\mathbf{r} < 0$ and $\mathbf{r} > 0$. Surprisingly, we have conducted the calculation for the two different asymptotic region; semi-plane domain consisted of $[0, \pi)$ and $\mathbf{r} = (0, \infty)$; And the complementary semi-plane domain ($\mathbf{r} \in (-\infty, 0)$ and $\theta \in [0, \pi)$); obtaining again the phase profile Eq. (7.3). Fig. 7.5 shows the theoretical asymmetric two-dimensional phase shielding soliton obtained by considering the whole domain of \mathbf{r} . It is built up by connecting the different stationary front solutions of (7.3). Notice that in this approximation for PSSs with semi-axial symmetry, the interface separating the different regions is abrupt [see Fig. 7.5]. This is a consequence of the coordinate system used to describe these solutions. The PSSs obtained numerically are smooth in this junction region [cf. Fig. 7.2].

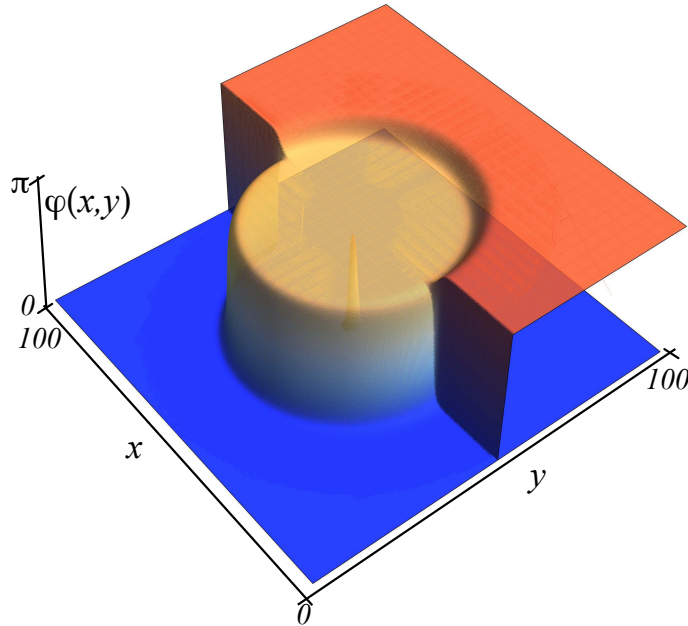


Figure 7.5: (color online) A $2D$ phase shielding soliton with semi-axial symmetry given at dominant order by the analytical function (7.4) with $\gamma = 0.15$, $\mu = 0.1$, and $\nu = -0.15$. The amplitude $R(x, y)$ is plotted simultaneously to illustrate the soliton position.

7.3 Phase front dynamics

The dynamics of phase fronts at dominant order is described by the equation obtained by replacing (7.1) and (7.2) in (4.20):

$$-\dot{\rho}_F(t)\partial_z\phi_F = -(\nu + \delta) - \frac{e^{-2\sqrt{\delta}\rho}}{\rho} + (\partial_\rho\phi_F)^2 - \gamma \sin(2\phi_F), \quad (7.5)$$

where we have defined the appropriated co-moving coordinate $z \equiv \rho - \rho_F$. Multiplying the above equation by $\partial_z\varphi_F$, and introducing the following inner product

$$\langle\langle f|g\rangle\rangle \equiv \int_{-\infty}^{\infty} \int_0^\pi fg\rho d\theta dz, \quad (7.6)$$

we obtain the following equation for the front dynamics,

$$\dot{\rho}_F = \frac{\tilde{A} + A\rho_F + Be^{-2\sqrt{\delta}\rho_F}}{C\rho_F}, \quad (7.7)$$

where

$$\begin{aligned} \tilde{A} &\equiv \langle\langle \gamma \sin(2\phi_F)z | \partial_\rho\phi_F \rangle\rangle, \\ A &\equiv \langle\langle [-(\nu + \delta) + (\partial_\rho\phi_F)^2] | \partial_\rho\phi_F \rangle\rangle, \\ B &\equiv \langle\langle e^{-2\sqrt{\delta}z} | \partial_\rho\varphi_F \rangle\rangle, \quad C \equiv \langle\langle \partial_\rho\varphi_F | \partial_\rho\varphi_F \rangle\rangle. \end{aligned} \quad (7.8)$$

Equation (7.7) can be interpreted as a Newton-type equation that describes a overdamping particle in the presence of a force composed by three terms: a constant, an inversely proportional to the position and an exponential force. The constant force is responsible for spreading the phase front to the outside, in opposition, the exponential force causes the phase front propagate towards to the position of the dissipative soliton in the center. The balance between these forces generates an equilibrium position for the phase front, which is consistent with the observed dynamics. At dominant order, phase dynamics is affected in two spatial dimensions by an extra term, which is inversely proportional to the distance. The exponential term is modified with a logarithmic correction. Therefore, for large distances phase shielding soliton dynamics in two dimensions is similar to that observed in one dimension.

Similarly, as we have done in Sec. 6.2.1, we could include higher order corrections in the amplitude of the modulus and get a more accurate expression for the structure and dynamics of phase fronts in two spatial dimensions. This analysis allows us to understand that PSSs are composed by dissipative solitons with different homogeneous phase [see Sec. 6.2.1].

Chapter 8

PSS in Physical Systems

In Chap. 4 we emphasized the universality of the PDNLS equation. Through an amplitude equation approach, it can be shown that the PDNLS equation is *present* in different physical systems. Based on this statement, one expects that results obtained in this context can be transposed to the original systems under study. In the following section we conduct a numerical study of an easy-plane ferromagnetic system in order to explore the emergence of PSS solutions in this system.

8.1 Magnetic wire

Solitons in magnetism have been intensively studied in past decades due to their possible technological applications. It is known that an easy-plane ferromagnetic spin chain in the presence of both a constant and a time-periodic external magnetic field perpendicular to the hard axis exhibits localized structures. Such structures are commonly referred to as localized precession states in a forced magnetic wire. Furthermore, experimental realizations of the model have already been achieved [78, 79].

The forced magnetic wire is described phenomenologically by the Landau-Lifshitz–Gilbert (LLG) equation. Following an amplitude equation approach, it can be proved that, in the quasi-reversible limit, the system can be described by the parametrically driven and damped nonlinear Schrödinger equation [23].

Let us consider a one-dimensional anisotropic Heisenberg ferromagnetic chain formed by N classical spins or magnetic moments subject to an external magnetic field. The direction of the chain is described by the z -coordinate, $\hat{z} = (0, 0, 1)$ and the external magnetic field is orthogonal to this direction, denoted by $\hat{x} = (1, 0, 0)$. When the quantum effects are small enough, the vector \mathbf{S}_i can be treated as a classical spin or a magnetic moment [23]. According to this latter assumption, the dynamics of the magnetic moment \mathbf{S}_i is governed by $\partial_t \mathbf{S}_i = -\gamma \mathbf{S}_i \times (\partial \mathcal{H} / \partial \mathbf{S}_i)$, where γ is the gyromagnetic constant and the Hamiltonian \mathcal{H} has the form,

$$\mathcal{H} = -J \sum_{i=1}^N \mathbf{S}_i \mathbf{S}_{i+1} + 2D \sum_{i=1}^N (S_i^z)^2 - g\mu H_x \sum_{i=1}^N S_i^x. \quad (8.1)$$

Here, J is the exchange coupling constant, H_x and D stand for the external magnetic field and the anisotropy energy, respectively.

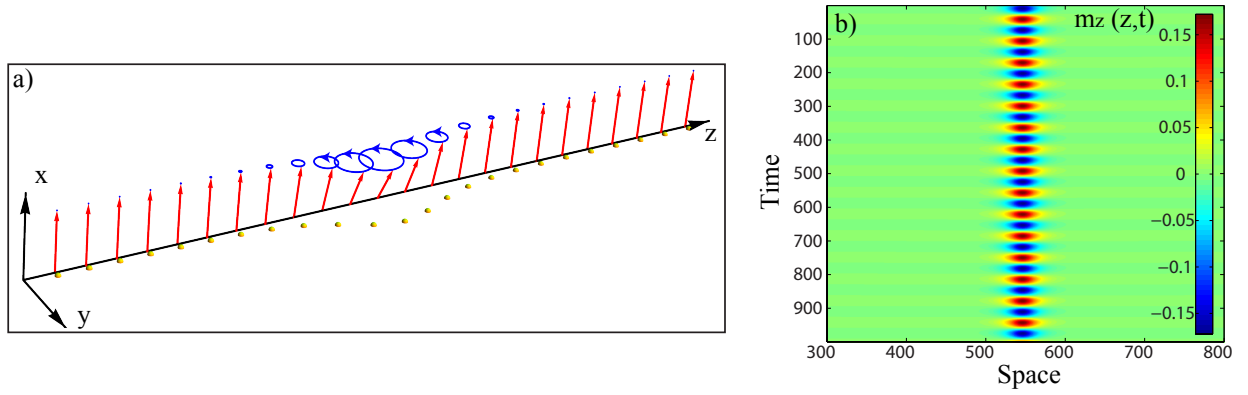


Figure 8.1: (a) Schematic representation of a soliton in a one-dimensional anisotropic ferromagnetic chain (magnetic wire). (b) Spatiotemporal evolution of a soliton for $L = 1024$, $H_0 = 4.800$, $\beta = 0.200$, $h_1 = 0.042$, $\alpha = 0.019$ and $\nu = -0.030$.

To study the continuous limit of this set of ordinary differential equations, that account for a magnetic wire, we assume that:

$$\mathbf{S}_i(t) \rightarrow \mathbf{S}(z, t), \quad (8.2)$$

and

$$\frac{Jdz^2}{\gamma^{-1}} \left(\frac{\mathbf{S}_{i+1} - 2\mathbf{S}_i + \mathbf{S}_{i-1}}{dz^2} \right) \rightarrow l_{ex} \partial_z^2 \mathbf{S}(z, t), \quad (8.3)$$

where l_{ex} denotes the characteristic interaction length. Moreover, introducing a phenomenological dissipative source, the Gilbert damping, the motion of the magnetization field is governed by the well known Landau-Lifshitz-Gilbert (LLG) equation [80],

$$\partial_\tau \mathbf{M} = \mathbf{M} \times [\mathbf{M}_{zz} - \beta(\mathbf{M} \cdot \hat{z}) + \mathbf{H}_e - \alpha \partial_\tau \mathbf{M}], \quad (8.4)$$

where $\mathbf{M} \equiv \mathbf{S}/M_s$ stands for the unit vector of the magnetization and M_s saturation magnetization. Here, we introduced the normalization $\{\tau \rightarrow \gamma M_s t, \beta \rightarrow 4D/\gamma, \mathbf{H}_e \rightarrow g\mu\mathbf{M}/\gamma M_s\}$. The parameter $\beta > 0$ accounts for the anisotropy constant (easy-plane magnetization), and α is the damping parameter. For several types of magnetic materials, this parameter is small [80]. When the magnetic field is time-dependent, the above model (8.4) is a time reversible system perturbed with injection and dissipation of energy, i.e. a quasi-reversible system, as long as this perturbation remains small.

As a result of the anisotropy and constant external field ($\mathbf{H}_e = H_0 \hat{x}$), the natural equilibrium of the previous model (8.4) corresponds to the magnetization field lying in the direction of the external magnetic field, $\mathbf{M} = \hat{x}$. When spatial coupling is ignored, it is easy to show that the dynamics around this equilibrium is described by a nonlinear oscillator with natural frequency $\omega_0^2 = H_0(\beta + H_0)$ [23]. It is noteworthy that in Eq. (8.4), the magnetization components are proportional to the external magnetic field, which therefore acts as a parametric forcing. Then if this field combines a constant and a time-periodic part ($\mathbf{H}_e = [H_0 + h_1(t)] \hat{x}$ where $h_1(t) \equiv \Gamma \cos(\omega t)$ oscillates about twice the natural frequency,

$\omega \equiv 2(\omega_0 + \nu)$, and ν is the detuning parameter), the system exhibits a parametric resonance at $\Gamma^2 (\beta/4\omega_0)^2 = \alpha^2 (H_0 + \beta/2)^2 + \nu^2$ for small parameters $\{\alpha, \nu, H_0, \Gamma\}$. In the parameter space (Γ, ν) , the region above this curve corresponds to the Arnold tongue. Dynamically speaking this resonance corresponds to an undamped precession of the magnetization unit vector around the direction of the external magnetic field with angular velocity ω_0 (Fig.8.1a).

8.1.1 PSS in the magnetic wire

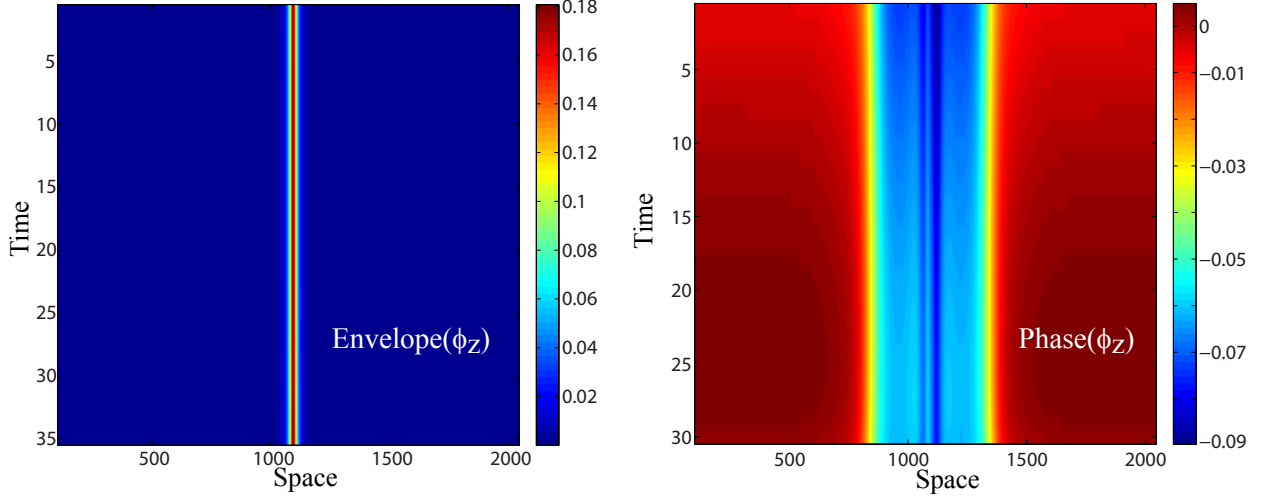


Figure 8.2: Stroboscopic spatiotemporal diagrams of the reconstructed envelope (left) and the phase angle ϕ_z (right) for $L = 2048$, $H_0 = 4.800$, $\beta = 0.200$, $h_1 = 0.042$, $\alpha = 0.019$ and $\nu = -0.030$. The appearance of two opposite fronts can be observed.

The chain of classical spins or magnetic wire subject to an external magnetic field represents a good physical system to study the formation of a phase shielding soliton. Numerical simulations of the magnetic wire for different values of the system size L are conducted. Following the same strategy, based on the Hilbert transform technique [see Sec. 2.3], the phase angle ϕ_z is rebuilt from the original data signal m_z . As expected, the phase of the dissipative soliton exhibits the formation of two counter-propagative fronts [cf. Fig. 8.2], which eventually form a phase structure surrounding the modulus of the soliton, similar to those observed for the PDNLS model [see Sec. 6.1]. A characteristic feature of this phase structure is the presence of a pronounced slot close to the position of the dissipative soliton. Note that this phenomenon also appears in the pendulum chain vertically vibrated [see Fig. 2.5 and Fig. 8.3]. Such large phase variation is a result of the nonlinear corrections of the envelope. These corrections correspond to higher-order terms that are not taken into account in the amplitude equation approach at dominant order (PDNLS). Such corrections are negligible far from the position of dissipative soliton but become relevant in the phase near the soliton core. The presence of corrective terms also affects the phase dynamics itself, as the phase front dynamics is led by an exponentially small force. This is notorious in the magnetic wire where the corrective terms cause the phase front solutions to reach their equilibrium states closer to the soliton position. The inclusion of higher order terms in the PDNLS equation is

necessary for a complete description of phase front dynamics in this magnetic system. This is a work in progress.

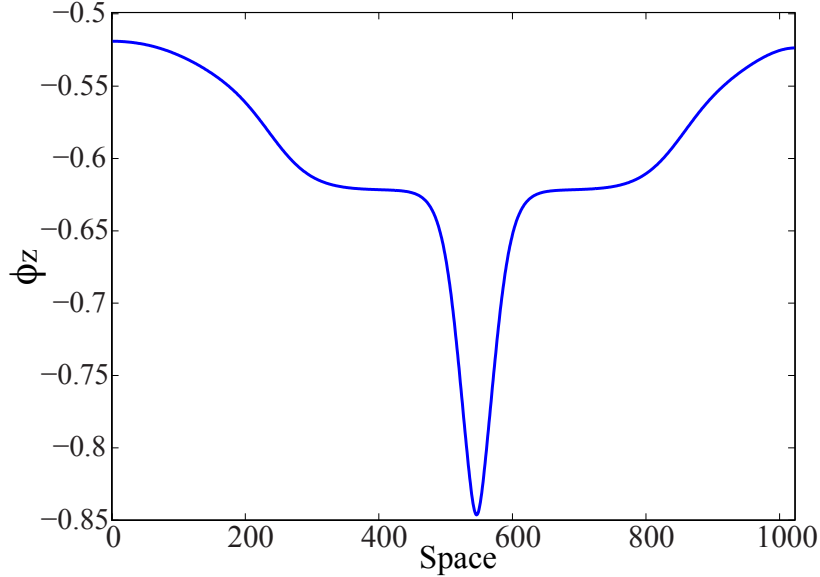


Figure 8.3: Steady (reconstructed) phase angle ϕ_z structure for $L = 1024$, $H_0 = 4.800$, $\beta = 0.200$, $h_1 = 0.042$, $\alpha = 0.019$ and $\nu = -0.030$.

8.2 Forced magnetic layer

An easy-plane ferromagnetic layer submitted to an external parametrical forcing has been analyzed within the framework of the LLG model. Such system exhibits the formation of patterns, domain walls and localized states near the parametric resonance. By means of the amplitude equation, an interaction law of $2D$ localized precession states has been derived [23]. However, no studies have been performed both numerical and theoretical, to characterize the phase emerging states located in the magnetic layer.

Let us introduce the main features of the description of a parametrically forced magnetic layer. Let us consider an anisotropic Heisenberg ferromagnetic layer formed by $N_x \times N_y$ classical spins or magnetic moments exposed to an external magnetic field, which is contained in the plane (x, y) and oriented in the direction $\hat{x} \equiv (1, 0, 0)$. Following the one-dimensional analysis exposed in section 8.1, we find that the motion of the magnetization field is governed by the Landau–Lifshitz–Gilbert equation [80]

$$\partial_\tau \mathbf{M} = \mathbf{M} \times [\nabla_\perp^2 \mathbf{M} - \beta(\mathbf{M} \cdot \hat{z}) + \mathbf{H}_e - \alpha \partial_\tau \mathbf{M}], \quad (8.5)$$

where $\nabla_\perp^2 \equiv \partial_{xx} + \partial_{yy}$ is the transverse Laplacian operator, $\mathbf{M} = \mathbf{S}/M_s$ stands for the unit vector of the magnetization, with M_s as the saturation magnetization. Again, we considered a normalization of scales and parameters $\{\tau \rightarrow \gamma M_s t, \beta \rightarrow 4D/\gamma M_s, \mathbf{H}_e \rightarrow g\mu\mathbf{H}/\gamma M_s\}$, where $\beta > 0$ is the uniaxial easy-plane anisotropy constant, and α is the damping parameter [see Sec. 8.1]. As in the one-dimensional case, the presence of damping $\alpha > 0$ and an external

and constant field $\mathbf{H}_e = H_0 \hat{x}$ lead to a magnetization in the direction of the external field $\mathbf{M} = \hat{x}$. When spatial coupling is ignored, it is easy to show that the dynamics around this equilibrium is described by a nonlinear oscillator with natural frequency $\omega_0 = \sqrt{H_0(\beta + H_0)}$.

Given that the magnetization components are proportional to the external magnetic field, it acts as a parametric forcing. Applying an external magnetic field with both a constant and a time periodic part of the form $\mathbf{H}_e = [H_0 + \Gamma \cos(\omega t)] \hat{x}$, oscillating about twice the natural frequency $\omega = 2(\omega_0 + \nu)$, where ν is the detuning parameter, the system exhibits a parametric resonance at $\Gamma^2(\beta/4\omega_0)^2 = \alpha^2(\beta/2 + H_0)^2 + \nu^2$ for small $\{\nu, H_0, \alpha, \Gamma\}$. Furthermore, The inclusion of spatial coupling yields to the formation of a localized state near the parametric resonance.

To understand the dynamics of such state, in the quasi-reversible limit $\Gamma \sim \nu \sim \alpha \ll \omega_0$ and close to the parametric resonance, let us consider the following ansatz for the three components of the magnetization

$$\begin{aligned} M_x &\approx 1 - \frac{M_y^2 + M_z^2}{2} \\ M_y &\approx \frac{1}{H_0} \left[1 + \frac{\Gamma}{H_0} \right] \partial_t M_z \\ M_z &\approx 4 \sqrt{\frac{\omega_0 H_0}{\beta(\omega_0^2 + 3H_0^2)}} \psi(\rho, t) e^{i(\omega_0 + \nu)t} + c.c. \end{aligned} \quad (8.6)$$

Introducing this into (8.5), after straightforward calculations and imposing a solvability condition [cf. Sec. 2.2.1] for the corrections of the above ansatz, we find that the system can be described by the parametrically driven and damped nonlinear Schrödinger equation

$$\partial_t \psi = -i\nu\psi - i|\psi|^2\psi - i\nabla_{\perp}^2 \psi - \mu\psi + \gamma\bar{\psi},$$

with $\gamma = \beta\Gamma/4\omega_0$ and $\mu = (\beta/2 + H_0)\alpha$. It is noteworthy that the procedure adopted for describing the magnetic plane is also valid for the magnetic wire analyzed in the last section 8.1, and therefore, that system (magnetic wire) can be described for the 1D-PDNLS model, in the quasi-reversible limit.

As discussed early [cf. Sec.4.4], there is no analytical solution for the two-dimensional PDNLS equation. However, from the approximated localized state (4.22), one can infer that for negative detuning, the localized breather magnetic solution appears by a saddle-node bifurcation when dissipation and energy injection are equal ($\gamma \sim \mu$ and $\nu < 0$). Furthermore, this solution is unstable when the uniform magnetization $\mathbf{M} = \hat{x}$ becomes unstable at Arnold tongue ($\gamma^2 = \nu^2 + \mu^2$, $\nu < 0$). The modulus width and height are given by $\sqrt{2\delta}$ and $1/\sqrt{\delta}$, respectively.

8.2.1 PSS in the magnetic layer

Numerical simulations in appropriate parameter regions of the magnetic layer show clearly the formation of localized precession states. Previous studies have performed a numerical fit of the magnetic solution with approximative solution (4.22), showing a good agreement [64].

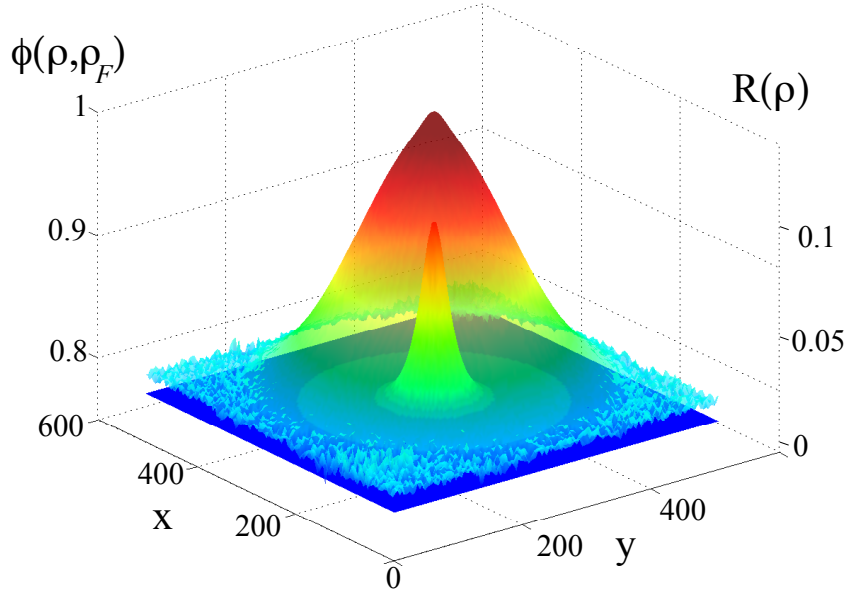


Figure 8.4: A phase shielding soliton obtained by a numerical simulation of equation (8.5) in a square magnetic plane $L \times L$ with $L = 512$, $H_0 = 0.10000$, $\beta = 1$, $h_1 = 0.00800$, $\alpha = 0.01900$ and $\nu = -0.00394$. The reconstructed phase in 2D $\phi_z(\rho, \rho_z)$ and the amplitude field $R(\rho)$ are represented simultaneously. The bell-like shaped reveals the presence of the characteristic slot, observed also in the 1D case, in the center of the plane.

From the analysis done for the 2D-PDNLS equation, an easy-plane ferromagnetic layer submitted to a external magnetic field that combines a constant and an oscillating part should present a shell-type phase structure. To capture the dynamical behavior of the phase, numerical simulations of the Landau-Lifshitz-Gilbert equation (8.5) over a square grid $L \times L$ for $L = 512$ are performed. This system size is large enough to exhibit PSS formation (based on the results obtained for 1D). Following the Hilbert transform technique [cf. Sec. 2.3] the phase has been reconstructed. Figure (8.4) depict a snapshot of a localized magnetic state for $H_0 = 0.1000$, $\lambda = 0.0100$, $\beta = 1.0000$, $\nu = -0.0035$ and $\Gamma = 0.0081$. As expected, a stable shielding phase is formed surrounding the soliton. In the same figure, we show the corresponding soliton solution.

As in the 1D magnetic case, this shell-type structure is always symmetric having a 2π rotation. It also present a modulo 2π periodicity. The phase front also reaches its stationary state closer to the typical slot present in the center. This produces a bell-like shape as we can observed in Fig. 8.4. In this situation, the slot is smaller that in the 1D case, and it can be seen on the top of the phase structure. Despite the numerical simulations reveal a stationary phase structure around a precession state—a phase shielding soliton—a deeper study is required in order to establish qualitatively and quantitatively the effect of the nonlinear corrections over the phase dynamics.

Conclusions & Future Work

Localized structures are ubiquitous phenomena in nature. During the last decade, a constant effort has been focused on determining the creation mechanisms of localized states, and thorough understanding of their properties. Undoubtedly, the next step to boost their potential applications is to advance the manipulation and control of these particle-type solutions. Parametric forcing offers a controllable mechanism to introduce energy into a system. Moreover, systems parametrically forced exhibit universal phenomena such as dissipative solitons, which are a natural extension of conservative ones. Close to the parametric resonance, the parametrically driven and damped nonlinear Schrödinger equation (PDNLS) models this kind of systems. This amplitude equation has been derived in several physical contexts to describe the appearance of patterns and localized states. Due to its universality, oscillatory localized state (dissipative solitons) are described in the context of PDNLS. These solutions are characterized for a bell-shaped modulus and a constant phase (UPS).

To prove the accuracy of the model describing parametrically forced systems, a theoretical and numerical study of the dynamical behavior of parametrically excited solitary waves in Faraday's water trough experiment is performed. Moreover, a theoretical and experimental method of manipulation of hydrodynamic solitons in a vertically driven rectangular water basin is presented, based on inhomogeneities of the system. Experimentally, the basin was tilted for angle, producing an inhomogeneity on the effective parameters of the system. As consequence, the soliton travels to equilibrium positions through a relaxation process. The steady point depends on the tilt angle, and can be pushed out of the basin if the angle is large enough. In the tilted system, dissipation, energy injection and detuning are inhomogeneous. Those effects are incorporated into the PDNLS model by promoting the dissipation, energy injection and detuning parameters (μ, γ, ν) as space dependent functions. We have deduced an equation for the position of hydrodynamic solitons. This equation is characterized by two terms: a constant speed and a linear relaxation term. The theoretical description reproduces well the hydrodynamic soliton dynamics observed experimentally.

Numerical simulations conducted for single dissipative solitons in homogeneous media showed the unexpected emergence of two-counter phase fronts, which propagate away from the soliton position. After a non-trivial dynamics the front phase reaches a steady point. The final phase structure, that surrounds the modulus, is composed by two of those phase fronts: the phase shielding soliton. Moreover, eight different types of localized states have been unveiled. They correspond to all possible PSS achievable by the dissipative soliton with phase in the range $[-\pi, \pi]$. The appearance of each phase configuration strongly depends of initial conditions. A slight change of these conditions can lead to a different phase shielding structure using the same system parameters. However, a full comprehension of their basin

of attraction as well as their stability is an open question.

Considering the asymptotic behavior of the amplitude solution away from the soliton position, an analytical expression was derived for the front phase in a semi-infinite domain. The stationary phase front represents heteroclinic orbits in the $\{\phi, \partial_x \phi\}$ space. Such states present different types of configurations. The dynamical behavior of these fronts exhibits a non-uniform translation that is ruled by two antagonistic forces generating stable equilibria. A deeper analysis of numerical simulations reveals that PSS solutions are composed of two qualitatively different regions: inner and outer regions. Both regions are separated by a crossover point between the exponential decay rates of the stable and the unstable UPS solution. Therefore, the PSSs are composed by both UPS solutions.

The PSS stability was obtained by means of numerical analysis. We found that the phase stability depends on the system size L . Below a critical value of L , the phase remains uniform, but for large enough values of it, the system destabilizes through an Andronov-Hopf bifurcation. We also show that the system also presents an instability for a given L , but for large values of the amplitude or the frequency of the forcing $\{\gamma, \nu\}$. Hence, the shielding phase solutions exist in a wide parameter region far from the limit $\mu \sim \gamma$. Furthermore, phase shielding structure is the only state of equilibrium exhibited for dissipative soliton in a large system. It is worth noting that, for more than two decades, the solitons studied in PDNLS (in the one-dimensional case as in the two dimensional) were always described with a constant phase. Typically, these localized solutions are characterized by two parameters δ_+ and x_0 , which determine its shape and position respectively. For its part, the characterization of phase shielding solitons has revealed a new parameter that brings an more accurately description for such solutions; The size of the phase structure. It should be remembered that the greater the amplitude of forcing (γ) the more compact is the phase structure, so does decreasing the detuning (ν). Therefore, this novel type of dissipative localized structure with non-trivial phase structure (PSS) offers a new perspective to the dissipative solitons naturally arising in parametrically forced system. Shell-like phase structure must play a significant role in soliton interaction, since bound states of two solitons show a complex phase structure [57, 30]. Experimental observations show an intricate temporal dynamics of dissipative solitons [60] which cannot be explained from uniform phase solitons.

To study the robustness of the phase dynamics around the soliton, the two-dimensional spatial extension is considered. It is well known that $2D$ -PDNLS has soliton type solutions with a constant phase [58], which are the natural extensions of the one-dimensional case. However, an analytical expression for these solutions is unknown. Considering a similar parameter region of phase shielding solitons in one dimension, we observe a rich phase fronts dynamics in two dimensions. More precisely, we could characterize two types of stable configurations in the two-dimensional case: an axially symmetric state and a semi-axially symmetric structure composed of two semicircular fronts. The phase front dynamics is also well described by a Newtonian-type equation in the asymptotic limit of large distance ($\rho \rightarrow \infty$). Again, this predicts a stable equilibrium position for the front that accounts for the shell-type phase structure.

The asymmetric two-dimensional PSS solution is characterized by being composed of all the solutions found in one dimension. Indeed, if one performs different cuts containing

the center (soliton position), one can recognize the observed solutions in one dimension. A surprising property of the shell-like structure observed is that if one calculates the phase change on a path that connects two opposite points with respect to the position of the soliton ($\int_{\Gamma} \vec{\nabla} \phi d\vec{s}$) within the region close to the position of the soliton one finds that this is zero. Nevertheless, if one takes this type of path far away from the soliton position, one finds $\int_{\Gamma} \vec{\nabla} \phi d\vec{s} = \pm\pi$. In conclusion, localized structures in parametrically forced systems have a rich and unexpected phase dynamics, creating novel types of localized states. It is expected that phase shielding solitons could be observed experimentally in simple coupled forced oscillators, such as vertically driven fluid layers in narrow cells, optical parametrical oscillators, driven magnetic media, among others.

To confirm the presence of the shell-type phase structure in one dimensional parametrically driven solitons, we studied an anisotropic Heisenberg ferromagnetic chain formed by N classical spins or magnetic moments subject to an external magnetic field. As expected, the phase of the dissipative soliton exhibits the formation of two counter-propagative fronts, analogously to those observed for the PDNLS model. A feature characteristic of this phase structure is the presence of a pronounced slot close to the position of dissipative soliton. Such large phase variation is a result of the nonlinear corrections of the envelope. These corrections corresponds to higher-order terms that are not taken into account in the amplitude equation approach at dominant order. Such corrections are negligible far from the position of dissipative soliton but become relevant in the phase near the soliton core. The presence of corrective terms also affects the phase dynamics itself, as the phase front dynamics is led by an exponentially small force. This is notorious in the magnetic wire where the corrective terms cause the phase front solutions to reach their equilibrium states closer to the soliton position. Recent studies have demonstrated that the parametrically driven and damped nonlinear Schrödinger equation does not account for all the localized structures observed in magnetic wire [23, 59]. Consequently, the inclusion of higher order terms in the PDNLS equation is necessary for a complete description of phase front dynamics in this magnetic system.

Additionally, in order to corroborate the results obtained for PSS in $2D$ -PDNLS, we analyzed the phase behavior of oscillatory dissipative solitons in an anisotropic Heisenberg ferromagnetic layer formed by $N_x \times N_y$ classical spins or magnetic moments exposed to an external magnetic field. The numerical simulations show the existence of a complicated structure for the phase. The characteristic slot, observed in $1D$ systems, is also present in the $2D$ case. As before, the relevance of the corrective terms is evident. The presence of corrective terms, usually related to the particular physical problem under study, has interesting consequences over the dynamics of the phase front as well as in its final configuration. However, we conclude that phase shielding solitons are a universal phenomenon, despite the modification that may experience because of higher-order terms. Still, a broader analysis of different systems, in order to establish the effect of each corrective term, is required and work in that direction is still in progress.

Bibliography

- [1] Eryk Infeld and George Rowlands. *Nonlinear Waves, Solitons and Chaos*. Cambridge University Press, New York, 2000.
- [2] Lord Rayleigh. On waves. *Philosophical Magazine Series 5*, 1:257–279, 1876.
- [3] D. J. Korteweg and G. De Vries. On the change of form of long waves advancing in a rectangular channel, and on a new type of long stationary waves. *Philosophical Magazine Series 5*, 39:422–443, 1895.
- [4] E. Fermi, J. Pasta, and S. Ulam. Studies of non linear problems. *Los Alamos, Document*, LA-19040, 1955.
- [5] N. J. Zabusky and M. D. Kruskal. Interaction of "Solitons" in a Collisionless Plasma and the Recurrence of Initial States. *Physical Review Letters*, 15:240–243, 1965.
- [6] C. S. Gardner, J. M. Greene, M. D. Kruskal, and R. M. Miura. Method for solving the Korteweg-de Vries equation. *Physical Review Letters*, 19:1095–1097, 1967.
- [7] P. D Lax. Integrals of nonlinear equations of evolution and solitary waves. *Communications in Pure and Applied Mathematics*, 21:467–490, 1968.
- [8] V. E. Zarkharov and A.B. Shabat. Exact theory of two-dimensional self-focusing and one-dimensional self modulation of waves in nonlinear media. *Soviet Physics Journal of Experimental and Theoretical Physics*, 34:62–69, 1972.
- [9] M. J. Ablowitz, D. J. Kaup, A. C. Newell, and H. Segur. Method for solving the sine-Gordon equation. *Physical Review Letters*, 30:1262–1264, 1973.
- [10] M. J. Ablowitz, D. J. Kaup, A. C. Newell, and H. Segur. The Inverse Scattering Transform-Fourier Analysis for Nonlinear Problems. *Studies in Applied Mathematics*, 53:249–315, 1974.
- [11] Y. S. Kivshar and B. A. Malomed. Dynamics of solitons in nearly integrable systems. *Review of Modern Physics*, 58:763–915, 1989.
- [12] D. J. Kaup. A perturbation expansion for the Zakharov-Shabat inverse scattering transform. *SIAM Journal of Applied Mathematics*, 31:121–133, 1976.
- [13] A. M. Turing. The chemical basis of the morphogenesis. *Philosophical Transactions of the Royal Society of London*, 237:37–72, 1952.

- [14] G. Nicolis and I. Prigogine. *Self-Organization in Non Equilibrium Systems*. Wiley, New York, 1977.
- [15] M. C. Cross and P. C. Hohenberg. Pattern formation outside of equilibrium. *Reviews of Modern Physics*, 65, 1993.
- [16] L. M. Pismen. *Patterns and interfaces in dissipative dynamics*. Springer Series in Synergetics, Berlin Heidelberg, 2006.
- [17] M. Cross and H. Greenside. *Pattern Formation and Dynamics in Nonequilibrium Systems*. Cambridge University Press, New York, 2009.
- [18] Nail Akhmediev and Adrian Ankiewicz. *Dissipative Solitons: From optics to Biology and Medicine*. Springer, Berlin Heidelberg, 2008.
- [19] O. Descalzi, M. Clerc, S. Residori, and G. Assanto. *Localized States in Physics: Solitons and Patterns*. Springer, New York, 2011.
- [20] M. Faraday. On a Peculiar Class of Acoustical Figures; and on Certain Forms Assumed by Groups of Particles upon Vibrating Elastic Surfaces. *Philosophical Transactions of the Royal Society*, 121:299–340, 1831.
- [21] Ignacio Ortega, Marcel G. Clerc, Claudio Falcón, and Nicolás Mujica. Subharmonic wave transition in a quasi-one-dimensional noisy fluidized shallow granular bed. *Physical Review E*, 81:046208, 2010.
- [22] P. Umbanhowar, F. Melo, and H. L. Swinney. Localized excitations in a vertically vibrated granular layer. *Nature*, 382:793, 1996.
- [23] Marcel G. Clerc, Saliya Coulibaly, and David Laroze. Localized states of parametrically driven easy-plane ferromagnetic wire. *Physica D*, 72:239, 2010.
- [24] Stefano Longhi. Stable multipulse states in a nonlinear dispersive cavity with parametric gain. *Physical Review E*, 53, 1996.
- [25] Jhon W. Miles. Surface-Wave Damping in Closed Basins. *Proceedings of the Royal Society*, 287, 1967.
- [26] I. V. Barashenkov, M. M. Bogdan, and V. I. Korovob. Stability Diagram of the Phase-Locked Solitons in the Parametrically Driven, Damped Nonlinear Schrödinger Equation. *Europhysics Letters*, 15, 1991.
- [27] Stefano Longhi. localized structures in optical parametric oscillation. *Physica Scripta*, 56, 1997.
- [28] Nail Akhmediev and Adrian Ankiewicz. *Dissipative Solitons*. Springer, Berlin Heidelberg, 2005.
- [29] I.V. Barashenkov and E.V. Zemlyanaya. Stable Complexes of Parametrically Driven, Damped Nonlinear Schrödinger Solitons. *Physical Review Letters*, 83, 1999.

- [30] Eyal Kenig, Boris A. Malomed, M. C. Cross, and Ron Lifshitz. Intrinsic localized modes in parametrically driven arrays of nonlinear resonators. *Physical Review E*, 80:046202, 2009.
- [31] N.V. Alexeeva, I.V. Barashenkov, and G. P. Tsironis. Impurity-Induced Stabilization of Solitons in Arrays of Parametrically Driven Nonlinear Oscillators. *Physical Review Letters*, 84, 2000.
- [32] W. S. Edwards and S. Fauve. Patterns and quasi-patterns in the Faraday experiment. *Journal of Fluid Mechanics*, 278:123–148, 1994.
- [33] P. B. Umbanhowar, F. Melo, and H. L. Swinney. Localized excitations in a vertically vibrated granular layer. *Nature*, 382:793–796, 1996.
- [34] R. Heinrichs, G. Ahlers, and D. S. Cannell. Traveling waves and spatial variation in the convection of a binary mixture. *Physical Review A*, 35:27612764, 1987.
- [35] Lev Landau and E. M. Lifshitz. *Mechanics*. Pergamon Press, United Kingdom, 1969.
- [36] Thor I. Fossen and Henk Nijmeijer. *Parametric Resonance in Dynamical Systems*. Springer, 2011.
- [37] Émile Mathieu. Mémoire sur Le Mouvement Vibratoire dune Membrane de forme Elliptique. *Journal de Mathématiques Pures et Appliquées*, 3:137–203, 1868.
- [38] Lord Rayleigh. On maintained vibrations. *Philosophical Magazine Series 5*, 15:229–235, 1883.
- [39] Lord Rayleigh. On the maintenance of vibrations by forces of double frequency, and on the propagation of waves through a medium endowed with a periodic structure. *Philosophical Magazine Series 5*, 24:145–159, 1887.
- [40] Marcel G. Clerc, Claudio Falcón, Cristián Fernández-Oto, and Enrique Tirapegui. Effective-parametric resonance in a non-oscillating system. *Europhysics Letters*, 98:30006, 2012.
- [41] L. D. Landau and D. Ter Haar. *Collected Paperes of L. D. Landau*. Gordon and Breach, 1965.
- [42] Jhon W. Miles. Parametrically excited solitary waves. *Journal of Fluid Mechanics*, 148, 1984.
- [43] Marcel G. Clerc, Saliya Coulibaly, and David Laroze. Localized states beyond the asymptotic parametrically driven amplitude equation. *Physical Review E*, 77:056209, 2008.
- [44] Jon Claerbout. *Fundamentals of Geophysical Data Processing*. McGraw-Hill, New York, 1976.
- [45] A. V. Oppenheim and R. W. Schaffer. *Digital Signal Processing*. Prentice Hall, 1975.

- [46] Michel Remoissenet. *Waves Called Solitons: Concepts and Experiments*. Springer-Verlag, Berlin Heidelberg, 1999.
- [47] P. G. Drazin and R. S. Johnson. *Solitons: an introduction (2nd ed.)*. Cambridge University Press, 1989.
- [48] J. M. Soto-Crespo, N. Akhmediev, and A. Ankiewicz. Pulsating, Creeping, and Erupting Solitons in Dissipative Systems. *Physical Review Letters*, 85:2937–2940, 2000.
- [49] Marcel G. Clerc, Pierre Couillet, and Enrique Tirapegui. The Maxwell-Bloch description of 1/1 resonances. *Optical Communications*, 167:159164, 1999.
- [50] Marcel G. Clerc, Pierre Couillet, and Enrique Tirapegui. Lorenz Bifurcation: Instabilities in Quasi-reversible Systems. *Physical Review Letters*, 83:3820–3823, 1999.
- [51] V. I. Arnold. *Geometrical Methods in the Theory of Ordinary Differential Equations*. Springer-Verlag, New York, 1988.
- [52] Zhang, Wenbin and Viñals, Jorge. Secondary Instabilities and Spatiotemporal Chaos in Parametric Surface-Waves. *Physical Review Letters*, 74, 1995.
- [53] P. Couillet, T. Frisch, and G. Sonnino. Dispersion-induced patterns. *Physical Review E*, 49:2087–2090, 1994.
- [54] J. Wu, R. Keolian, and I. Rudnick. Observation of a nonpropagating hydrodynamic soliton. *Physical Review Letters*, 52:1421–1424, 1984.
- [55] de Varcárcel G. J., Staliunas K., Roldán Eugenio, and V. J. Sánchez-Morcillo. Transverse patterns in degenerate optical parametric oscillation and degenerate four-wave mixing. *Physical Review A*, 54, 1996.
- [56] Bondila Mariana, Barashenkov Igor V., and Bogdan Mikhail M. Topography of attractors of the parametrically driven nonlinear Schrödinger equation. *Physica D*, 87, 1995.
- [57] Barashenkov I. V. and Zemlyanaya E. V. Soliton complexity in the damped-driven nonlinear Schrödinger equation: Stationary to periodic to quasiperiodic complexes. *Physical Review E*, 83, 2011.
- [58] I. V. Barashenkov, N. V. Alexeeva, and E. V. Zemlyanaya. Two- and Three-Dimensional Oscillons in Nonlinear Faraday Resonance. *Physical Review Letters*, 89:104101, 2002.
- [59] M. G. Clerc, S. Coulibaly, and D. Laroze. Interaction law of 2D localized precession states. *Europhysics Letters*, 90:38005, 2010.
- [60] Wei Wang, Xinlong Wang, Junyi Wang, and Rongjue Wei. Dynamical behavior of parametrically excited solitary waves in Faraday’s water trough experiment. *Physics Letters A*, 219:74–78, 1996.
- [61] M. Clerc, P. Couillet, and E. Tirapegui. The stationary instability in quasi-reversible systems and the Lorenz pendulum. *International Journal of Bifurcation and Chaos*, 11:591–603, 2001.

- [62] M. G. Clerc, P. Couillet, N. Vandenbergh, and E. Tirapegui. Quasi-reversible instabilities of closed orbits. *Physics Letters A*, 287:198–204, 2001.
- [63] C. Sulem and P.L. Sulem. *Nonlinear Schroedinger Equations: Self-Focusing and Wave Collapse*. Applied Mathematical Sciences, Vol. 139, Springer-Verlag, 1999.
- [64] O. Bang, Y. S. Kivshar, A. V. Buryak, A. De Rossi, and S. Trillo. Two-dimensional solitary-waves in media with quadratic and cubic nonlinearity. *Physical Review E*, 58:5057–5069, 1998.
- [65] E. Caboche, F. Pedaci, P. Gevet, S. Barland, M. Giudici, J. Tredicce, G. Tissoni, and L. A. Lugiato. Microresonator defects as sources of drifting cavity solitons. *Physical Review Letters*, 102:163901, 2009.
- [66] M. I. Molina, Y. V. Kartashov, L. Torner, and Y. S. Kivshar. Surface solitons in chirped photonic lattices. *Optics Letters*, 29:2905, 2007.
- [67] M. I. Molina, Y. V. Kartashov, L. Torner, and Y. S. Kivshar. Spatially localized modes in two-dimensional chirped photonic lattices. *Physical Review A*, 77:053813, 2008.
- [68] Gordillo, Leandro and Sauma, Tania and Zárata, Yair and Espinoza, Ignacio and Clerc, Marcel G. and Mujica, Nicolas. Can non-propagating hydrodynamic solitons be forced to move? *European Physical Journal D*, 62:39–49, 2010.
- [69] M.G. Clerc, S. Coulibaly, N. Mujica, R. Navarro, and T. Sauma. Soliton pair interaction law in parametrically driven newtonian fluid. *Philosophical Transactions of the Royal Society A*, 367:3213–3226, 2009.
- [70] Leonardo Gordillo. *Non-Propagating Hydrodynamic Solitons in a Quasi-One Dimensional Free Surface Subject to Vertical Vibrations*. PhD thesis, Universidad de Chile; F.C.F.M., departamento de Física, 2012.
- [71] H. Arfken, G. and Weber. *Mathematical Methods for Physicists*. Elsevier Academic Press, Burlington, 2001.
- [72] Xinlong Wang and Rongjue Wei. Oscillatory patterns composed of the parametrically excited surface-wave solitons. *Physical Review E*, 57:2405–2410, 1998.
- [73] Clerc, Marcel G. and Coulibaly, Saliya and Garcia-Ñustes, Mónica A. and Zárata, Yair. Dissipative localized states with shieldlike phase structure. *Physical Review Letters*, 107:254102, 2010.
- [74] Marcel G. Clerc, Saliya Coulibaly, Mónica A. Garcia-Ñustes, and Yair Zárata. Phase shielding soliton in parametrically driven systems. *To Be Published in Phys. Rev. E*, 2013.
- [75] S. H. Strogatz. *Nonlinear Dynamics and Chaos: With Applications to Physics, Biology, Chemistry and Engineering*. Addison Wesley, Reading, 1994.
- [76] J. Hale and H. Kocak. *Dynamics and Bifurcations*. Texts in Applied Mathematics. Springer-Verlag, 1991.

- [77] L. Berge. Wave collapse in physics: principles and applications to light and plasma waves. *Physics Reports*, 303:259–360, 1998.
- [78] A. B. Ustinov, B. A. Kalinikos, V. E. Demidov, and S. O. Demokritov. Formation of gap solitons in ferromagnetic films with a periodic metal grating. *Physical Review B*, 81:180406, 2010.
- [79] A. B. Ustinov, V. E. Demidov, A. V. Kondrashov, B. A. Kalinikos, and S. O. Demokritov. Observation of the Chaotic Spin-Wave Soliton Trains in Magnetic Films. *Physical Review Letters*, 106:017201, 2011.
- [80] G. Bertotti, I. D. Mayergoyz, and C. Serpico. *Nonlinear Magnetization Dynamics in Nanosystems*. Elsevier, 2009.

Appendices

Appendix A

Contributions

A.1 Can non-propagating hydrodynamic solitons be forced to move?

L. Gordillo, T. Sauma, Y. Zárate, I. Espinoza, M.G. Clerc, and N. Mujica.

European Physics Journal D 62, 3949 (2011) DOI: 10.1140/epjd/e2010-10331-8

Abstract

Development of technologies based on localized states depends on our ability to manipulate and control these nonlinear structures. In order to achieve this, the interactions between localized states and control tools should be well modelled and understood. We present a theoretical and experimental study for non-propagating hydrodynamic solitons in a vertically driven rectangular water basin, based on the inclination of the system. Experiments show that tilting the basin induces non-propagating solitons to drift towards an equilibrium position through a relaxation process. Our theoretical approach is derived from the parametrically driven damped nonlinear Schrödinger equation which models the system. The basin tilting effect is modelled by promoting the parameters that characterize the system, e.g. dissipation, forcing and frequency detuning, as space dependent functions. A motion law for these hydrodynamic solitons can be deduced from these assumptions. The model equation, which includes a constant speed and a linear relaxation term, nicely reproduces the motion observed experimentally.

Can non-propagating hydrodynamic solitons be forced to move?

L. Gordillo^{1,a}, T. Sauma¹, Y. Zárate¹, I. Espinoza², M.G. Clerc¹, and N. Mujica¹

¹ Departamento de Física, FCFM, Universidad de Chile, Casilla 487-3, Santiago, Chile

² Departamento de Física, Pontificia Universidad Católica de Chile, Av. Vicuña Mackenna 4860, Santiago, Chile

Received 1st June 2010 / Received in final form 15 October 2010

Published online 17 December 2010 – © EDP Sciences, Società Italiana di Fisica, Springer-Verlag 2010

Abstract. Development of technologies based on localized states depends on our ability to manipulate and control these nonlinear structures. In order to achieve this, the interactions between localized states and control tools should be well modelled and understood. We present a theoretical and experimental study for *handling* non-propagating hydrodynamic solitons in a vertically driven rectangular water basin, based on the inclination of the system. Experiments show that tilting the basin induces non-propagating solitons to drift towards an equilibrium position through a relaxation process. Our theoretical approach is derived from the parametrically driven damped nonlinear Schrödinger equation which models the system. The basin tilting effect is modelled by promoting the parameters that characterize the system, e.g. dissipation, forcing and frequency detuning, as space dependent functions. A motion law for these hydrodynamic solitons can be deduced from these assumptions. The model equation, which includes a constant speed and a linear relaxation term, nicely reproduces the motion observed experimentally.

1 Introduction

During the last years, emerging macroscopic particle-type solutions or localized states in macroscopic extended dissipative systems have been observed in different fields, such as: domains in magnetic materials, chiral bubbles in liquid crystals, current filaments in gas discharge, spots in chemical reactions, localized states in fluid surface waves, oscillons in granular media, isolated states in thermal convection, solitary waves in nonlinear optics, just to mention a few. The variety of this type of phenomena evidences the universality of these particle-type solutions. Although these states are spatially extended, they exhibit properties typically associated with particles. Consequently, one can characterize them with a family of continuous parameters such as position, amplitude and width. Hence, these coherent states are particle-type solutions. This is exactly the type of description and strategy used in fundamental physical theories like quantum mechanics and particle physics. Indeed, localized states emerging in extended dissipative systems are composed by a large number of atoms or molecules (of the order of Avogadro's number) that behave coherently. The paradigmatic example of a macroscopic localized state is the existence of solitons, as those reported in fluid dynamics, nonlinear optics and Hamiltonian systems [1]. These solitons arise from a robust balance between dispersion and nonlinearity. The generalization of this concept to dissipative and out of

equilibrium systems has led to several studies in the last decades, in particular to the definition of *localized structures* intended as patterns appearing in a restricted region of space [2,3].

In one-dimensional spatial systems, an adequate geometrical theoretical description of localized states has been established based on spatial trajectories connecting a steady state with itself. They arise as homoclinic orbits from the viewpoint of dynamical systems theory (see the review [4] and references therein), while domain walls or fronts are seen as spatial trajectories joining two different steady states – heteroclinic curves – of the corresponding spatial dynamical system [5]. Localized patterns can be understood as homoclinic orbits in the Poincaré section of the corresponding spatial-reversible dynamical system [4–7]. They can also be understood as a consequence of the front interaction with oscillatory tails [8,9]. There is another type of stabilization mechanism that generates localized structures without oscillatory tails based on non-variational effects [10,11], where front interaction is led by the non-variational terms [12].

Quasi-reversible systems¹ are the natural theoretical framework in which one expects to observe localized structures. Time-reversible and Hamiltonian systems exhibit a family of localized states described by a set of continuous parameters [1]. Thus, when one considers energy injection and dissipation, only few or none solutions of the

¹ Time-reversible systems subjected to small injection and dissipation of energy [13–17].

^a e-mail: ljgordillo@gmail.com

family survive. The prototype model that presents localized structures or dissipative solitons in quasi-reversible systems is the parametrically driven damped nonlinear Schrödinger equation [18]. This model has been derived in several contexts to describe patterns and localized structures, such as vertically oscillating layer of water [19–21], nonlinear lattices [22], optical fibers [23], Kerr type optical parametric oscillators [24], magnetization in an easy-plane ferromagnetic exposed to an oscillatory magnetic field [25–28], and parametrically driven damped chain of pendula [29,30].

In the last two decades, the properties and mechanisms of creation of localized structures have been established as well as their interactions. However, few studies have been focused on manipulation and control of these coherent states. In the pioneering work of Wu et al. [32], the authors mention that hydrodynamic non-propagating solitons are sensitive to depth gradients. They found that solitons move toward less deep regions with an average velocity of 0.05 cm/s for a 3° tilt angle. This fact suggests that tilting the basin can be used as a spatial control tool, as it induces motion of solitons. A quantitative detailed study of the dynamics of the soliton needs to be performed in order to achieve this. Recent efforts have been accomplished in the context of optical cavities in semiconductors [31], through the use of a phase gradient which induces a drift of cavity solitons.

The aim of this manuscript is to characterize theoretically and experimentally a method of manipulation and control of non-propagating hydrodynamic solitons in a vertically driven rectangular water container based. More precisely, this control is attained by tilting the bottom surface normal with respect to gravity. Close to the Faraday instability, the parametrically driven damped nonlinear Schrödinger equation models this system. The effect of the container inclination is incorporated into the amplitude equation through space-dependent dissipation, injection and detuning. Considering that the tilt angle is small, we deduce an equation for the position of non-propagating hydrodynamic solitons. This equation is characterized by two terms: a constant speed and a linear relaxation process. Therefore, at a given inclination of the cell, the dissipative soliton travels to an equilibrium position through a relaxation process. In the case that the inhomogeneous injection and dissipation of energy are of the same order, the dominant mechanism in the propulsion of dissipative solitons is governed by the inhomogeneous detuning. Experimentally, we have found good agreement with the proposed dynamics of dissipative hydrodynamic solitons under the influence of tilt angle.

The manuscript is organized as follows: the description of the experimental setup and the procedures used in the characterization of the dynamics of dissipative solitons in a tilted cell are presented in Section 2. The theoretical description of the basin subjected to vertical oscillations and deduction of the equation for the position of dissipative solitons under the influence of an inclination is presented in Section 3. Finally, the conclusions are presented in Section 4.

2 Motion of non-propagating hydrodynamic soliton in tilted container

Non-propagating hydrodynamic solitons arise when a quasi 1-D rectangular basin filled with water is excited vertically at certain range of frequencies and amplitudes [32]. These localized states have a subharmonic nature depicted by oscillations at half the forcing frequency. They appear as localized transverse *sloshing* structures on the free surface. The dissipative solitons nucleate from disturbances of the stable flat state. In practice, they can be created by perturbing the water surface with a paddle in such a way that the swaying resembles solitons typical *sloshing* motion.

2.1 Experimental setup and procedure

The experiments are done with a rectangular plexiglas basin, $L_x = 50.0$ cm long, $L_y = 2.54$ cm wide and $L_z = 10.0$ cm high. The cell was carefully machined on a plexiglas block to ensure parallelism of lateral walls. The basin is filled up to $H = 2$ cm in depth with a mixture of 252 cm³ of water, 2 cm³ of Kodak Photo Flo[®] 200² and some drops of black ink. The mixture is prepared a day before measurements are done. Free surface saturation with contaminants plays an important role for reproducibility [33].

The cell is driven sinusoidally by an electromechanical shaker lying on a three-point leveling system which allows longitudinal tilting (see Fig. 1). The tilt angle ϕ is considered positive for a counter-clockwise rotation of the cell with respect to the horizontal when visualized from the front. The shaker is fed with an amplified sine wave signal generated by a function/arbitrary waveform generator and a power amplifier. Thus, the cell vibration is along the axis of the shaker, with form $y(t) = A \sin(\omega t)$. Solitons can exist at frequencies $f = \omega/2\pi$ slightly below 11 Hz, and normalized accelerations $\Gamma = A\omega^2/g$ around 0.15. The basin acceleration is measured using a piezoelectric accelerometer attached to its bottom surface. It is connected to a signal conditioner, from which the acceleration signal is measured by a lock-in amplifier synchronized with the forcing signal (see Fig. 2a). Acceleration values are provided with precision of 0.001 g. An analog tilt sensor is also placed on the external bottom of the basin. This MEM device is connected to an analog/digital converter which measures angle values within an error of 0.01°.

Two different types of measurements are made on the free surface. Sequences of images taken with a high speed camera provide spatial measurements. On the other hand, local measurements are done using the phase fluctuations of the output signal of a resonant capacitive device.

² This chemical product creates a film which improves significantly wetting at the walls.

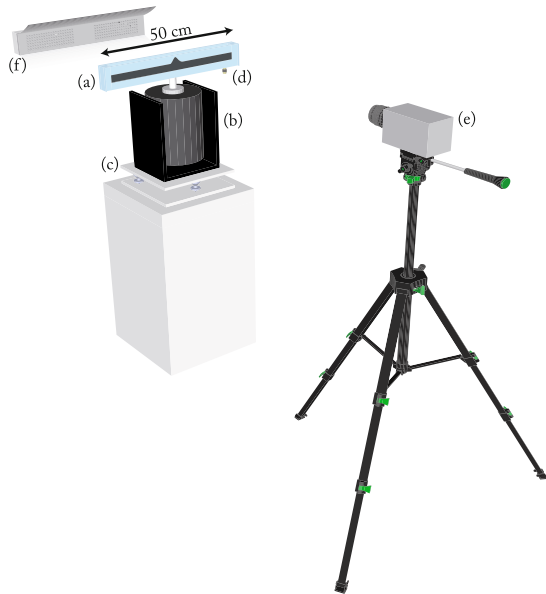


Fig. 1. (Color online) The basin filled with a dyed mixture of water and Kodak Photo Flo (a) is vibrated vertically by an electromechanical shaker. (b). The tilt angle ϕ can be controlled using a three-point level system. Positive ϕ means counter-clockwise rotation of the cell with respect to the horizontal when visualized from the front (c). Acceleration is measured using an accelerometer (d). A high speed camera (e) acquires images of the fluid illuminated from behind by an array of LED lamps (f).

2.1.1 Profile extraction from images

Figure 2a shows the general scheme of the devices involved in the image acquisition process. The basin is illuminated from behind with a LED array as it is shown in Figure 1. This allows a good contrast between the dyed mixture and the white background in the images. Imaging can also be synchronized with an external signal so stroboscopic sequences can be acquired. When this is done, the phase between the the forcing and the camera sync signal is fixed in such a way that the soliton seems to be steady at its maximum.

A Matlab program that uses an adaptive threshold finder³ detects the contact line between the free surface and the frontal wall from greyscale images. To increase vertical resolution, the algorithm interpolates the vertical position in the grey level domain to match a local threshold.

2.1.2 Local capacitive measurements

When an insulated thin wire is immersed in a conducting fluid, it behaves as an electrical cylindrical capacitor. The

³ By adaptive, we mean that background light local mean value is used for determining a local threshold.

capacity is proportional to the length of the fluid coating the wire. By means of this, a fixed wire can provide measurements of the fluid level at a single point of the horizontal domain.

Capacity fluctuations can be obtained by connecting the device to a RLC forced circuit (cf. Fig. 2b). When the fluid is in equilibrium, the frequency of the input signal can be tuned up into resonance, typically $f_{RLC} \approx 70$ kHz. At this point, the phase on the resistance voltage becomes linear to capacity variations. High sensitive response in the phase can be attained by choosing properly the circuit elements. In order to measure phase fluctuations, the output signal is connected to a Lock-In amplifier which is synchronized with the RLC circuit forcing input signal (see Fig. 2b).

2.2 Experimental results

We report measurements performed at a fixed vibration frequency $f = 10.4$ Hz and acceleration amplitudes around $\Gamma = 0.1$, region in which the existence and features of non-propagating hydrodynamic solitons have been studied in detail [21]. Typical tilt angles ϕ are between $\pm 1^\circ$.

2.2.1 Spatio-temporal diagrams

Figures 3a and 3b show spatio-temporal diagrams for two different solitons with different time scales and tilt angles. Contact line profiles are extracted using the procedure explained in 2.1.1 and plotted against time.

In Figure 3a, a soliton stands at a fixed position on the center of the basin. Here, $\phi = 0$ and $\Gamma = 0.088$. The camera acquisition rate is 400 Hz, so the soliton fast *sloshing* motion can be observed. However, motion beneath the water baseline cannot be detected as no contrast is available. Thus, the contact lines at the front and rear walls switch on the image at each half cycle.

Figure 3b shows a long-time acquisition for $\phi = -0.42^\circ$ and $\Gamma = 0.110$. The soliton was created at $t = 0$ and images were taken stroboscopically at a fixed rate of 650 mHz. The diagram shows the motion of the particle-type solution, in this case toward shallower regions. These dissipative solitons can be attracted to lateral boundaries and even pinned on them depending on the driving amplitude and frequency [34]. In this study, solitons remain far enough from lateral walls as they move across the principal axis. Lateral boundary effects are negligible if a soliton is a few centimeters apart from the wall.

The trajectories of the dissipative solitons reveal non-trivial time dependence. At a first stage, the center of the solution attains rapidly a constant speed. Wu et al. referred to this short-time scale stage in their work [32]. At a long-time scale stage, solitons converge to a fixed position rather than to a constant velocity as is clearly illustrated in Figure 3b.

Long-time acquisitions were strongly motivated by the fact that the initial velocity for short-time acquisition depends on the locus where the soliton is created. The break

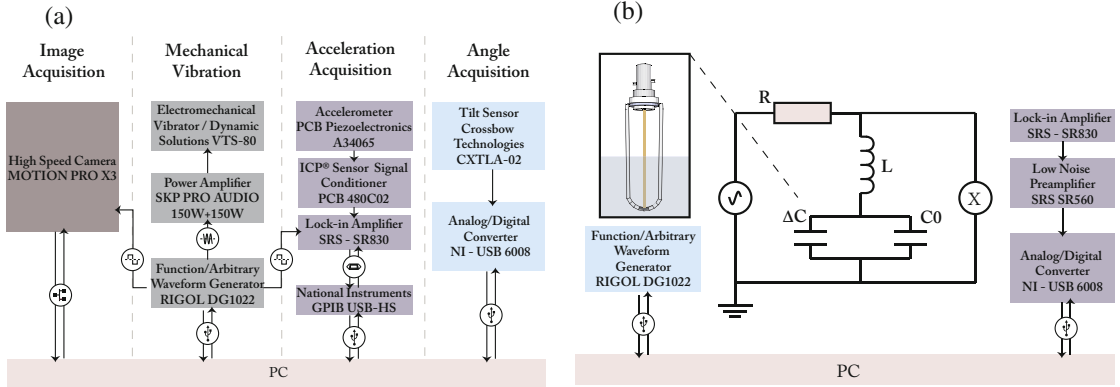


Fig. 2. (Color online) (a) The scheme shows the measurement procedures used for spatial acquisitions. (b) Local acquisitions scheme. The capacitor ΔC represents capacity fluctuations and can be negative. C_0 represents parasitic and zero-level capacity.

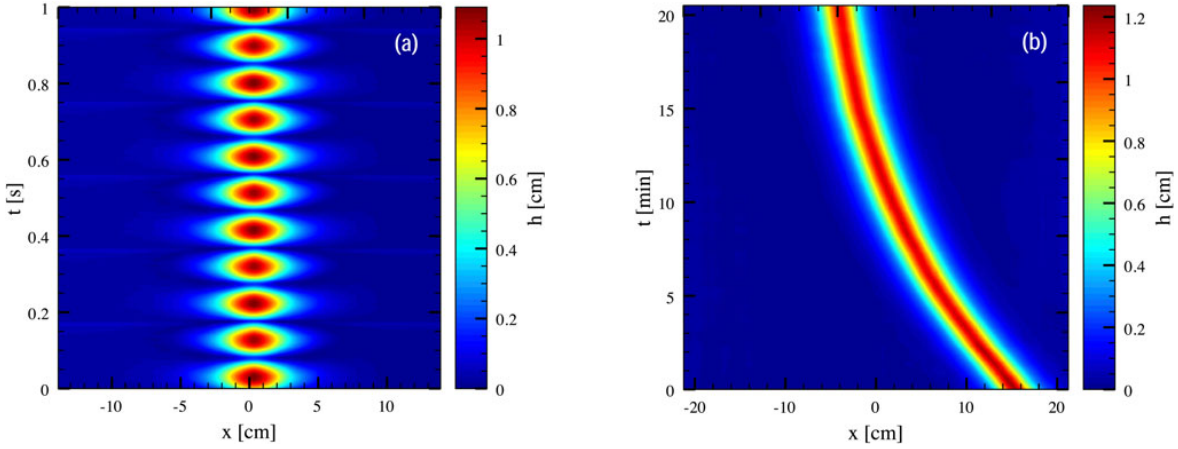


Fig. 3. (Color online) Spatio-temporal diagrams for solitons at different timescales. (a) A soliton *slashes* back and forth with half the driven frequency, at $\Gamma = 0.088$ and $\phi = 0$. (b) A soliton travels to a shallower region for $\phi = -0.42^\circ$ (clockwise rotation). Here, $f = 10.4$ Hz and $\Gamma = 0.110$. Images are taken stroboscopically when the soliton reaches its maximum after every eight cycles.

of translational symmetry suggests that the speed does not depend only on the depth gradient but also on the local depth.

2.2.2 Velocity vs. position

Soliton dynamics on tilted basins can be well understood by means of the velocity versus position plane. Figure 4a shows *phase plane tracks* for different solitons at different angles. Time series were run twice for each angle to check experimental reproducibility.

For each image sequence, the contact line profile is fitted using the 4-parameters function predicted by theory: $h(x) = A_s \operatorname{sech}[(x - x_o)/w] + h_0$ (see Sect. 3.1, Fig. 8 and Ref. [21]). The positions x_o plotted in Figure 4a are obtained from the parameter which represents the position at which maximum height takes place. Velocities, on the

other axis, are evaluated by differentiating smoothed position data with respect to time.

From the results obtained in the central area of the cell – where edge effects are negligible – the diagram shows that soliton are governed by the simple motion law (cf. Fig. 4a)

$$\dot{x}_0 = -\frac{1}{\tau(\phi)} [x_0 - P(\phi)], \quad (1)$$

where x_0 stands for the position of the maximum of the dissipative soliton, ϕ is the tilt angle of the basin, τ accounts for a relaxation time which characterizes the dynamics of x_0 , P/τ is a characteristic speed of propagation and P is the equilibrium position towards which the dissipative soliton converges.

The model (1) is invariant under spatial and time translations as expected. Lateral boundary effects appear as a change in the slope for positions above $|x_0| = 15$ cm (see Fig. 4a). This equation implies that solitons are

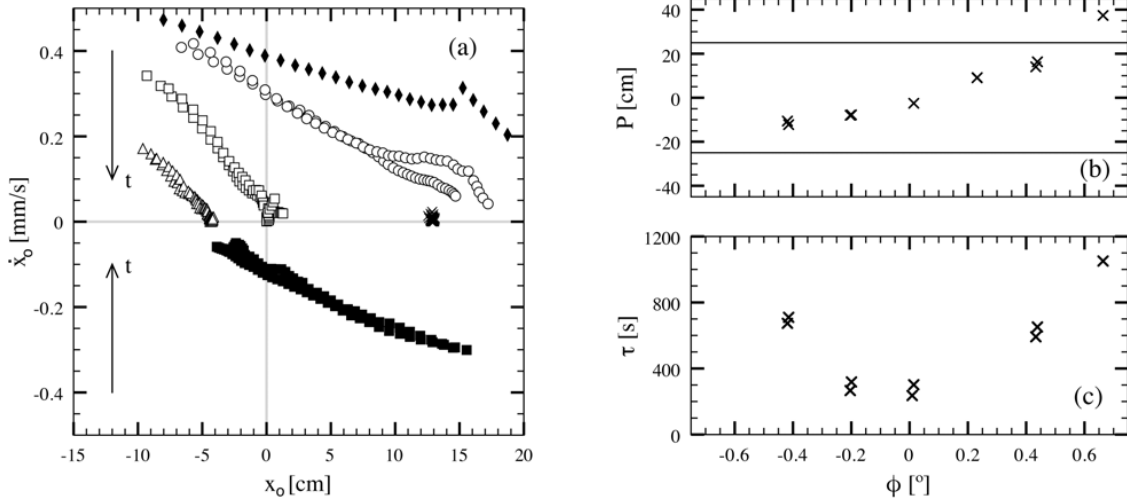


Fig. 4. (a) Soliton velocity \dot{x}_o versus position x_o plots for different tilt angles ϕ : -0.42° (\blacksquare), -0.20° (\triangle), -0.01° (\square), 0.23° (\times), 0.43° (\circ), 0.66° (\blacklozenge) at constant vertical $\Gamma = 0.131$. The arrows show time direction in the series of points. Solitons can propagate upward (\circ, \blacklozenge), downward ($\triangle, \square, \blacksquare$), or even stay at their position (\times), depending on their initial position with respect to equilibrium. Two experiments are shown for each angle except for $\phi = -0.66^\circ$ (\blacklozenge). (b) Equilibrium position versus tilt angle. P is located in shallower regions as ϕ increases. For $\phi = -0.66^\circ$ (\blacklozenge), the equilibrium position is *virtually* located beyond the basin edge (indicated by horizontal solid lines). (c) Position decay time τ dependence on ϕ . As ϕ increases, convergence to equilibrium position becomes slower. In (b) and (c) errorbars of each realization, obtained by confidence values of fitted parameters, are smaller than symbol size. The scatter of two data points for each angle show that the final errors due to reproducibility are of order of the symbol size.

attracted to an equilibrium position $P(\phi)$ following an exponential law.

Both the equilibrium position P and the exponential decay time τ depend on ϕ . As the tilt angle increases, the equilibrium position is pulled out from the center of the basin even surpassing the basin boundaries. Figure 4a shows phase-space tracks on which solitons get pinned at their equilibrium positions after moving *upward*⁴ or *downward*, respectively. Angle dependence of these two parameters is shown in Figure 4b. Note that the decay time τ is larger for larger angles. Dependence on the angle is plotted in Figure 4c.

2.2.3 Local shape

Solitons amplitude is very sensitive to the fluid depth in homogeneous layers ($\phi = 0$) as it is shown in Figure 5a (symbol \blacksquare).

When the basin is tilted, traveling solitons change as they move across the basin. Their amplitude decrease as they move to their equilibrium position. Two cases can be well identified depending on the tilt angle.

When the skew angle is higher than 1° so the equilibrium position is beyond lateral boundaries, the amplitude variations can be understood in terms of the local mean depth as it is shown in Figure 5 (symbols $\square, \triangle, \circ, \diamond$).

By contrast, when the tilt angle is small enough to allow equilibrium inside the boundaries (symbol $+$), the

amplitude dependence becomes non trivial. Solitons still decrease their amplitude as they move but dependence with local mean depth is not monotonic. Amplitude minimum occurs very close to equilibrium position.

Figure 6 shows soliton local mean phase θ as function of position for two tilt angles, $\phi = -2^\circ$ and $\phi = 2^\circ$. To measure θ , we obtain the maximum soliton height as a function of time $A_s(x_o, t)$ for two periods of oscillation while the soliton moves across the basin. This function is then fitted to $A_s(x_o)|\cos(\omega t + \theta)|$ for different soliton positions across the cell. Despite the large errorbars, a weak spatial dependence of θ is observed. Theoretically, local phase is related to the ratio μ/γ (see 3.1). The weak dependence of θ on x is consistent with the weak dissipation space dependence that will be presented below. However, a spatial dependence of γ can not be discarded completely.

2.2.4 Soliton parameters and physical quantities

Results have shown that solitons parameters: amplitude and phase have different behaviors when the soliton propagates. Amplitude variations are important while phase remains almost constant when the soliton moves. One is tempted to ask how physical quantities as dissipation rate and detuning are related to these parameters when motion occurs.

Soliton damping rate depends mainly on three mechanisms: viscous effects in the boundary layers at walls, at the free surface and capillary hysteresis at the contact

⁴ We define *upward* direction against depth gradient.

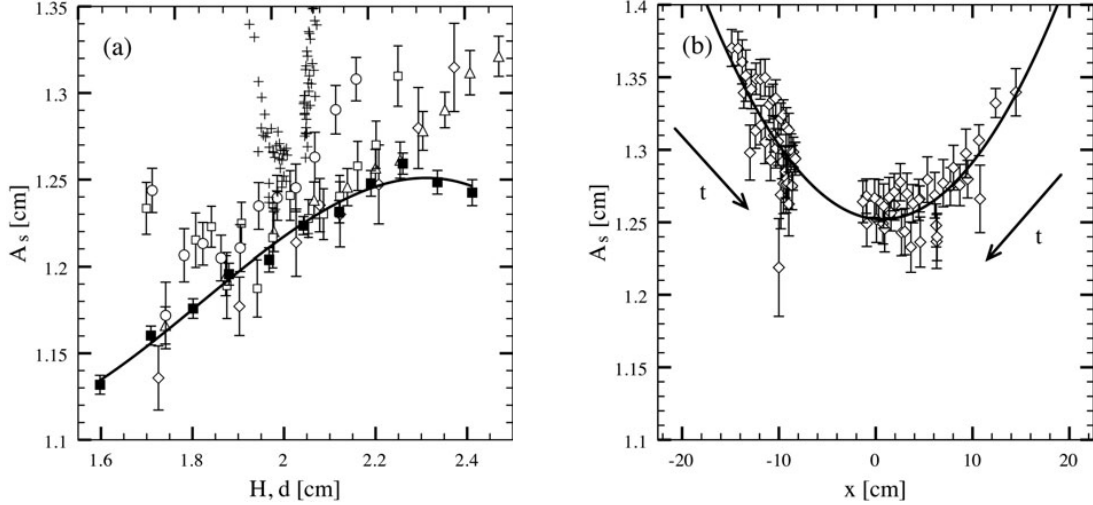


Fig. 5. (a) Soliton amplitude A_s versus fluid depth H for an homogeneous fluid layer ($\blacksquare, \phi = 0^\circ$). In addition, A_s versus the soliton local mean depth d (at each position as it moves toward its equilibrium) is plotted for different ϕ : -2.0° (\triangle), -1.0° (\square), 0.3° ($+$), 1° (\circ) and $+2^\circ$ (\diamond). Errorbars for $\phi = 0.3^\circ$ are shown in (b). In all the tilted cases, the solitons equilibrium positions are located beyond domain boundaries, except for $\phi = 0.3^\circ$. For all cases $f = 10.4$ Hz and $\Gamma = 0.117$. (b) Soliton amplitude versus position for $\phi = 0.3^\circ$. Here, the equilibrium position lies inside the basin. Consequently, A_s develops a minimum. Arrows indicate the time direction for each data set. Here, $f = 10.4$ Hz and $\Gamma = 0.121$. In both figures, solid lines are guides to the eye.

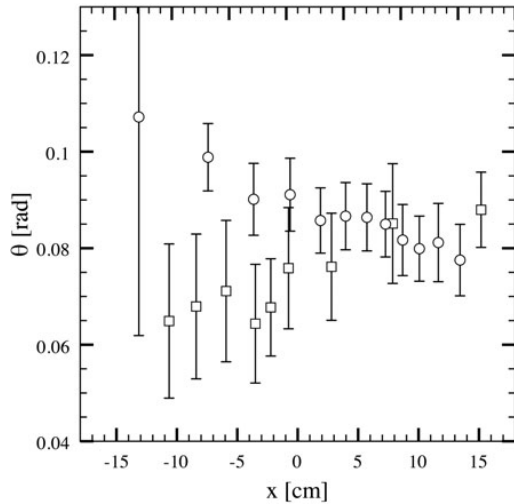


Fig. 6. Soliton local mean phase θ as function of position x for $\phi = -2^\circ$ (\circ) and $\phi = 2^\circ$ (\square) for $\Gamma = 0.118$. Errorbars are computed from confidence values of fitted parameters.

lines [33]. As water depth changes along the basin, dissipation may become non uniform as well.

To measure how dissipation changes along the basin for a fixed angle, local capacitive measurements are performed with the soliton placed at several positions. When the soliton is close enough to the capacitive sensor, the vibration of the basin is interrupted. The soliton amplitude decays exponentially to the flat state. The damping rate

is obtained by applying linear fits to data on the semilog plane. Figure 7a shows the damping factor for different positions with $\phi = -0.9^\circ$. Similar data have been obtained for the pattern state, Faraday waves, which coexists in the same region of parameters.

Experimental measurements of the soliton decay rates show high variance. This is due to the lack of a large enough separation of timescales of the different modes. Oscillation rate is just five times larger than the damping rate. In spite of this, Figure 7a shows that the damping rate for solitons is sensitive to tilting and has a tendency to decrease towards shallower water, at least more than Faraday waves damping rate.

The fact that damping rate (and dissipation) increases for increasing depth is consistent with Miles [33] dissipation estimations for homogeneous layers. His theoretical estimations for the three mechanisms point to different height dependences for each one of them: damping rate of viscous effects at the walls first decreases as function of H and then increases after a characteristic length; surface damping rate is a decreasing function of H ; finally, the contact line damping rate increases as function of H . Our results indicate that probably the first and third mechanisms are dominant. Miles also stresses the fact that the basin wall polishing has a strong effect on dissipation, which could explain the large scatter of damping rates across the cell and the correlation between lower and larger damping rates for solitons and Faraday waves.

Detuning is related with the forcing frequency and the natural frequency of the first transverse mode which supports the soliton. As this natural frequency depends on the fluid depth (see [33]), detuning may change across

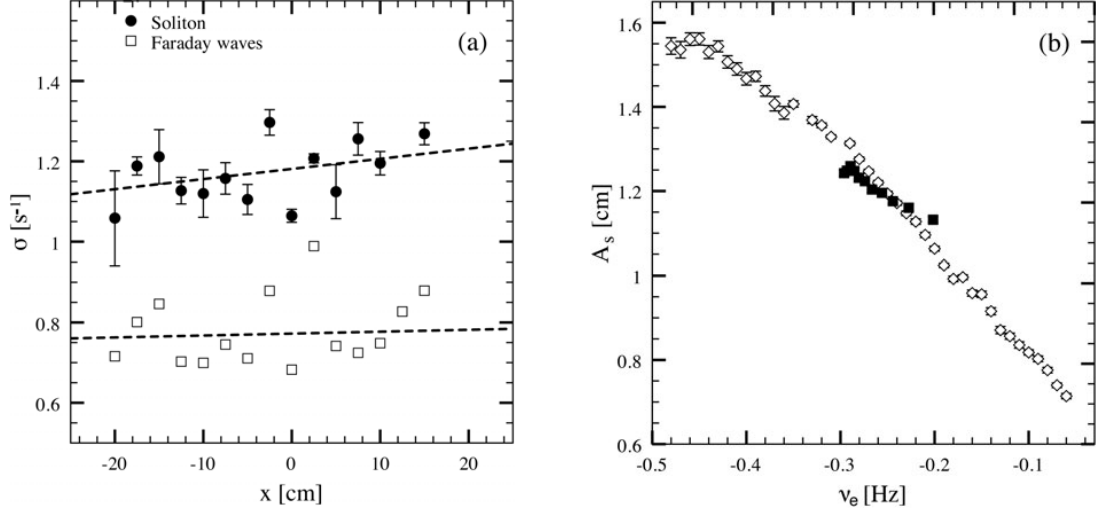


Fig. 7. (a) Amplitude damping rate versus position for Faraday waves (\square) and dissipative solitons (\bullet) for $\phi = -0.9^\circ$ and $\Gamma = 0.111$. Errorbars of soliton data are obtained from statistics of four acquisitions. Faraday waves damping rates were measured once. Solitons decay rate dependence on ϕ seems to be asymmetrical revealing non-homogeneity along the principal axis of the basin. (b) Soliton amplitude versus experimental detuning $\nu_e = f/2 - f_o$ for $\phi = 0^\circ$. Open symbols (\diamond) correspond to variations of forcing frequency f [$\nu_e = \nu_e(f)$]; solid symbols (\blacksquare) correspond to variations of fluid depth H [$\nu_e = \nu_e(H)$]. In the first case, $\Gamma = 0.125$, whereas for the second case, $\Gamma = 0.117$. The plot shows high sensitivity of A_s to detuning parameter ν_e .

the basin too. Detuning measurements are not performed directly. Instead, amplitude sensitivity to detuning parameter is measured.

Figure 7b presents the amplitude dependence on the experimental detuning $\nu_e = f/2 - f_o$ for an homogeneous layer at a fixed forcing amplitude. Here, f_o is the natural frequency of the first transverse mode ($f_o = 5.47$ Hz for $H = 2$ cm). f_o depends on the basin's geometry and layer depth H through the gravity wave dispersion relation

$$\omega_o^2 = gk \tanh(kH), \quad (2)$$

where $\omega_o = 2\pi f_o$. Thus, ν_e can be controlled by variation of f or H (symbols \diamond and \blacksquare respectively). In Figure 7b, the data obtained by varying H are the same as those presented in Figure 5a (\blacksquare). The agreement with the data obtained by changing f is quite good.

The importance of these physical quantities will be discussed in Section 4.

3 Theoretical description

The dynamics of a layer of incompressible fluid that is driven by a sinusoidal force with frequency Ω normal to the free surface is modeled by the dimensionless parametrically driven and damped nonlinear Schrödinger equation [19,20]

$$\partial_t \psi = -i\nu\psi - i|\psi|^2\psi - i\partial_{xx}\psi - \mu\psi + \gamma\bar{\psi}, \quad (3)$$

where the order of parameter $\psi(x, t)$ is a one dimensional complex field, and $\bar{\psi}$ stands for the complex conjugate

of ψ . The surface displacement from flat interface $h(x, t)$ and the velocity potential at the free surface $\phi(x, t)$ are slave variables which are of the form $h = \psi e^{-i\Omega t/2} + c.c.$ and $\phi(x, t) = -i\psi e^{-i\Omega t/2} + c.c.$, respectively (see [20] and references therein). The detuning parameter is ν , which is proportional to the difference between $\Omega/2$ and the resonant standing wave angular frequency. The damping parameter is μ , which is proportional to the kinematic viscosity of the fluid, which accounts for the dissipation mechanisms of the system and γ is the forcing acceleration amplitude. For $\mu = \gamma = \eta = 0$, equation (3) becomes the well-known nonlinear Schrödinger equation [1], which describes the envelope of an oscillatory system. This model is a time reversal Hamiltonian system with the transformation $\{t \rightarrow -t, \psi \rightarrow \bar{\psi}\}$. The terms proportional to μ and γ break the time reversal symmetry, and represent energy dissipation and injection, respectively. The higher-order terms in equation (3) are ruled out by a scaling analysis, since $\mu \ll 1$, $\nu \sim \mu \sim \gamma$, $|\psi| \sim \mu^{1/2}$, $\partial_x \sim \mu^{1/2}$, and $\partial_t \sim \mu^{1/2}$.

3.1 Dissipative solitons

A trivial state of equation (3) is the homogeneous state $\psi_0 = 0$, which represents the flat or quiescent solution of the fluid layer. For negative ν , the parametrically driven damped nonlinear Schrödinger equation exhibits localized states supported asymptotically by the quiescent state. In order to obtain these localized states we use the transformation $\psi(x, t) = R(x, t)e^{i\theta(x, t)}$. Then the parametrically

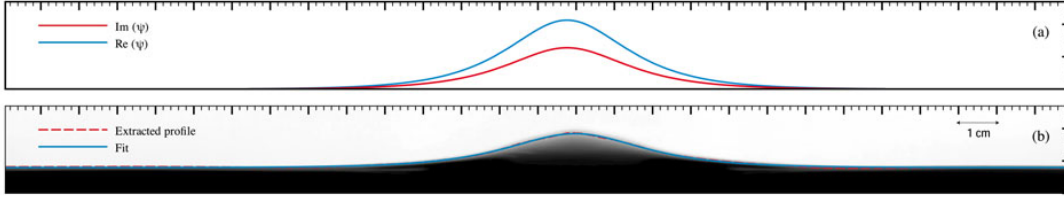


Fig. 8. (Color online) Dissipative soliton in parametrically resonant systems. (a) Stable dissipative soliton observed in the parametrically driven damped nonlinear Schrödinger equation model (3). (b) Snapshot of a non-propagating hydrodynamic soliton observed in a vertically driven 50 cm long and 2.54 cm wide rectangular container, filled with $H = 2$ cm of water. The solid blue and red curve are, respectively, instantaneous surface profile and fit $h(x) = A_s \operatorname{sech}[(x - x_0)/w] + h_0$. Adjusted relevant parameters are $A_s/H = 0.523 \pm 0.001$ and $w/H = 0.786 \pm 0.004$.

driven damped nonlinear Schrödinger equation reads

$$\begin{aligned} \partial_t R &= 2\partial_x R \partial_x \theta + \partial_{xx} R \theta - \mu R + \gamma R \cos(2\theta), & (4) \\ R \partial_t \theta &= -\nu R - R^3 - \partial_{xx} R + R(\partial_x \theta)^2 - \gamma R \sin(2\theta). & (5) \end{aligned}$$

A non trivial steady homoclinic solution – solutions that connect quiescent state with itself – of the previous model is (dissipative solitons, see [25] and references therein)

$$\cos(2\theta_0) = \frac{\mu}{\gamma}, \quad (6)$$

$$R_{\pm}(x) = \sqrt{2\delta_{\pm}} \operatorname{sech}\left(\sqrt{\delta_{\pm}}[x - x_0]\right), \quad (7)$$

where $\delta_{\pm} \equiv -\nu \pm \sqrt{\gamma^2 - \mu^2} = -\nu - \gamma \sin(2\theta_0)$. The amplitude and width of the dissipative solitons are characterized by $\sqrt{2\delta_{\pm}}$ and $1/\sqrt{\delta_{\pm}}$, respectively. As consequence of the spatial translation symmetry of model (3), the dissipative solitons are a family of states parameterized by a continuous parameter x_0 . This parameter stands for the position of the maximum of the localized state. Figure 8 shows a typical dissipative soliton observed in the parametrically driven damped nonlinear Schrödinger equation and the typical dissipative soliton observed experimentally, which shows a very good agreement with expression (7). Note that the above model has localized states if $\nu < 0$, $\gamma \geq \mu$ and $\gamma^2 < \mu^2 + \nu^2$. In this region, the relation $\cos(2\theta) = \mu/\gamma$ has four solutions in the interval $[-\pi, \pi]$. From this relation, one can infer that the localized states appear or disappear by simultaneous saddle-node bifurcations when $|\gamma| = \mu$. The quiescent state becomes unstable at $\gamma^2 = \mu^2 + \nu^2$, therefore the dissipative soliton becomes unstable at $\gamma^2 = \mu^2 + \nu^2$ with $\nu < 0$. The stable dissipative solitons are characterized by $\operatorname{Re}(\psi)\operatorname{Im}(\psi) > 0$, so both fields are simultaneously positive or negative [25]. Hence, there are two stable dissipative solitons, which are related by the reflection symmetry ($A \rightarrow -A$). These solutions correspond to dissipative solitons in phase or out of phase. From expression (7), one can infer that increasing the forcing amplitude γ , the amplitude and the width of stable dissipative soliton increases and decreases, respectively.

3.2 Effect of basin inclination

As mentioned in section 2.2.4. The inclination of the basin is responsible of inhomogeneous dissipation, injection and detuning (cf. Figs. 5–7). From Figure 7, we can infer that the non-propagating hydrodynamic soliton dissipates less energy in shallow water regions, but changes are small. Direct measurements of energy injection are difficult to realize. However, the local phase measurements (see Fig. 6) show that it does not exhibit significant changes along the channel. Thus, using the relation (5), we conclude that energy injection has a similar spatial behavior to energy dissipation. From the previous statement, considering the formula (7) and the behavior of the soliton amplitude as a function of channel position and detuning, we infer that the detuning has a convex behavior along the channel. In fact, this is a simple consequence of small tilting angles. The local depth can be considered as a function of space: $d(x) = H - x \tan(\phi)$. The correction can be considered as a small perturbation. A Taylor series expansion of ω_o from equation (2) shows that detuning will be a power series of x . The quadratic term turns out to be a good approximation for angles as large as 1° .

To account for these effects in our theoretical description, we consider that detuning, dissipation and injection of energy parameters in parametrically driven damped nonlinear Schrödinger equation become all inhomogeneous, i.e.

$$\begin{aligned} \mu(x) &= \mu + \mu_1(x), \\ \nu(x) &= \nu + \nu_1(x), \\ \gamma(x) &= \gamma + \gamma_1(x). \end{aligned}$$

For small tilt angles, the inhomogeneous terms can be considered as perturbations ($\mu_1(x) \ll 1$, $\gamma_1(x) \ll 1$ and $\nu_1(x) \ll 1$). Hence, equations (4) and (5) read

$$\begin{aligned} \partial_t R &= 2\partial_x R \partial_x \theta + \partial_{xx} R \theta - \mu R + \gamma R \cos(2\theta) \\ &\quad - \mu_1(x) R + \gamma_1(x) R \cos(2\theta), \\ R \partial_t \theta &= -\nu R - R^3 - \partial_{xx} R + R(\partial_x \theta)^2 - \gamma R \sin(2\theta) \\ &\quad - \nu_1(x) R - \gamma_1(x) R \sin(2\theta). \end{aligned} \quad (8)$$

One expects that for small angles, the dissipative solitons are persistent. However, inhomogeneity generates two effects: (i) localized states are modified by the perturbation,

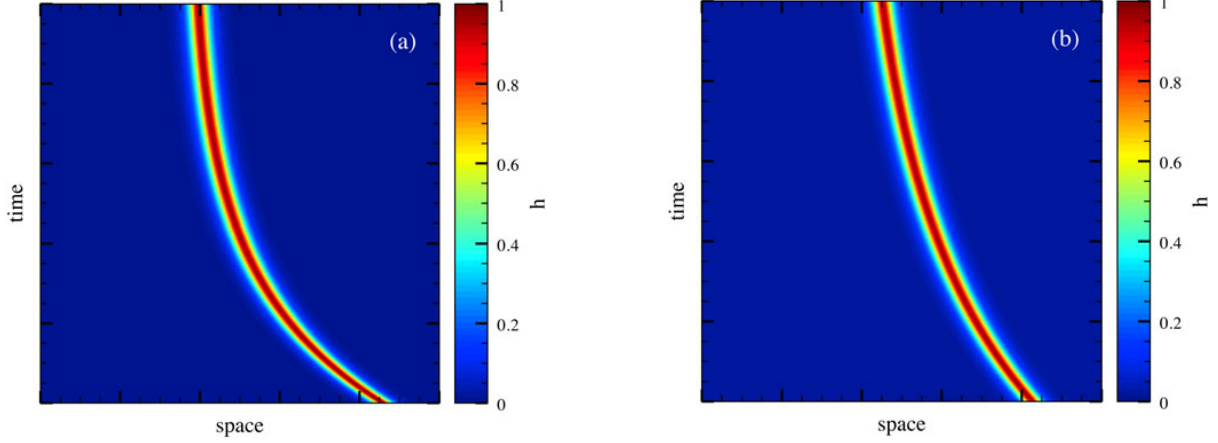


Fig. 9. (Color online) Spatio-temporal diagram of dissipative solitons obtained by numerical simulations of parametrically driven damped nonlinear Schrödinger equation model (3) over 250 points with periodic boundary conditions. The diagrams show 8400 cycles calculated with a time resolution of 1/200 period. (a) $\gamma(x) = 0.40$, $\nu(x) = -0.12 + 0.03x - 0.04x^2$, and $\mu(x) = 0.10$. (b) $\gamma(x) = 0.40$, $\nu(x) = -0.12 + 0.03x - 0.04x^2$, and $\mu(x) = 0.10 - 0.03x + 0.04x^2$.

and (ii) the spatial translational mode of the dissipative solitons – Goldstone mode – acquires a dynamic as a result of the translational symmetry breaking. Motivated by the experimental results, we have considered dissipation, injection and detuning with a quadratic profile along the basin. The space-time diagram of Figure 9 illustrates the typical behavior observed. The soliton propagates into an equilibrium position through a relaxation dynamics – that is, the soliton speed decays systematically until it finds an equilibrium position.

To account for these effects, we consider the following ansatz

$$R(x, t) = R_+(x - x_0(t)) + r(x, x_0),$$

$$\theta(x, t) = \theta_0 + \varphi(x, x_0),$$

where $r(x, x_0)$ and $\varphi(x, x_0)$ are the corrective functions, respectively. Besides, we consider the variable $x_0(t)$ as a slow variable, that is, $\ddot{x}_0 \ll \dot{x}_0 \ll 1$, where $\dot{x}_0(t)$ is the same order of the perturbation. Introducing the above expressions in the set of equations (8) and linearizing the perturbations functions, one finds at leading order

$$2\partial_x \varphi \partial_x R_+ + \partial_{xx} \varphi R_+ = 2\gamma \varphi \sin(2\theta_0) R_+ + \mu_1(x) R_+ - \gamma_1(x) \cos(2\theta_0) R_+ - \partial_z R_+ \dot{x}_0, \quad (9)$$

$$R_+ \partial_t \varphi = [-\nu - \gamma \sin(2\theta_0) - 3R_+^2 - \partial_{xx}] r - \nu_1(x) R_+ - 2\gamma R_+ \cos(2\theta_0) \varphi - \gamma_1(x) R_+ \sin(2\theta_0), \quad (10)$$

where $z \equiv x - x_0(t)$ is the coordinate in the co-moving frame. Multiplying equation (9) by the integral factor R_+

and after straightforward calculations, we obtain

$$\begin{aligned} \varphi(x) = & \int^x \frac{dx'}{R_+^2(x')} \int^{x'} dx'' [\mu_1(x'') - \gamma_1(x'')] R_+^2(x') \\ & + \int^x \frac{2\gamma \sin(2\theta_0) dx'}{R_+^2(x')} \int^{x'} dx'' \varphi(x'') R_+^2(x') \\ & - \int^x \frac{\dot{x}_0}{2} dx', \end{aligned} \quad (11)$$

which is a Fredholm integral equation for the field φ [35]. To solve the above integral equation, we consider the limit $\gamma \sin(2\theta_0) = \sqrt{\gamma^2 - \mu^2} \ll 1$, which is equivalent to consider similar injection and dissipation of energy ($\gamma \sim \mu$). Based on this assumption, we can use the approximation

$$\begin{aligned} \varphi \approx & \int^x \frac{dx'}{R_+^2(x')} \int^{x'} dx'' [\mu_1(x'') - \gamma_1(x'')] R_+^2(x') \\ & - \int^x \frac{\dot{x}_0}{2} dx'. \end{aligned} \quad (12)$$

It is important to note that one can iteratively calculate the corrections to the previous approximation in a power series in the small parameter $\sqrt{\gamma^2 - \mu^2}$ [35]. Introducing the linear operator

$$\mathcal{L} \equiv -\nu - \gamma \sin(2\theta_0) - 3R_+^2 - \partial_{xx},$$

equation (10) can be rewritten as

$$\mathcal{L} r = R_+ \partial_t \varphi + 2\gamma R_+ \cos(2\theta_0) \varphi + \nu_1 R_+. \quad (13)$$

To solve this linear equation, we use the Fredholm alternative [2]. Accordingly, we introduce the following inner product

$$\langle f|g \rangle = \int_{-\infty}^{\infty} f(x)g(x) dx.$$

The linear operator \mathcal{L} is self-adjoint ($\mathcal{L} = \mathcal{L}^\dagger$) under this definition. The kernel of this linear operator – the set of functions $\{v\}$ that satisfy $\mathcal{L}v = 0$ – is of dimension 1. As a result of spatial translation invariance, one has $\mathcal{L}\partial_x R_+ = 0$. Therefore, the field r has a solution if the following condition is satisfied⁵

$$0 = \langle \partial_x R_+ | R_+ \partial_t \varphi + 2\gamma R_+ \cos(2\theta_0) \varphi + \nu_1(x) R_+ \rangle. \quad (14)$$

Using the approximation (12), and considering the dominant terms and after straightforward calculations, yields to

$$\begin{aligned} \dot{x}_0 = & \frac{1}{\int_{-\infty}^{\infty} dx \partial_x R_+^2(x) x} \left[2 \int_{-\infty}^{\infty} dx \partial_x R_+^2(x) \int^x dx' \frac{1}{R_+^2(x')} \right. \\ & \times \int^{x'} dx'' (\mu_1(x'') - \gamma_1(x'')) R_+^2 \\ & \left. + \int_{-\infty}^{\infty} dx \partial_x R_+^2 \cdot \frac{\nu_1(x)}{\mu} \right]. \quad (15) \end{aligned}$$

This expression gives us information of the dynamics of dissipative soliton as a function of spatial disturbance. For small angles and considering the experimental observations, we can consider as a first approximation

$$\begin{aligned} \mu(x) &= \mu + \bar{\mu}_1 x + \bar{\mu}_2 x^2, \\ \gamma(x) &= \gamma + \bar{\gamma}_1 x + \bar{\gamma}_2 x^2, \\ \nu(x) &= \nu + \bar{\nu}_1 x + \bar{\nu}_2 x^2. \end{aligned}$$

The experimental results allow us to infer that the coefficients $\bar{\mu}_2, \bar{\gamma}_2$ are small, and that $\bar{\nu}_2$ is not small. Then, formula (15) can be rewritten

$$\begin{aligned} \dot{x}_0 = & \frac{1}{\int_{-\infty}^{\infty} dx \partial_x R_+^2(x) x} \left[2 \int_{-\infty}^{\infty} dx \partial_x R_+^2 \int^x dx' \frac{1}{R_+^2} \right. \\ & \times \int^{x'} dz (\bar{\mu}_1 - \bar{\gamma}_1) z R_+(z)^2 + \int_{-\infty}^{\infty} dz \partial_z R_+(z)^2 \frac{\bar{\nu}_1}{\gamma} z \\ & + \left\{ 4 \int_{-\infty}^{\infty} dx \partial_x R_+^2 \int^x dx' \frac{1}{R_+^2} \right. \\ & \times \int^{x'} dz (\bar{\mu}_2 - \bar{\gamma}_2) z R_+(z)^2 \\ & \left. \left. + 2 \int_{-\infty}^{\infty} dz \partial_z R_+(z)^2 \cdot \frac{\bar{\nu}_2}{\gamma} z \right\} x_0(t) \right]. \quad (16) \end{aligned}$$

⁵ This is known as the solvability condition or Fredholm alternative.

Consequently, the position of the maximum of the dissipative soliton is ruled by equation (1), where

$$\begin{aligned} \tau^{-1} = & \frac{1}{\int_{-\infty}^{\infty} dx \partial_x R_+^2(x) x} \left[4 \int_{-\infty}^{\infty} dx \partial_x R_+^2 \int^x dx' \frac{1}{R_+^2} \right. \\ & \times \int^{x'} dz (\bar{\mu}_2 - \bar{\gamma}_2) z R_+(z)^2 \\ & \left. + 2 \int_{-\infty}^{\infty} dz \partial_z R_+(z)^2 \frac{\bar{\nu}_2}{\gamma} z x_0(t) \right], \\ P = & \frac{\tau}{\int_{-\infty}^{\infty} dx \partial_x R_+^2(x) x} \left[2 \int_{-\infty}^{\infty} dx \partial_x R_+^2 \int^x dx' \frac{1}{R_+^2} \right. \\ & \left. \times \int^{x'} dz (\bar{\mu}_1 - \bar{\gamma}_1) z R_+(z)^2 + \int_{-\infty}^{\infty} dz \partial_z R_+(z)^2 \frac{\bar{\nu}_1}{\gamma} z \right]. \end{aligned}$$

Therefore, model (1) allows us to capture the dynamics of dissipative solitons observed experimentally in the forced tilted basin with water and numerical simulations of the equation parametrically driven damped nonlinear Schrödinger equation. Figure 9 presents numerical simulation results obtained considering a quadratic dependence on space for both detuning and dissipation. The dynamic evolution shown by these numerical simulations agree very well with experimental results.

It is important to note that when injection and dissipation of energy are of the same order, the system is well described by model (1). However, phase does not exhibit significant corrections in comparison with the maximum amplitude of the soliton. This is consistent with experimental observations.

4 Conclusions

Localized structures are ubiquitous in nature. During the last decade, a constant effort has been focused on the creation mechanisms and features of localized states. Undoubtedly, the next step to boost their potential applications is to advance the manipulation and control of these particle-type solutions. Here, we have presented a theoretical and experimental study of a method of manipulation and control of hydrodynamic solitons in a vertically driven rectangular water basin, based on the tilting of the system.

Experimentally, for a given tilt angle, solitons travel to equilibrium positions through a relaxation process. Long acquisitions are required to observe this behavior, because of the large decay time of the velocity. The equilibrium position depends on the tilt angle, and can be pushed out of the basin if the angle is large enough.

In this system, dissipation, energy injection and detuning are inhomogeneous. Dissipation grows in the direction of depth gradient, but changes are small. Indirect evidence from soliton local phase indicates that energy injections varies less or similarly than dissipation. In contrast, the detuning exhibits a convex behavior along the channel and has shown to have a strong effect on soliton dynamics.

Close to the parametric resonance, the parametrically driven damped nonlinear Schrödinger equation models

this system. The effects of the tilting of the basin are incorporated into this model through space-dependent dissipation, energy injection and detuning. We have deduced an equation for the position of hydrodynamic solitons. This equation is characterized by two terms: a constant speed and a linear relaxation term. The theoretical description reproduces well the hydrodynamic soliton dynamics observed experimentally.

We gratefully acknowledge S. Coulibaly for fruitful discussions. M.G.C. is thankful for the financial support of FONDECYT project 1090045. L.G. thanks the grant support of CONICYT. The authors are also grateful for the fundings of ACT project 127.

References

1. A.C. Newell, *Solitons in Mathematics and Physics* (Society for Industrial and Applied Mathematics, Philadelphia, 1985)
2. See, e.g., L.M. Pismen, *Patterns and Interfaces in Dissipative Dynamics* (Springer Series in Synergetics, Berlin Heidelberg, 2006), and references therein.
3. M. Cross, H. Greenside, *Pattern Formation and Dynamics in Nonequilibrium Systems* (Cambridge University Press, New York, 2009)
4. P. Couillet, *Int. J. Bifur. Chaos* **12**, 2445 (2002)
5. W. van Saarloos, P.C. Hohenberg, *Phys. Rev. Lett.* **64**, 749 (1990)
6. P.D. Woods, A.R. Champneys, *Physica D* **129**, 147 (1999)
7. G.W. Hunt, G.J. Lord, A.R. Champneys, *Comput. Methods Appl. Mech. Eng.* **170**, 239 (1999)
8. M.G. Clerc, C. Falcon, *Physica A* **356**, 48 (2005)
9. U. Bortolozzo, M.G. Clerc, C. Falcon, S. Residori, R. Rojas, *Phys. Rev. Lett.* **96**, 214501 (2006)
10. O. Thual, S. Fauve, *J. Phys. (Paris)* **49**, 1829 (1988)
11. O. Thual, S. Fauve, *Phys. Rev. Lett.* **64**, 282 (1990)
12. V. Hakim, Y. Pomeau, *Eur. J. Mech. B* **S10**, 137 (1991)
13. M. Clerc, P. Couillet, E. Tirapegui, *Phys. Rev. Lett.* **83**, 3820 (1999)
14. M. Clerc, P. Couillet, E. Tirapegui, *Opt. Commun.* **167**, 159 (1999)
15. M. Clerc, P. Couillet, E. Tirapegui, *Prog. Theor. Phys.* **S139**, 337 (2000)
16. M. Clerc, P. Couillet, E. Tirapegui, *Int. J. Bifur. Chaos* **11**, 591 (2001)
17. M.G. Clerc, P. Encina, E. Tirapegui, *Int. J. Bifur. Chaos* **18**, 1905 (2008)
18. I.V. Barashenkov, E.V. Zemlyanaya, *Phys. Rev. Lett.* **83**, 2568 (1999)
19. J.W. Miles, *J. Fluid Mech.* **148**, 451 (1984)
20. W. Zhang, J. Viñal, *Phys. Rev. Lett.* **74**, 690 (1995)
21. M.G. Clerc, S. Coulibaly, N. Mujica, R. Navarro, T. Sauma, *Phil. Trans. R. Soc. A* **367**, 3213 (2009)
22. B. Denardo, B. Galvin, A. Greenfield, A. Larraza, S. Putterman, W. Wright, *Phys. Rev. Lett.* **68**, 1730 (1992)
23. J.N. Kutz, W.L. Kath, R.D. Li, P. Kumar, *Opt. Lett.* **18**, 802 (1993)
24. S. Longhi, *Phys. Rev. E* **53**, 5520 (1996)
25. I.V. Barashenkov, M.M. Bogdan, V.I. Korobov, *Europhys. Lett.* **15**, 113 (1991)
26. M.G. Clerc, S. Coulibaly, D. Laroze, *Phys. Rev. E* **77**, 056209 (2008)
27. M.G. Clerc, S. Coulibaly, D. Laroze, *Int. J. Bifur. Chaos* **19**, 2717 (2009)
28. M.G. Clerc, S. Coulibaly, D. Laroze, *Physica D* **239**, 72 (2010)
29. N.V. Alexeeva, I.B. Barashenkov, G.P. Tsironis, *Phys. Rev. Lett.* **84**, 3053 (2000)
30. M.G. Clerc, S. Coulibaly, D. Laroze, *Int. J. Bifur. Chaos* **19**, 3525 (2009)
31. E. Caboche, F. Pedaci, P. Genevet, S. Barland, M. Giudici, J. Tredicce, G. Tissoni, L.A. Lugiato, *Phys. Rev. Lett.* **102**, 163901 (2009)
32. J. Wu, R. Keolian, I. Rudnick, *Phys. Rev. Lett.* **52**, 1421 (1984)
33. J.W. Miles, *Proc. Roy. Soc. A* **297**, 459 (1967)
34. W. Wei, W. Xinlong, W. Junyi, W. Rongjue, *Phys. Lett. A* **219**, 74 (1996)
35. G. Arfken, H. Weber, *Mathematical Methods for Physicists* (Elsevier Academic Press, Burlington, 2001).

A.2 Dissipative localized states with shieldlike phase structure

Marcel G. Clerc, Saliya Coulibaly, Mónica A. Garcia-Nústes, and Yair Zárate

Physical Review Letters 107, 254102 (2011) DOI: 10.1103/PhysRevLett.107.254102

Abstract

A novel type of parametrically excited dissipative solitons is unveiled. It differs from the well-known solitons with constant phase by an intrinsically dynamical evolving shell-type phase front. Analytical and numerical characterizations are proposed, displaying quite a good agreement. In one spatial dimension, the system shows three types of stationary solitons with shell-like structure whereas in two spatial dimensions it displays only one, characterized by a π -phase jump far from the soliton position.

Dissipative Localized States with Shieldlike Phase Structure

Marcel G. Clerc,¹ Saliya Coulibaly,² Mónica A. Garcia-Ñustes,¹ and Yair Zúrate¹

¹*Departamento de Física, Facultad de Ciencias Físicas y Matemáticas, Universidad de Chile, Casilla 487-3, Santiago, Chile*
²*Laboratoire de Physique des Lasers, Atomes et Molécules, CNRS UMR 8523, Université des Sciences et Technologies de Lille–59655 Villeneuve d'Ascq Cedex, France, EU*

(Received 30 June 2011; published 14 December 2011)

A novel type of parametrically excited dissipative solitons is unveiled. It differs from the well-known solitons with constant phase by an intrinsically dynamical evolving shell-type phase front. Analytical and numerical characterizations are proposed, displaying quite a good agreement. In one spatial dimension, the system shows three types of stationary solitons with shell-like structure whereas in two spatial dimensions it displays only one, characterized by a π -phase jump far from the soliton position.

DOI: 10.1103/PhysRevLett.107.254102

PACS numbers: 05.45.Yv, 89.75.Kd

Macroscopic systems maintained out of equilibrium are characterized by the possibility of the emergence of particle-type solutions or localized states. These states have been observed in different fields such as magnetic materials, liquid crystals, gas discharge, chemical reactions, fluids, granular media, and nonlinear optics media, among others (see the reviews [1–3], and references therein). Although these states are spatially extended, they exhibit properties typically associated with particle-like states. Consequently, one can characterize them with a family of continuous parameters such as position, amplitude, and width. For time-reversible systems where injection and dissipation of energy can be viewed as perturbations—quasireversible systems [4]—the prototype model that exhibits localized states is the parametrically driven damped nonlinear Schrödinger equation [5]. This model has been derived in several contexts to describe the appearance of patterns and localized structures, such as vertically vibrated Newtonian fluid layers [6], nonlinear lattices [7], optical fibers [8], Kerr type optical parametric oscillators [9], easy-plane ferromagnetic materials exposed to an oscillatory magnetic field [10], and a parametrically driven damped chain of pendula [11]. One of the greatest benefits of this model is to present analytical solutions for localized states characterized by a constant phase and a bell-like shape for the amplitude [10].

In this Letter, we show that localized states of quasireversible parametric systems present an unexpectedly rich phase front dynamics. More precisely, the stationary localized states have a shell-type structure in the phase, for a large range of parameters. These stable structures are of three types. We term these solutions phase shielding solitons. Using the asymptotic amplitude equation, valid far from the position of the localized states, we determine analytically the shape of phase fronts and its dynamics. This dynamics is characterized by the juxtaposition of two forces, one due to relative stability between the phases and the other related to spatial variations of the tail of the dissipative soliton. As a result of this force balance, these

localized states exhibit a phase structure that shields the soliton. Numerical simulations show quite good agreement with our analytical predictions.

The envelope of an oscillation for extended conservative systems in the presence of small energy injection through a parameter modulation and energy dissipation—via damping phenomena—is described by the parametrically driven damped nonlinear Schrödinger equation

$$\partial_t \psi = -i\nu\psi - i|\psi|^2\psi - i\partial_{xx}\psi - \mu\psi + \gamma\bar{\psi}, \quad (1)$$

where the envelope $\psi(x, t)$ is a one-dimensional complex field, $\bar{\psi}$ stands for the complex conjugate of ψ , and $\{x, t\}$ describe, respectively, the spatial and temporal coordinates. The detuning parameter is ν , which is proportional to the difference between half of the forcing frequency and the natural frequency of the oscillator field. μ is the damping parameter, and γ stands for the forcing amplitude of the parametric forcing. The higher-order terms in Eq. (1) are ruled out by a scaling analysis, since $\mu \ll 1$, $\nu \sim \mu \sim \gamma$, $|\psi| \sim \mu^{1/2}$, $\partial_x \sim \mu^{1/2}$, and $\partial_t \sim \mu^{1/2}$.

Introducing the following change of variables $\psi = R(x, t)e^{i\varphi(x, t)}$ in Eq. (1), the model reads

$$\partial_t R = 2\partial_x R \partial_x \varphi + R \partial_{xx} \varphi - \mu R + \gamma R \cos(2\varphi), \quad (2)$$

$$\partial_t \varphi = -\nu - R^2 - \frac{\partial_{xx} R}{R} + (\partial_x \varphi)^2 - \gamma \sin(2\varphi), \quad (3)$$

where R and φ stand for the amplitude and phase of ψ , respectively. The previous set of equations in the region of parameters $-\nu - \sqrt{\gamma^2 - \mu^2} \geq 0$, exhibit stationary dissipative solitons of the form $R_s(x, x_0) = \sqrt{2\delta} \operatorname{sech}(\sqrt{\delta}[x - x_0])$ and $\varphi_s = \arccos(\mu/\gamma)/2$ with $\delta \equiv -\nu + \sqrt{\gamma^2 - \mu^2}$ [10] [see Fig. 1(a)]. Hence, the localized states are defined as having a bell shape in the modulus and a constant phase. However, when we try to observe the previous solution, numerical simulations show that an unexpected and rich phase dynamics arises. Such dynamics initially establishes a bell shape in the modulus

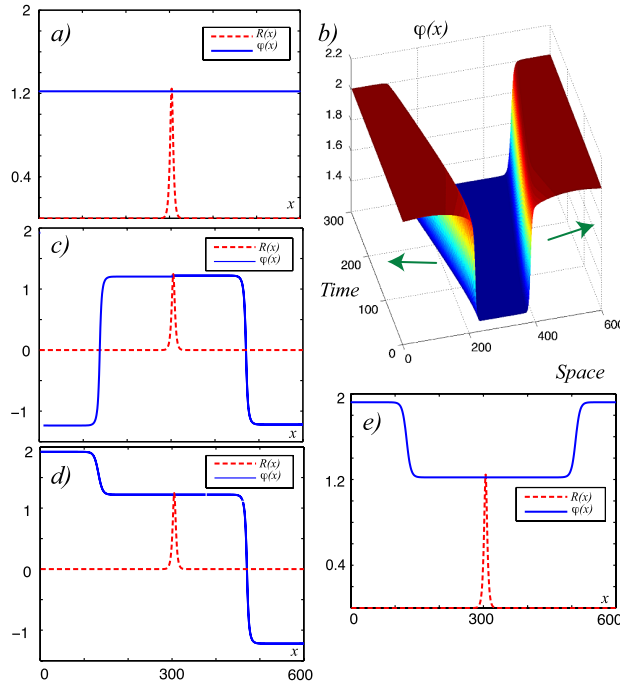


FIG. 1 (color online). Solitons in the parametrically driven damped nonlinear Schrödinger equation: (a) soliton with constant phase; (b) space-time diagram for the phase $\varphi(x, t)$ of Eq. (1) with $\gamma = 0.123$, $\nu = -0.093$, and $\mu = 0.100$; (c), (d), and (e) solitons with phase shell-like structure obtained numerically from Eq. (1) for $\gamma = 0.083$, $\nu = -0.063$, and $\mu = 0.058$.

of the amplitude. Then, a constant phase appears around the position of the localized state. At a latter stage, after some intricate transients, a pair of fronts that connect different phase equilibrium emerge. These equilibria are characterized by $\cos(2\varphi_0) = \mu/\gamma$. Finally, a rather slow dynamics of phase front propagation is established, which ends with the formation of a pair of stationary fronts that connect steady states. Figure 1(b) illustrates the above described time evolution of phase dynamics. The system has four phase equilibria in the range from $-\pi$ to π . Therefore, the stable dissipative solitons have three types of shell-like phase structures. Figures 1(c)–1(e) outline these solutions. Because of the fact that the function $\cos(2\varphi)$ has period π , the phase difference at the ends of the dissipative soliton can be zero or π (cf. Fig. 1). Thus, this last localized state is characterized by a phase difference given by zero around the core and π at the ends. It is important to mention that dissipative solitons represented in Figs. 1(a), 1(c), and 1(e), are homoclinic orbits for the spatial system in polar representation $\{R, \varphi\}$. However, the dissipative soliton shown in Fig. 1(d) corresponds to a heteroclinic solution. In Cartesian representation $\{\text{Re}(A), \text{Im}(A)\}$ all these solutions correspond to homoclinic orbits.

For the purpose of understanding and capturing the wealth of these phase front solutions, let us consider

Eq. (1) in a semi-infinite domain, with zero flux boundary conditions. The system can exhibit a dissipative soliton located at one edge, with the phase formed by a single front [see Fig. 2(a)]. In addition it is worth noting that these phase fronts emerge at a distance far from the core of the soliton, i.e., at a distance much larger than $1/\sqrt{\delta}$. Accordingly, $R(x, x_0) \approx 2\sqrt{2\delta}e^{-\sqrt{\delta}(x-x_0)}$ for $x - x_0 \gg 0$, with x_0 at the left edge of the region of interest. Together with Eq. (2) this approximation leads to the following Newton-type equation

$$\partial_{xx}\varphi = 2\sqrt{\delta}\partial_x\varphi + \mu - \gamma\cos(2\varphi). \quad (4)$$

This equation has heteroclinic solutions corresponding to phase fronts, which analytically are well described by

$$\varphi_F(x, x_f) \approx \arctan\left[\sqrt{\frac{\gamma + \mu}{\gamma - \mu}} \tanh\frac{\sqrt{\gamma^2 - \mu^2}(x - x_f)}{2\sqrt{\delta}}\right], \quad (5)$$

where x_f accounts for the position of phase front, i.e., the point at which the spatial derivative of the phase front has its global maximum. Thus, the phase front solutions are parametrized by a continuous parameter x_f . Figure 2 shows the numerically computed phase fronts, which present a difference of 1% with respect to expression (5). Notice that if one considers the first correction to the previous equation $\varphi \approx \varphi_F + \partial_x\varphi_F/2\sqrt{\delta}$ this difference decreases to 0.8%.

As it can be also seen from Fig. 2(b), this front displays an unexpected dynamical behavior characterized by a non-uniform translation. To describe this dynamics, we promote the front position to a time-dependent function $x_f(t)$. Hence, using Eq. (3) and formula (5), we obtain

$$-\dot{x}_f\partial_x\varphi_F = -(\nu + \delta) - 8\delta e^{-2\sqrt{\delta}x} + (\partial_x\varphi_F)^2 - \gamma\sin(2\varphi_F), \quad (6)$$

where \dot{x}_f stands for the time derivative of x_f . Multiplying the above equation by $\partial_z\varphi_F$ with $z \equiv x - x_f$, and introducing the following inner product $\langle f|g \rangle \equiv \int fg dz$, we obtain the following equation for the phase front after straightforward calculations,

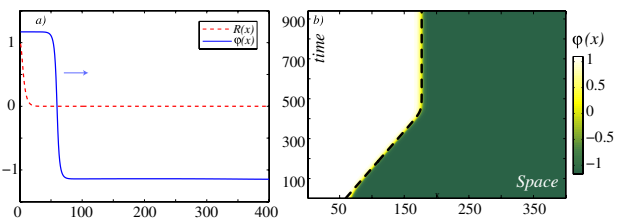


FIG. 2 (color online). Phase propagation: (a) phase front profile considering half of the dissipative soliton; (b) spatiotemporal diagram of phase front obtained from Eq. (1) by $\gamma = 0.083$, $\nu = -0.063$, and $\mu = 0.058$. The dashed curve is the numerical solution obtained using Eq. (7).

$$\dot{x}_f = A + B e^{-2\sqrt{\delta}x_f}, \quad (7)$$

where

$$A \equiv \frac{\langle (\nu + \delta + \gamma \sin(2\varphi_F) - (\partial_z \varphi_F)^2) | \partial_z \varphi_F \rangle}{\langle \partial_z \varphi_F | \partial_z \varphi_F \rangle},$$

$$B \equiv 8\delta \frac{\langle e^{-2\sqrt{\delta}z} | \partial_z \varphi_F \rangle}{\langle \partial_z \varphi_F | \partial_z \varphi_F \rangle}$$

are real numbers, which can be either positive or negative depending on the shape of the phase front. For example, when one considers a front that increases monotonically with the spatial coordinate, A (B) is a negative (positive) constant. The term proportional to A accounts for the constant speed at which the larger phase invades the smaller value. This speed can be understood as a consequence of the energy difference between these states. Hence, this term gives rise to phase fronts propagating towards the soliton position. Conversely, the term proportional to B accounts for the effect of spatial variation of the tail of the amplitude soliton, which induces a force that leads to phase fronts moving away from the localized state. Consequently, the superposition of these two opposing forces generates a stable equilibrium for the position of the phase front, which is consistent with the dynamics illustrated in the space-time diagram in Fig. 2. The dashed curve in Fig. 2(b) represents the solution obtained from Eq. (7), using the above formulas A and B . Modifying the parameters, we observe that as γ increases the equilibrium position is smaller; i.e., the shell-type structure surrounding the soliton decreases. Instead, as ν increases the equilibrium position of the phase front also grows.

Considering now the soliton located at the center of the spatial region, a small disturbance on the system produces some complex transients on the phase dynamics, ending by the formation of a pair of fronts propagating in opposite directions away from the soliton core. The dynamics of these fronts differs from that of the single front by the inclusion of an interaction process which decays exponentially with the distance between the fronts. As the system displays two types of phase fronts monotonically increasing or decreasing, then the soliton exhibits three different types of shield structures in its phase, as shown in Fig. 1. Hence, the dissipative solitons in parametrically driven systems have a rich dynamics of phase fronts.

To understand the correspondence between the constant phase solitons and phase shielding solitons, we have performed a numerical linear stability analysis similar to the one made in Ref. [12], considering both the control parameters and size of the system L . When L is small enough the spectrum—set of eigenvalues associated with the linear stability analysis—is characterized by being centered on an axis parallel to the imaginary one [cf. Fig. 3(b)], where every single eigenvalue has negative real part. Increasing L the set of eigenvalues begin to collide creating a curve of eigenvalues (a continuum). For a critical value of L this

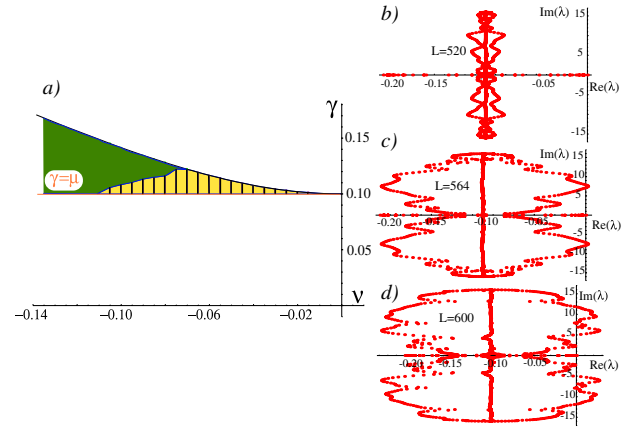


FIG. 3 (color online). Stability of solitons: (a) schematic representation of bifurcation diagram in the $\gamma - \nu$ space for $\mu = 0.050$, the shaded region corresponds to the phase shielding soliton region, and the striped area is the region of soliton with constant phase. (b), (c), and (d) are the spectra of the soliton with constant phase before (system size $L = 520$), during ($L = 564$), and after ($L = 600$) the bifurcation, respectively, for $\gamma = 0.263$, $\mu = 0.050$, and $\nu = -0.083$.

curve collides with the imaginary axis at a nonzero frequency [cf. Fig. 3(c)]. Therefore the system exhibits an Andronov-Hopf bifurcation. Figure 3 outlines the spectrum before, during, and after the bifurcation.

From previous numerical analysis, one can infer that the soliton with homogeneous phase is unstable, over a wide parameter region, for sufficiently large values of L . In short, there exists a critical value of L for which the soliton with constant phase is unstable to small perturbations in phase and amplitude. Because of the analytical complexity of this analysis, we have only determined numerically this critical value. For a system size smaller than the critical one, we observe that for parameters $0 < \gamma - \mu \ll 1$, the soliton with constant phase is stable. Increasing the forcing amplitude γ , the soliton becomes unstable by an Andronov-Hopf bifurcation similar to the one shown in Fig. 3. This figure illustrates the region in parameter space where this solution is stable and unstable. In the shaded region in Fig. 3, we found stable phase shielding solitons.

To study the robustness of the phase dynamics around the soliton, we consider the two-dimensional spatial extension of Eq. (1), that is, the ∂_{xx} operator is replaced by a two-dimensional Laplacian operator $\nabla^2 = \partial_{xx} + \partial_{yy}$. It is well known that this equation has soliton type solutions with a constant phase [13], which are the natural extensions of the one-dimensional case. However, an analytical expression for these solutions is unknown. Considering a similar parameter region of phase shielding solitons in one dimension, we observe a rich phase fronts dynamics in two dimensions. If one slightly perturbs the soliton, after some complex transient in the phase dynamics we observe the appearance of a circular phase front that spreads slowly.

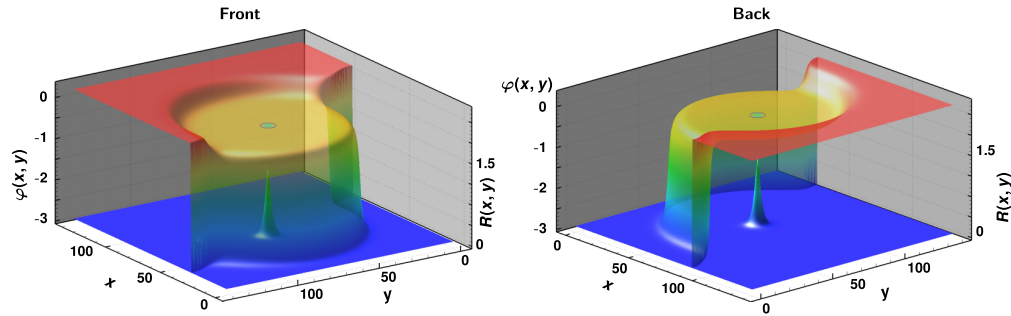


FIG. 4 (color online). Front and back view of a stationary phase shielding soliton observed in two dimensions for the parametrically driven damped nonlinear Schrödinger equation with $\gamma = 0.140$, $\nu = -0.068$, and $\mu = 0.125$. The phase and amplitude field are represented simultaneously. The colored shadow renders the phase shell-like structure $[\varphi(x, y)]$ that surrounds the amplitude soliton localized at the center $[R(x, y)]$.

For later times, the front becomes asymmetric, giving rise to another front. Finally, the two fronts become stationary, creating a shieldlike structure around the soliton. Figure 4 shows the stationary phase structure observed numerically in a two-dimensional system. It is important to note that we only see phase shielding structure as a state of equilibrium for dissipative soliton in a large system size. The two-dimensional solution is characterized by being composed of all the solutions found in one dimension. Indeed, if one performs different cuts containing the center (soliton position), one can recognize the observed solutions in one dimension (see Fig. 1). A surprising property of the shell-like structure observed is that if one calculates the phase change on a path that connects two opposite points with respect to the position of the soliton ($\int_{\Gamma} \vec{\nabla} \varphi d\vec{s}$) within the region close to the position of the soliton one finds that this is zero. Nevertheless, if one takes this type of path far away from the soliton position, one finds $\int_{\Gamma} \vec{\nabla} \varphi d\vec{s} = \pm \pi$.

In conclusion, localized structures in parametrically forced systems have a rich and unexpected phase dynamics, creating novel types of localized states. We expect that phase shielding solitons could be observed experimentally in simple coupled forced oscillators, such as vertically driven fluid layers in narrow cells, optical parametrical oscillators, driven magnetic media, and a chain of coupled oscillators.

Shell-like phase structure must play a significant role in soliton interaction, since bound states of two solitons show a complex phase structure [14]. Experimental observations show an intricate temporal dynamics of dissipative solitons [15] which cannot be explained from uniform phase solitons. Work in this direction is in progress.

The authors thank C. Falcón for fruitful discussions. The authors acknowledge financial support by the ANR-CONICYT 39, “Colors.” M.G.C. and M.A.G-N. are thankful for the financial support of FONDECYT

Projects No. 1090045 and No. 3110024, respectively. M.G.C. also acknowledges ACT Project No. 127.

-
- [1] *Localized States in Physics: Solitons and Patterns*, edited by O. Descalzi, M. Clerc, S. Residori, and G. Assanto (Springer, New York, 2010).
 - [2] H.G. Purwins, H.U. Bodeker, and Sh. Amiranashvili, *Adv. Phys.* **59**, 485 (2010).
 - [3] T. Ackemann, W.J. Firth, and G.L. Oppo, *Adv. At. Mol. Opt. Phys.* **57**, 323 (2009).
 - [4] M. Clerc, P. Couillet, and E. Tirapegui, *Phys. Rev. Lett.* **83**, 3820 (1999); *Int. J. Bifurcation Chaos Appl. Sci. Eng.* **11**, 591 (2001); *Opt. Commun.* **167**, 159 (1999); *Phys. Lett. A* **287**, 198 (2001); *Prog. Theor. Phys. Suppl.* **139**, 337 (2000).
 - [5] I. V. Barashenkov and E. V. Zemlyanaya, *Phys. Rev. Lett.* **83**, 2568 (1999).
 - [6] J. W. Miles, *J. Fluid Mech.* **148**, 451 (1984); W. Zhang and J. Viñals, *Phys. Rev. Lett.* **74**, 690 (1995); X. Wang and R. Wei, *Phys. Rev. E* **57**, 2405 (1998); M. G. Clerc *et al.*, *Phil. Trans. R. Soc. A* **367**, 3213 (2009).
 - [7] B. Denardo *et al.*, *Phys. Rev. Lett.* **68**, 1730 (1992).
 - [8] J. N. Kutz *et al.*, *Opt. Lett.* **18**, 802 (1993).
 - [9] S. Longhi, *Phys. Rev. E* **53**, 5520 (1996).
 - [10] I. V. Barashenkov, M. M. Bogdan, and V. I. Korobov, *Europhys. Lett.* **15**, 113 (1991); M. G. Clerc, S. Coulibaly, and D. Laroze, *Physica (Amsterdam)* **239D**, 72 (2010).
 - [11] N. V. Alexeeva, I. V. Barashenkov, and G. P. Tsironis, *Phys. Rev. Lett.* **84**, 3053 (2000).
 - [12] N. V. Alexeeva, I. V. Barashenkov, and D. E. Pelinovsky, *Nonlinearity* **12**, 103 (1999).
 - [13] I. V. Barashenkov, N. V. Alexeeva, and E. V. Zemlyanaya, *Phys. Rev. Lett.* **89**, 104101 (2002).
 - [14] I. V. Barashenkov and E. V. Zemlyanaya, *Phys. Rev. E* **83**, 056610 (2011); E. Kenig *et al.*, *Phys. Rev. E* **80**, 046202 (2009).
 - [15] W. Wei *et al.*, *Phys. Lett. A* **219**, 74 (1996).

A.3 Phase shielding soliton in parametrically driven systems

Marcel G. Clerc, Mónica A. Garcia-Nústes, Yair Zárate, and Saliya Coulibaly

Physical Review E 87, 052915 (2013) DOI: 10.1103/PhysRevE.87.052915

Abstract

Parametrically driven extended systems exhibit dissipative localized states. Analytical solutions of these states are characterized by a uniform phase and a bell-shaped modulus. Recently, a type of dissipative localized state with a nonuniform phase structure has been reported: the phase shielding solitons. Using the parametrically driven and damped nonlinear Schrödinger equation, we investigate the main properties of this kind of solution in one and two dimensions and develop an analytical description for its structure and dynamics. Numerical simulations are consistent with our analytical results, showing good agreement. A numerical exploration conducted in an anisotropic ferromagnetic system in one and two dimensions indicates the presence of phase shielding solitons. The structure of these dissipative solitons is well described also by our analytical results. The presence of corrective higher-order terms is relevant in the description of the observed phase dynamical behavior.

Phase shielding soliton in parametrically driven systems

Marcel G. Clerc,^{*} Mónica A. García-Ñustes,[†] and Yair Zárate

Departamento de Física, Facultad de Ciencias Físicas y Matemáticas, Universidad de Chile, Casilla 487-3, Santiago, Chile

Saliya Coulibaly[‡]

Laboratoire de Physique des Lasers, Atomes et Molécules, CNRS UMR No. 8523, Université des Sciences et Technologies de Lille, 59655 Villeneuve d'Ascq Cedex, France

(Received 13 September 2012; revised manuscript received 7 February 2013; published 24 May 2013)

Parametrically driven extended systems exhibit dissipative localized states. Analytical solutions of these states are characterized by a uniform phase and a bell-shaped modulus. Recently, a type of dissipative localized state with a nonuniform phase structure has been reported: the phase shielding solitons. Using the parametrically driven and damped nonlinear Schrödinger equation, we investigate the main properties of this kind of solution in one and two dimensions and develop an analytical description for its structure and dynamics. Numerical simulations are consistent with our analytical results, showing good agreement. A numerical exploration conducted in an anisotropic ferromagnetic system in one and two dimensions indicates the presence of phase shielding solitons. The structure of these dissipative solitons is well described also by our analytical results. The presence of corrective higher-order terms is relevant in the description of the observed phase dynamical behavior.

DOI: [10.1103/PhysRevE.87.052915](https://doi.org/10.1103/PhysRevE.87.052915)

PACS number(s): 89.75.Kd, 05.45.Yv

I. INTRODUCTION

Particle-type solutions or macroscopic localized states arising in systems out of equilibrium have been observed in a wide range of physical systems. Examples include magnetic materials, liquid crystals, gas discharge systems, chemical reactions, fluids, granular media, and nonlinear optics media (see [1–3] and references therein). The variety of systems exhibiting these solutions confers them a universal nature. Given their particlelike properties, one can characterize them by a family of continuous parameters such as position, amplitude, and size. A prototypical model that exhibits dissipative localized states or dissipative solitons in the quasireversible limit—systems under the assumption of small injection and dissipation of energy [4–8]—is the parametrically driven and damped nonlinear Schrödinger (PDNLS) equation [9,10]

$$\partial_t \psi = -i\nu\psi - i|\psi|^2\psi - i\partial_{xx}\psi - \mu\psi + \gamma\bar{\psi}, \quad (1)$$

where $\psi(x,t)$ is a complex field that accounts for the envelope of the oscillation in the system under study. The variable $\bar{\psi}$ stands for the complex conjugate of ψ ; $\{x,t\}$ denote the spatial and temporal coordinates, respectively; ν is the detuning parameter, which is proportional to the difference between half the forcing frequency and the natural frequency of the oscillator field; μ is the damping parameter, which accounts for the energy dissipation processes; and γ is the amplitude of the parametric forcing. It is important to note that Eq. (1) describes an oscillatory focusing medium with dispersive coupling [11] since the nonlinear and spatial coupling terms have the same sign. For $\nu < 0$, $\gamma \sim \mu \ll 1$, and $\mu^2 < \gamma^2 < \nu^2 + \mu^2$, the PDNLS model admits analytical localized states characterized by a uniform phase and a bell-like shape for the modulus of the amplitude—uniform phase solitons

(UPSs) [9,10]. Figure 1 shows a typical dissipative soliton in a polar coordinate representation [$\psi(x,t) = R(x,t)e^{i\varphi(x,t)}$] observed in the parametrically driven and damped nonlinear Schrödinger equation.

The PDNLS model has been derived in various physical contexts. Indeed, the PDNLS equation can be deduced from the amplitude equation approach in the parametrically driven pendulum chain [12–14]. Using the same approach in the context of magnetic systems for an easy-plane ferromagnetic spin chain exposed to both a constant and a time-periodic external magnetic field perpendicular to the hard axis, the PDNLS equation was obtained by means of the Landau-Lifshitz-Gilbert equation [15,16]. Additional physical scenarios where the PDNLS model can be derived include surface waves in vertically oscillating layers of water [17–19], localized structures in nonlinear lattices [20], and the Kerr-type optical parametric oscillator [21].

Recently, we have shown that the phase of dissipative solitons exhibits an unexpected dynamical behavior in the PDNLS equation [22]. More precisely, we have found that, for a large range of parameters, PDNLS soliton solutions show dynamical phase fronts that, after some transient behavior, reach a stationary state surrounding the soliton core. Due to its shieldlike phase structure, this type of dissipative localized state has been denominated a phase shielding soliton (PSS). Using the asymptotic expression for the amplitude, valid far from the core of the soliton, we have determined analytically the shape of the phase fronts and their dynamics. The above analysis allows us to characterize the different type of shieldlike structures of the phase. Performing a numerical stability analysis and using the size of the system L as a control parameter, we have proved that UPS solutions lose their stability through a Andronov-Hopf bifurcation followed by the appearance of the PSS as the stable solution of the system.

The emergence of phase fronts on dissipative solitons represents an alternative perspective in the study of parametrically

^{*}marcel@dfi.uchile.cl

[†]mgarcianustes@ing.uchile.cl

[‡]saliya.coulibaly@phlam.univ-lille1.fr

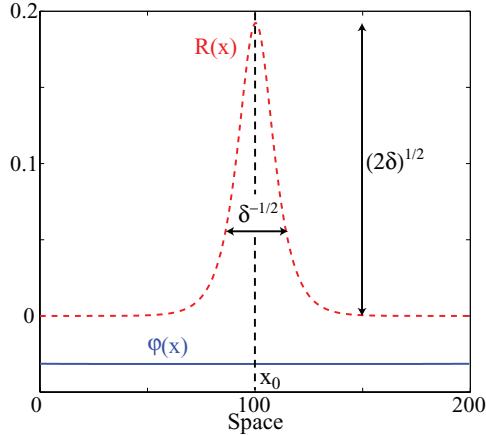


FIG. 1. (Color online) Modulus $R(x)$ (red dashed line) and phase $\phi(x)$ (blue solid line) of a UPS in the parametrically driven and damped nonlinear Schrödinger equation with $\mu = 0.1000$, $\nu = -0.0122$, $\gamma = 0.1002$, $\delta = 0.0185$, and $L = 200$. Here x_0 stands for the position of the maximum of the soliton amplitude. The soliton width and height are indicated.

driven systems. Until now, the phase of single solitons was considered uniform in most of the aforementioned physical systems. However, a more complete analysis could demonstrate the existence of PSS solutions in such physical scenarios. In the present paper we extend the analytical and numerical studies of phase shielding solitons in one-dimensional (1D) and 2D cases. We also analyze the appearance of PSS solutions in an easy-plane ferromagnetic spin system in both 1D and 2D configurations. For this purpose, we organize the paper in the following way. In Sec. II we review the main features of the PDNLS equation and the analytical solution of the UPS and its stability. We then introduce the phase shielding soliton solutions. An analytical description of PSS solutions and their dynamics is presented. A numerical stability analysis is also performed to establish the connection between the UPS and PSS solutions. To show the existence of the PSS in physical systems, we study in Sec. III an easy-plane ferromagnetic classical spin chain exposed to an external magnetic field. The existence, stability properties, and dynamical evolution of the phase shielding solitons in two-dimensional extended systems are analyzed in Sec. IV. In Sec. V we consider a physical example of a parametrically driven system in two dimensions: a forcing magnetic layer. We conclude with a summary in Sec. VI.

II. DISSIPATIVE SOLITONS IN THE PDNLS MODEL IN ONE DIMENSION

For $\mu = \gamma = 0$, Eq. (1) becomes the well-known nonlinear Schrödinger equation [23], which describes the envelope of an oscillatory coupled system. This model is a time-reversible Hamiltonian system with the reflection symmetry $\{t \rightarrow -t, \psi \rightarrow \bar{\psi}\}$. However, the terms proportional to the energy dissipation μ and the injection γ break this symmetry. The higher-order terms in Eq. (1) are ruled out by a scaling analysis where $\mu \ll 1$, $\nu \sim \mu \sim \gamma$, $|\psi| \sim \mu^{1/2}$, $\partial_x \sim \mu^{1/2}$, and $\partial_t \sim \mu^{1/2}$.

A trivial solution of Eq. (1) is the homogeneous (quiescent) state $\psi_0 = 0$. For $\nu < 0$, ψ_0 becomes unstable through a subcritical stationary bifurcation at $\gamma^2 = \mu^2 + \nu^2$ (the Arnold tongue) [11]. Inside this region the system has three uniform solutions $\psi_0 = 0$, and $\psi_{\pm} = \sigma \pm i\sqrt{(\mu - \gamma)(\mu + \gamma)}\sigma$, where $\sigma = \sqrt{(\gamma - \mu)(-\nu + \sqrt{\gamma^2 - \nu^2})}/2\gamma$. These three states merge through a pitchfork bifurcation at $\gamma^2 = \mu^2 + \nu^2$ when $\nu > 0$. However, for positive detuning, ψ_0 is stable only when $\gamma < \mu$ because this state exhibits a spatial instability at $\gamma = \mu$ [24], which gives rise to a spatially periodic state with a wave number $k_c = \sqrt{\nu}$.

A. Solitons with constant phase

For negative detuning, the PDNLS equation exhibits localized states or dissipative solitons supported asymptotically by the quiescent state. In order to obtain the localized states, we introduce the Madelung transformation $\psi = R(x, t)e^{i\phi(x, t)}$ in Eq. (1). Separating the imaginary and real parts, we obtain the set of equations

$$\partial_t R = 2\partial_x R \partial_x \phi + R \partial_{xx} \phi - \mu R + \gamma R \cos(2\phi), \quad (2)$$

$$\partial_t \phi = -\nu - R^2 - \frac{\partial_{xx} R}{R} + (\partial_x \phi)^2 - \gamma \sin(2\phi), \quad (3)$$

where R and ϕ denote the amplitude and phase of the field ψ , respectively. In the parameter region $\gamma \geq \mu$ and $-\nu \pm \sqrt{\gamma^2 - \mu^2} \geq 0$, we get nontrivial steady homoclinic solutions of the form [9,10]

$$R_s(x, x_0) = \sqrt{2\delta_{\pm}} \operatorname{sech}(\sqrt{\delta_{\pm}}[x - x_0]), \quad (4)$$

$$\cos(2\phi_s) = \mu/\gamma, \quad (5)$$

where the parameter $\delta_{\pm} \equiv -\nu \pm \sqrt{\gamma^2 - \mu^2}$ and x_0 stands for the position of the maximum of the soliton, which will be called the core of the soliton in what follows. The modulus width and height are given by $\sqrt{2\delta_{\pm}}$ and $1/\sqrt{\delta_{\pm}}$, respectively (see Fig. 1). Hence Eqs. (4) and (5) show that such states have a bell-shaped modulus and a uniform phase (UPS).

Equation (5) shows that the system can generate dissipative solitons when the injection of energy exceeds its dissipation. As a consequence of the spatial translational invariance of Eq. (1), the dissipative solitons constitute a family of states parametrized by a continuous parameter x_0 corresponding to their Goldstone mode [25]. This parameter stands for the position of the core of the localized state (see Fig. 1). In brief, the above model admits soliton solutions in the $\{\mu, \nu, \gamma\}$ region bounded by $\nu < 0$, $\mu \leq \gamma$, and $\gamma^2 < \mu^2 + \nu^2$. Under these conditions, the relation $\cos(2\phi_s) = \mu/\gamma$ admits four equilibria in the interval $[\pi, -\pi]$. As a consequence of the symmetry $\psi \rightarrow -\psi$ of Eq. (1), if ϕ_s is a solution then $\phi_s \pm \pi$ is also a solution. Figure 2 illustrates this relation and the respective stability regions of the different particle-type solutions. From this figure one can infer that the localized states appear or disappear by simultaneous saddle-node bifurcations when the injection and dissipation of energy are equal ($|\gamma| = \mu$). The stable solutions are characterized by $\operatorname{Re}(\psi)\operatorname{Im}(\psi) < 0$ [$\operatorname{Re}(\psi)\operatorname{Im}(\psi) > 0$] for $\gamma > 0$ ($\gamma < 0$), thus both fields have different signs when $\gamma > 0$ [15]. In contrast, the solution with a bell-shaped modulus $|\psi|$ [Eq. (4)] also appears through

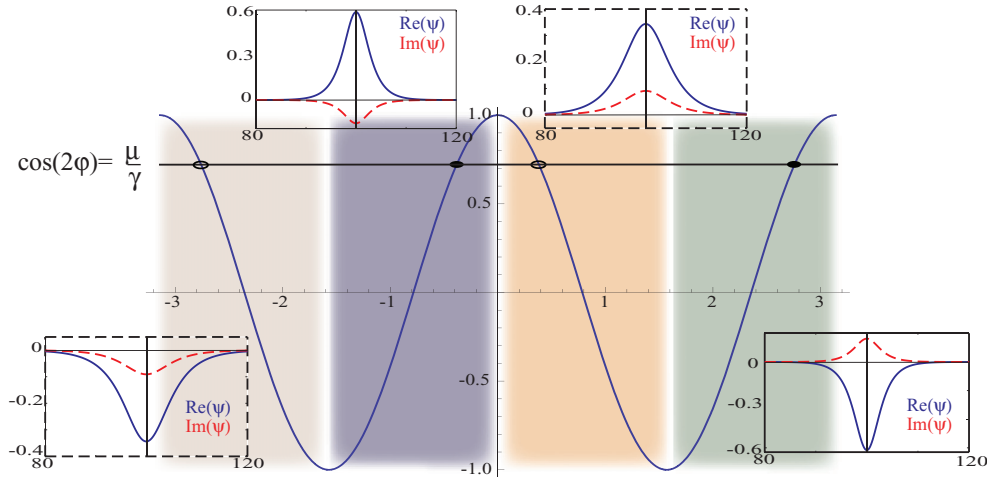


FIG. 2. (Color online) Schematic representation of the different stability regions (colored shadow) of dissipative solitons. The circles represent the different solutions of $\cos(2\varphi_s) = \mu/\gamma$: closed (open) circles correspond to stable (unstable) localized states. The insets depict the different types of dissipative solitons with $\mu = 0.10$, $\gamma = 0.13$, $\nu = -0.12$, and $L = 200$, where $\delta_+ = 0.203$ and $\delta_- = 0.037$.

a saddle-node bifurcation at $\gamma = \mu$ where $\delta_{\pm} = -\nu$. The solutions of Eq. (4) with δ_- are unstable.

B. Phase shielding soliton

Previous works have reported additional amplitude bifurcations when ν is increased far from the tip of the Arnold tongue where the maximum of $|\psi|$ undergoes period doubling, quasiperiodicity, and finally chaos [26]. Usually, the phase field of the dissipative soliton state is considered uniform. However, further numerical analysis reveals unexpected and rich phase dynamics of single solitons in parametrically driven systems [22], which reaches a nonuniform steady phase.

A soliton is created by slightly perturbing an initial homogenous state. The parameters are chosen to fulfill the conditions for the appearance of UPS solutions, i.e., $\nu < 0$, $\gamma^2 < \mu^2 + \nu^2$, and $\mu \leq \gamma$. Initially, the perturbation quickly evolves to a well-defined bell-shaped amplitude. At the same time, the phase becomes uniform around the core of the localized state followed by some intricate transient that rapidly goes away from the system. The front propagation is characterized by a rather slow motion (see Fig. 3), which suddenly reaches a steady state. From this initial behavior a pair of counterpropagative fronts emerges, which propagates in a rather slow motion, reaching suddenly a steady state (see Fig. 3). Near the soliton core, the phase takes the value corresponding to the stable uniform soliton (UPS), i.e., the value $-\varphi_s$ or $-\varphi_s + \pi$. Conversely, far from the soliton position, the asymptotic values in $(-\infty, \infty)$ tend to the unstable UPS phase values either φ_s or $\varphi_s - \pi$. Hence the number of configurations is given by different combinations of equilibrium connections (unstable-stable-unstable). There are eight stationary configurations that connect different phase equilibria. Figure 4 displays all the different phase shielding solitons. These steady phase structures depend strongly on initial conditions and are equally likely to appear in the same region of parameters.

1. Analytical approach at dominant order

To provide an analytical background to these phase structure dynamics, we take advantage of the $x \rightarrow -x$ symmetry of the PDNLS model [Eq. (1)]. We consider a semi-infinite domain whose origin corresponds to the core position of the soliton x_0 . Numerical results show that the phase presents a single front that emerges at a position $x_f \gg 1/\sqrt{\delta_+}$, where x_f represents the point with the highest spatial variation of the phase. In the region $x \gg 1/\sqrt{\delta_+}$, the soliton modulus R decays exponentially [see Fig. 6(a)].

Defining $\Delta \equiv 1/\sqrt{\delta_+}$, which accounts for the width of the soliton bell-shaped amplitude (see Fig. 1), we propose the

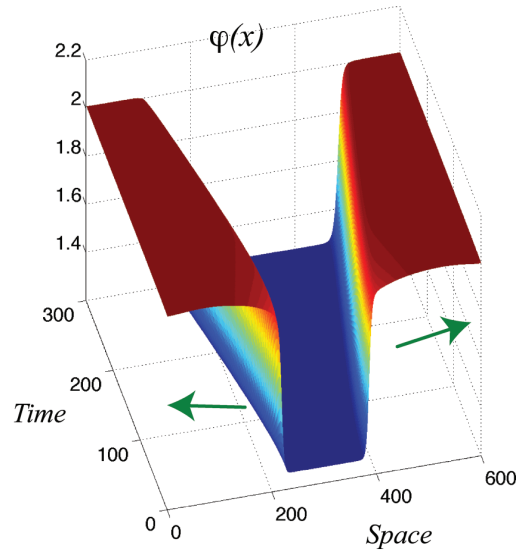


FIG. 3. (Color online) Phase propagation of the dissipative soliton. Spatiotemporal diagram of phase $\varphi(x,t)$ for $\gamma = 0.123$, $\mu = 0.100$, and $\nu = -0.093$.

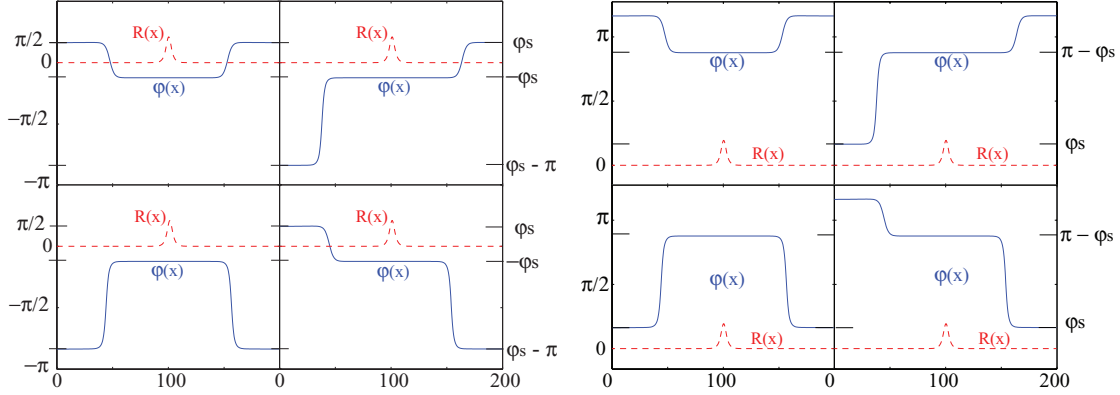


FIG. 4. (Color online) Different phase shielding soliton states in the parametrically driven damped nonlinear Schrödinger equation with $\mu = 0.10$, $\nu = -0.12$, $\gamma = 0.14$, and $L = 200$. The PSS states supported by the inner uniform phases $-\varphi_s$ and $\pi - \varphi_s$ are shown on the right and left, respectively. Dashed (red) and solid (blue) lines account for the modulus and phase of the complex field ψ , respectively.

following ansatz for the modulus and the phase of the soliton:

$$R(x \gg \Delta, x_0) = 2\sqrt{2\delta_+}e^{-f(x, x_0)} \quad (6)$$

and

$$\varphi(x) = \varphi_F(x - x_f), \quad (7)$$

respectively. At dominant order, we consider $f(x, x_0) \approx \sqrt{\delta_+}(x - x_0)$. In this approximation, $R(x, x_0)$ coincides with the asymptotic exponential decay of the stable UPS modulus.

Substituting the former ansatz in (2) and (3), we obtain two different equations. The first one allows us to get analytically the dominant profile of the phase front. The second one describes the phase front dynamical behavior. Accordingly, the phase profile is characterized by

$$\partial_{xx}\varphi_F = 2\sqrt{\delta_+}\partial_x\varphi_F + \mu - \gamma \cos(2\varphi_F). \quad (8)$$

Introducing the effective potential energy $U(\varphi_F) \equiv -\mu\varphi_F + (\gamma/2)\sin(2\varphi_F)$, Eq. (8) can be written as a Newton-type equation that describes a particle moving in a tilted periodic potential with an injection of energy proportional to the speed $\partial_x\varphi_F$,

$$\partial_{xx}\varphi_F = -\frac{\partial U}{\partial\varphi_F} + 2\sqrt{\delta_+}\partial_x\varphi_F. \quad (9)$$

Hence the solutions of the above equation correspond to stationary phase fronts. The uniform equilibrium states of Eq. (8) coincide with the phase equilibria of $\cos(2\varphi_s) = \mu/\gamma$ in the range from $-\pi$ to π . Therefore, the phase front solutions represent heteroclinic orbits in the $\{\varphi, \varphi_x\}$ space that interpolate from one equilibrium to another of the Newton-type equation (9) (see Fig. 5).

Defining the change of variable $x = 2\sqrt{\delta_+}x'$ in Eq. (8), we can perform an asymptotic series $\varphi_F(x) = \varphi_0 + \Gamma\varphi_1(x) + \Gamma^2\varphi_2(x) + \dots$, with $\Gamma \equiv 1/4\delta \ll 1$, which at first order has the analytical solution

$$\varphi_F(x, x_f) \approx \varphi_0 = \begin{cases} f_{\text{sol}} - \pi & \text{for } [-\pi, -\pi/2) \\ f_{\text{sol}} & \text{for } (-\pi/2, -\pi/2) \\ f_{\text{sol}} + \pi & \text{for } (\pi, \pi/2], \end{cases} \quad (10)$$

where

$$f_{\text{sol}} = \arctan \left[\sqrt{\frac{\gamma \pm \mu}{\gamma \mp \mu}} \tanh \frac{\sqrt{\gamma^2 - \mu^2}(x - x_f)}{2\sqrt{\delta_+}} \right]. \quad (11)$$

Note that the phase front solutions are also parametrized by the continuous parameter x_f . Figure 6 shows the numerically computed phase front profiles, which present a difference of 1% with respect to expression (10). If one considers the dominant correction $\varphi_F \approx \varphi_0 + \partial_x\varphi_0/4\sqrt{\delta}$, this difference decreases to 0.8%.

Considering the complete soliton domain, we obtain the eighth possible shell-like configuration that we have previously observed in numerical simulations (see Fig. 4).

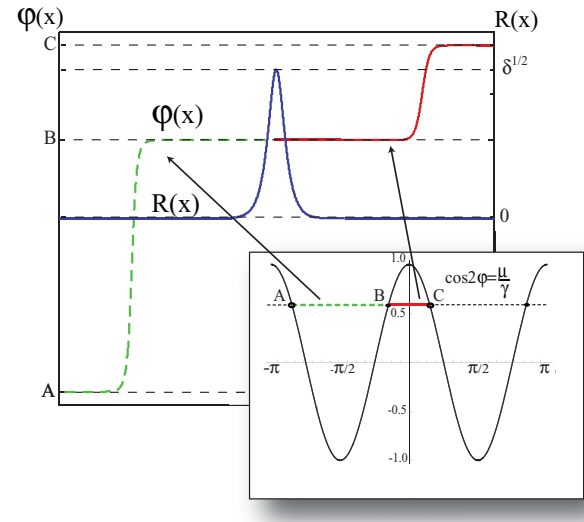


FIG. 5. (Color online) Schematic representation of the stationary phase front structure that connects different equilibrium solutions (A–C) of the Newton-type equation (9). The inset is a schematic representation of the potential $U(\varphi_F)$.

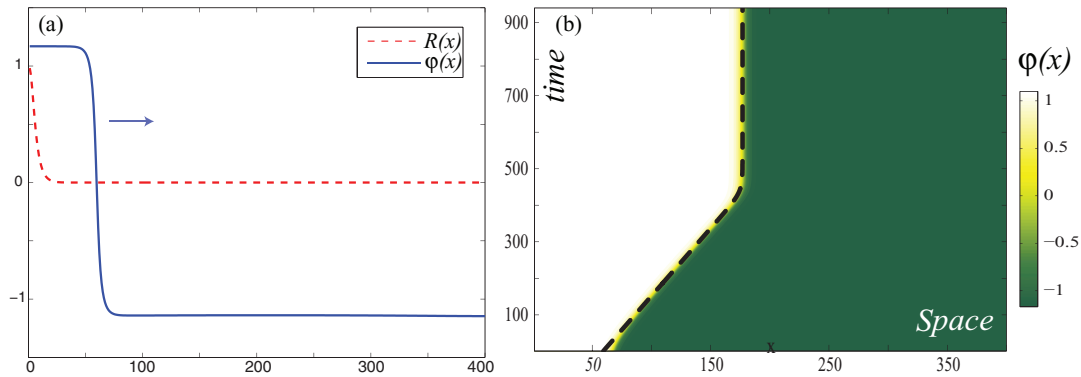


FIG. 6. (Color online) Phase propagation: (a) phase front profile considering half of the dissipative soliton and (b) spatiotemporal diagram of the phase front obtained from Eq. (1) with $\gamma = 0.083$, $\nu = -0.063$, and $\mu = 0.058$. The dashed curve is the numerical solution obtained using Eq. (17).

2. Higher-order corrections

A deeper analysis of numerical simulations reveals that PSS solutions are composed of two qualitatively different regions: inner and outer regions. The inner and outer regions stand for the central and asymptotic parts of the PSS, respectively. Note that the asymptotic phase of the PSS in the inner and outer regions coincides with the phase of the stable and unstable UPSs, respectively (see Fig. 4). Therefore, the PSS can be understood as a soliton buildup by the stable (inner region) and unstable (outer region) UPS solutions. To illustrate this statement, Fig. 7 shows the logarithm of the PSS modulus as a function of the space. Clearly, there is a crossover region

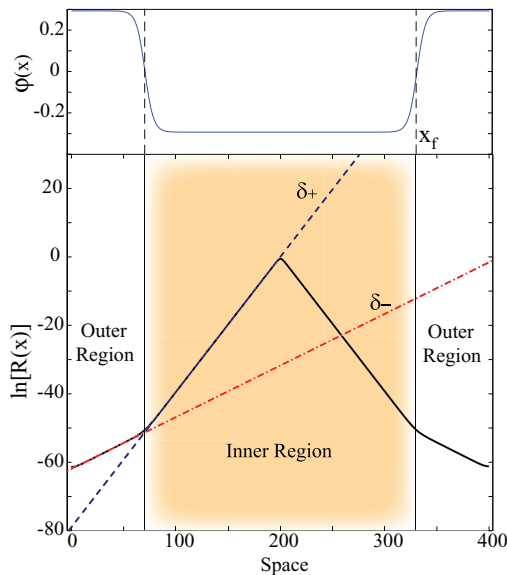


FIG. 7. (Color online) Phase $\varphi(x)$ as a function of the space (top) and logarithm of the PSS modulus $R(x)$ (bottom) with $\mu = 0.1$, $\nu = -0.09$, $\gamma = 0.12$, and $L = 400$. Inner and outer regions are defined. The exponential decay value changes from $\sqrt{\delta_+} = 0.3946$ (theoretical $\sqrt{\delta_+} = 0.3954$) inside the inner region to $\sqrt{\delta_-} = 0.1508$ (theoretical $\sqrt{\delta_+} = 0.1538$) in the outer region. The transition point between both regions coincides with the phase front position x_f .

between both exponential decay rates of the UPS solution that is characterized by a transition point. Such a point outlines the border transition between the inner and outer regions and corresponds to the phase front core position x_f . Therefore, the PSS exponential decay rate $f(x, x_0)$ must be amended by

$$f(x, x_0) \approx \sqrt{\delta_+}(x - x_0) + B(x, x_f), \quad (12)$$

with

$$B(x, x_f) \equiv [\sqrt{\delta_-} - \sqrt{\delta_+}] \Theta(x - x_f)(x - x_f), \quad (13)$$

where $\Theta(x - x_f)$ denotes the Heaviside function. Note that the function $f(x, x_0)$ is a smooth function. However, its approximation (12) is continuous but not differentiable at $x = x_f$.

Using the amended ansatz (12), Eqs. (8) and (9) can be reobtained in the inner and outer regions. In the inner region, Eqs. (8) and (9) remain the same. In contrast, these equations are modified by substituting the value δ_+ for δ_- in the outer region. Following the same procedure showed in Sec. II B 1, the amended front phase is obtained

$$\varphi_0(x) = \arctan \left[\sqrt{\frac{\gamma \pm \mu}{\gamma \mp \mu}} \tanh \frac{\sqrt{\gamma^2 - \mu^2}(x - x_f)}{2\delta(x, x_f)} \right], \quad (14)$$

with

$$\delta(x, x_f) \equiv [\sqrt{\delta_+} + (\sqrt{\delta_-} - \sqrt{\delta_+}) \Theta(x - x_f)]. \quad (15)$$

In this approximation the phase fronts are continuous but not differentiable at $x = x_f$, emphasizing that the PSS is composed of the stable and unstable UPS solutions.

It is important to note that ansatz (6) considers a uniform exponential decay rate of the modulus. Such an assumption leads, at dominant order, to the obtention of phase front solutions [Eq. (10)]. Higher-order corrections allow us to get an improved description of the phase shield soliton where the modulus also exhibits an amplitude shielding structure (see Fig. 7). However, this structure is exponentially suppressed in comparison to the soliton height $\sqrt{2\delta_+}$. In contrast, the phase shielding structure is order one. Therefore, a possible experimental characterization of the PSS must be achieved by means of phase measurements.

C. Phase front dynamics

As discussed in the previous section, the transient preceding the formation of the phase profile is governed by the fronts dynamics. Here we propose an analytical study of the dynamical evolution of these fronts. For this purpose let us consider the typical evolution of a soliton in a semi-infinite system, as shown in Fig. 6. As can be seen from the figure, the front displays a dynamical behavior characterized by a nontrivial motion. For the sake of simplicity, let us consider the ansatz (6) and (7) at dominant order where $f(x, x_0) \approx \sqrt{\delta}(x - x_0)$ and $\delta \equiv \delta_+$. Substituting in Eq. (3), we obtain the equation for position of the core

$$-\dot{x}_f \partial_x \varphi_F = -(v + \delta) - 8\delta e^{-2\sqrt{\delta}x} + (\partial_x \varphi_F)^2 - \gamma \sin(2\varphi_F). \quad (16)$$

In order to account for the front dynamics $x_f(t)$ has been promoted to a time-dependent function. The time derivative of x_f is given by \dot{x}_f .

Multiplying the above equation by $\partial_z \varphi_F(z)$ with $z \equiv x - x_f$ and introducing the inner product $\langle f | g \rangle \equiv \int f g dz$, we obtain, after straightforward calculations, an ordinary differential equation for the core of the phase front

$$\dot{x}_f = A + B e^{-2\sqrt{\delta}x_f}, \quad (17)$$

where

$$A \equiv \frac{\langle [v + \delta + \gamma \sin(2\varphi_F) - (\partial_z \varphi_F)^2] | \partial_z \varphi_F \rangle}{\langle \partial_z \varphi_F | \partial_z \varphi_F \rangle}$$

and

$$B \equiv 8\delta \frac{\langle e^{-2\sqrt{\delta}z} | \partial_z \varphi_F \rangle}{\langle \partial_z \varphi_F | \partial_z \varphi_F \rangle}$$

are real numbers, which can be either positive or negative, depending on the shape of the phase front. For example, when one considers a front that increases monotonically with the spatial coordinate, A (B) is a negative (positive) constant. The term proportional to A accounts for the constant speed at which the larger phase value invades the smaller one, giving rise to a phase front that propagates towards the position of the soliton x_0 . This speed can be understood as a consequence of the effective potential energy $U(\varphi_F)$ difference between both equilibria. In contrast, the term proportional to B accounts

for the effect of spatial variation of the tail of the amplitude soliton, which induces a force that leads to phase fronts moving away from the position of the soliton. Consequently, the superposition of these two antagonistic forces generates a stable equilibrium for the position of the phase front, which is consistent with the dynamical behavior illustrated by the spatiotemporal diagram of Fig. 6(b). Solving Eq. (17), we get an analytical solution for the typical trajectory

$$x_f(t) = \frac{\ln\left(\frac{B}{A}\right)}{2\sqrt{\delta}} + \frac{\ln(e^{-2\sqrt{\delta}A(t-t_0)} - 1)}{2\sqrt{\delta}} - A(t - t_0). \quad (18)$$

The dashed curve shown in Fig. 6(b) is obtained using the above formula wherein A and B are used as fitting parameters. Note that the constant $\ln(B/A)/2\sqrt{\delta}$ accounts for the steady equilibrium position of the front, which corresponds to the characteristic size of the shell structure in the phase. For higher-order corrections of the phase, we obtain a similar expression for the dynamics of the front.

D. Stability analysis for the uniform phase soliton

As we have already shown, the uniform phase and phase shielding solitons are solutions of the PDNLS model (1). Thus a natural question arises: What are the bifurcation scenarios of these solutions? Here we examine this question, performing a numerical linear stability analysis based on Ref. [15]. Given the complexity of the linear operator, an analytical stability analysis is not affordable. We consider small perturbations ρ and Ω around the solutions $R_s(x)$ and φ_0 , respectively, i.e.

$$R = R_s(x) + \rho(x, t), \quad \varphi = \varphi_0 + \Omega(x, t), \quad (19)$$

where $\rho, \Omega \ll 1$. Substituting in (2) and (3) and linearizing, we obtain

$$\partial_t \rho = 2\partial_x R_s \partial_x \Omega + R_s \partial_{xx} \Omega + 2\sqrt{\gamma^2 - \mu^2} \Omega R_s \quad (20)$$

and

$$R_s \partial_t \Omega = \delta \rho - 3R_s^2 \rho - \partial_{xx} \rho - 2\mu R_s \Omega, \quad (21)$$

respectively. Equations (20) and (21) represent an eigenvalue problem that can be written in the matrix representation

$$\begin{pmatrix} \dot{\rho} \\ \dot{\Omega} \end{pmatrix} = \mathbb{M} \begin{pmatrix} \rho \\ \Omega \end{pmatrix}, \quad (22)$$

where

$$\mathbb{M} \equiv \begin{pmatrix} 0 & 2\partial_x R_s(x) \partial_x - R_s(x) \partial_{xx} - 2R_s(x) \sqrt{\gamma^2 - \mu^2} \\ \frac{1}{R_s(x)} [\delta - 3R_s(x)^2 - \partial_{xx}] & -2\mu \end{pmatrix}. \quad (23)$$

An analytical solution to Eq. (22) is a difficult task [15]. Therefore, to solve it we adopt a numerical strategy. In order to obtain the spectrum, a set of eigenvalues associated with the linear stability analysis, we proceed to discretize in space with grid points $x \rightarrow j\Delta x$, $F(x, t) \rightarrow F(j\Delta x, t) \equiv F_j(t)$ with $j = 1, \dots, N$, where N is the number of points of the system and $L = N\Delta x$. In such a case, the differential operator \mathbb{M} with spatiotemporal coefficients turns into a matrix of rank $2N$. We

also consider $\mu = \mu_0$ and $x_0 = L/2$ for different values of $\{\gamma, v\}$ in the region of existence of solitons, i.e., $\gamma^2 \leq v^2 + \mu^2$ and $v < 0$.

The L parameter controls the size effect. Changing N with Δx fixed, we can easily vary it. In previous reports, this parameter was not considered as a relevant parameter system, being usually a small constant. We shall see that the parameter L plays a main role in the stability properties of dissipative states.

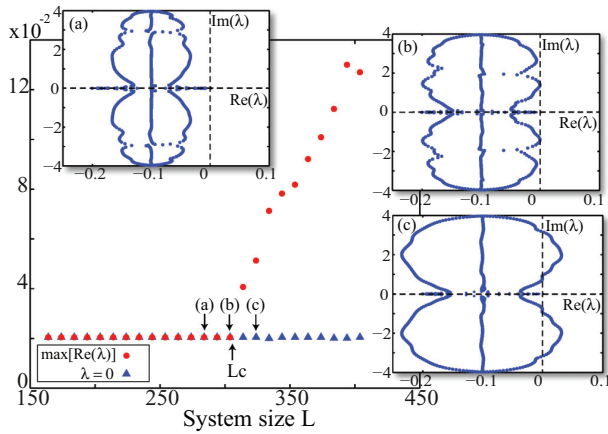


FIG. 8. (Color online) Real part of the largest eigenvalue $\max[\text{Re}(\lambda)]$ (red circles) and the eigenvalue related to the Goldstone mode (blue triangles) as a function of system size. The stability of solitons is shown in the spectra of the soliton with constant phase (a) before (system size $L = 284$), (b) during ($L = 304$), and (c) after ($L = 324$) the bifurcation for $\gamma = 0.105$, $\mu = 0.1$, and $\nu = -0.05$.

Hence let us consider L as a control parameter with the system parameters $\{\mu, \nu, \gamma\}$ fixed. When L is small enough the spectrum is characterized by being centered on an axis parallel to the imaginary one, where every single eigenvalue has a negative real part. Such behavior of the eigenvalues is typical of quasireversible systems [5,7]. Increasing L , the set of eigenvalues begins to collide, creating a continuum set. Up to a critical value of L_c , where some of them cross the imaginary axis at a nonzero frequency, the set exhibits an Andronov-Hopf bifurcation [27,28]. The inset Figs. 8(a)–8(c) outline the spectrum before, during, and after the bifurcation, respectively. The main plot of Fig. 8 illustrates the real part of the largest eigenvalue $\max[\text{Re}(\lambda)]$ (red circles) and the eigenvalue related to the Goldstone mode (blue triangles) as a function of the system size L . As a result of the translational invariance, the eigenvalue related to the Goldstone mode is at the origin of the complex plane [25]. For $\gamma = 0.105$, $\mu = 0.1$, and $\nu = -0.05$, we observe that [see Fig. 8(a), inset] below the critical value $L_c = 304$, the largest eigenvalue corresponds to the Goldstone mode. Close to the bifurcation, the largest conjugate pair of eigenvalues crosses the real axis destabilizing the uniform phase solution [see Figs. 8(b) and 8(c), insets].

The numerical stability analysis of UPS solutions reveals a strong dependence on the system size. Such a result is in accordance with the inner and outer region crossover. The inner region has a definite length for a given set of system parameters $\{\mu, \nu, \gamma\}$. If the system size is small enough (L is less than the length of the inner region), the crossover does not occur. Then the PSS solution cannot appear and the UPS is a stable solution. For L greater than the length of the inner region, the UPS destabilizes, generating the PSS solution.

Given that the exponential decay of the stable UPS, and therefore the length of the inner region, is a function of the system parameters $\{\mu, \nu, \gamma\}$ it is natural to infer that by varying such parameters with L fixed, the UPS destabilization will take place as well. Indeed, following the above strategy, we perform a numerical stability analysis of the UPS varying γ for L fixed

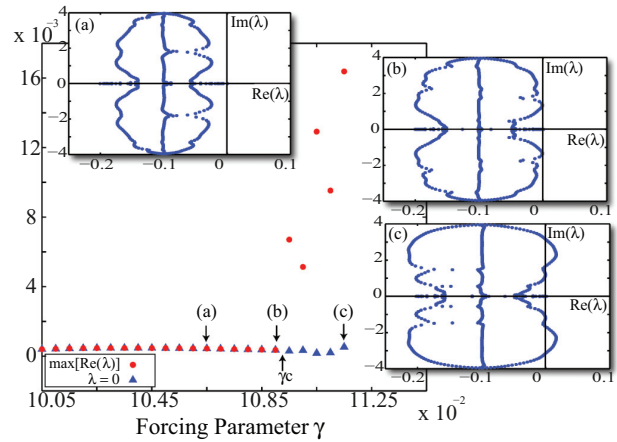


FIG. 9. (Color online) Real part of the largest eigenvalue $\max[\text{Re}(\lambda)]$ (red circles) and the eigenvalue related to the Goldstone mode (blue triangles) as a function of the forcing parameter γ . The stability of solitons is shown in the spectra of the soliton with constant phase (a) before ($\gamma = 0.1065$), (b) during ($\gamma = 0.1090$), and (c) after ($\gamma = 0.1115$) the bifurcation for $\mu = 0.1$ and $\nu = -0.05$ with $L = 280$ fixed.

with $\mu = 0.1$ and $\nu = -0.05$. We choose the same parameter region $\{\nu, \gamma\}$ with $L = 280$ (before bifurcation; see Fig. 8) to ensure an initial stable UPS solution. Figure 9 displays the eigenvalue spectrum evolution as γ varies. As before, up to a critical γ_c , the system exhibits an Andronov-Hopf bifurcation, which leads to the appearance of a PSS solution similar to the one observed in Figs. 8(a)–8(c).

In brief, the above instability mechanism is a robust phenomenon. Figure 10 displays the UPS stability over a wide parameter region $\{\nu, \gamma\}$ for $\mu = 0.05$ and $L = 400$ fixed. For a system size smaller than the critical one, we observe that for the parameters $0 < \gamma - \mu \ll 1$, the soliton with constant phase is stable. Notwithstanding, increasing the forcing amplitude γ or the detuning parameter ν , the soliton becomes unstable again by an Andronov-Hopf bifurcation.

In the case that the system size is large enough, the UPS solution exhibits an Andronov-Hopf bifurcation that leads to a PSS solution. Further increasing the system parameters $\{\nu, \gamma\}$, a secondary bifurcation leads to a periodic soliton like those

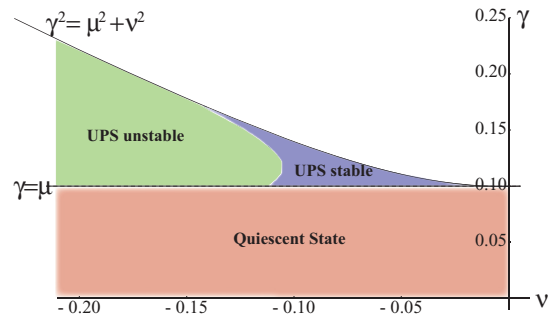


FIG. 10. (Color online) The PSS bifurcation diagram in the γ - ν space obtained by solving (22) numerically for $\mu = 0.050$ and $L = 400$.

observed in Ref. [26]. Conversely, for small L the Andronov-Hopf bifurcation leads directly to localized periodic solitons without a secondary one.

To verify these results, we have also performed a stability analysis of solutions in a Cartesian representation of the field ψ . We introduce the linear transformation $\psi = \mathcal{X} + i\mathcal{Y}$ in Eq. (1). Separating into real and imaginary parts, we obtain

$$\partial_t \mathcal{X} = \nu \mathcal{Y} + (\mathcal{X}^2 + \mathcal{Y}^2) \mathcal{Y} + \partial_{xx} \mathcal{Y} - \mu \mathcal{X} + \gamma \mathcal{X}, \quad (24)$$

$$\partial_t \mathcal{Y} = -\nu \mathcal{X} - (\mathcal{X}^2 + \mathcal{Y}^2) \mathcal{X} - \partial_{xx} \mathcal{X} - \mu \mathcal{Y} - \gamma \mathcal{Y}, \quad (25)$$

$$\begin{pmatrix} \delta \dot{\mathcal{X}} \\ \delta \dot{\mathcal{Y}} \end{pmatrix} = \begin{pmatrix} -\mu + \gamma - R_s^2 \sqrt{\gamma^2 - \mu^2} / \gamma & \nu + R_s^2 (2\gamma - \mu) / \gamma + \partial_{xx} \\ -\nu - R_s^2 (2\gamma + \mu) / \gamma - \partial_{xx} & -\mu - \gamma + R_s^2 \sqrt{\gamma^2 - \mu^2} / \gamma \end{pmatrix} \begin{pmatrix} \delta \mathcal{X} \\ \delta \mathcal{Y} \end{pmatrix}. \quad (28)$$

This system (28) yields results similar to those already observed using the polar representation.

III. PHASE SHIELDING SOLITON IN PHYSICAL SYSTEMS

In Sec. I we emphasized the universality of the PDNLS equation. Through an amplitude equation approach it can be shown that the equation is present in different physical systems. Based of this statement, one expects that results obtained in this context can be transposed to the original systems. In the following section we conduct numerical studies in an easy-plane ferromagnetic system in order to explore the observation of PSS solutions in such a system.

A. Forced magnetic wire

Solitons in magnetism have been intensively studied in past decades due to their possible technological applications. It is known that an easy-plane ferromagnetic spin chain in the presence of both a constant and a time-periodic external magnetic field perpendicular to the hard axis exhibits localized structures. Such structures are commonly refer to as localized precession states in a forced magnetic wire. Furthermore, experimental realizations of the model have been already achieved [29,30].

The forced magnetic wire is described phenomenologically by the Landau-Lifshitz-Gilbert (LLG) equation. Following an amplitude equation approach, it can be proved that, in the quasireversible limit, the system can be described by the parametrically driven and damped nonlinear Schrödinger equation [16].

Let us consider a one-dimensional anisotropic Heisenberg ferromagnetic chain formed by N classical spins or a magnetic moment subject to an external magnetic field. The direction of the chain is described by the z coordinate $\hat{z} = (0,0,1)$ and the external magnetic field is orthogonal to this direction, denoted by $\hat{x} = (1,0,0)$.

When the quantum effects are small enough, the vector \mathbf{S}_i can be treated as a classical spin or a magnetic moment

respectively. The solution for this set of equations (24) and (25) is

$$\mathcal{X}_s = R_s \cos(\varphi_0), \quad (26)$$

$$\mathcal{Y}_s = R_s \sin(\varphi_0), \quad (27)$$

where R_s and φ_0 are given by formulas (4) and (5) with $\delta_+ = \delta$.

We follow the same procedure shown above and take into account small perturbations ($\delta \mathcal{X}, \delta \mathcal{Y} \ll 1$) around the solutions $(\mathcal{X}, \mathcal{Y})$. Linearizing and using relations (4) and (5), we get the dynamical system

[16]. According to this latter assumption, the dynamics of the magnetic moment \mathbf{S}_i is governed by $\dot{\mathbf{S}}_i = -\gamma \mathbf{S}_i \times (\partial \mathcal{H} / \partial \mathbf{S}_i)$, where γ is the gyromagnetic constant and the Hamiltonian \mathcal{H} has the form

$$\mathcal{H} = -J \sum_{i=1}^N \mathbf{S}_i \mathbf{S}_{i+1} + 2D \sum_{i=1}^N (S_i^z)^2 - g\mu H_x \sum_{i=1}^N S_i^x. \quad (29)$$

Here J is the exchange coupling constant and H_x and D stand for the external magnetic field and the anisotropy energy, respectively.

To study the continuum limit of this set of ordinary differential equations, which accounts for a magnetic wire, we can assume that

$$\mathbf{S}_i(t) \rightarrow \mathbf{S}(z,t) \quad (30)$$

and

$$\frac{Jdz^2}{\gamma^{-1}} \left(\frac{\mathbf{S}_{i+1} - 2\mathbf{S}_i + \mathbf{S}_{i-1}}{dz^2} \right) \rightarrow l_{ex} \partial_z^2 \mathbf{S}(z,t), \quad (31)$$

where l_{ex} denotes the characteristic interaction length. Moreover, introducing a phenomenologically dissipative source, the Gilbert damping, the motion of the magnetization field is governed by the well-known Landau-Lifshitz-Gilbert equation [31]

$$\partial_\tau \mathbf{M} = \mathbf{M} \times [\mathbf{M}_{zz} - \beta(\mathbf{M} \cdot \hat{z}) + \mathbf{H}_e - \alpha \partial_\tau \mathbf{M}], \quad (32)$$

where $\mathbf{M} \equiv \mathbf{S}/M_s$ stands for the unit vector of the magnetization and M_s is the saturation magnetization. We have also introduce the normalization $\{\tau \rightarrow \gamma M_s t, \beta \rightarrow 4D/\gamma, \mathbf{H}_e \rightarrow g\mu \mathbf{M}/\gamma M_s\}$. Here $\beta > 0$ accounts for the anisotropy constant (easy-plane magnetization) and α the damping parameter. For several types of magnetic materials, this parameter is small [31]. When the magnetic field is time dependent, the above model (32) is a time-reversible system perturbed with injection and dissipation of energy, i.e., a quasireversible system, as long as this perturbation remains small.

As a result of the anisotropy and constant external field ($\mathbf{H}_e = H_0 \hat{x}$), the natural equilibrium of the previous model (32) corresponds to the magnetization field lying in the direction of the external magnetic field $\mathbf{M} = \hat{x}$. When spatial

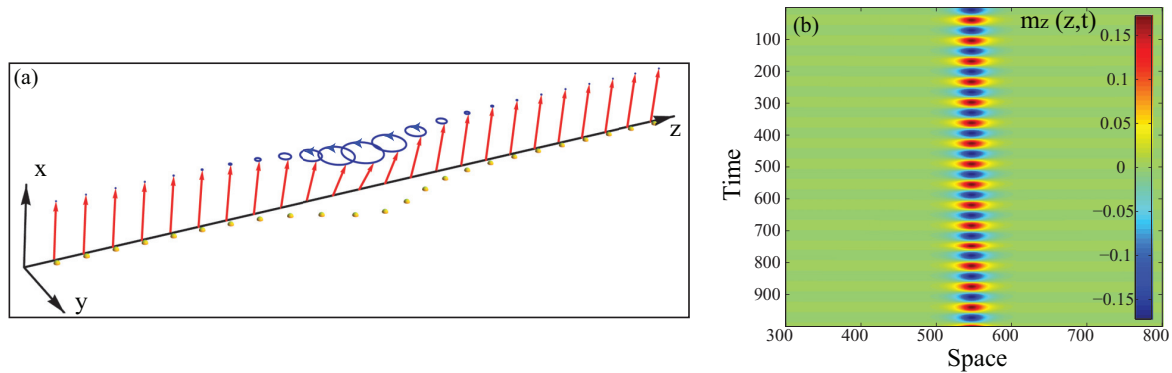


FIG. 11. (Color online) (a) Schematic representation of a soliton in a one-dimensional anisotropic ferromagnetic chain (magnetic wire). (b) Spatiotemporal evolution of a soliton for $L = 1024$, $H_0 = 4.800$, $\beta = 0.200$, $h_1 = 0.042$, $\alpha = 0.019$, and $\nu = -0.030$.

coupling is ignored, it is easy to show that the dynamics around this equilibrium is described by a nonlinear oscillator with natural frequency $\omega_0^2 = H_0(\beta + H_0)$ [16]. It is worth noting that in Eq. (32) the magnetization components are proportional to the external magnetic field, which therefore acts as a parametric forcing. Then if this field combines a constant and a time-periodic part ($\mathbf{H}_e = [H_0 + h_1]\hat{x}$, where $h_1 = \Gamma \cos(\omega t)$) oscillates about twice the natural frequency, $\omega \equiv 2(\omega_0 + \nu)$, and ν is the detuning parameter), the system exhibits a parametric resonance at $\Gamma^2(\beta/4\omega_0)^2 = \alpha^2(H_0 + \beta/2)^2 + \nu^2$ for small parameters $\{\alpha, \nu, H_0, \Gamma\}$. In the parameter space (Γ, ν) , the region above this curve corresponds to the Arnold tongue. Dynamically speaking, this resonance corresponds to an undamped precession of the magnetization unit vector around the direction of the external magnetic field with angular velocity ω_0 [Fig. 11(a)]. Thus, rewriting Eq. (32) for one of the components, for instance, m_z , after some calculations, considering

$$m_x^2 \approx 1 - \frac{m_y^2 + m_z^2}{2} \quad (33)$$

and

$$m_y \approx \frac{1}{H_0} \left[1 + \frac{\Gamma}{H_0} \right] \dot{m}_z, \quad (34)$$

one can obtain, in the weakly nonlinear regime [16],

$$\begin{aligned} \ddot{m}_z = & -\omega_0^2 m_z + (\beta + 2H_0)\partial_z^2 m_z - \mu \dot{m}_z - \frac{\dot{h}_1}{H_0} \dot{m}_z \\ & + (\beta + 2H_0)h_1 m_z + \frac{\beta(H_0 + h_1)}{2}(m_y^2 + m_z^2)m_z, \end{aligned} \quad (35)$$

where $\mu \equiv \alpha(H_0\beta/2)$ and $\gamma = \beta\Gamma/4\omega_0$ are, respectively, the effective driving strength and the detuning parameter.

Now, close to the parametric resonance, we can introduce the following ansatz [14,16] into Eq. (32):

$$m_z = 4 \sqrt{\frac{\omega_0 H_0}{\beta(\omega_0^2 + 3H_0^2)}} \text{Re}[A(z,t)]e^{i(\omega_0 + \nu)t} + W(z,t,A), \quad (36)$$

where $W(z,t,A)$ stands for a small correction. Linearizing and imposing the solvability condition for $W(z,t,A)$, one obtains the amplitude equation of the oscillations at dominant order

(the parametrically driven and damped nonlinear Schrödinger equation)

$$\partial_t A = -i\nu A - i|A|^2 A - i\partial_{ZZ} A - \mu A + \gamma \bar{A}, \quad (37)$$

where $Z \equiv \sqrt{2\omega_0/(\beta + 2H_0)}z$. The terms proportional to $\{\nu, \gamma, \mu\}$ stand for the detuning, effective driving, and damping of the magnetic system.

This equation has different homogeneous states, where the simplest one is $A = 0$, representing a constant magnetization along the external field direction ($\mathbf{M} = \hat{x}$). Single solitons are among the nontrivial steady states of Eq. (37) [15]. Other stationary state solutions of the PDNLS in the magnetic context can be found in Refs. [14,16,32,33].

1. The PSS in the magnetic wire

The chain of classical spins or magnetic wire subject to an external magnetic field represents an adequate physical system to study the formation of a phase shielding soliton. Different works have studied these magnetic localized states by means of the LLG model. Direct numerical simulations of Eq. (32) close to the Arnold tongue for negative detuning and for small values of dissipation and damping ($\mu \sim \gamma \ll 1$) reveal the formation of a localized precession state. Figure 11(b) shows the spatiotemporal evolution of the m_z component for this soliton.

However, phase shielding solitons are characterized for their phase structure. Therefore, we must extract information of the instantaneous phase angle ϕ_z from the knowledge of the oscillatory field $m_z(z,t)$. With this aim, we compute the instantaneous phase using the Hilbert transform technique for signal processing [34]. Let us recall that the original real field $m_z(z,t)$, can be express as

$$m_z(x,t) = \text{Re}[R(x,t)e^{i\phi(x,t)}], \quad (38)$$

where $\text{Re}(\cdot)$ represent the real part, $R(x,t)$ the modulus of the envelope, and $\phi(x,t)$ the phase.

The Hilbert transform technique reconstructs a complex variable $\theta_z = \theta_r + i\theta_i$ from the original real data θ_r and its one-sided Fourier transform $S_r(\omega)$,

$$S_r(\omega) = \int_{-\infty}^{\infty} \theta_r(x,t)\Theta(\omega)e^{-i\omega t} dt, \quad (39)$$

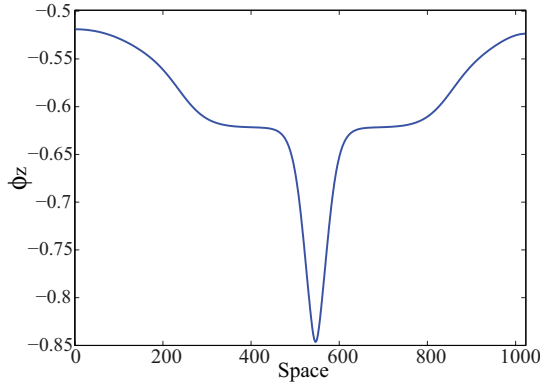


FIG. 12. (Color online) Reconstructed phase angle ϕ_z for $L = 1024$, $H_0 = 4.800$, $\beta = 0.200$, $h_1 = 0.042$, $\alpha = 0.019$, and $\nu = -0.030$. The appearance of two opposite fronts can be observed.

where $\Theta(\omega)$ is the Heaviside step function. To obtain the one-sided Fourier transformer of the imaginary part $S_i(\omega)$, we used the relation

$$S_i(\omega) = H(\omega)S_r(\omega), \quad (40)$$

where

$$H(\omega) = \begin{cases} -i, & 0 \leq \omega < \pi \\ i, & -\pi \leq \omega < 0 \end{cases} \quad (41)$$

is a 90° phase shifter or Hilbert transformer [35].

Calculating the inverse Fourier transform of $S_i(\omega)$, we get the imaginary part $\theta_i(x, t)$ of the complex variable. Hence the modulus $R(x, t)$ and phase $\phi(x, t)$ can be easily rebuilt from the real data. This method gives a good description of the modulus and phase for band-limited signals.

Using the above described Hilbert procedure, we analyze the spatial structure of the phase at different times. Figure 12 displays the phase $\phi_z(x)$ at a given value t for $L = 1024$. The presence of two stationary but opposite fronts, quite similar to those seen in previous numerical analysis of the parametrically driven and damped nonlinear Schrödinger equation, is clear.

The phase also exhibits a slot or hole at the center of the spatial phase angle. The appearance of this hole is a consequence of the nonlinear terms present at the original model. As we show above, the amplitude equation is an approximation, at dominant order, of the original system. Higher-order corrections are not taken into account [36]. Since the simulations of the magnetic system are directly from the LLG model, they include all the nonlinear corrections. Usually such corrections are not discernible in the modulus, but become relevant in the phase, especially close to the center of the soliton. Away from the core, the nonlinear corrections decreases exponentially, hence the formation of the slot close to the center.

Another important consequence of the nonlinear corrections is related to the phase front dynamics. Numerical simulations reveal that the phase fronts reach their steady state closer to the core of the soliton than in the usual parametrically driven and damped nonlinear Schrödinger equation. Since the magnetic dissipative soliton is a precession state, the phase angle ϕ_z exhibits a modulo 2π temporal periodicity. Therefore, there is a continuous change in the phase values

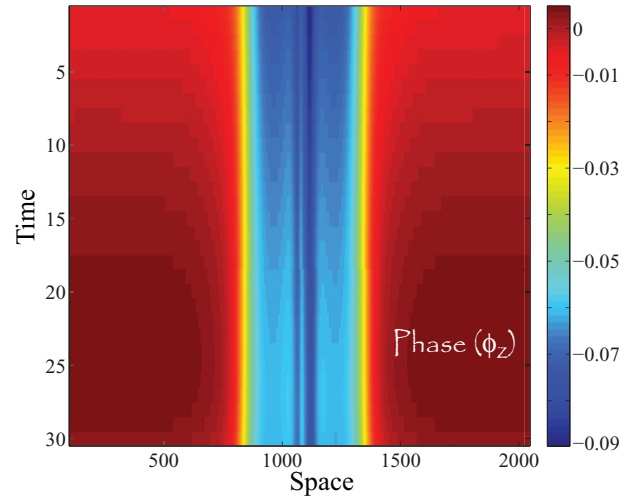
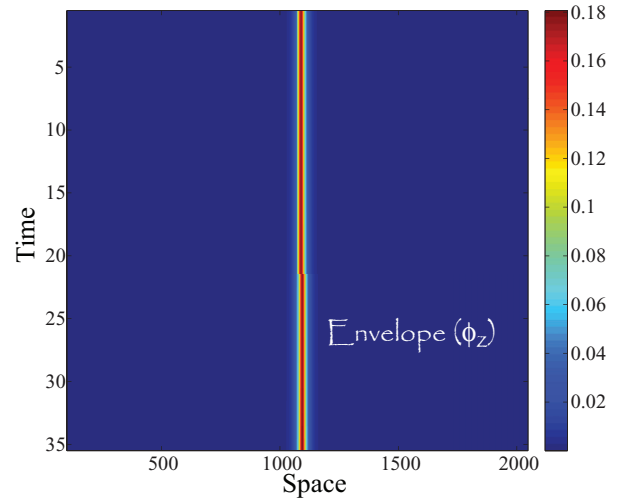


FIG. 13. (Color online) Stroboscopic spatiotemporal diagrams of the reconstructed envelope (top) and the phase angle ϕ_z (bottom) for $L = 2048$, $H_0 = 4.800$, $\beta = 0.200$, $h_1 = 0.042$, $\alpha = 0.019$, and $\nu = -0.030$. The spatial slot displayed by the phase has been removed.

close to the ends $(0, L)$ that introduces a fictitious periodic motion of the phase front around the center. To evaluate the phase dynamical behavior and the front positions, we take stroboscopic snapshots with the same periodicity as that of the soliton oscillation. Figure 13 displays the stroboscopic phase evolution of the phase structure. It is clear that a magnetic phase shielding soliton is formed. In order to emphasize the phase fronts, we have removed the slot in the vicinity of the center. The amplitude of the envelope is shown to stress the soliton position. Different numerical simulations with $L = 512, 1024$, and 2048 support this observation. It is important to note that all the observed phase shielding solitons are symmetric. Asymmetric solitons have not been observed so far in the magnetic wire.

In brief, the phase fronts in the magnetic wire reach a steady state, allowing the formation of a phase shielding soliton; the shielding phase is established closer to the soliton core position, in comparison with the PSS observed in the PDNLS equation; and the phase shield structure is always symmetric

[Fig. 4(a)]. The presence of nonlinear corrections plays an important role in the structure and dynamical behavior of the magnetic PSS.

IV. PHASE SHIELDING SOLITON IN TWO DIMENSIONS

Localized structures presented in the previous sections are considered only in one spatial dimension. In the present section we will study the existence, stability properties, and dynamical evolution of the two-dimensional extension of the phase shielding soliton. Such extensions are not evident. Conservative solitons observed in the nonlinear Schrödinger equation in one spatial dimension collapse in two spatial dimensions [37], i.e., these solutions are unstable in two spatial dimensions. Most of the experimental observations of localized structures in parametrically driven systems have been reported in two spatial dimensions, for instance, in fluid surface waves [38], oscillons in granular media [39], and isolated states in thermal convection [40]. Note that all these observations have been realized in dissipative systems. Furthermore, the greatest difficulty in characterizing theoretically localized states in two spatial dimensions is the lack of analytical expressions of these states.

In the context of conservative systems in two spatial dimensions perturbed with energy injection through parametrically temporal modulation and dissipation—*quasireversible systems* [4–8]—the prototypical model is the parametrically driven and damped nonlinear Schrödinger equation

$$\partial_t \psi = -i\nu\psi - i|\psi|^2\psi - i\nabla_{\perp}^2\psi - \mu\psi + \gamma\bar{\psi}, \quad (42)$$

where $\psi(\rho, \theta, t)$ is a complex field that accounts for the envelope of the oscillation for the system under study, $\nabla_{\perp}^2 \equiv (1/\rho)[\partial_{\rho}(\rho\partial_{\rho})] + (1/\rho^2)\partial_{\theta\theta}$ is the Laplacian operator in polar coordinates, $\rho > 0$, and $\theta \in [0, 2\pi]$. Equation (42) has been derived in two-spatial-dimensional physical systems such as the parametrically driven magnetic layer [32] and Kerr-type optical parametric oscillators [21]. In the conservative limit ($\mu = \gamma = 0$), the above equation is the nonlinear Schrödinger equation. This model is widely applied to understand wave phenomena in hydrodynamics, nonlinear optics, nonlinear acoustics, quantum condensates, heat pulses in solids, and various other nonlinear instability phenomena [41]. The nonlinear Schrödinger equation is a universal model for weakly dispersive and nonlinear media.

It is well known that Eq. (42) exhibits stable nonpropagative dissipative solitons in two spatial dimensions [42]. In contrast, in the conservative limit, Eq. (42) has unstable soliton solutions, which exhibit blowup in finite time [37]. The above phenomenon disappears in the model (42) as a result of the balance between injection and energy dissipation. In order to understand the existence, stability properties, and dynamical evolution of dissipative solitons shown by Eq. (42), let us to consider the ansatz

$$\psi = R_s(\rho, t)e^{i\phi(\rho, t)}. \quad (43)$$

Note that the above ansatz presents axial symmetry; that is, there is not an explicit dependence on the angle θ . This assumption is based on the numerical simulations, where we

do not observe significant angular dependence. Inserting (43) in Eq. (42), we obtain

$$\begin{aligned} \partial_t R_s &= 2\partial_{\rho} R_s \partial_{\rho} \phi + \frac{R_s}{\rho} \partial_{\rho} \phi + R_s \partial_{\rho\rho} \phi - \mu R_s \\ &+ \gamma R_s \cos(2\phi), \end{aligned} \quad (44)$$

$$\begin{aligned} R_s \partial_t \phi &= -\nu R_s - R_s^3 - \frac{\partial_{\rho} R_s}{\rho} - \partial_{\rho\rho} R_s + R_s (\partial_{\rho} \phi)^2 \\ &- \gamma R_s \sin(2\phi). \end{aligned} \quad (45)$$

Analogously to the one-dimensional problem, let us assume a constant phase $\phi = \phi_0$; thus

$$\cos(2\phi_0) = \frac{\mu}{\gamma}, \quad (46)$$

$$\partial_{\rho\rho} R_s = \delta R_s - R_s^3 - \frac{\partial_{\rho} R_s}{\rho}, \quad (47)$$

where $\delta \equiv -\nu + \sqrt{\gamma^2 - \mu^2}$. As we have mentioned before, there is not an analytical solution of the localized state in two dimensions [42]. However, using the variational method, one can obtain a good approximation [32,43]

$$R_s(\rho) \approx A_0 \sqrt{\delta} \operatorname{sech}\left(B_0 \sqrt{\frac{\delta}{2}} \rho\right), \quad (48)$$

where $A_0 = 2.166$ and $B_0 = 1.32$. However, this approximation does not describe the asymptotic behavior of the dissipative soliton. The asymptotic behavior of the dissipative soliton is of the form

$$R_s(\rho \rightarrow \infty) \rightarrow \frac{e^{-\sqrt{\delta}\rho}}{\sqrt{\rho}}. \quad (49)$$

The interaction of a pair of dissipative solitons that is of exponential type as a function of the distance between solitons has been characterized in Ref. [32]. Numerical simulations of an easy-plane ferromagnetic layer submitted to a magnetic field that combines a constant and an oscillating part show good agreement with this interaction law.

A. Numerical observation of phase shielding solitons in two dimensions

The existence of 2D solitons described by the PDNLS (42) raises the question of whether it is possible to observe a shielding phase in this case. Based on the previous simulations carried out in one dimension, we explore a similar parameter region in the 2D case, close to the Arnold tongue, in order to observe the possible formation of phase shielding solitons.

Indeed, we have characterized two type of phase shielding configurations. The first type consists of a phase front with axial symmetry in the range $[0, 2\pi]$. The connected uniform states are, analogously to the 1D case, given by the phase equilibria determined by relation (46). Figure 14 shows the typical structure of this symmetrical state around the soliton position. If we consider a 1D stationary front solution in a semi-infinite domain ($\rho > 0$), the 2D symmetric phase solution corresponds to a 2π rotation around an axis whose origin is placed at the position of the dissipative soliton. It is important to note that the process of formation of this symmetrical state is complex since one needs special initial conditions close to the equilibrium state.

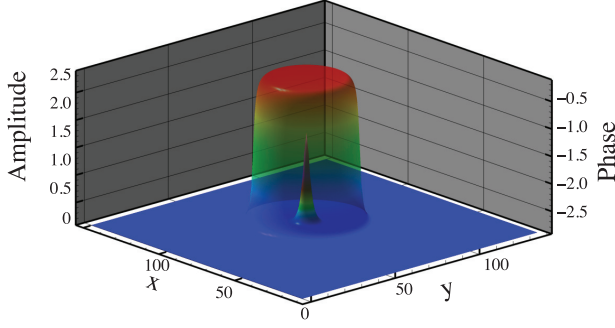


FIG. 14. (Color online) Front view of a stationary 2D symmetric phase shielding soliton observed in two-dimensional numerical simulations of the parametrically driven and damped nonlinear Schrödinger equation with $\gamma = 0.560$, $\nu = -0.068$, and $\mu = 0.250$. The phase and amplitude field are represented simultaneously. Colored shadow renders the phase shell-like structure $\varphi(x, y)$ that surrounds the amplitude soliton localized at the center $R(x, y)$.

The second type is characterized by a phase front axially symmetric from $[0, \pi]$ and an analogous front with different asymptotic states from $[\pi, 2\pi]$, i.e., each phase front has semi-axial symmetry. The process of formation of this configuration starts with a well-formed 2D soliton that is slightly perturbed. After some complex phase transient state, the system exhibits the appearance of a circular phase front that spreads rather slowly. Figure 15(a) displays this primary stage. However, asymptotically, the circular structure becomes asymmetrical, giving rise to a new semicircular front that still propagates in the range $[\pi, 2\pi]$ [see Fig. 15(b)]. Finally, the whole structure becomes stationary, creating a 2D asymmetric phase shielding soliton. Unlike the symmetric case, the steady phase solutions coincide only with a π rotation around the soliton position as the center of rotation [see Fig. 15(c)]. Additionally, numerical simulations performed in a close region of parameters show the same dynamical behavior. Figure 16 give us a comparison between the stationary configuration of this shieldlike phase and the soliton size for a different set of parameter values $\{\mu, \nu, \gamma\}$.

It is noteworthy that this second type of two-dimensional state is characterized by being composed of all the solutions found in one dimension. Indeed, if one performs different cuts containing the center (soliton position), one can recognize the observed solutions in one dimension (see Fig. 4). Another interesting property is the following: If one calculates the phase change on a path that connects two opposite points with respect to the soliton position ($\int_{\Gamma} \vec{\nabla} \varphi d\vec{s}$) within the region close to the position of the soliton one finds that this is zero. Nevertheless, if one takes this type of path far away from the soliton position, one finds $\int_{\Gamma} \vec{\nabla} \varphi d\vec{s} = \pm\pi$.

As an additional remark we would like to point out the stability of the 2D phase shielding solitons. Axially symmetric PSSs are attained only by setting up special initial conditions close to the steady state. A slight perturbation in its modulus leads to a symmetry breaking where the axial symmetry is lost and a semiaxial symmetry appears. Hence, numerically, the second type of PSS solitons has a large basin of attraction.

B. Analytic approach to PSSs in two dimensions

In this section we will discuss an analytical approach for the shielding phase solitons in two dimensions. From numerical simulations (see Fig. 16), we can observe that the phase emerges far from the soliton position. In the same manner as in Sec. II B1, to obtain the dominant phase correction we consider the exponential asymptotic decay of the modulus. Under this consideration ($\rho \rightarrow \infty$), we use the ansatz

$$R_s(\rho \rightarrow \infty) \cong \frac{e^{-\sqrt{\delta}(\rho-\rho_0)}}{\sqrt{\rho}}, \quad (50)$$

$$\phi(\rho \rightarrow \infty) = \phi_F(\rho - \rho_F(t)), \quad (51)$$

where ρ_0 describes the soliton position, i.e., corresponds to the position of the maximum amplitude of the soliton modulus. Moreover, we have promoted the position of the phase front core to a time-dependent function $\rho_F(t)$. We consider that the PSSs possess an axial symmetry for the modulus and the phase. For the sake of simplicity and without loss of generality, we can choose $\rho_0 = 0$ as the coordinate origin; at dominate order, we get a similar Newton-type equation as in the 1D case

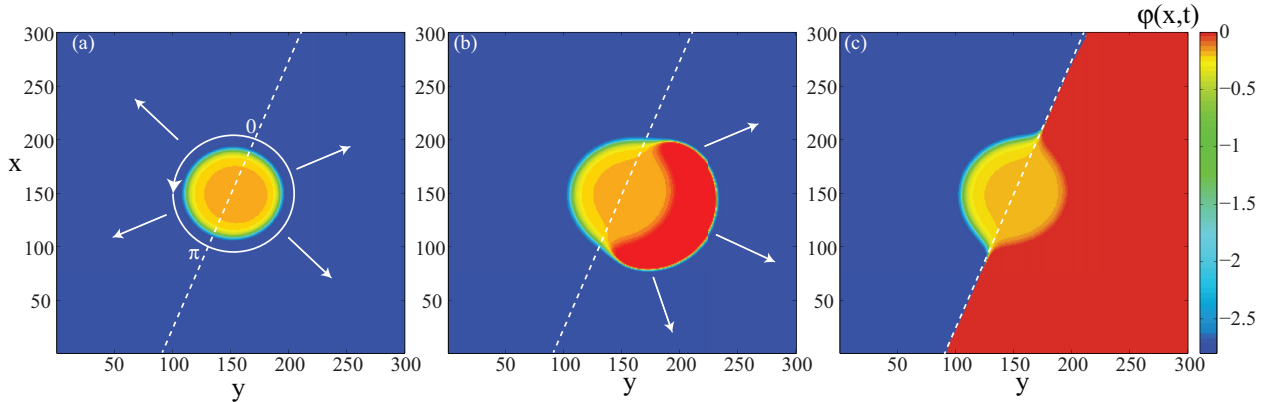


FIG. 15. (Color online) Snapshots of the phase evolution of a typical 2D PSS after a perturbation with $\gamma = 0.083$, $\nu = -0.063$, and $\mu = 0.058$. (a) Initially the soliton is slightly disturb. A circular front starts to propagate. (b) An additional propagative semicircular front appears. (c) The final steady configuration exhibiting a semi-axial symmetry. The dashed curve represents the θ axis.

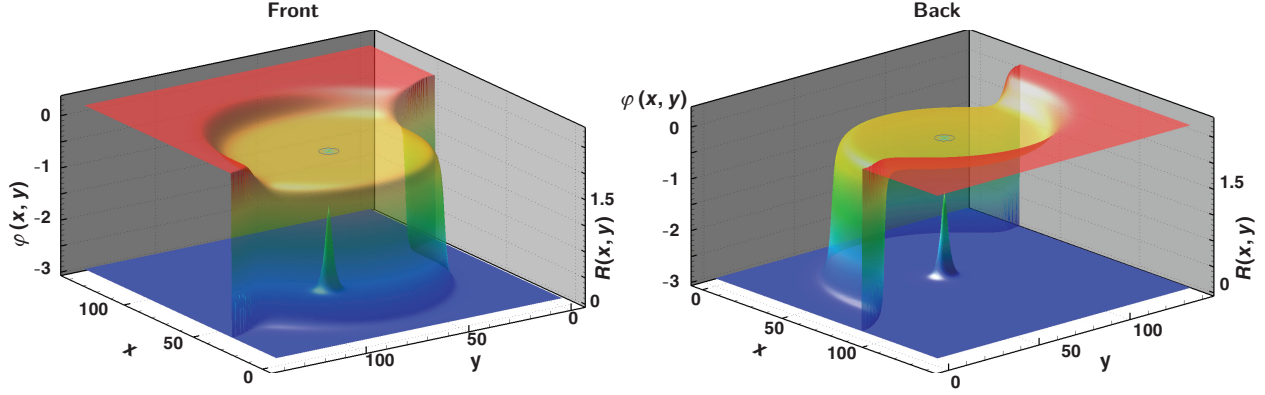


FIG. 16. (Color online) Front and back views of a stationary phase shielding soliton observed in two dimensions for the parametrically driven and damped nonlinear Schrödinger equation with $\gamma = 0.140$, $\nu = -0.068$, and $\mu = 0.125$. The phase and amplitude field are represented simultaneously. Colored shadow renders the phase shell-like structure $\varphi(x, y)$ that surrounds the amplitude soliton localized at the center $R(x, y)$.

($\rho \gg 1$)

$$\partial_{\rho\rho}\phi_F \approx 2\sqrt{\delta}\partial_{\rho}\phi_F + \mu - \gamma \cos(2\phi_F). \quad (52)$$

Thus 2D phase solutions have a front solution at dominant order of the form

$$\phi(\rho, \theta, \rho_F) \approx \arctan \left[\frac{\sqrt{\gamma \pm \mu}}{\sqrt{\gamma \mp \mu}} \tanh \frac{\sqrt{\gamma^2 - \mu^2}(\rho - \rho_F)}{2\sqrt{\delta}} \right]. \quad (53)$$

This solution agrees with numerical simulations, as we illustrate in Fig. 17. To account analytically for the axial or semiaxial symmetry of two-dimensional PSSs, let us introduce an adequate coordinate system $\{\mathbf{r}, \theta\}$, where $\mathbf{r} \in (-\infty, \infty)$, $|\mathbf{r}| = \rho$, and $\theta \in [0, \pi)$, which is not the usual polar coordinate. Considering $R_s \equiv R_s(\mathbf{r}, t)$ and $\phi \equiv \phi(\mathbf{r}, t)$ for the semiplane domain consisting of $[0, \pi)$ and $\mathbf{r} = (0, \infty)$, we replace the ansatz (50) in (47), obtaining again Eq. (52). Therefore, we have deduced a phase front solution with the required

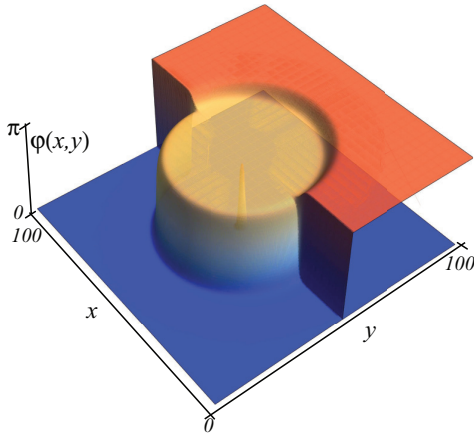


FIG. 17. (Color online) A 2D phase shielding soliton with semiaxial symmetry given at dominant order by the analytical function (53) with $\gamma = 0.15$, $\mu = 0.1$, and $\nu = -0.15$. The amplitude $R(x, y)$ is plotted simultaneously to illustrate the soliton position.

semiaxial symmetry. Analogously to the complementary semiplane domain $\mathbf{r} \in (-\infty, 0)$ and $\theta \in [0, \pi)$, we can find the complementary phase front solution. Taking the whole domain of \mathbf{r} and considering the different stationary front solutions of (52), we build up at dominant order a phase front with the asymmetrical shape observed in numerical simulations (see Fig. 16). Notice that in this approximation for PSSs with semiaxial symmetry, the interface separating the different regions is abrupt (see Fig. 17), which is a consequence of the coordinate system used to describe these solutions. The PSSs obtained numerically are smooth in this junction region (see Fig. 16).

C. Front dynamics

The front dynamics of phase fronts at dominant order is described by the equation obtained by replacing (50) and (51) in (45),

$$-\dot{\rho}_F(t)\partial_z\phi_F = -(\nu + \delta) - \frac{e^{-2\sqrt{\delta}\rho}}{\rho} + (\partial_{\rho}\phi_F)^2 - \gamma \sin(2\phi_F), \quad (54)$$

where we have defined the appropriated comoving coordinate $z \equiv \rho - \rho_F$. Multiplying the above equation by $\partial_z\phi_F$ and introducing the inner product

$$\langle\langle f|g \rangle\rangle \equiv \int_{-\infty}^{\infty} \int_0^{\pi} f g \rho d\theta dz, \quad (55)$$

we obtain the following equation for the front dynamics:

$$\dot{\rho}_F = \frac{\tilde{A} + A\rho_F + B e^{-2\sqrt{\delta}\rho_F}}{C\rho_F}, \quad (56)$$

where

$$\begin{aligned} \tilde{A} &\equiv \langle\langle \gamma \sin(2\phi_F) z | \partial_{\rho}\phi_F \rangle\rangle, \\ A &\equiv \langle\langle [-(\nu + \delta) + (\partial_{\rho}\phi_F)^2] | \partial_{\rho}\phi_F \rangle\rangle, \\ B &\equiv \langle\langle e^{-2\sqrt{\delta}z} | \partial_{\rho}\phi_F \rangle\rangle, \quad C \equiv \langle\langle \partial_{\rho}\phi_F | \partial_{\rho}\phi_F \rangle\rangle. \end{aligned} \quad (57)$$

Equation (56) can be interpreted as a Newton-type equation that describes an overdamping particle in the presence of a

force composed of three terms: a constant, a term inversely proportional to the position, and an exponential force. The constant force is responsible for spreading the phase front to the outside; in contrast, the exponential force causing the phase front propagates towards the position of the dissipative soliton in the center. The balance between these forces generates an equilibrium position for the phase front, which is consistent with the observed dynamics. At dominant order the phase dynamics is affected in two spatial dimensions by an extra term, which is inversely proportional to the distance. The exponential term is modified by a logarithmic correction. Therefore, for large distances the phase shielding soliton dynamics in two dimensions is similar to that observed in one dimension.

Similarly to Sec. II B2, we can include higher-order corrections in the amplitude of the modulus and get more accurate solutions for the structure and dynamics of phase fronts in two spatial dimensions. This allows us to understand that PSSs are composed of dissipative solitons with a different homogeneous phase (see Sec. II B2).

V. FORCED MAGNETIC LAYER

An easy-plane ferromagnetic layer submitted to an external parametric forcing has been analyzed within the framework of the LLG model. Such a system exhibits the formation patterns, domain walls, and localized states near a parametric resonance. By means of the amplitude equation, an interaction law of 2D localized precession states has been derived [32]. However, the magnetic layer lacks a phase numerical study for its localized structures.

Let us introduce the main features of the description of a parametrically forced magnetic layer. Let us consider an anisotropic Heisenberg ferromagnetic layer formed by $N_x \times N_y$ classical spins or magnetic moments exposed to an external magnetic field, which is contained in the plane (x, y) and oriented in the direction $\hat{x} \equiv (1, 0, 0)$. Following the one-dimensional analysis exposed in Sec. III, we can find that the motion of the magnetization field is governed by the Landau-Lifshitz-Gilbert equation [31]

$$\partial_t \mathbf{M} = \mathbf{M} \times [\nabla_{\perp}^2 \mathbf{M} - \beta(\mathbf{M} \cdot \hat{z}) + \mathbf{H}_e - \alpha \partial_t \mathbf{M}], \quad (58)$$

where $\nabla_{\perp}^2 \equiv \partial_{xx} + \partial_{yy}$ is the Laplacian operator and $\mathbf{M} = \mathbf{S}/M_s$ stands for the unit vector of the magnetization, with M_s the saturation magnetization. Again, we have considered a normalization of scales and parameters $\{\tau \rightarrow \gamma M_s t, \beta \rightarrow 4D/\gamma M_s, \mathbf{H}_e \rightarrow g\mu\mathbf{H}/\gamma M_s\}$, where $\beta > 0$ is the uniaxial easy-plane anisotropy constant and α is the damping parameter. Like the one-dimensional case, the presence of damping $\alpha > 0$ and an external and constant field $\mathbf{H}_e = H_0 \hat{x}$ leads to a magnetization in the direction of the external field $\mathbf{M} = \hat{x}$. When spatial coupling is ignored, it is easy to show that the dynamics around this equilibrium is described by a nonlinear oscillator with natural frequency $\omega_0 = \sqrt{H_0(\beta + H_0)}$.

Given that the magnetization components are proportional to the external magnetic field, it acts as a parametric forcing. Applying an external magnetic field with both a constant and a time periodic part of the form $\mathbf{H}_e = [H_0 + \Gamma \cos(\omega t)]\hat{x}$, oscillating about twice the natural frequency $\omega = 2(\omega_0 + \nu)$, where ν is the detuning parameter, the system exhibits a

parametric resonance at $\Gamma^2(\beta/4\omega_0)^2 = \alpha^2(\beta/2 + H_0)^2 + \nu^2$ for small $\{\nu, H_0, \alpha, \Gamma\}$.

The inclusion of spatial coupling yields the formation of a localized state near the parametric resonance. To understand the dynamics of such a state, in the quasireversible limit $\Gamma \sim \nu \sim \alpha \ll \omega_0$ and close to the parametric resonance, we can introduce the following ansatz into (58):

$$\begin{aligned} M_x &\approx 1 - \frac{M_y^2 + M_z^2}{2}, & M_y &\approx \frac{1}{H_0} \left[1 + \frac{\Gamma}{H_0} \right] \dot{M}_z, \\ M_z &\approx 4 \sqrt{\frac{\omega_0 H_0}{\beta(\omega_0^2 + 3H_0^2)}} \psi(\rho, t) e^{i(\omega_0 + \nu)t} + \text{c.c.} \end{aligned} \quad (59)$$

After straightforward calculations and imposing a solvability condition for the corrections of the above ansatz, we find that the system can be described by the parametrically driven damped nonlinear Schrödinger equation

$$\partial_t \psi = -i\nu\psi - i|\psi|^2\psi - i\nabla_{\perp}^2 \psi - \mu\psi + \gamma\bar{\psi},$$

with $\gamma = \beta\Gamma/4\omega_0$ and $\mu = (\beta/2 + H_0)\alpha$.

As we have discussed early, there is not an analytical solution for the two-dimensional PDNLS equation. However, from the approximated localized state (48), one can infer that for negative detuning, the localized breather magnetic solution appears by a saddle-node bifurcation when dissipation and energy injection are equal ($\gamma \sim \mu$ and $\nu < 0$). Furthermore, this solution is unstable when the uniform magnetization $\mathbf{M} = \hat{x}$ becomes unstable at the Arnold tongue ($\gamma^2 = \nu^2 + \mu^2$ and $\nu < 0$). The modulus width and height are given by $\sqrt{2\delta}$ and $1/\sqrt{\delta}$, respectively.

A. The PSS in the magnetic layer

Numerical simulations in appropriate parameter regions of the magnetic layer show clearly the formation of localized precession states. Previous studies have performed a numerical fit of the magnetic solution with the approximative solution (48), showing good agreement [43]. According to our analysis of the 2D PDNLS equation, an easy-plane ferromagnetic layer submitted to an external magnetic field that combines a constant and an oscillating part should present a shell-type phase structure. To capture the dynamical behavior of the phase, we perform numerical simulations of the Landau-Lifshitz-Gilbert equation (58) over a square grid $L \times L$ for $L = 512$. This system size is large enough to exhibit PSS formation (based on the results that we have obtained in one spatial dimension). Following the Hilbert transform technique, we have reconstructed the phase. Figure 18 depicts a snapshot of a localized magnetic state for $H_0 = 0.1000$, $\lambda = 0.0100$, $\beta = 1.0000$, $\nu = -0.0035$, and $\Gamma = 0.0081$. As we expected, a stable shielding phase is formed surrounding the soliton. In the same figure, we show the corresponding soliton solution.

As in the 1D magnetic case, this shell-type structure is always symmetric having a 2π rotation. A modulo 2π periodicity is also present. The phase front also reaches its stationary state closer to the typical slot present in the center. This produces a bell-like shape as we can observed in Fig. 18.

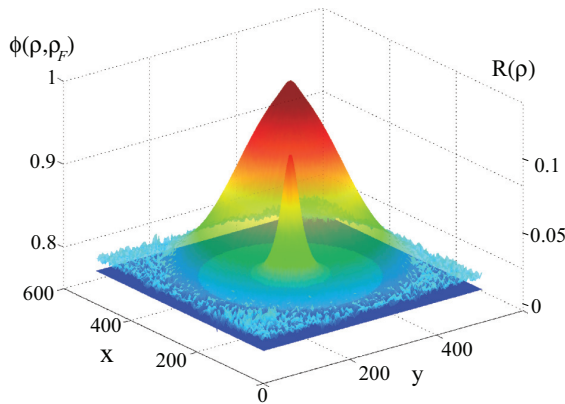


FIG. 18. (Color online) Phase shielding soliton obtained by a numerical simulation of Eq. (58) in a square magnetic plane $L \times L$ with $L = 512$, $H_0 = 0.100\,00$, $\beta = 1$, $h_1 = 0.008\,00$, $\alpha = 0.019\,00$, and $\nu = -0.003\,94$. The reconstructed phase in two dimensions $\phi_z(\rho, \rho_z)$ and the amplitude field $R(\rho)$ are represented simultaneously. The bell-like shape reveals the presence of the characteristic slot, observed also in the 1D case, in the center of the plane.

In this situation, the slot is smaller than in the 1D case and it can be appreciated at the top of the phase structure.

Despite the numerical simulations revealing a stationary phase structure around a precession state—a phase shielding soliton—a deeper study is required to establish qualitatively and quantitatively the effect of the nonlinear corrections over the phase dynamics.

VI. CONCLUSION

Parametrically forced systems exhibit oscillatory localized solutions, which are an extension to dissipative systems of conservative breathers. We have shown the emergence and characterization of unexpected phase structures surrounding the modulus of a localized state: the phase shielding soliton. Different types of localized states have been observed in numerical simulations. The appearance of each phase configuration strongly depends of initial conditions. A slight change of these conditions can lead to a different phase shielding structure using the same system parameters. However, a full comprehension of their basin of attraction as well as their stability is an open question.

Because of the universality of this phenomenon, we have described this type of oscillatory localized state in the context of the parametrically driven and damped nonlinear Schrödinger equation. Considering the asymptotic behavior of the amplitude solution away from the soliton position, we have derived an analytical expression for the front phase in a semi-infinite domain. The stationary phase front represents heteroclinic orbits in the $\{\varphi, \partial\varphi\}$ space. Such states present different types of configurations. The dynamical behavior of these fronts exhibits a nonuniform translation that is ruled by two antagonistic forces generating stable equilibria.

A deeper analysis of numerical simulations reveals that PSS solutions are composed of two qualitatively different

regions: inner and outer regions. Both regions are separated by a crossover point between the exponential decay rates of the stable and the unstable UPS solution. Therefore, the PSSs are composed of both UPS solutions.

We investigate the PSS stability by means of numerical analysis. We find that the phase stability is dependent on the system size L . Below a critical value of L , the phase remains uniform, but for large enough values of it, the system destabilizes through an Andronov-Hopf bifurcation. We also show that the system also presents an instability for a given L , but for large values of the amplitude or the frequency of the forcing $\{\gamma, \nu\}$. Hence the shielding phase solutions exist in a wide parameter region far from the limit $\mu \sim \gamma$. Both critical values are related to the length of the inner region, i.e., to the exponential decay of the stable solution.

To confirm the presence of the shell-type phase structure in parametrically driven solitons, we have studied an anisotropic Heisenberg ferromagnetic chain formed by N classical spins or magnetic moments subject to an external magnetic field. As we expected, the phase of the dissipative soliton exhibits the formation of two counterpropagative fronts, analogously to those observed for the PDNLS model.

A feature characteristic of this phase structure is the presence of a pronounced slot close to the position of dissipative soliton. Such large phase variation is a result of the nonlinear corrections of the envelope. These corrections corresponds to higher-order terms that are not taken into account in the amplitude equation approach at dominant order. Such corrections are negligible far from the position of dissipative soliton but become relevant in the phase near the soliton core.

The presence of corrective terms also affects the phase dynamics itself, as the phase front dynamics is led by an exponentially small force. This is notorious in the magnetic wire where the corrective terms cause the phase front solutions to reach their equilibrium states closer to the soliton position.

Recent studies have demonstrated that the parametrically driven and damped nonlinear Schrödinger equation does not account for all the localized structures observed in magnetic wire [32,44]. Consequently, the inclusion of higher order terms in the PDNLS equation is necessary for a complete description of phase front dynamics.

We have extended the phase analysis to the two-dimensional case. The parametrically driven and damped nonlinear Schrödinger equation exhibits two types of configurations: an axially symmetric state and a semiaxial symmetry composed of two semicircular fronts. The phase front dynamics is also well described by a Newtonian-type equation in the asymptotic limit of large distance ($\rho \rightarrow \infty$). We have derived a dynamical equation that predicts a stable equilibrium position for the front and accounts for the shell-type phase structure. It is worth noting that the phase front dynamics is led again by an exponentially small force. Hence small perturbations can change radically shell-type phase structures of phase shielding solitons.

We investigate the phase behavior of oscillatory dissipative solitons in an anisotropic Heisenberg ferromagnetic layer formed by $N_x \times N_y$ classical spins or magnetic moments exposed to an external magnetic field. The numerical simulations show the existence of a complicated structure for the phase.

The characteristic slot, observed in 1D systems, is also present in the 2D case. As before, the relevance of the corrective terms is evident.

The presence of corrective terms has another interesting consequence. Usually the corrective terms are related to the particular physical problem under study. The particularity of these additional terms can produce the observation of different phase phenomena for different physical systems. Therefore, we expect the observation of a variety of different phenomena in other physical systems. Still, a broader analysis of different systems, in order to establish the effect of each corrective term, is required.

In brief, close to the parametric resonance, one expects that the dynamics is well described by the parametrically driven and damped nonlinear Schrödinger equation. Indeed, this amplitude equation has been derived in several physical contexts to describe the appearance of patterns and localized states. Far from the parametric resonance, the PDNLS equation has been used as prototypical model of the dynamics. We

show that the localized state exhibited by this model has an unexpected and intriguing shell-type phase structure. We expect that this type of phase behavior would be observed on several parametrically driven systems such as mechanical, optical, granular, fluid, magnetic, and chemical systems.

ACKNOWLEDGMENTS

The authors are grateful for fruitful discussions with L. Gordillo, N. Perinet, C. Falcón, and D. Laroze and to the anonymous referee for providing constructive comments and help in improving the contents of this paper. The authors acknowledge financial support from the ANR-CONICYT 39 (Grant No. ANR-2010-INTB-402-02), “Colors.” M.G.C. and M.A.G-N. are grateful for the financial support from FONDECYT Projects No. 1120320 and No. 3110024, respectively. Y.Z. acknowledges financial support from CONICYT by Beca Magister Nacional.

-
- [1] *Localized States in Physics: Solitons and Patterns*, edited by O. Descalzi, M. Clerc, S. Residori, and G. Assanto (Springer, Berlin, 2011).
- [2] H.-G. Purwins, H. U. Bödeker, and Sh. Amiranashvili, *Adv. Phys.* **59**, 485 (2010).
- [3] T. Ackemann, W. Firth, and G. Oppo, *Adv. At. Mol. Opt. Phys.* **57**, 323 (2009).
- [4] M. Clerc, P. Couillet, and E. Tirapegui, *Int. J. Bifurcat. Chaos* **11**, 591 (2001).
- [5] M. Clerc, P. Couillet, and E. Tirapegui, *Phys. Rev. Lett.* **83**, 3820 (1999).
- [6] M. Clerc, P. Couillet, and E. Tirapegui, *Prog. Theor. Phys. Suppl.* No. 139, 337 (2000).
- [7] M. Clerc, P. Couillet, and E. Tirapegui, *Opt. Commun.* **167**, 159 (1999).
- [8] M. Clerc, P. Couillet, N. Vandenbergh, and E. Tirapegui, *Phys. Lett. A* **287**, 198 (2001).
- [9] J. Miles, *J. Fluid Mech.* **83**, 153 (1977).
- [10] I. V. Barashenkov and E. V. Zemlyanaya, *Phys. Rev. Lett.* **83**, 2568 (1999).
- [11] V. I. Arnold, *Geometrical Methods in the Theory of Ordinary Differential Equations* (Springer, New York, 1983).
- [12] N. V. Alexeeva, I. V. Barashenkov, and G. P. Tsironis, *Phys. Rev. Lett.* **84**, 3053 (2000).
- [13] M. G. Clerc, S. Coulibaly, and D. Laroze, *Int. J. Bifurcat. Chaos* **11**, 3525 (2009).
- [14] M. G. Clerc, S. Coulibaly, and D. Laroze, *Phys. Rev. E* **77**, 056209 (2008).
- [15] I. Barashenkov, M. Bogdan, and V. Korobov, *Europhys. Lett.* **15**, 113 (1991).
- [16] M. G. Clerc, S. Coulibaly, and D. Laroze, *Physica D* **239**, 72 (2010).
- [17] W. Zhang and J. Viñals, *Phys. Rev. Lett.* **74**, 690 (1995).
- [18] M. Clerc, S. Coulibaly, N. Mujica, R. Navarro, and T. Sauma, *Philos. Trans. R. Soc. London Ser. A* **367**, 3213 (2009).
- [19] X. Wang and R. Wei, *Phys. Rev. E* **57**, 2405 (1998).
- [20] B. Denardo, B. Galvin, A. Greenfield, A. Larraza, S. Putterman, and W. Wright, *Phys. Rev. Lett.* **68**, 1730 (1992).
- [21] S. Longhi, *Phys. Rev. E* **53**, 5520 (1996).
- [22] M. G. Clerc, S. Coulibaly, M. A. Garcia-Ñustes, and Y. Zárate, *Phys. Rev. Lett.* **107**, 254102 (2011).
- [23] A. C. Newell, *Solitons in Mathematics and Physics* (Society for Industrial and Applied Mathematics, Philadelphia, 1985).
- [24] P. Couillet, T. Frisch, and G. Sonnino, *Phys. Rev. E* **49**, 2087 (1994).
- [25] L. M. Pismen, *Patterns and Interfaces in Dissipative Dynamics*, Springer Series in Synergetics (Springer, Berlin, 2006).
- [26] M. Bondila, I. V. Barashenkov, and M. M. Bogdan, *Physica D* **87**, 314 (1995).
- [27] S. H. Strogatz, *Nonlinear Dynamics and Chaos: With Applications to Physics, Biology, Chemistry and Engineering* (Addison-Wesley, Reading, MA, 1994).
- [28] J. Hale and H. Koçak, in *Dynamics and Bifurcations*, edited by J. E. Marsden, L. Sirovich, M. Golubitsky, W. Jäger, and F. John, Texts in Applied Mathematics, Vol. 3 (Springer, New York, 1991).
- [29] A. B. Ustinov, V. E. Demidov, A. V. Kondrashov, B. A. Kalinikos, and S. O. Demokritov, *Phys. Rev. Lett.* **106**, 017201 (2011).
- [30] A. B. Ustinov, B. A. Kalinikos, V. E. Demidov, and S. O. Demokritov, *Phys. Rev. B* **81**, 180406 (2010).
- [31] G. Bertotti, I. D. Mayergoyz, and C. Serpico, *Nonlinear Magnetization Dynamics in Nanosystems* (Elsevier, Amsterdam, 2009).
- [32] M. G. Clerc, S. Coulibaly, and D. Laroze, *Europhys. Lett.* **90**, 38005 (2010).
- [33] I. V. Barashenkov and E. V. Zemlyanaya, *Phys. Rev. E* **83**, 056610 (2011).
- [34] J. Claerbout, *Fundamentals of Geophysical Data Processing* (McGraw-Hill, New York, 1976).
- [35] A. V. Oppenheim and R. W. Schaffer, *Digital Signal Processing* (Prentice Hall, Englewood Cliffs, NJ, 1975).

- [36] M. Cross and H. Greenside, *Pattern Formation and Dynamics in Nonequilibrium Systems* (Cambridge University Press, New York, 2009).
- [37] L. Berge, *Phys. Rep.* **303**, 260 (1998).
- [38] W. S. Edwards and S. Fauve, *J. Fluid Mech.* **278**, 123 (1994).
- [39] P. B. Umbanhowar, F. Melo, and H. L. Swinney, *Nature (London)* **382**, 793 (1996).
- [40] R. Heinrichs, G. Ahlers, and D. S. Cannell, *Phys. Rev. A* **35**, 2761 (1987).
- [41] C. Sulem and P.-L. Sulem, in *Nonlinear Schrödinger Equations: Self-Focusing and Wave Collapse*, edited by J. E. Mardson and L. Sirovich, Applied Mathematical Sciences, Vol. 139 (Springer, New York, 1999).
- [42] I. V. Barashenkov, N. V. Alexeeva, and E. V. Zemlyanaya, *Phys. Rev. Lett.* **89**, 104101 (2002).
- [43] O. Bang, Y. S. Kivshar, A. V. Buryak, A. De Rossi, and S. Trillo, *Phys. Rev. E* **58**, 5057 (1998).
- [44] M. G. Clerc, S. Coulibaly, and D. Laroze, *Europhys. Lett.* **97**, 30006 (2012).